FULLERENE C_{60} BASED NANOSTRUCTURES BY SELF-ASSEMBLY AND MOLECULAR RECOGNITION

By

CHRISTOPHER BONGANI MTSHALI

Thesis submitted in partial fulfilment of the requirements for the degree of Doctor of Philosophy at the University of Zululand.

Supervisor: Prof. M. Maaza
Nanoscience Laboratories, MRD,
IThemba LABS

Co-supervisor: Prof. O.M. Ndwandwe
Department of Physics and Engineering
University of Zululand

2012

DECLARATION

I, the undersigned, hereby declare that the work contained in this thesis is my own original work and that I have not previously in its entirety or in part submitted it at any university for a degree.

Signature: ……

Date: ……

ACKNOWLEDGEMENTS

I would like to thank my GOD, the creater of the universe and the author of life itself for physical, emotional, and mental strength.

I would also like to extend my appreciation to:

- Prof. M. Maaza for the project, constant supervision, motivation and finacial support throughtout the period of the project.
- Prof.OM.Ndwandwe for constant co-supervion, support and making sure that the project is finished.
- Dr.L. Kotsedi for the direction, correction of this document, analysis and interpretation of the results.
- Dr.BD.Ngom for guidance in results analysis and interpretation, and publications.
- Dr.JB.Kana-kana for helping with results interpretation.
- Dr.R.Butcher for his help with XRD data collection and interpretation.
- Dr.M.Nkosi for his help with AFM and interpretation of the results.
- Dr. Wojciech Przybylowicz for the collection of PIXE data, plotting, analysis, and interpretation.
- Dr. Manikandan from CSIR for Raman results.
- Dr.R.Nemutudi for the support, encouragement and constant monitoring of this work.
- Dr.C.Pineda for support and guidance through interaction during presentations.
- P. Sechogela for helping with proton irradiation experiment.
- Van de Graaff technical and workshop team for technical support.
- All MRD staff especially sisi Lusanda for being kind supportive and making the MRD a home away from home.
- My family for everything because without them I wouldn't have finished this project.
- My primary and high school principals Mrs B.KuBheka and Mr.PN.Mthethwa for their guidance and support I will never forgget.
- All who contributed directly or indirectly, I say thank you.

ABSTRACT

The drive to have biological compatibility, light weight and low cost materials and hard coating which can withstand hard environments such as those in space and nuclear reactors has met with a lot of challenges such as radiation and heat. These challenges pose a threat to the function of expensive components used in space and nuclear reactors. Therefore, Carbon-Carbon composites been an alternative choice for fusion reactor plasma facing components because of their low atomic number, superior thermal shock resistance, higher melting temperature (graphite sublimes at ~3600K), high thermal conductivity and low neutron activation. So, studying how irradiation changes the structure and properties of solid targets is necessary in order to understand the irradiation-induced degradation of components in the nuclear reactors. Although carbon structures have been studied quite extensively, fullerene C_{60} nanostructures have not received much attention. Furthermore, carbon nanostructures experience a self-healing process when subjected to intense conditions, this created a scope to explore and investigate the effects of such conditions on the nanostructures of fullerene with an additional aim of discovering new properties. Indeed this study has discovered that C_{60} nanostructures cannot withstand reactor conditions but new vital properties such as magnetism were discovered forming a long term project in the creation of biocompatible light weight room temperature magnets to be applied in electronics.

CONTENT

CHAPTER 1 1
BACKGROUND AND SCOPE OF INVESTIGATION 1
1.1. Introduction 1
1.2. Motivation 1
1.3. Problem identification 2
1.4. Research aims and objectives 3
1.5. Scope of the thesis 3
1.6. Background and overview 4
1.6.1. Carbon (C) 4
1.6.2. Carbon allotrope to be investigated 6
1.6.2.1. Fullerenes 6
1.6.2.2. Properties of C_{60} 6
1.6.2.3. Polymerization of Fullerenes 8
1.7. References 16
CHAPTER 2 25
CHARACTERIZATION TECHNIQUES 25
Introduction 25
2.1. Stereo microscope 25
2.2. Scanning Electron Microscope (SEM) 26
2.3. Atomic force microscopy (AFM) 28
2.4. Transmission Electron Microscope (TEM) 31
2.5. Raman spectroscopy 32
2.6. Fourier Transform Infrared Spectroscopy (FTIR) 34
2.7. X-ray Diffraction (XRD) 36
2.8. Proton Induced X-ray Emission (PIXE) 39
2.9. References 40
CHAPTER 3 42
MATERIALS AND EXPERIMENTS 42
3.1. Synthesis of C_{60} nanorods 42
3.2. Irradiation of nanorods on Si (111) substrate 46
3.1.1. Proton irradiation 46

3.1.2. Gamma irradiation 49
3.1.3. Fast neutron irradiation 51
3.3. Annealing effects experiment 53
3.4. Reference 55
CHAPTER 4 56
PROTON IRRADIATION 56
Abstract 56
4.1. Introduction 56
4.2. Experiments methods 57
4.3. Results and discussion 58
4.3.1. Optical microscope 58
4.3.2. Electron Microscope (EM) 64
4.3.3. Raman spectroscopy 67
4.3.4. FTIR spectroscopy 73
4.3.5. X-ray diffraction (XRD) 75
4.3.6. Optical images after soaking in toluene 81
4.3.7. SEM images after soaking in toluene 87
4.3.8. High Resolution Transmission Electron Microscope (HRTEM) 92
4.3.9. Magnetism in Fullerene C_{60} nanorods 94
4.3.10. Proton Induced X-ray Emission (PIXE) 99
4.3.11. Magnetism measurement experiment 100
4.4. References 102
CHAPTER 5 107
GAMMA IRRADIATION 107
Abstract 107
5.1. Introduction 107
5.2. Experiment details 109
5.3. Results and Discussion 109
5.3.1. SEM Gamma irradiation study 109
5.3.2. Raman spectroscopy 116
5.3.3. FT-IR spectroscopy 127
5.4. References 130
CHAPTER 6 132
NEUTRON RADIATION 132

Abstract 132
6.1. Introduction 132
6.2. Experiment details 134
6.3. Results and discussion 134
6.3.1. Optical microscope 134
6.3.2. Grazing X-ray diffraction analysis (GAXRD) 139
6.4. References 145
CHAPTER 7 148
ANNEALLING EFFECTS 148
Abstract 148
7.1. Introduction 148
7.2. Experiment details 149
7.3. Results and Discussion 149
7.3.1. Optical microscope 149
7.3.2. Scanning Electron Microscope (SEM) 154
7.3.3. Raman spectroscopy 159
7.4. Conclusion 163
7.5. References 164
CHAPTER 8 167
CONCLUSION AND OUTLOOK 167
8.1. Synthesis of nanorods 167
8.2. Protons irradiation 167
8.3. Gamma irradiation 169
8.4. Neutron irradiation 169
8.5. Annealing effects 169
8.6. Appendix 171

FIGURES

Figure 1. 1: Rutherford Atomic model of carbon. 4
Figure 1. 2: Models of eight allotropes of carbon: (a) diamond, (b) graphite, (c) lonsdaleite, (d) C_{60}, (e) C_{540}, (f) C_{70}, (g) amorphous carbon and (h) a carbon nanotube [17]. 5
Figure 1. 3: Illustration of C_{60} molecule showing the arrangement of the atomic bonds. 7
Figure 1. 4: Different types of active site for polymerization [45]..... 8
Figure 1. 5: (a) The structure of the 2D polymeric planes, (b) the rhombohedral 2D polymer structure 9
Figure 1. 6: (a) Structure of the linear polymer chains observed at room temperature, (b) the azafullerene dimer [46-48]. 9
Figure 1. 7: Pressure-Temperature phase diagram of C_{60} [49]..... 10
Figure 1. 8: Polymeric phases of C_{60} [59] 12
Figure 1. 9: Raman spectra of Polymeric phases of C_{60} [59]. 13
Figure 1. 10: Representative of different polymer structures: (a) Orthorhombic 1D (linear), (b) Tetragonal 2D, and (c) Rhombohedral 2D polymerized C_{60} phases. 15
Figure 2. 1: Schematic diagram of Optical microscope [1]. 26
Figure 2. 2: Schematic diagram of Scanning Electron Microscope (SEM). 27
Figure 2. 3: The interaction of an electron beam with the sample [2]. 28
Figure 2. 4: Electron micrograph of AFM cantilever image with a tip. 29
Figure 2. 5: Diagram of atomic force microscope (AFM) 30
Figure 2. 6: Diagram of Transmission Electron Microscope (TEM) [6]. 31
Figure 2. 7: Energy level diagram showing the states involved in Raman signal. 33
Figure 2. 8: Schematic diagram of a Raman spectrometer..... 34
Figure 2. 9: Schematic diagram of FTIR machine..... 35
Figure 2. 10: FTIR fingerprint for spectrum analysis [12-14]..... 36
Figure 2. 11: Schematic diagram showing typical arrangement of atoms within a crystal and diffracted beam. 37
Figure 2. 12: X-ray diffraction setup in θ-2θ geometry..... 38
Figure 3. 1: C_{60} (99.9% purity Sigma Aldrich) powder in a bottle. 42
Figure 3. 2: The dissolution of C_{60} (99% purity Sigma Aldrich) powder in toluene performed at ~25^0C under normal light. 43

Figure 3.3: A Miyazawa liquid-liquid interfacial precipitation of C_{60} fullerene nanorods immediately after layering isopropanol (IPA) atop freshly prepared C_{60} fullerene-toluene solution [1,2]. 44
Figure 3. 4: growth phase of C_{60} nanorods at room temperature show (a) incomplete process, (b) almost complete process, and complete process. 45
Figure 3.5: Schematic diagram of the van der Graff accelerator LABS with dotted line showing beam line used for proton irradiation. 46
Figure 3.6: Irradiation chamber (a) outside the chamber and (b) inside part of the chamber with dotted line showing the direction of the beam. 47
Figure 3.7: The ladder used to mount samples with dots showing the position of the beam in relation to the sample being irradiated. 48
Figure 3.8: Schematic diagram of the orientation of the sample with the beam hitting the sample directly perpendicular. 48
Figure 3.9: Schematic diagram showing the production of gamma rays from decay process of cobalt-60. Draw the figure. 50
Figure 3. 10: Schematic diagram of gamma rays of energy 1.17 and 1.33 MeV interacting with the sample of C_{60} nanorods on Si substrate. 50
Figure 3. 11: Diagram showing the irradiation position and the source arrangement. 52
Figure 3. 12: AJA Orion 5 Sputtering System at university of Zululand. 54

Figure 4. 1: Optical image of C_{60} nanorods on Si substrate before proton beam irradiation. 58
Figure 4.2: (a) Optical images of proton irradiated C_{60} nanorods on Si (111) substrate showing proton irradiated area by fluence of 1.79 10^{16} ions/cm^2 indicated by a circle and (b) zoomed in irradiated area. 59
Figure 4.3: (a) Optical images of proton irradiated C_{60} nanorods on Si (111) substrate showing proton irradiated area by fluence of 3.58 10^{16} ions/cm^2 indicated by a circle and (b) zoomed in irradiated area. 60
Figure 4.4: (a) Optical images of proton irradiated C_{60} nanorods on Si (111) substrate showing proton irradiated area by fluence of 5.37×10^{16} ions/cm^2 indicated by a circle and (b) zoomed in irradiated area. 61
Figure 4.5: (a) Optical images of proton irradiated C_{60} nanorods on Si (111) substrate showing proton irradiated area by fluence of 7.16×10^{16} ions/cm^2 indicated by a circle and (b) zoomed in irradiated area. 62

Figure 4.6: (a) Optical images of proton irradiated C_{60} nanorods on Si (111) substrate showing proton irradiated area by fluence of 8.96×10^{16} ions/cm^2 indicated by a circle and (b) zoomed in irradiated area. 63

Figure 4.7: Scanning electron microscopy image of nanorods of fullerene C_{60} on a Si (111) substrate before proton irradiation. 64

Figure 4.8: Transmission electron microscope (TEM) images of nanorod of fullerene C_{60} on a Si (111) substrate before irradiation. 65

Figure 4. 9: AFM image of nanorods of fullerene C_{60} on a Si (111) substrate before irradiation. 66

Figure 4.10: Raman spectra of as purchased fullerene C_{60} powder and non-irradiated C_{60} nanorods on Si (111) substrates. 67

Figure 4.11: Raman spectra of C_{60} nanorods subjected to fluence ranging from 1.79×10^{16} to 8.96×10^{16} ions/cm^2 of 2 MeV protons. 68

Figure 4.12: (a) Variation of the Raman intensities vs. irradiation fluences for Ag(1) and Ag(2) modes of irradiated C_{60} nanorods on Si (111). 70

Figure 4.13: FTIR spectra of pristine $C_{60,}$ non-irradiated and irradiated fullerene C_{60} nanorods. 74

Figure 4.14: Possible various structures formed after irradiation of C_{60} + C_{60} nanostructure [18]. 75

Figure 4.15: Model of the C_{60} molecules in a nanorod with the diffraction plane highlighted [19]. 76

Figure 4.16: X-ray diffraction patterns of as purchased fullerene C_{60} powder and non-irradiated C_{60} nanorods on Si (111) wafer. 77

Figure 4.17: X-ray diffraction patterns of the 2 MeV protons irradiated C_{60} nanorods subjected to the following doses: (a) 1.79×10^{16}, (b) 3.58×10^{16}, (c) 5.37×10^{16}, (d) $7.16 \times 10^{16}$and (e) 8.96×10^{16} ions/cm^2. 78

Figure 4.18: Normalised intensity versus fluence of X-ray diffraction peaks fitted with Lorentz fitting for the irradiated nanorods. 79

Figure 4.19: Normalised peak position versus fluence of X-ray diffraction peaks fitted with Lorentz fitting for the irradiated nanorods. 80

Figure 4.20: Optical image of C_{60} nanorods on Si (111) substrate showing proton irradiated area (big arrow) with fluence of 1.79×10^{16} ions/cm^2 and non-irradiated area (small arrow). 82

Figure 4.21: Optical image of C_{60} nanorods on Si (111) substrate showing proton irradiated area (big arrow) with fluence of 3.58×10^{16} ions/cm^2 and non-irradiated area (small arrow).83
Figure 4.22: Optical image of C_{60} nanorods on Si (111) substrate showing proton irradiated area (big arrow) with fluence of 5.37×10^{16} ions/cm^2 and non-irradiated area (small arrow).84
Figure 4.23: Optical image of C_{60} nanorods on Si (111) substrate showing proton irradiated area (big arrow) with fluence of 7.16×10^{16} ions/cm^2 and non-irradiated area (small arrow).85
Figure 4.24: Optical image of C_{60} nanorods on Si (111) substrate showing proton irradiated area (big arrow) with fluence of 8.96 10^{16} ions/cm^2 and non-irradiated area (small arrow)... 86
Figure 4.25: SEM image of irradiated C_{60} nanorods with a fluence of 1.79×10^{16} ions/cm^2 on Si (111) substrate after being soaked in toluene. 87
Figure 4.26: SEM image of irradiated C_{60} nanorods with a fluence of 3.58×10^{16} ions/cm^2 on Si (111) substrate after being soaked in toluene. 88
Figure 4.27: SEM image of irradiated C_{60} nanorods with a fluence of 5.37×10^{16} ions/cm^2 on Si (111) substrate after being soaked in toluene. 89
Figure 4.28: SEM image of irradiated C_{60} nanorods with a fluence of 7.16×10^{16} ions/cm^2 on Si (111) substrate after being soaked in toluene. 90
Figure 4.29: SEM image of irradiated C_{60} nanorods with a fluence of 8.96×10^{16} ions/cm^2 on Si (111) substrate after being soaked in toluene. 91
Figure 4.30: HRTEM image of C_{60} nanorod before proton irradiation at 2 MeV on a copper grid. 93
Figure 4.31: HRTEM image of C_{60} nanorod irradiated by 2 MeV protons at 8.96×10^{16} ions/cm^2 fluence on a copper grid showing planes with different orientation..... 94
Figure 4. 32: PIXE spectrum of C_{60} powder on araldite Al 102 um filter showing no impurities. 99
Figure 4. 33: PIXE spectrum of C_{60} powder on araldite kapton 180 um filter showing S and Br with very small Fe peak. 100
Figure 4. 34: M vs. T for an irradiated C_{60} nanorods at 8.96 10^{16} ions/cm^2 in an applied field of 1 T (substrate [H-Si(111)] contribution subtracted). 101

Figure 5. 1: SEM image of C_{60} nanorods on Si (111) substrate irradiated gamma rays at 50 kGy dose. 110
Figure 5. 2: SEM image of C_{60} nanorods on Si (111) substrate irradiated gamma rays at 100 kGy dose. 111

Figure 5. 3: SEM image of C_{60} nanorods on Si (111) substrate irradiated gamma rays at 200 kGy dose. 112
Figure 5. 4: SEM image of C_{60} nanorods on Si (111) substrate irradiated gamma rays at 600 kGy dose 113
Figure 5. 5: SEM image of C_{60} nanorods on Si (111) substrate irradiated gamma rays at 800 kGy dose. 114
Figure 5. 6: SEM image of C_{60} nanorods on Si (111) substrate irradiated gamma rays at 1 MGy (1000 kGy) dose 115
Figure 5. 7: Raman spectra of C_{60} nanorods on Si (111) substrate before and after gamma irradiation at doses ranging from 50 kGy to 1 MGy (1000 kGy). 117
Figure 5. 8 (a-b): Raman spectra of Ag (2) Raman modes of C_{60} nanorods on Si (111) substrate before and after gamma irradiation at doses ranging from 50 kGy to 1 MGy (1000 kGy) 119
Figure 5. 9 (a-b): Variation of the Raman shift vs. irradiation dose for Ag (2) mode of irradiated C_{60} nanorods on Si (111). 122
Figure 5. 10 (a-b): Variation of the intensity versus irradiation dose for Ag (1) mode of irradiated C_{60} nanorods on Si (111). 124
Figure 5.11 (a-b): Variation of the FWHM vs. irradiation dose for Ag (1) mode of irradiated C_{60} nanorods on Si (111). 125
Figure 5. 12: FTIR spectra of pristine $C_{60,}$ non-irradiated and irradiated fullerene C_{60} nanorods, ... 128
Figure 5. 13: FTIR spectra of pristine $C_{60,}$ non-irradiated and irradiated fullerene C_{60} nanorods showing shift due to the formation of nanorods 129
Figure 6.1: Optical microscopy image of nanorods of fullerene C_{60} on a Si (111) substrate before neutron irradiation. 135
Figure 6.2: Optical microscopy image of nanorods of fullerene C_{60} on a Si (111) substrate after neutron irradiation at 3.6×10^{17}n/cm^2. 136
Figure 6.3: Optical microscopy image of nanorods of fullerene C_{60} on a Si (111) substrate after neutron irradiation at 9.6×10^{17}n/cm^2. 137
Figure 6.4: Optical microscopy image of nanorods of fullerene C_{60} on a Si (111) substrate after neutron irradiation at 1.6×10^{18}n/cm^2. 138
Figure 6.5: GAXRD patterns of C_{60} nano-rods irradiated at different fast neutron fluences. 140

Figure 6.6: GAXRD patterns of C_{60} nanorods irradiated at different fast neutron fluencies for the 111 peak. 141
Figure 6.7: GAXRD patterns of C_{60} nanorods irradiated at different fast neutron fluencies for labelled peaks. 141
Figure 6.8: Grazing X-ray diffraction peaks intensities fitted with Lorentz fitting for the irradiated nanorods. 142
Figure 6.9: Grazing X-ray diffraction peaks FWHM fitted with Lorentz fitting for the irradiated nanorods. 143
Figure 6.10: Grazing X-ray diffraction peaks FWHM fitted with Lorentz fitting for the irradiated nanorods. 144
Figure 7.1: Optical image of nanorods of fullerene C_{60} on a Si (111) substrate before annealing. 150
Figure 7.2: Optical image of nanorods of fullerene C_{60} on a Si (111) after annealing at 400 ^{o}C. 151
Figure 7. 3: SEM image of nanorods of fullerene C_{60} on a Si (111) after annealing at 600 ^{o}C. 152
Figure 7. 4: Optical image of nanorods of fullerene C_{60} on a Si (111) after annealing at 800 ^{o}C. 153
Figure 7.5: SEM image of nanorods of fullerene C_{60} on a Si (111) substrate before annealing. 155
Figure 7.6: SEM image of nanorods of fullerene C_{60} on a Si (111) substrate after annealing at 400 ^{o}C. 156
Figure 7.7: SEM image of nanorods of fullerene C_{60} on a Si (111) substrate after annealing at 600 ^{o}C. 157
Figure 7.8: SEM image of nanorods of fullerene C_{60} on a Si (111) after annealing at 800 ^{o}C. 158
Figure 7.9: Raman spectra of nanorods of fullerene C_{60} on a Si (111) substrate before annealing, at 400 ^{o}C, at 600 ^{o}C and at 800 ^{o}C. 160
Figure 7.10: Lorentz fitted Raman spectra of nanorods of fullerene C_{60} on a Si (111) substrate annealed at 600 ^{o}C. 161
Figure 7.11: Lorentz fitted Raman spectra of nanorods of fullerene C_{60} on a Si (111) substrate annealed at 800 ^{o}C. 162

EQUATIONS

Equation 2. 1..... 33
Equation 2. 2..... 38
Equation 2. 3..... 39

TABLES

Table 1. 1: Summary of major physical characteristics of C_{60} molecules 171
Table 1. 2: Physical constants for the crystalline C_{60} in the solid state..... 172
Table 1. 3: Summary of possible application of fullerene C_{60} **[69].** 173

Table 3. 1: Various doses used for proton irradiation of individual samples..... 49
Table 3. 2: Various doses used for gamma irradiation of individual samples..... 51
Table 3. 3: Various doses used for fast neutron irradiation of individual samples..... 53

Table 4. 1: Position, FWHM and relative intensity of Ag (1) and Ag (2) modes. 69

Table 5. 1: Position, FWHM and relative intensity of Ag (1) and Ag (2) modes. 120

Table 7. 1: Lorentz fitted values of D- and G-peaks at 600 ^{0}C and 800 ^{0}C. 163

LIST OF SYMBOLS

π – Mathematical constant, sometimes written is approximately equal to **3.14159.**

λ – Wavelenght (nm)

ω – Raman shift (cm^{-1})

γ – Gamma ray

μ – Micron (10^{-6})

α – Alpha (the first letter of the Greek alphabet means the beginning)

θ – Theta (angle in normally in degrees)

h - Planck's constant = 6.626068 × 10-34 m2 kg / s

Å – Angstrom = 1.0 $x10^{-10}$

e^- - electron (1.60217646 x 10-19 C)

υ– speed of light divided by wavelength

Δ – mathematical difference or change

LIST OF ABBREVIATIONS

SEM	– Scanning Electron Microscope
XRD	– X-ray Diffraction
PIXE	– Particle Induced X-ray Emission
FTIR	– Fourier Transform Infrared
TEM	– Transmission Electron Microscope
HRTEM	– High Resolution Transmission Electron Microscope
AFM	– Atomic Force Microscope
FWHM	– Full Width Half Maximum
RSA	– Republic of South Africa
LLIP	– Liquid-Liquid Interfacial Precipitate
1D	– 1 Dimension
2D	– 2 Dimension
FCC	– Face Centered Cubic
BCC	– Body Centerd Cubic
P-T	– Pressure and Temperature
HPHT	– High Pressure and High Temperature
RT	– Room Temperature
CCD	– Charge-Coupled Device
CRT	– Cathode Ray Tube
Si (Li)	– Silicon Lithium detector
HPGe	– High Purity Germanium detector

MRD – Materials Research Department

LABS – Laboratory for Accelerator Based Sciences

HOPG – Highly Oriented Pyloric Graphite

MWCNT – Multi-Walled Carbon Nanotube

SWCNT – Single-Walled Carbon Nanotube

GAXRD – Grazing Angle X-ray Diffraction

LIST OF PUBLICATIONS

C.B.Mtshali, L. Kotsedi, B.D. Ngom, C.L.Ndlangamandla, O.M. Ndwandwe, M.Maaza, "Structural investigation of 2 MeV proton-irradiated fullerene nanorods", Nucl. Instr. Meth. B (2012), http://dx.doi.org/10.1016/j.nimb.2012.12.002

C. Mtshali, D. Hamidi, T. Kerdja, P. Buah-Bassuah, H. Haneda, M. Maaza, "Laser beam deflectometry and C_{60} polymerized nanorods dynamics by surface interdiffusion", ***optics communication***, Volume 285, Issue 15, 1 July 2012, Pages 3272–3275).

C. Ndlangamandla, **C. Mtshali**, M. Sithole, B. Ngom, O. Ndwandwe, M. Maaza, "Effect of pH on the morphology and orientation of Fe_2O_3 nanostructures grown using aqueous chemical method***", South African Institute of Physics proceedings 2011***, ISBN: 978-186888-688-3, pages 238-242.

CHAPTER 1

BACKGROUND AND SCOPE OF INVESTIGATION

1.1. Introduction

Nanotechnology is a multi-disciplinary field (i.e. design, characterization, production and application of structures) of growing global importance, both as the fundamental and applied research field. The driving force behind research in nano-sized materials is because of their ability to tailor their physical and chemical properties, in addition to their multi-functionalities. The growing societal demand for high speed and high density information storage systems, and the need for green energy production technologies have increased the activity in this research area.

Nano-sized materials have unique properties which are different from their corresponding bulk form and even enhanced in some cases. These size dependent properties are due mainly to shape anisotropy, quantum confinement as well as surface effects [1-6]. These unique properties of the nano-systems have attracted much interest in the research community due to their various possible applications.

1.2. Motivation

The continuous rising need for energy worldwide has put a great strain on the power grid. In South Africa alone, electricity consumption has been growing rapidly since early 1990's, and large amount of electricity is produced from coal and thereby increasing air pollution which attribute to the problem of global warming. To counteract this problem, there are a number of alternatives to be considered, ranging from renewable energy, bio-fuel and nuclear reactors. Although the alternatives are seen as future solutions to the electricity crisis, there are problems associated with them i.e. renewable energy like solar panels are easily affected by weather conditions, bio-fuel can lead to the shortage of food since it uses crops that are meant

for human consumption. Nuclear power generation has been earmarked as the attractive alternative for power supply in Republic of South Africa because of its high power output ability to produce more electricity than bio-fuel and renewable energy.

Although nuclear reactors have the ability to produce more electricity, there are some shortcomings with the robustness of the materials used in its components, and this could result in decommissioning of the plant after a long run of operation. Therefore, Carbon-Carbon composites can be an alternative choice for fusion reactor plasma facing components because of their low atomic number, superior thermal shock resistance, higher melting temperature (graphite sublimes at ~3600K), high thermal conductivity and low neutron activation [7].

The irradiation studies conducted decades ago tell us that bombardment of solids with energetic particles creates defects and thus deteriorates the materials [8]. Studying how irradiation changes the structure and properties of solid targets is necessary in order to understand the irradiation-induced degradation of components in the nuclear reactors.

Fullerene nanostructures are one of carbon based structures which have not been well investigated under the same conditions experienced in the reactor. Furthermore, carbon nanostructure experience self-healing process when subjected to intense conditions [9, 10], this creates a scope to explore and investigate the effects of such conditions on the nanostructures of fullerene. The motivation of this study is the fact that new discoveries and applications of fullerene nanostructures are possible which can then contribute to the research worldwide.

1.3. Problem identification

In a nuclear reactor, radiation is a major factor when it comes to the components facing the plasma. Therefore, it is imperative to ensure that the nuclear reactor components can withstand such harsh conditions during its operation, but this is not the case at the present moment [11].

Radiation damages that occur on the reactor components can result in their physical properties being altered [12]. Also these changes coupled with dose and temperature gradients, generally leads to significant component stresses and distortions which can lead to coolant flow bypass, neutron streaming and control rod channel distortion [13,14]. These challenges have persisted in many nuclear reactors and a lot of research is being conducted in trying to solve these problems.

The use of multi-layered nanostructures of carbon is one of the possible solutions to curb component failure due to nuclear radiation, but a lot of research still needs to be done in order to accumulate sufficient data.

1.4. Research aims and objectives

a) Synthesis of C_{60} nanostructures.
b) Investigation of protons, gamma rays, and neutrons irradiation on C_{60} nanostructures
c) Investigating the annealing effects and thermal stability of C_{60} nanostructures.

1.5. Scope of the thesis

In chapter one, the properties of C_{60} as an individual molecule and in crystal form are discussed, followed by different methods of synthesizing C_{60} nanorods and nanostructures.

In chapter 2, the characterization techniques used in this project are fully described, and then chapter 3 is about the synthesis of C_{60} nanorods using liquid-liquid interfacial precipitate method (LLIP).

Chapters 4 to 7 constitute major part of this thesis; these chapters are arranged in a sequence of their contribution in this document and the amount of work it carries. Chapter 4 contains in addition to physical effect of protons on C_{60} nanorods a study of the magnetic properties of the irradiated C_{60} results which forms the basis of a long term project in magnetism.

n chapter 5, the effect of gamma rays irradiation on C_{60} nanorods are presented and discussed, and in chapter 6 the effect of fast neutron irradiation of C_{60} nanorods investigated.

Chapter 7 deals with the effect of annealing temperature on C_{60} nanorods with the emphases on transformation of C_{60} nanorods versus temperature. All the results are concluded and the future work proposition is also highlighted in Chapter 8.

1.6. Background and overview

1.6.1. Carbon (C)

Carbon is element number six on the periodic table with six protons and six electrons in its stable form as shown in figure 1.1.

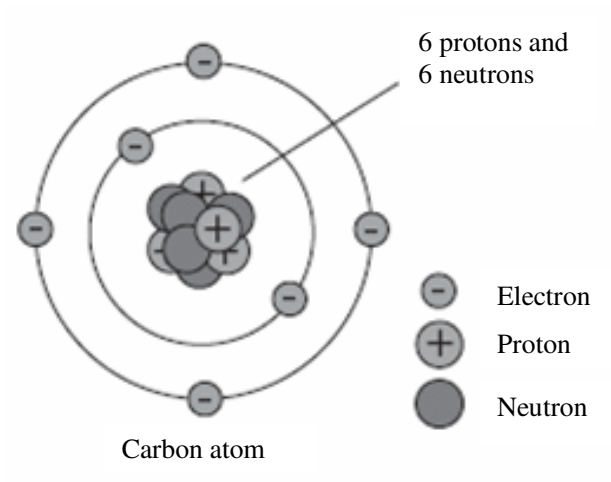

Figure 1. 1: Rutherford Atomic model of carbon.

The name carbon itself originates from Latin word "carbo" which means charcoal. It has one of the highest strength fibers and good lubricating properties when it is in graphite form. When carbon atoms are bonded in a diamond structure, they are crystals with the highest hardness. It has also been shown that carbon can be non-crystalline (vitreous carbon) which can act as absorber and helium gas barriers [15]. A great deal of the physical and chemical properties of carbon are yet to be fully understood and new allotropes have been discovered such as the fullerene molecules [16], carbon nano-tubes (CNTs) and the hexagonal polytypes of diamond which are all shown in figure 1.2 [17].

In this study will be focusing on Fullerene C_{60} because of its interesting properties and potential application in various spheres of technology.

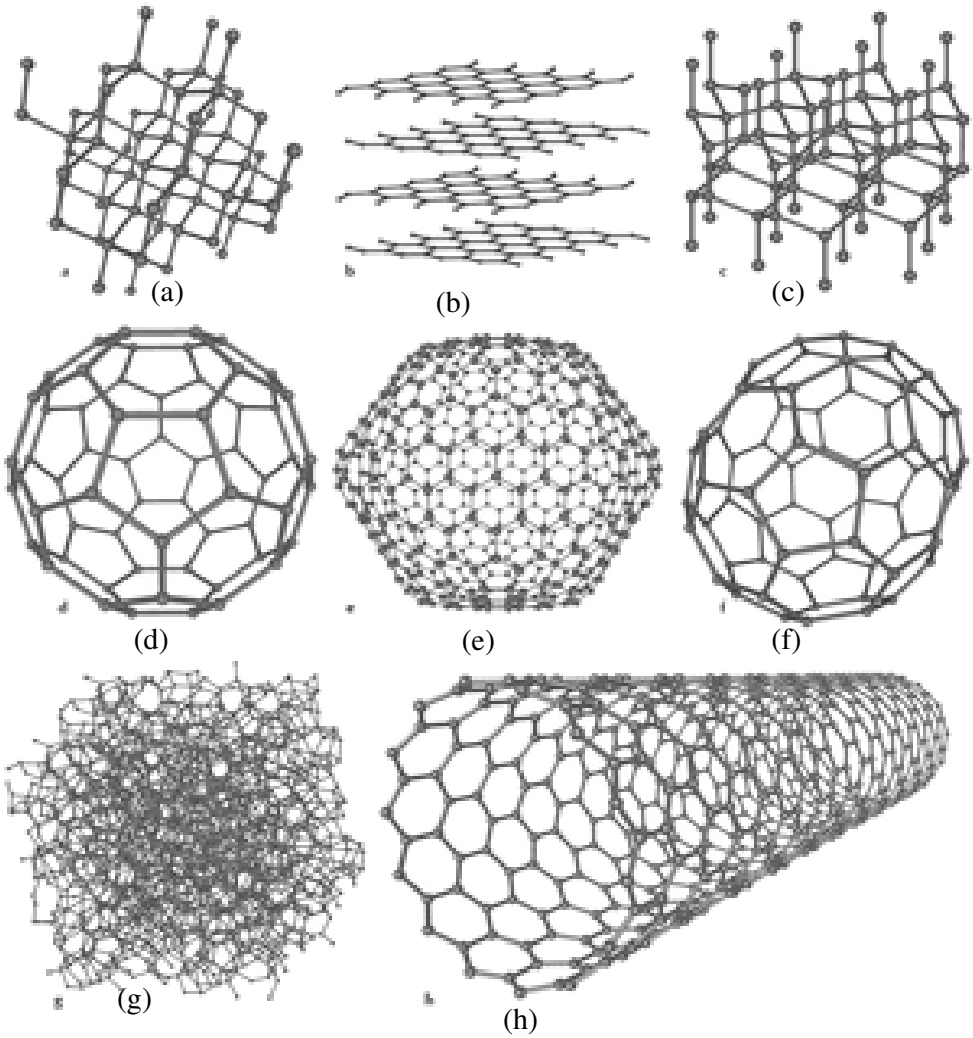

Figure 1. 2: Models of eight allotropes of carbon: (a) diamond, (b) graphite, (c) lonsdaleite, (d) C_{60}, (e) C_{540}, (f) C_{70}, (g) amorphous carbon and (h) a carbon nanotube [17].

1.6.2. Carbon allotrope to be investigated

1.6.2.1. Fullerenes

Fullerenes are allotropes of carbon which have both spherical and cylindrical forms, the spherical fullerenes are known as buckyballs, and cylindrical ones as buckytubes. These molecules are composed entirely of carbon and are members of carbon nanotubes structural family which are called buckytubes. The first fullerene to be discovered was C_{60}, and the existence of C_{60} was predicted by Eiji Osawa [18, 19], in his investigations he noticed that the structure of a corannulene molecule was a subset of a soccer-ball shape, he then hypothesized that a full ball shape carbon based molecule could exist.

Harold Kroto et al discovered C_{60} while evaporating graphite target in a helium ambience using laser ablation technique [20]. Kroto, Curl, and Smalley were awarded the 1996 Nobel Prize in Chemistry for their roles in the discovery of this molecule. In 1991, Donald Huffman and Wolfgang Krätschmer from Max Planck Institute-Heidelberg and Donald Huffman from University of Arizona-Tucson came out with a method of producing fullerenes in large quantities [21], but fullerenes purification remains a challenge to chemists and to a large extent determines fullerene prices [22-24].

1.6.2.2. Properties of C_{60}

Fullerene C_{60} is a molecule that consists of 60 carbon atoms, bonded together by both single and double bonds, forming 12 pentagonal rings and 20 hexagonal rings joined together to form a soccer ball shaped molecule [25]. The carbon atoms in fullerene C_{60} are sp^2 hybridized, and each atom is bonded to three other carbon atoms. The C_{60} molecule has two bond lengths, whereby the 6:6 bonds ring can be considered to be “double bonds” and are shorter than the 5:6 bonds.

C_{60} is not “superaromatic” as it tends to avoid double bonds in the pentagonal rings, this results in poor electron delocalization [26] as shown in fig.1.3. As a result C_{60} behaves like an electron deficient alkenes and reacts readily with electron rich species [27]. These two types of bonds indicate that the $\pi-$ electrons are not delocalized evenly over all bonds. Rationalizing that the shorter bond lengths belongs to a [6,6] ring junction (C=C bond between two hexagons) and larger ones to a [5,6] ring junction (C-C bond between one

pentagon and one hexagon) due to the greater forces of attraction between atoms sharing bonds [28-32], as one should expect that double bonds should be stronger and shorter than the single bonds. The bonding requirements is that all valence electrons be satisfied in this molecule, it is to be assumed that C_{60} has filled molecular orbitals [33].

The C_{60} molecule is highly symmetric with the largest number of symmetry operations. Fullerene C_{60} molecules exhibit an insulating behaviour [34] and has an external diameter of about 0.711nm with a density of 1.65 $g.cm^{-3}$ and a lattice constant a~ 1.415nm [35] as shown in table 1.1 and figure 1.2. Fullerenes are electrophilic because they attract electrons [36]. Properties of this molecule can also be altered by endohedral doping process, exohedral process and the resulting structure is often referred to as fullerites. Doping the fullerene leads to a charge transfer between the fullerene and the dopant, giving rise to additional transport and new optical properties [37-40].

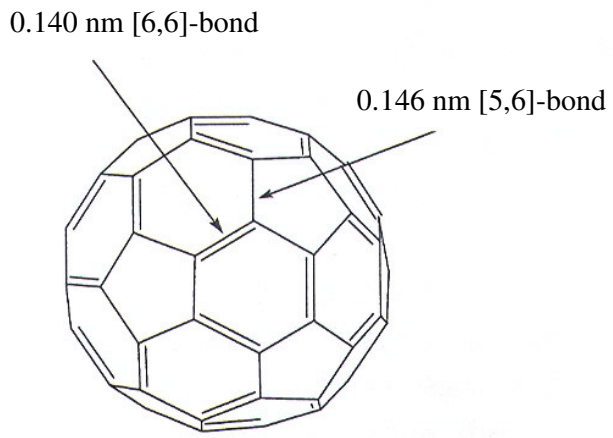

Figure 1. 3: Illustration of C_{60} molecule showing the arrangement of the atomic bonds.

1.6.2.3. Polymerization of Fullerenes

Polymerization is a chemical reaction in which monomers are linked together to form large molecules whose molecular weight is the multiples of the monomers. In the same way, the polymerization of fullerene molecules is a chemical reaction in which fullerene molecules are linked together via chemical reaction, to form large fullerene molecules whose molecular weight is a multiple of that of the monomer [41, 42].

It is known that at room temperature the fullerene molecules can undergo crystallization to form various crystal structures and these structures can transform to other structures via phase transition phenomena due to external stimuli such as pressure and temperature [43]. This characteristic has been observed in C_{60}, making it to polymerize and self-assemble to form rods with different diameter from few nanometers up to a micrometer regime and lengths of up to centimetres [44].

The polymerization in C_{60} molecules normally occurs at unsaturated sites, i.e. at the [6:6] double bonds but to a lesser extend at the single bonds site [5:6] as shown in figure 1.4. During polymerization process different shapes of these nanostructures are formed depending on different factors e.g. pressure, volume, time dynamics, etc. as shown in figure 1.5 and 1.6 [45-48].

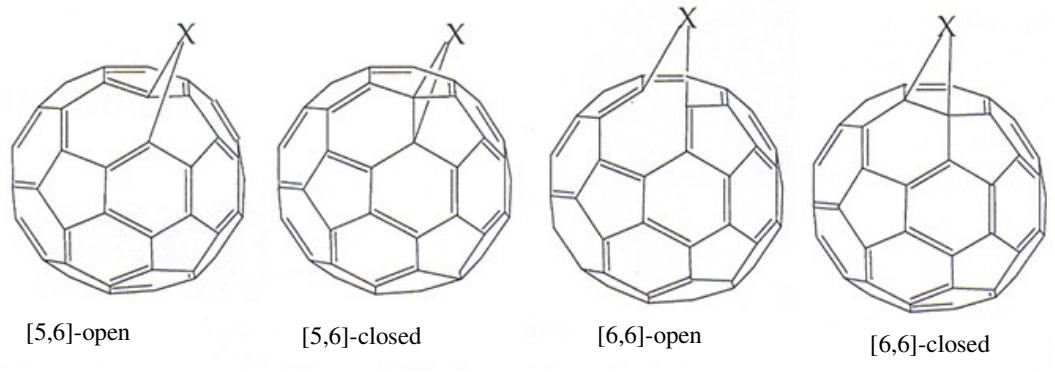

Figure 1. 4: Different types of active site for polymerization [45]

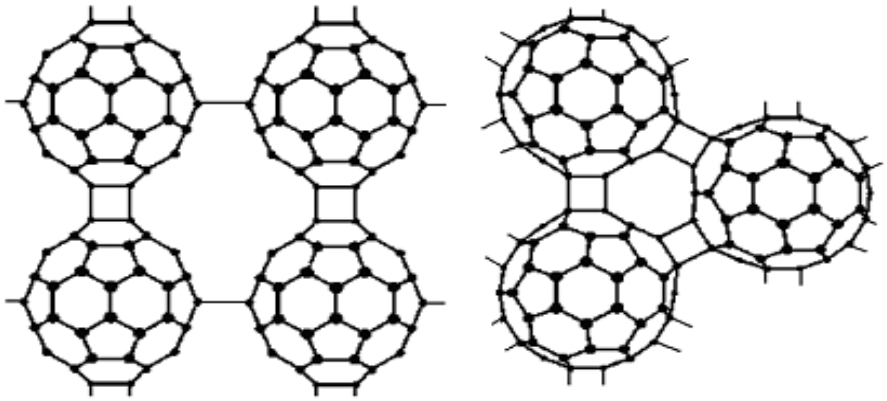

(a) **(b)**

.

Figure 1. 5: (a) The structure of the 2D polymeric planes, (b) the rhombohedral 2D polymer structure

(a)

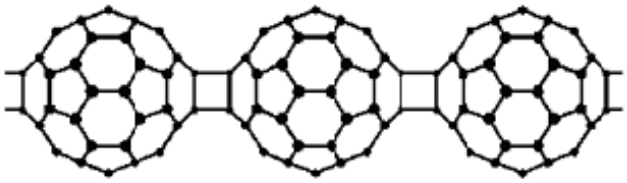

(b)

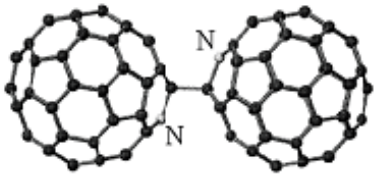

Figure 1. 6: (a) Structure of the linear polymer chains observed at room temperature, (b) the azafullerene dimer [46-48].

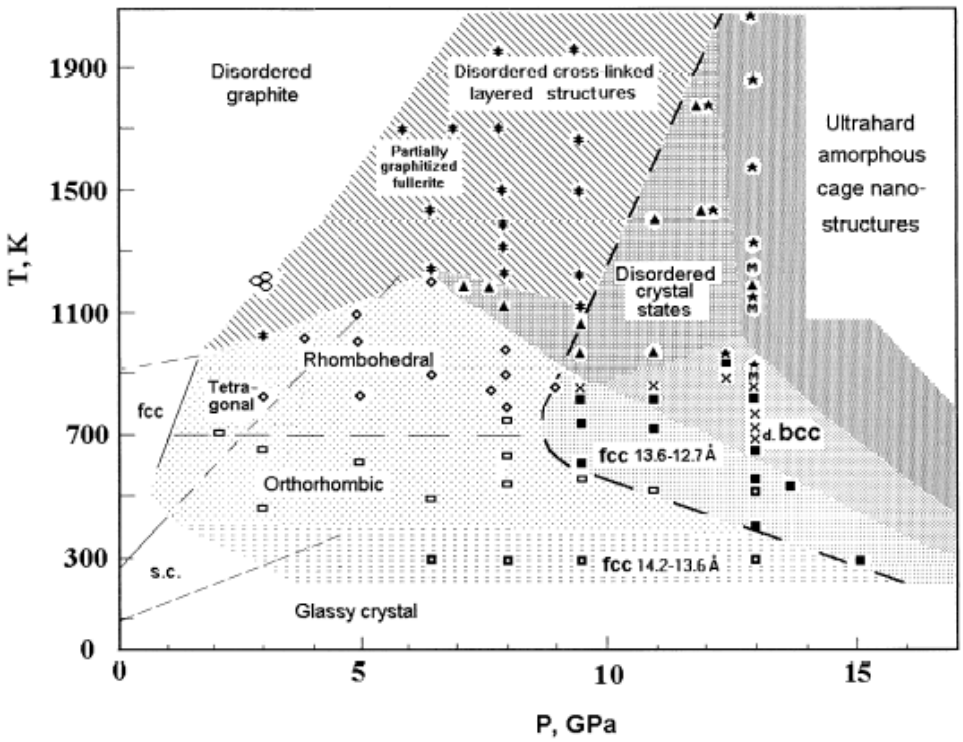

Figure 1. 7: Pressure-Temperature (P-T) phase diagram of C_{60} [49].

1.6.2.3.1. Pressure induced C_{60} polymerization

C_{60} polymerization is the first form of polymerization that was observed [49-54], which produced an intricate and history dependent phase diagram in P - T space as shown in figure 1.7.

According to P-T phase diagram, at moderate pressures between 3-8 GPa and temperatures above 400 K, cyclo-addition process occurs whereby C_{60} molecules within the cubic van der Waals crystal begin to bond. During this process the hexagon-hexagon double bonds on adjacent molecules break and form sp^3-type bridging bonds which result to the formation of linear chains within orthorhombic polymeric-like structures. At higher temperatures and pressure above 3 GPa, a rhombohedral structure is formed while tetragonal structure is only formed below 3 GPa.

At temperature around 1000 K the molecules collapse, producing disordered materials with hardness in the order of 10-100 times that of normal graphite. Above 9 GPa, fcc- and bcc-like structures persist but at around 1100K breakdown of the molecules occurs. The resultant disordered materials are reported to have hardness that can scratch the (111) face of diamond making them amongst the hardest known materials [54-58]. Applying pressure result to the transformation of fcc structure of C_{60} into orthorhombic consisting of a polymerized linear chain of C_{60} molecules.

Rao et al. observed and reported that under moderate external pressure, C_{60} films are transformed into a toluene insoluble product which was also confirmed through infrared and Raman studies. Furthermore laser based desorption mass spectrometry indicated the presence of oligomers as large as $(C_{60})_{20}$. The conclusion was that such experimental observations indicate that the polymerization reaction is associated with the (2+2) cycloaddition reaction.

This reaction involves the photoexcitation of the triplets states of C_{60} wherein the double bonds of the neighbouring molecules react to form a polymerized chain, linked through a 4-membered ring [59-64]. The polymerization of C_{60} was also observed when pristine solid C_{60} was subjected to high pressure of about ~5 GPa and high temperature around ~800 K [65]. A comparison with the Raman spectrum (figure1.9 and 1.10) of starting C_{60} shows that at high temperature and pressure (HPHT) treatment, all the discernable modes soften. In particular the Ag Raman mode at 1469 cm^{-1} was seen to shift to 1460 cm^{-1} and develop a shoulder. It was observed that the treatment of the fullerene in the pressure range below ~8 GPa and at temperature of about ~750 K results in the formation of linear C_{60} chains along the (110) (figure 1.9 and 1.10.) direction of the original fcc lattice leading to an orthorhombic phase.

Increasing temperature provides an additional intermolecular bonding in either (111) or (100) planes and the synthesis of a rhombohedral or tetragonal phase (figure1.9.). Above ~8 GPa very hard, 3D polymeric structures are formed (figure 1.8, figure 1.9 and table 1.4).

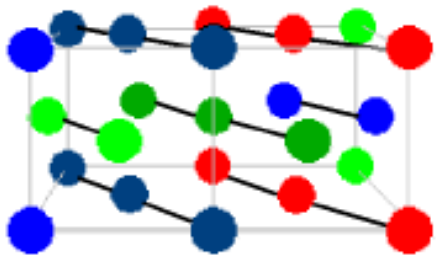

(a) Orthorhombic (1D)

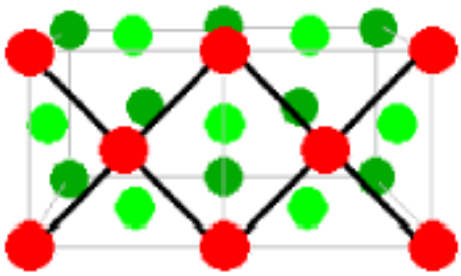

(b) Tetragonal (2D)

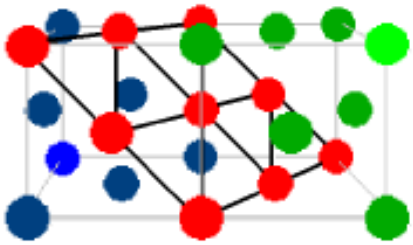

(c) Rhombohedral (2D)

Figure 1. 8: Polymeric phases of C_{60} [59]

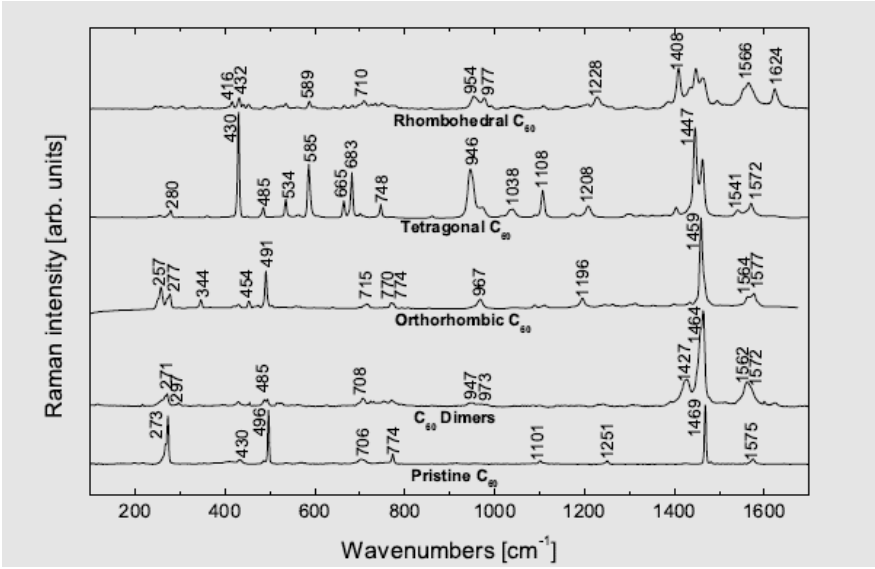

Figure 1. 9: Raman spectra of Polymeric phases of C_{60} [59].

Table 1.4: The position of the Ag (2) mode in the RT Raman spectrum for various phases.

Phase	**No. of intermolecular (double) bonds per molecule**	**Ag (2) mode position (cm^{-1})**
Pristine	0	1469
Dimmers	1	1464
Orthorhombic	2	1459
Tetragonal	4	1448
Rhombohedral	6	1407

1.6.2.3.2. Photo-induced C_{60} polymerization

This is the second polymerization process that uses photons of a specific wavelength which depends on the time of irradiation [66]. This process was clearly observed using X-ray photoelectron spectroscopy which showed that when photons of known wavelength are applied to the system during polymerization process of C_{60}, the average number of bonds connecting adjacent molecules increases with irradiation time and saturates just below the value of six.

Longer irradiation times increase the amount of the photo transformed phase and decrease that of the pristine C_{60}. It was found that the C_{60} infrared peak at 1428 cm^{-1} diminishes while there is an increase in the photopolymer peak at 1424cm^{-1} when irradiation time is increased and it was also confirmed using XRD analysis. This change corresponds to the relative weight of the two phases and this was reported when C_{60} fine powder was irradiated with 1.5 kW Xe lamp having power density of 0.2 $W.cm^{-2}$ to 0.4 $W.cm^{-2}$.

1.6.2.3.3. The Liquid-Liquid Interfacial polymerization

This is the third way of forming nanorods of C_{60}. This method was initially pioneered by K. Miyazawa from the National Institute of Materials Sciences at Tsukuba-Japan [68], using two organic solvents [toluene ($C_6H_5CH_3$) and isopropoxide alcohol ($CH_3CHOHCH_3$)] to create an interface where the polymerization process of C_{60} molecules occurs. In this process, the pristine C_{60} powder is dissolved into $C_6H_5CH_3$ solvent and the mixture is then put into well cleaned container and then $CH_3CHOHCH_3$ is gently poured onto the mixture to prevent interfacial diffusion. The two liquids $C_{60}/C_6H_5CH_3$ and $CH_3CHOHCH_3$ create an interface with $CH_3CHOHCH_3$ on top. The polymerization of C_{60} will then occur at the interface and the nanorods will grow into the $C_{60}/C_5CH_6CH_3$ mixture [68] governed by time dynamics resulting in different structures fig.1.10.

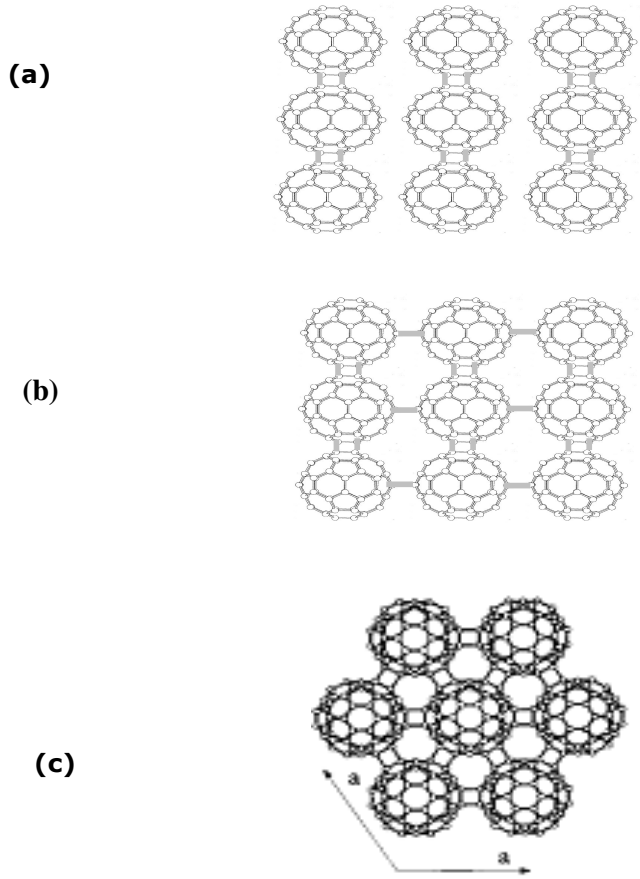

Figure 1. 10: Representative of different polymer structures: (a) Orthorhombic 1D (linear), (b) Tetragonal 2D, and (c) Rhombohedral 2D polymerized C_{60} phases.

1.7. References

1. **van Ruitenbeek, J.M.,** Quantum Properties, Physical Chemistry, Conductance Quantisation in Metallic Point Contacts, *arXiv:cond-mat/9910394v1 [cond-mat.mes-hall]* 25 Oct 1999

2. **Boyen, H.G., et al.** Chemically Induced Metal-to-Insulator Transition in Au55 Clusters: Effect of Stabilizing Ligands on the Electronic Properties of Nanoparticles, *Physical Review Letters* 87, 276401, 2001.

3. **Cheshnovsky, O., Taylor, K., Conceicao, J., and Smalley, R.,** Ultraviolet photoelectron spectra of mass-selected copper clusters: Evolution of the 3d band, *Physical Review Letters* 64, 1785, 1990.

4. **Wu, H., Desal, S., and Wang, L.S.,** Electronic Structure of Small Titanium Clusters: Emergence and Evolution of the 3d Band, *Physical Review Letters* 76, 212, 1996.

5. **Lin, M., Andres, R., and Reifenberger, R.,** Observation of the discrete electron energy states of an individual nanometer-size supported gold cluster, *Physical Review Letters* 67, 477, 1991.

6. **Palmer, R., Pratontep, S., and Boyen, H.G.,** Nanostructured surfaces from size-selected clusters, *Nature Materials* 2, 443, 2003.

7. http://www.atomicengines.com/engines.html, http://en.wikipedia.org/wiki/Carbon

8. **Rob, H., Telling, P., Ewels, A., Barbary, E.L., and Heggie Malcom, I.,** Wigner defects bridge the graphite gap, *Nature*, 2003; doi:10.1038/nmat876,1-5

9. **Onoe, J., Ochiai, Y., Ito, T., et al. ,** Electronic and electron-transport properties of peanut-shaped C_{60} polymers, *Journal of Physics: Conference Series,* 61, No. 1., 899-903.

10. **Ono, J., et al,** *Nature* 2007.

11. http://holbert.faculty.asu.edu/eee460/dfg/index.html (2010)

12. **Santos, A. B., Araujo, E. S., Araujo, P. L. B., and Pacheco, A. P. L.,** combined effect of gamma radiation and graphite concentration (powder and nanosheets) in composites prepared with poly(methyl methyl methacrylate), *2007 International Nuclear Atlantic Conference* - INAC 2007 Santos, SP, Brazil, September 30 to October 5, 2007 ASSOCIAÇÃO BRASILEIRA DE ENERGIA NUCLEAR – ABEN ISBN: 978-85-99141-02-1

13. **Burchell, T.D., et al.,** The effects of Neutron irradiation on the structure or carbon-carbon composites, *Journal of Nuclear Materials*, 191-194, 1992

14. **Maruyama, N. and Harayama, M.,** Neutron irradiation effect on thermal conductivity and dimensional change of graphite materials, *Journal of Nuclear Materials,* 195, 44-50, 1992.

15. http://en.wikipedia.org/wiki/Amorphous_carbon, Andrea Carlo Ferrari and John Robertson, Raman spectroscopy of amorphous, nanostructured, diamond-like carbon, and nanodiamond, Phil. Trans. R. Soc. Lond. A 362, 2477–2512, 2004.

16. **Kroto, H. W., Allaf, A. W., and Balm, S. P.,** C_{60}: Buckminsterfullerene, *Chemical Review*, 91, 1213-1235, 1999.

17. http://accuracyandaesthetics.com/?p=444 (2010)

18. **Kroto, H. W., Allaf, A. W., and Balm, S. P.,** C_{60}: Buckminsterullerene, *Chemical Review*, 91, 1213-1235, 1991.

19. **Kroto, H. W., Heath, J. R., O'Brien, S. C., Curl, R. F., and Smalley, R. E.,** C_{60}: Buckminsterfullerene, *Nature* 318, 162 – 163, 1985; doi:10.1038/318162a0.

20. **Kroto, H. W., Allaf, A. W., and Balm, S. P.,** C_{60}: Buckminsterfullerene, *Chemical Review*, 91, 1213-1235, 1999.

21. **Pierson H.,** HANDBOOK OF CARBON, GRAPHITE, DIAMOND ANDFULLERENES Properties, Processing and Applications , Consultant and Sandia National Laboratories (retired) Albuquerque, New Mexico, NOYES PUBLICATIONS Park Ridge, New Jersey, U.S.A. ISBN: O-8155-1339-9.

22. **Wu, M., Patrick, P., Leong, T., Lei' C., Hwang, J., and Man, C.,** Magnetic and Optical Studies in K_3C_{60}, *Chinese Journal of Physics* 35, 6-7, 1997.

23. **Kamara´s, K., Iwasa, L., and Forro, T.E.,** Infrared spctra of one- and two-dimensional fullerene polymer structures: RbC_{60} and rhombohedral C_{60}, *Physcal Review B: Condense Matter 3*rd series, 55, 17.

24. **Tagmatarchis, N., and Prato, M.,** Carbon-based materials: From fullerene nanostructures to functionalized carbon nanotubes, *Pure Applied Chemistry*, Volume 77, No. 10, 1675–1684, 2005.

25. **Rohlfing, E.A., Cox, D.M., and Kaldor A.,** Production and characterization of supersonic carbon cluster beams, *Journal of Chemical Physics*, 81, 3322, 1984.

26. **Pusztai, T., Oszla´nyi, G., Faigel, G., Kamara´s, K., Gra´na´sy, L., and Pekker, S.,** Bulk structure of phototransformed C_{60}, *Solid State Communications* 111, 595–599, 1999.

27. **Wagberg, T., Stenmark, P., and Sundqvist, B.,** Structural aspects of two-dimensional polymers: Li_4C_{60}, Na_4C_{60} and tetragonal C_{60}. Raman spectroscopy and X-ray diffraction, *Journal of Physical Chemistry of Solids* 65, 317, 2004.

28. **Yasukawa, M., and Yamanaka, S.,** Synthesis of Li_xC_{60}(x=1–28) fullerides under high-pressure and high-temperature conditions and their electrical properties, Chemi*cal Physics Letters* 341, 464, 2001.

29. **Margadonna, S., Pontiroli, D., Belli, M., Shiroka, T., Riccò, M., and Brunelli, M.,** Li_4C_{60}: A Polymeric Fulleride with a Two-Dimensional Architecture and Mixed Interfullerene Bonding Motifs, *Journal American Chemical Society* 126, 15032, 2004.

30. **Ricc`o, M., Shiroka, T., Belli, M., Pontiroli, D., Pagliari, M., Ruani, G., Palles, D., Margadonna, S., and Tomaselli, M.,** Unusual polymerization in the Li_4C_{60} fulleride, *Physical Review* B 72, 155437, 2005.

31. **Ruoff, R., and Ruoff, A.,** The bulk modulus of C_{60} molecules and crystals: A molecular mechanics approach, *Applied Physics Letters* 59, 1553, 1991.

32. **Taylor, R., and Walton, D.,** The chemistry of fullerenes, *Nature* 363, 685, 1993.

33. **Dresselhaus, M.S., Dressehaus, G., and Eklund, P.C.,** Science of Fullerenes and Carbon Nanotubes (Academic Pres, New York 1996.

34. **Wang, S., Liut, K,, Zhus, L, Rens, Z., Shent, W., Shent, X., and Lis. Y.,** A study on fullerene incorporated into a porous silicon matrix (photoluminescence), Journal of Physics: *Condense Matter* 7, 8833-8838, 1995.

35. **Dresselhaus, M.S., Dresselhaus, G. and Eklund, P.C.,** Science of Fullerenes and Carbon Nanotubes, Academic Press, California, 1996.

36. **Miessler, G. L., Tarr, D.A**. Inorganic Chemistry (3 ed.). Pearson Education International. ISBN 0-13-120198-0, 2004.

37. **Mitchel, D. R., Malcolm Brown, Jr R., Spires, T. L., Romanovicz, D. K., and Lagow, R.J.** "The Synthesis of Megatubes: New Dimensions in Carbon Materials". Inorganic Chemistry 40: 2751. doi:10.1021/ic000551q, 2001.

38. **Harigaya, K.,** Electronic structures in C_{60}-polymers, arXiv:cond- mat/9604113v1 [cond-mat.mtrl-sci] 17 (1996)

39. **Sano, N.,** Synthesis of carbon 'onions' in water, *Nature (London)* 414: 506. doi:10.1038/35107141, 2001.

40. **Maniwa, Y., Ikejiri, H., Tou, H., Masubuchi, S., Kazama, S., Yasukawa, M. and Yamanaka, S.,** NMR Studies of Alkali-Doped C_{60} Polymers, *AIP Conference Proceeding* 590, 443-446 (2001).

41. **Zhu, Z.T., Musfeldt, J. L., Kamara´s, K., Adams, G. B. and Page, J. B., Davydov, V. A., Kashevarova, L. S., and Rakhmanina, A. V.,** Far-infrared vibrational properties of tetragonal C_{60} polymer, *Physical Review* B, 65, 085413.

42. **Okada, S., Saito, S.,** Electronic structure and energetics of pressure-induced two-dimensional C_{60} polymers, *Physical Review* B, 59, No.3, 1999-I.

43. **Yamanaka, S., Kubo, A., Inumaru, K., Komaguchi, K., Kini, N.S., Inoue, T., Irifune, T.,** Electron Conductive Three-Dimensional Polymer of Cuboidal C_{60}, *Physical Review Letters* 96, 076602, 2006.

44. **Nunez-Regueiro, M., Marques, L., Hodeau, J.-L., Bethoux, O., Perroux, M.,** Polymerized Fullerite Structures, *Physical Review Letters* 74, 278, 1995.

45. **Iwasa, Y., Arima, T., Fleming, R.M., Siegrist, T., Zhou, O., Haddon, R.C., Rothberg, L.J., Lyons, K.B., Carter, H.L., Jr., Hebard, A.F., Tycko, R., Dabbagh ,G., Krajewski, J.J., Thomas, G.A., Yagi, T.,** New Phases of C_{60} Synthesized at High Pressure, *Science* 264, 1570, 1994.

46. **Rao, A.M., Zhou, P., Wang, K.A., Hager, G.T., Holden, J.M., Wang, Y., Lee, W.T., Bi, X.X., Eklund, P.C., Cornett, D.S., Duncan, M.A., Amster I.J.,** Infrared and Raman studies of pressure-polymerized C_{60}, *Science* 259, 955, 1993.

47. **Kroto, H.,** Tilden Lecture: Semistable molecules in the laboratory and in space, *Chemical Society Review*, 11, 435 – 491, 1982, DOI: 10.1039/CS9821100435

48. **Reinov, M. V., and Yurovskaya, M. A.,** The formation of [5,6]- and [6,6]-open fulleroid structures, *Russian Chemical Review* 76,715, doi:10.1070/RC2007v076n08ABEH003695, 2007

49. **Herbig, E.,** The Diffuse Interstellar Bands IV - The Region 4400-6850 A, *Astrophysics Journal* 196, 129, 1975.

50. **Leger, A. and Puget, J.,** Identification of the "unidentified" IR emission features of interstellar dust? *Astrophysics Letters* 137, L5, 1984.

51. **Dietz, T., Duncan, M., Powers, D., and Smalley, R.,** Laser production of supersonic metal cluster beams, *Journal of Chemical Physics* 74,6511, 1981; doi:10.1063/1.440991

52. **Croton, H.,** Introduction, *Carbon* 30, 1139, 1992.

53. **Curl, R.,** Pre-1990 evidence for the fullerene proposal, *Carbon* 30, 1149, 1992.

54. **Okada, S., Saito, S.,** Electronic structure and energetics of pressure-induced two-dimensional C_{60} polymers, *Physical Review* B 59, No.3, 1999-I.

55. **Iwasa, Y., Arima, T., Fleming, R. M., Siegrist, T., Zhou, O., Haddon, R. C., Rothberg, L. J., Lyons, K. B., Carter Jr, H. L.., Hebard, A. F., Tycko, R., Dabbagh, G., Krajewski, J. J., Thomas, G. A., and Yagi, T.,** New Phases of C_{60} Synthesized at High Pressure, *Science*, 264, 1570, 1994.

56. **Núñez-Regueiro, M., Marques, L., Hodeau, J -L., Béthoux, O., and Perroux, M.,** Polymerized Fullerite Structures, *Physical Review Letters*, 74, 278, 1995.

57. **Marques, L. and Hodeau, J. -L.,** Pressure and temperature diagram of polymerized fullerite, *Physical Review*, B 54, R12633, 1996.

58. **Sundar, C. S., Sahu, P. C., Sastry, V. S., Rao, G. V. N., Sridharan, V., Premila, M., Bharathi, A., Hariharan, Y., and Radhakrishnan, T. S.,** Pressure-induced polymerization of fullerenes: A comparative study of C_{60} and C_{70}, *Physical Review*, B 53, 8180–8183, 1996.

59. **van Loosdrecht, P. H. M., Verheijen, M. A., Meekes, H., van Bentum, P. J. M., and Meijer, G.,** Lattice vibrations in crystalline C_{70}, *Physical Review* B 47, 7610–7613, 1993.

60. **Vaughan, G. B. M., Chabre, Y. and Dubois, D.,** Effect of Stacking Disorder on the Orientational Ordering Transition of Solid C_{60}, *Europhysics Letters*, 31, 525, 1995.

61. **Kawamura, H., Kobayashi, M. Akahama, Y., Shinohar, H., Sato, H. and Saito Y.,** Orientational ordering in solid C_{70} under high pressure, *Solid State Communications*, 83, 563, 1992.

62. **Lundin, A., Soldatov, A. and Sundqvist, B.,** Compressibility and Structure of C_{70}, *Europhysics Letters*, 30, 469, 1995.

63. **Premila, M., Sundar, C. S., Sahu, P. Ch., Bharathi, A., Hariharan, Y., Muthu, D. V. S., and Sood, A.K.,** Pressure induced dimerisation of C_{70}, *Solid State Communications*, 104, 4, 237-242, 1997.

64. **Clougherty P. D.,** Ferroelectricity in $(K@C_{60})n$, arXiv:cond-mat/0212525v1 [cond-mat.mtrl-sci], 2002

65. **Núñez-Regueiro, M., Marques, L., Hodeau, J –L., Béthoux, O., and Perroux, M.,** Polymerized: Fullerite Structures, *Physical Review Letters* 74, 278, 1995

66. **Zhou, P., Dong, Z., Rao, A.M. and Eklund, P.C.,** Reaction mechanism for the photopolymerization of solid fullerene C_{60}, *Chemistry and Physics. Letters* 211, 337, 1993.

67. **Miyazawa, K., Kuwasaki, Y., Obayashi, A., and Kuwabara, M.,** C_{60} nanowhiskers formed by the liquid-liquid interfacial precipitation-method, *Journal of Materials Res*. 17, 1, 2002.

68. **Pusztai, T., Oszla´nyi, G., Faigel, G., Kamara´s, K., Gra´na´sy, L., Pekker, S.,** Bulk structure of phototransformed C_{60}, *Solid State Communications* 111, 595–599, 1999.

69. **Li, C., Chen, Y., Wang, Y., Iqba, Z., Chhowalla, M., and Mitra, S.,** A fullerene–single wall carbon nanotube complex for polymer bulk heterojunction photovoltaic cells, Journal of Materials Chemistry, 2007, 17, 2406–2411, http://www.nano-c.com/fullereneapp.html, http://www.nano-c.com/fullereneapp.html (2010)

CHAPTER 2

CHARACTERIZATION TECHNIQUES

Introduction

This chapter briefly describes important characterization techniques used in the study. These techniques are stereo microscopy, scanning electron microscopy (SEM), transmission electron microscopy (TEM), and atomic force microscopy (AFM) to study the morphology, Raman and Fourier Transform Infra-Red (FTIR) spectroscopy for molecular vibration and phonon study, X-ray diffraction (XRD) for the determination of the microstructure, and proton induced x-ray emission (PIXE).

2.1. Stereo microscope

It is a type of microscope which uses visible light and a system of lenses to study small samples. It is designed for low magnification of different types of samples in different states. The whole concept is based on the illumination of the sample with light and observing the light reflected into the objective lenses which forms an image of the sample. As the light travels into the lens, refraction occurs when it passes through a medium with a different refractive index. It then produces three-dimensional visualization by using two separate optical paths with two objective lenses and two eyepieces to provide slightly different viewing angles to the eyes. It also overlaps microphotography for recording and examining the topography which can be displayed on a computer screen for detail analysis as shown in figure 2.1.

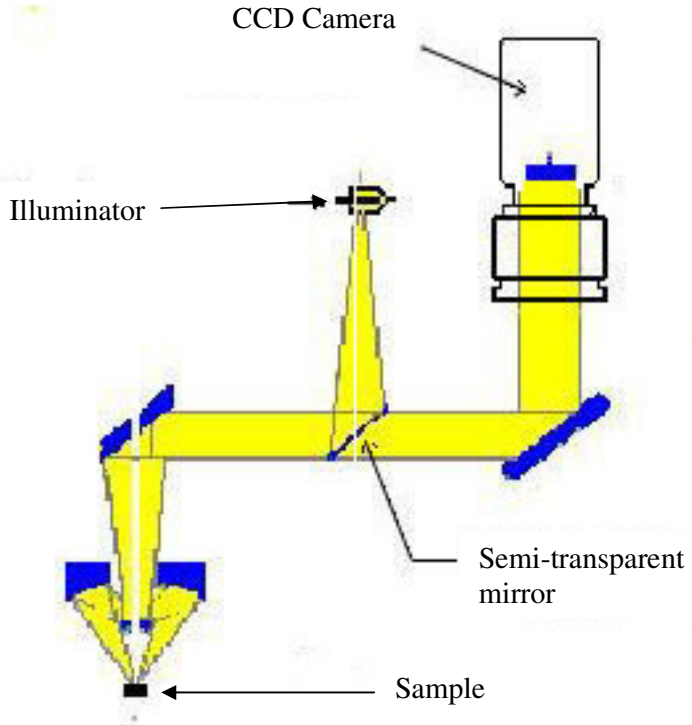

Figure 2. 1: Schematic diagram of an Optical microscope [1].

2.2. Scanning Electron Microscope (SEM)

Scanning electron microscope (SEM) is a nondestructive technique that uses beam of electrons to produce an image. Electrons are thermonically emitted by cathode tungsten filament within an electron gun at the top of the microscope, following the process described in reference [2]. These electrons are accelerated down a vertical path in the microscope which is under vacuum to interact with the sample as shown in figure 2.2. The beam is directed and controlled by a series of magnetic lenses, which then focuses the beam down onto the sample.

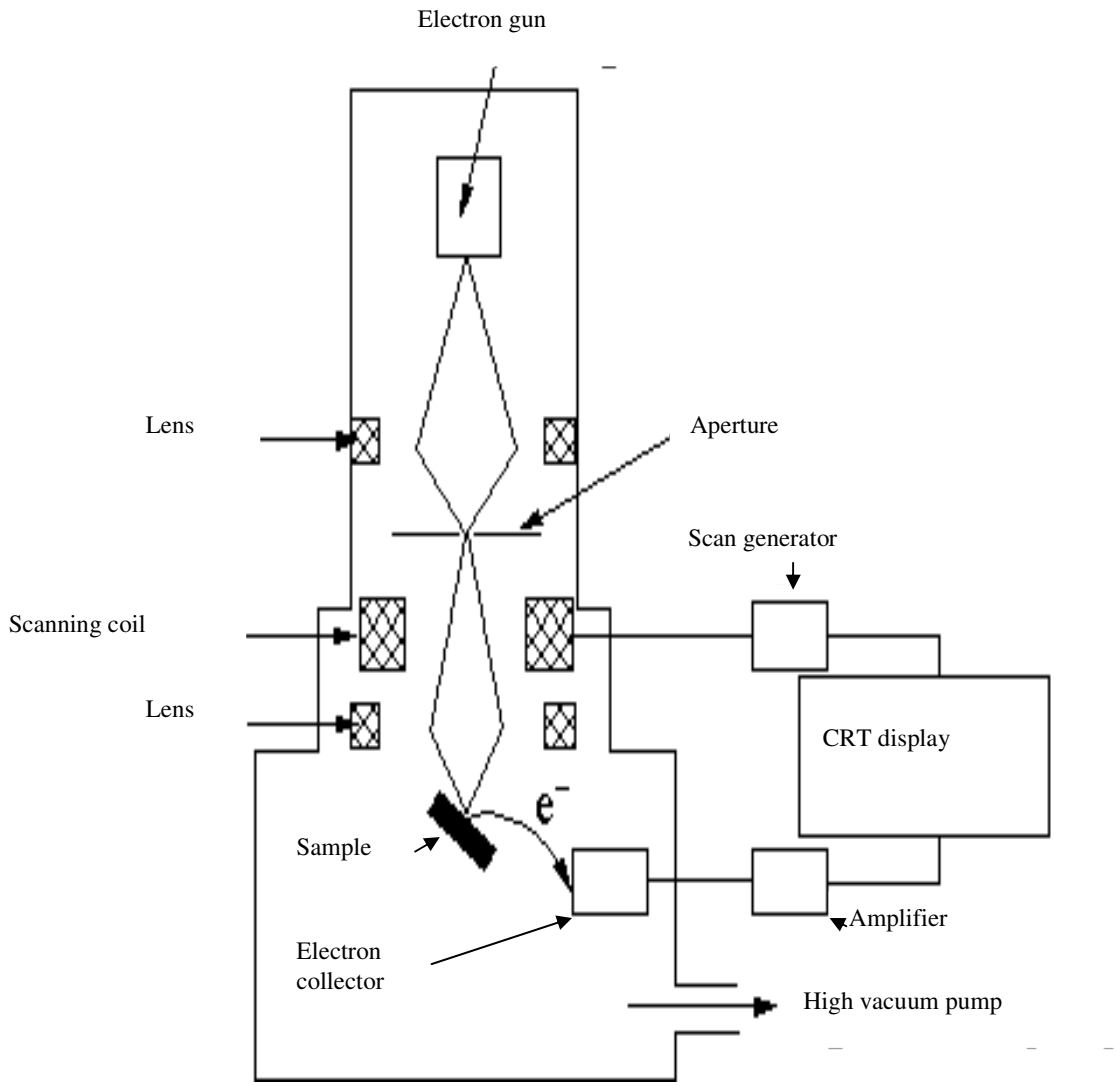

Figure 2. 2: Schematic diagram of Scanning Electron Microscope (SEM) [2].

The electrons then interact with the sample. During interaction electrons are ejected from the sample and also the x-rays are produced in the process as shown in figure 2.3. The electrons and x-rays are then collected by their respective detectors and converted into a signal that is finally sent into a computer screen to produce an image.

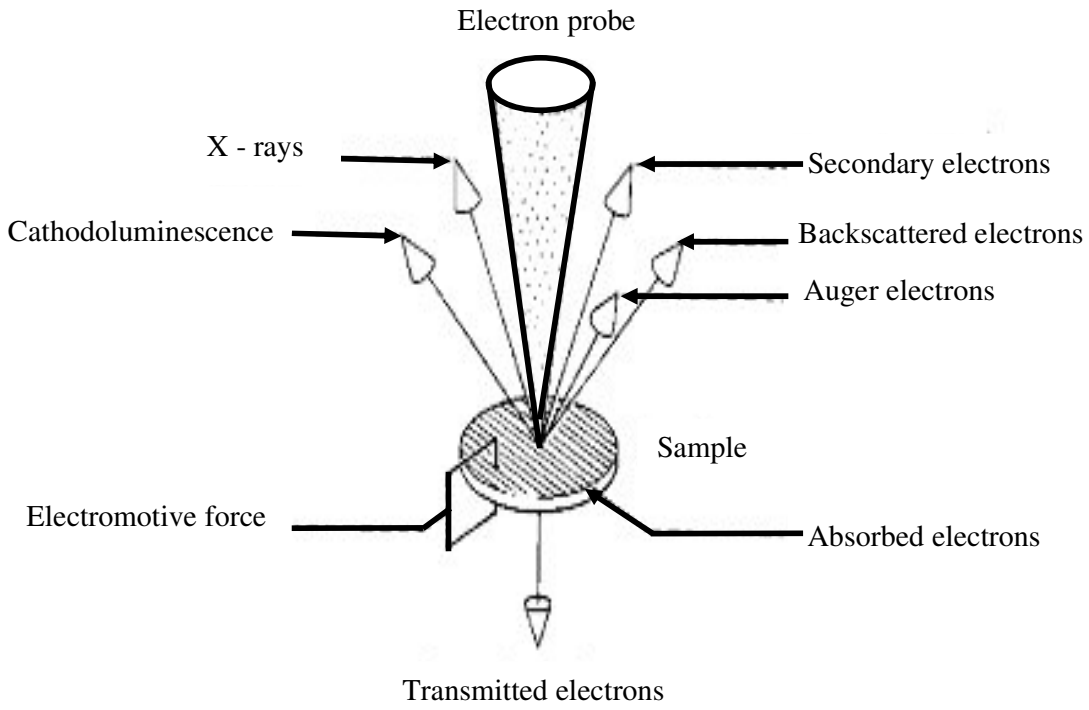

Figure 2. 3: The interaction of an electron beam with the sample [2].

2.3. Atomic force microscopy (AFM)

Atomic force microscopy is one of the non-destructive techniques used for imaging, measuring dimensions, and manipulating matter at the nanoscale. It consists of a cantilever with a sharp tip with a radius of curvature of the order of nanometers (10^{-9}m) at its end. This is used to scan the specimen surface as shown in figure 2.4.

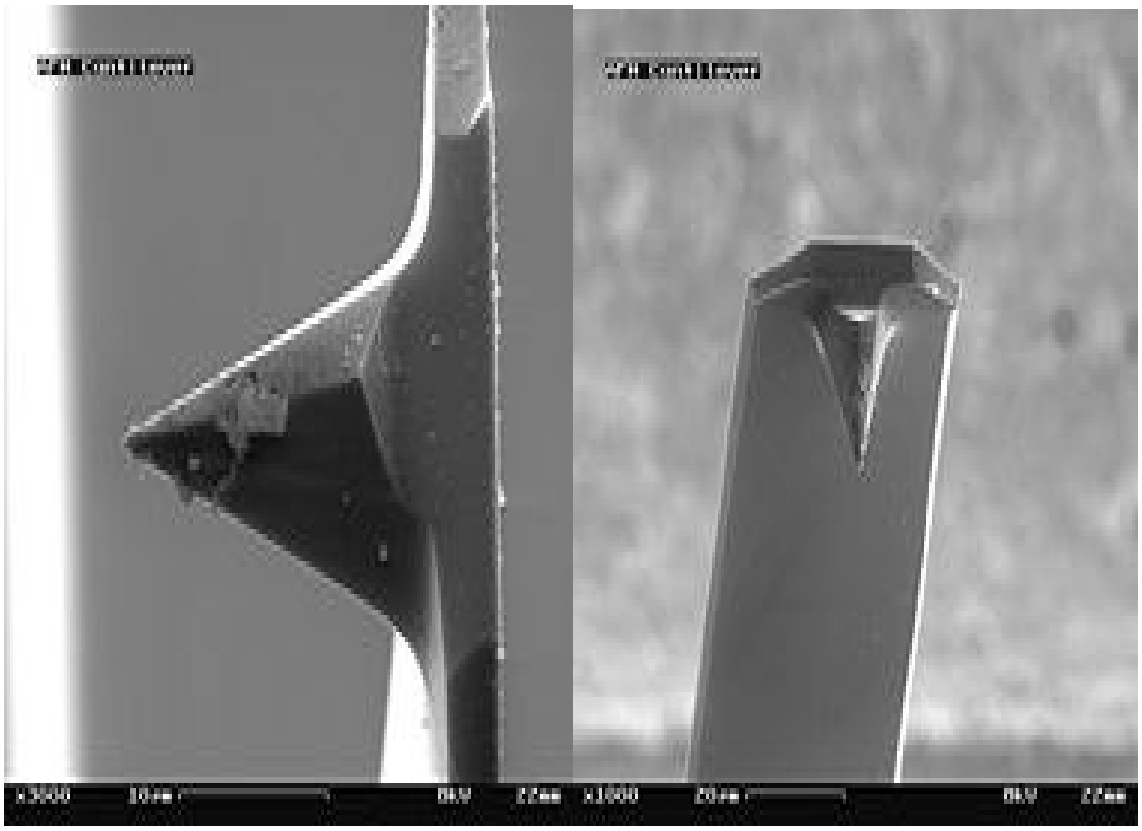

Figure 2. 4: Electron micrograph of AFM cantilever image with a tip [3].

When the tip is brought into proximity of a sample surface, Coulombic forces between the tip and the sample lead to a deflection of the cantilever. Typically, the deflection is measured using a laser spot reflected from the top surface of the cantilever into an array of photodiodes as shown in figure 2.5.

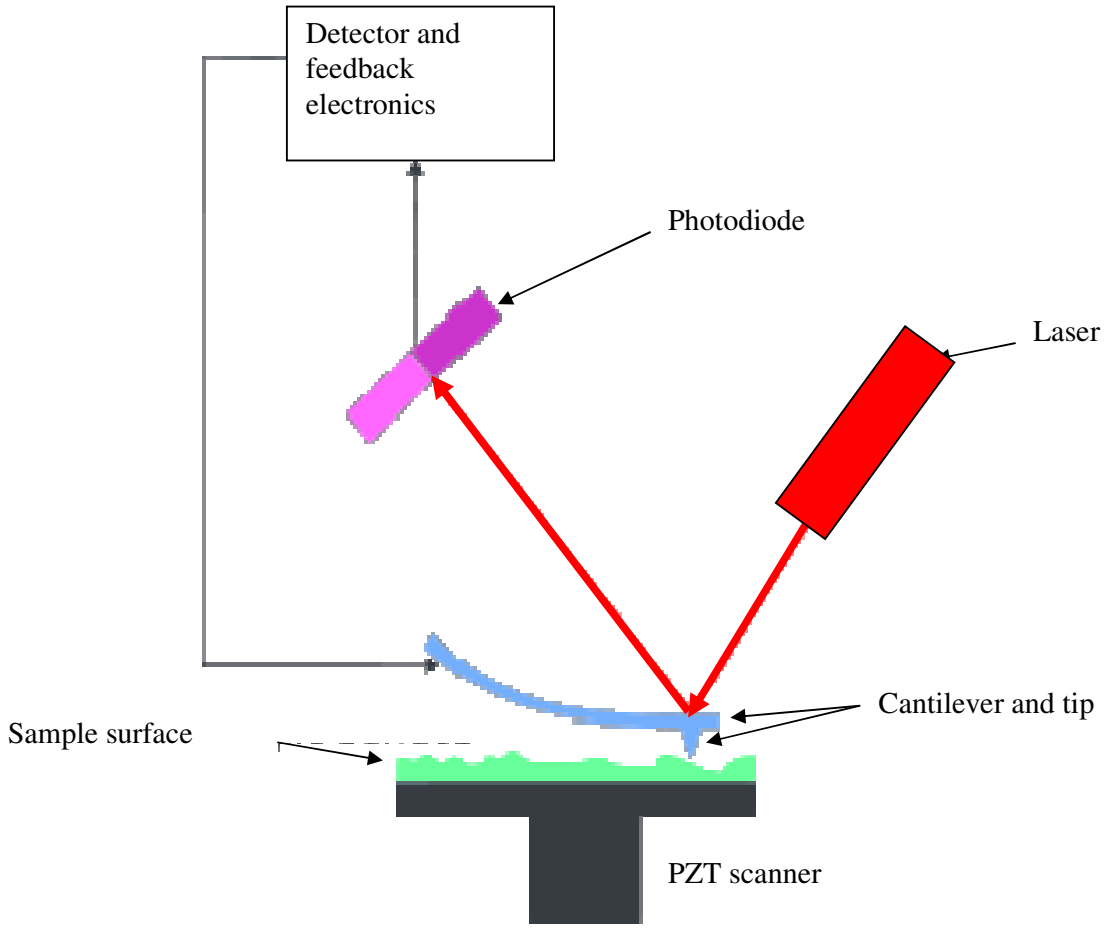

Figure 2. 5: Diagram of atomic force microscope (AFM) [3]

During the measurement, the sample is placed on the electromechanical stage. In order to obtain the image of topology of the sample, a tip is tapped across a sample surface and the change in the vertical position (denoted the "z" axis) which reflects the topography of the surface is fed back to a photo-detector. The collection of the height data for a succession of lines is constructed to form a three dimensional map of the surface features. Details about this technique are found in reference [3-5].

2.4. Transmission Electron Microscope (TEM)

This is a technique which is used to examine the specimen structure, composition or properties in submicroscopic details. This technique is significantly involved in numerous fields such as biology, chemistry and materials science. It works like a projector except that it shines a beam of electrons through the specimen and the beam is transmitted through the specimen onto a phosphor screen to be displayed as an image. It usually consists of four sections; electron source, electromagnetic lens system, sample holder, and imaging system as shown in figure 2.6

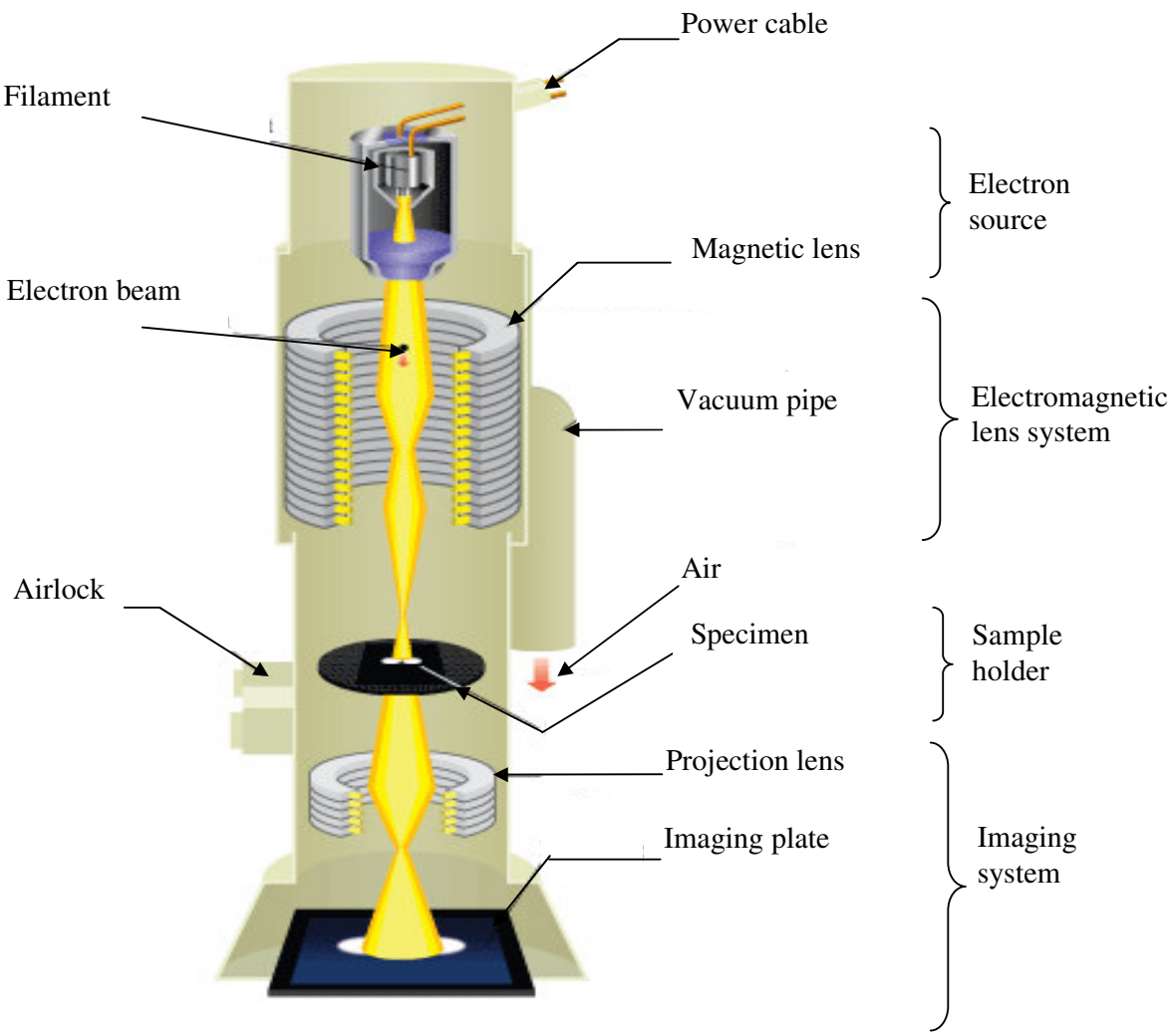

Figure 2. 6: Diagram of Transmission Electron Microscope (TEM) [6].

The electron source consists of a cathode which is tungsten filament that emits electrons when heated and the electrons are then confined by a negative cap into a focused beam. The positive anode then accelerates electrons towards the specimen through a small hole of the anode. The electron beam from the source is focused using electromagnetic lens and metal apertures in order to let electrons with small energy range to pass through so that they can have well defined beam. The sample holder is a platform equipped with a mechanical arm for holding the specimen and controlling its position. The imaging system consists of another electromagnetic lens system and a screen. This electromagnetic lens system contains two lens systems, one for refocusing the electrons after they pass through the specimen, and the other for enlarging the image and projecting it onto the screen. The screen has a phosphorescent plate which glows when being hit by electrons. Image forms in a way similar to photography [6].

2.5. Raman spectroscopy

It is a non-destructive technique requiring no sample preparation. It is used to study vibrational, rotational and translational modes in a system. It is performed by illuminating a sample with a monochromatic light with a specific wavelength. This monochromatic light is scattered by the sample atoms in three processes, Rayleigh scattering, Stokes Raman scattering and anti-Stokes Raman scattering as shown in the energy diagram in figure 2.7.

Rayleigh scattering is the process whereby the energy of the scattered light is equal to that of incident monochromatic light, while in Stokes Raman scattering process the energy of the incident light is greater than that of the final scattered light, thereby causing lower frequency shift and the anti-Stokes Raman scattering occurs when energy of the incident light is less than that of the final scattered light thereby causing a higher frequency shift.

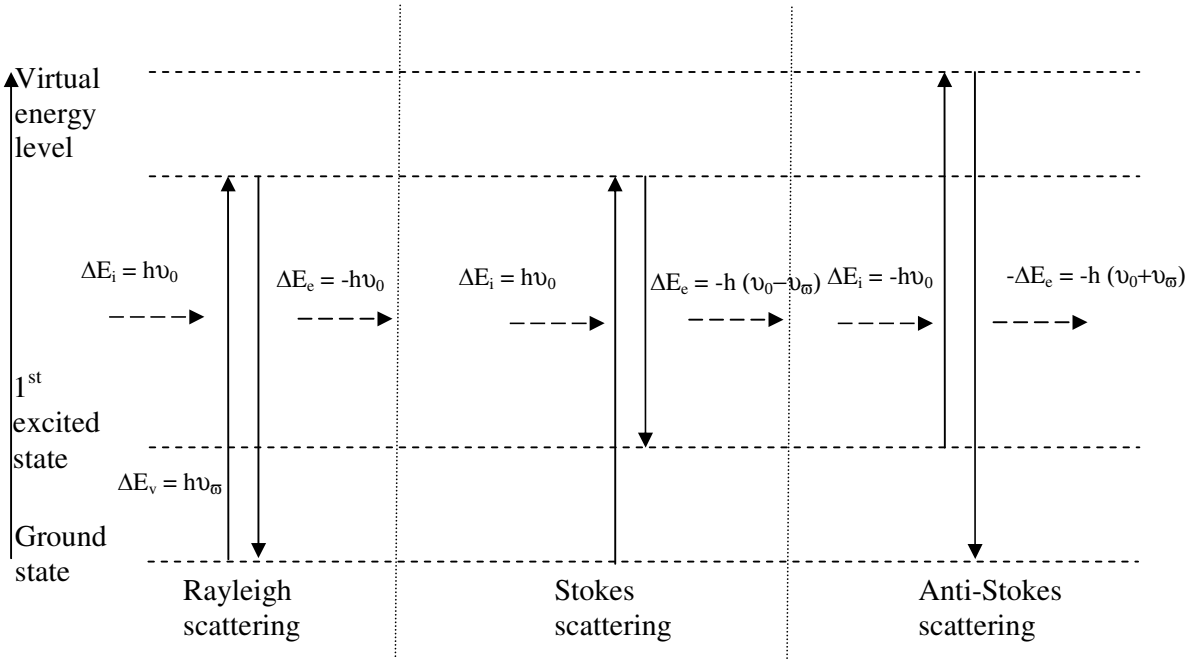

Figure 2. 7: Energy level diagram showing the states involved in Raman signal.

Rayleigh scattered wavelengths are filtered out while the rest are collected and dispersed onto a charge-coupled device (CCD) detector as shown figure 2.8 and the data is plotted as Raman shift versus intensity. The intensity represents the amount of deformation and a change of structure while Raman shift determines the vibrational and rotational states of the sample. Raman shift is expressed in wavenumbers (cm^{-1}) which is given by equation 2.1.

$$\Delta\omega = \frac{1}{\lambda 0} + \frac{1}{\lambda 1} \quad \text{..... Equation 2. 1}$$

where Δw is the Raman shift expressed in wavenumber, λ_0 is the excitation wavelength, and λ_1 is the Raman spectrum wavelength. Most commonly, the units chosen for expressing wavenumber in Raman spectra is inverse centimeters (cm^{-1}). Check reference [7-11] for full description of this technique.

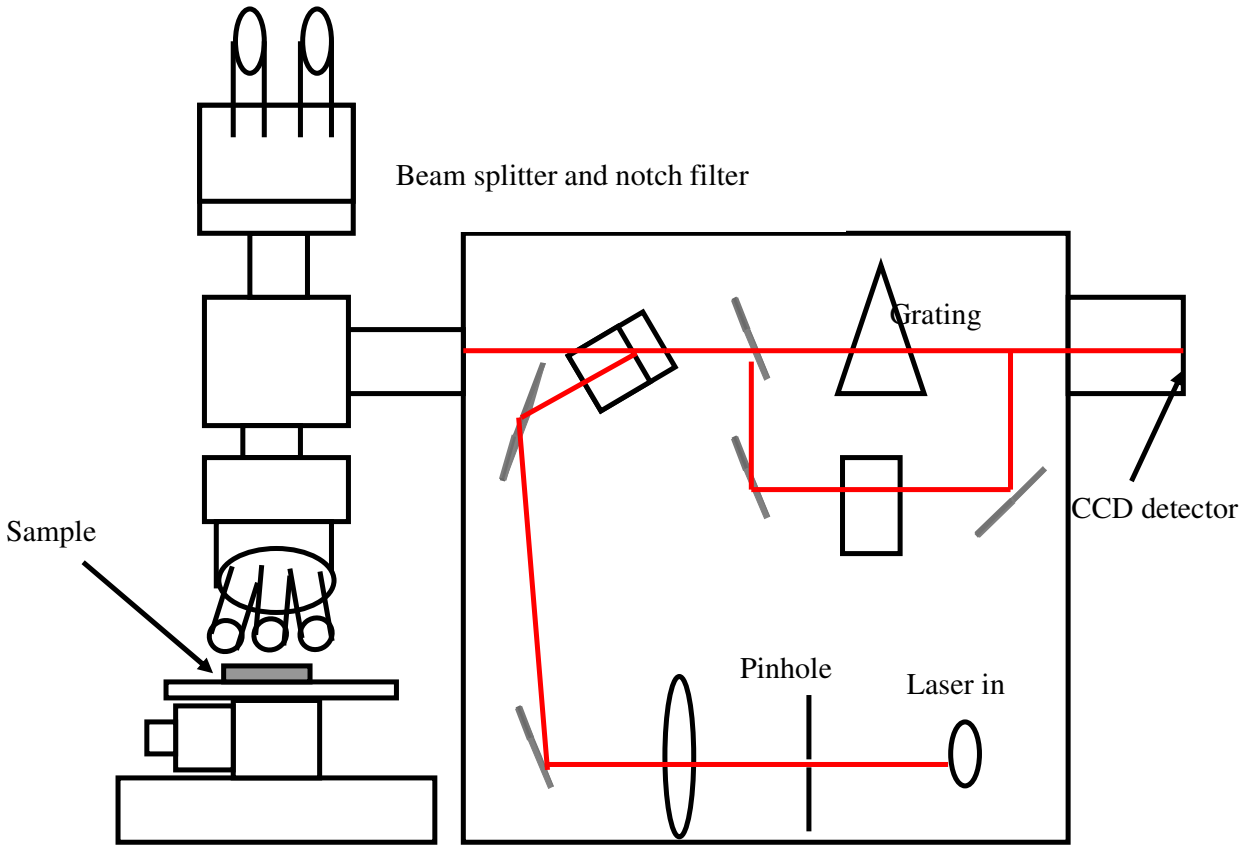

Figure 2. 8: Schematic diagram of a Raman spectrometer [7].

2.6. Fourier Transform Infrared Spectroscopy (FTIR)

Fourier Transform Infrared spectroscopy (FTIR) is a complementary technique to Raman spectroscopy. It is a useful technique for the qualitative study of a wide range of substances such as solids, liquids, and gases. It uses the infrared region of the electromagnetic spectrum and it is divided into three regions; the near-, mid- and far infrared.

The near infrared has wavelength range of approximately 14000-4000 cm^{-1} and it is used to study harmonic vibrations of molecules. The mid-infrared has wavelength range of approximately 4000 - 400 cm^{-1} and it is used to study the fundamental vibrational and rotational modes of molecules. The far infrared has wavelength range of approximately 400-10 cm^{-1} and is used for rotational spectroscopy. The mid-infrared was used in this study to

study vibrational mode of bonds by passing an infrared light through the sample as shown in figure 2.9.

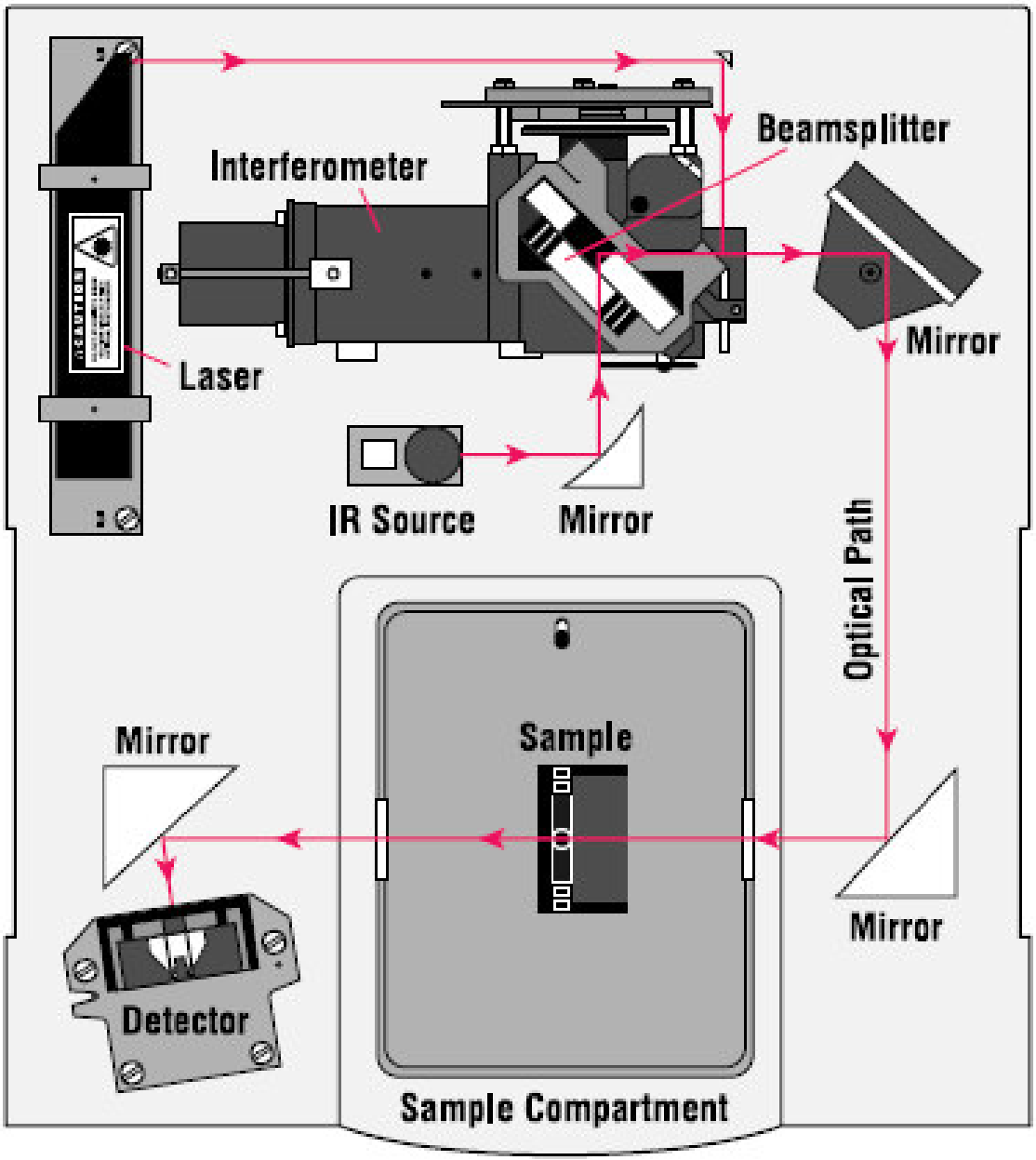

Figure 2. 9: Schematic diagram of FTIR machine [7].

When this infrared light interacts with the matter, chemical bonds will react to the infrared light either by coupling with the photons of the same wavelength as that of the vibrating atoms, thereby amplifying those modes. When the frequency of the IR is the same as the vibrational frequency of a bond, absorption occurs.

Transmitted light reveals the amount of energy absorbed that is achieved by measuring the wavelength using Fourier transform instrument which generate transmittance or absorbance spectrum. The information about the molecular structure of the sample is obtained from the analysis of the position, shape and intensity of the peaks in the spectrum. The spectrum is analyzed using common absorption bands as shown in figure 2.10. The details are found in reference [12-14]

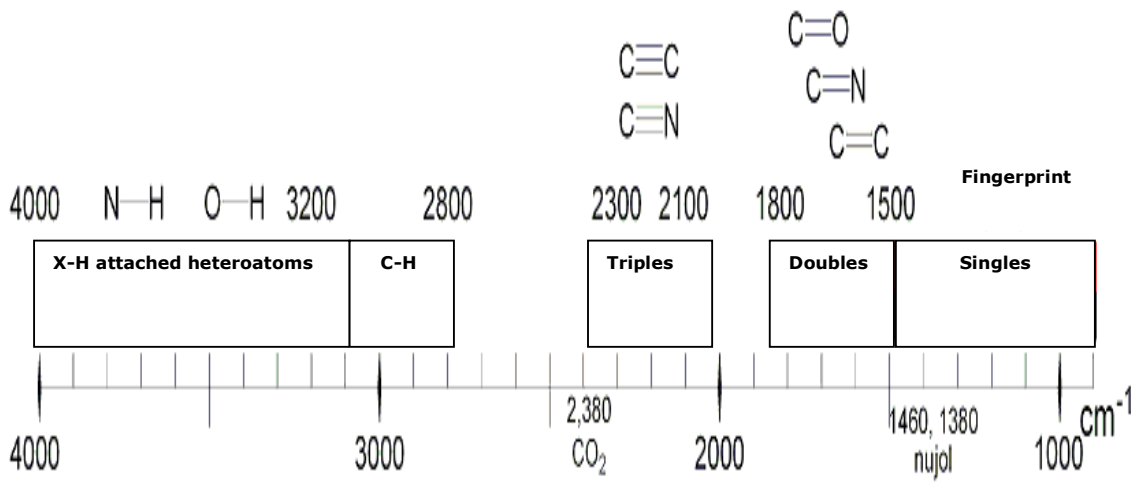

Figure 2. 10: FTIR fingerprint for spectrum analysis [12-14].

2.7. X-ray Diffraction (XRD)

X-ray diffraction (XRD) is a versatile, non-destructive analytical technique used for microstructural determination of materials by probing a sample with a beam of x-rays. During this process, x-rays are diffracted into a direction of angle 2θ resulting in destructive and constructive interference of the diffracted beam as shown in figure 2.11. Since destructive interference beam cancel each other out, only constructive interference beam is collected by a

detector in accordance to Bragg's law. The intensity of the collected beam from the detector is plotted against the angle of 2θ. The resulted spectrum is used to determine the mean positions of the atoms in the crystal. For maximum collection of data the stage is rotated as shown in figure.2.12.

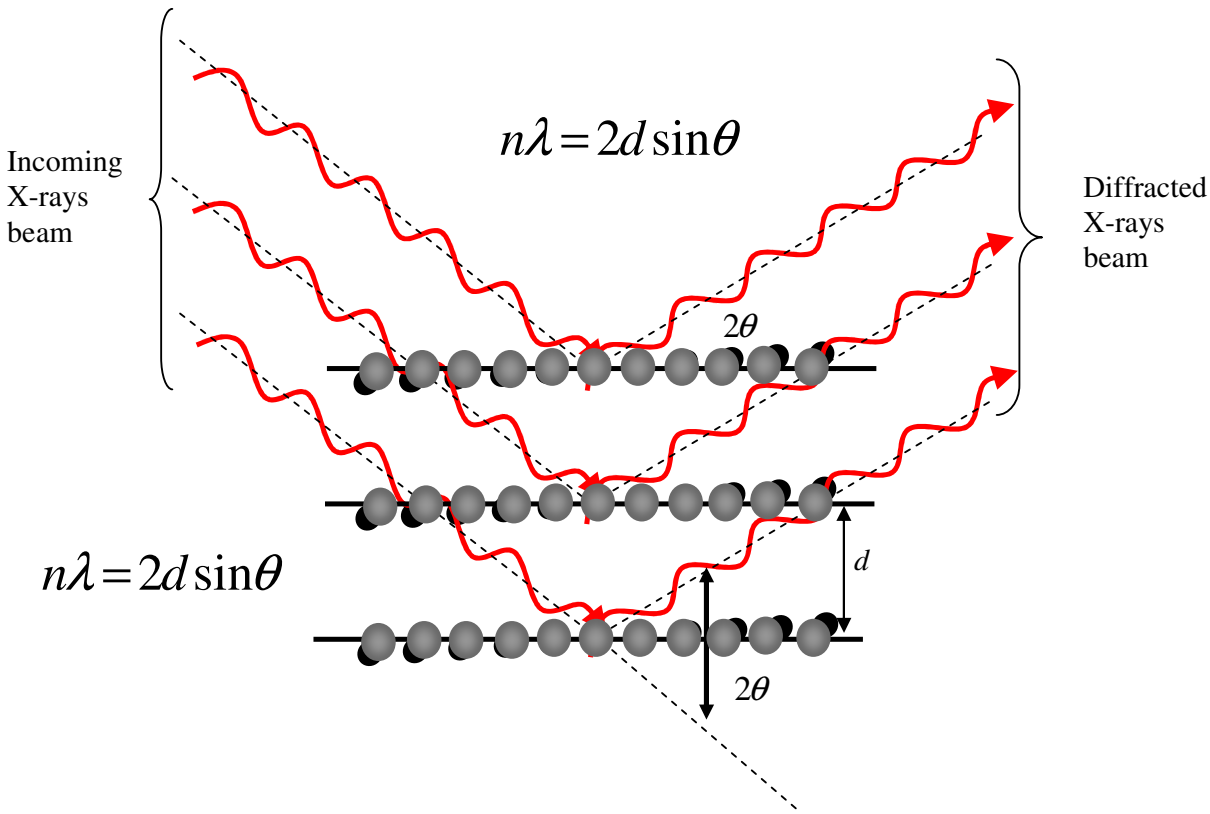

n = an interger-1, 2, 3….etc [n=1 for our calculations]

λ = the wavelength of the incident X-radiation, symbolized by the Greek letter lambda and, in our case, equal to 1.54 angstroms.

d = Spacing between atomic planes

Figure 2. 11: Schematic diagram showing typical arrangement of atoms within a crystal and diffracted beam.

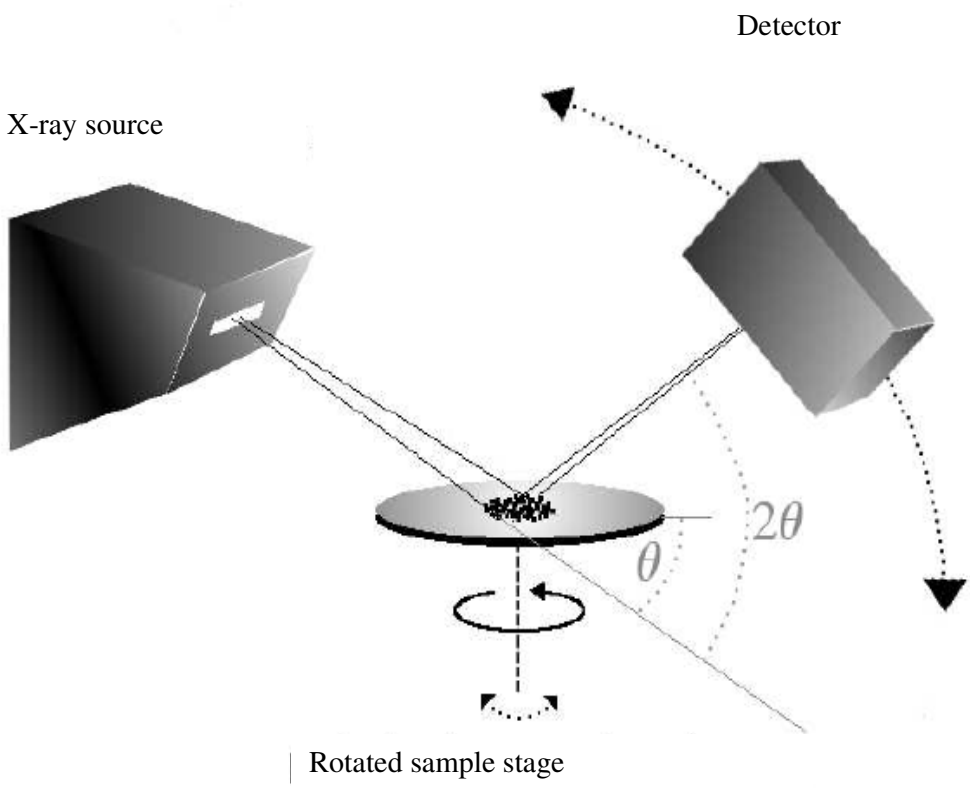

Figure 2. 12: X-ray diffraction setup in □-2□ geometry [15].

The distance between the planes of atoms is obtained from Bragg's Law as shown in equation 2.2

$$n\lambda = 2d\sin\theta$$ ……**Equation 2. 2**

The direction of these planes is obtained by comparing diffraction data against a database maintained by the International Centre for Diffraction Data. These are then used to calculate the lattice parameter by using equation associated with the structure obtained i.e. for the case of a cubic lattice. A lattice constant can be calculated using equation 2.3.

$$d = \frac{a}{\sqrt{h^2 + k^2 + l^2}}$$ ..... **Equation 2. 3**

Detailed processes of this technique can be checked in reference **[15-18]**

2.8. Proton Induced X-ray Emission (PIXE)

PIXE is a powerful and relatively simple analytical technique that can be used to identify and quantify trace elements ranging from Aluminium (Al) to Uranium (U). It uses protons to probe samples. Protons of 1-4 MeV are most often used. X-ray detection is usually done by energy dispersive semiconductor detectors such as Si(Li) or High Purity Germanium detectors.

Basic principle of PIXE involves charged particle moving through the material. As a charged particle moves through a material, it loses energy primarily by exciting electrons in the atoms. Electrons in the inner shells of the atom (predominantly the K and L shells) are given enough energy to cause them to be ejected, resulting in an unstable electron atomic configuration. Electrons from higher shells in the atom then 'drop down' to fill these vacancies, and in so doing, give off excess energy in the form of X-rays. The energies of these X-rays are characteristics of the element and therefore can be used to identify elemental composition.

On the other hand, by measuring intensities of characteristic X-ray lines one can determine concentrations of almost all elements in the sample. Furthermore, X-ray production yields are high and continuum background in PIXE is low. Therefore the detection limits are about two orders of magnitude better than with electron beams. PIXE spectra are usually collected in energy-dispersive mode and all elements with atomic numbers above 10 (Na and above) can in principle be detected at once. The characteristic X-rays of lighter elements are absorbed in the windows of routinely used Si(Li) or HPGe detectors. Typically reported sensitivities are 10-20 ppm for Na to Cl and 1-10 ppm for Ca and heavier elements. No information related to chemical identity, coordination chemistry or oxidation state of a particular element could be directly obtained [19].

2.9. References

[1] http://www.sv.vt.edu/classes/MSE2094_NoteBook/96ClassProj/experimental/optical.html (2010)

[2] http://www.uga.edu/caur/semnote1.htm# (2010)

[3] http://en.wikipedia.org/wiki/Atomic_force_microscopy (2010)

[4] http://www.mansic.eu/documents/PAM1/Frangis.pdf (2010)

[5] http://www.weizmann.ac.il/Chemical_Research_Support/surflab/peter/afmworks/ (2010)

[6] http://universe-review.ca/R11-13-microscopes.htm (2010)

[7] www.chm.bris.ac.uk/pt/diamond/stuthesis/chapter2.htm (2010)

[8] www.patents.com/us-7361501.html) (2010)

[9]http://www.perkinelmer.com/CMSResources/Images/44-74565MAN_Raman20Questions.pdf (2010)

[10] **Lyon, L.A., Keating, C. D., Fox, A. P., Baker, B. E., He, L., Nicewarner, S. R., Mulvaney S. P., and Natan, M. J.,** Raman Spectroscopy, *Analytical Chemistry* 70, 341R-361R, 1998.

[11] http://en.wikipedia.org/wiki/Raman_spectroscopy (2010)

[12] www.nuance.northwestern.edu › KECK-II › Instruments (2010)

[13] http://en.wikipedia.org/wiki/Fourier_transform_infrared_spectroscopy (2010)

[14] http://mmrc.caltech.edu/FTIR/FTIRintro.pdf] http://www.newport.com/Introduction-to-FT-IR-Spectroscopy/405840/1033/content.aspx (2010)

[15] http://serc.carleton.edu/research_education/geochemsheets/techniques/XRD.html (2010)

[16] R. James, Connolly, for EPS400-002, Introduction to X-Ray Powder Diffraction, Spring 2007,

[17] http://epswww.unm.edu/xrd/xrdclass/01-XRD-Intro.pdf (2010)

[18] http://www.bccmeteorites.com/XRD.PDF (2010)

[19] http://tlabs.ac.za/matservices.htm (2010)

CHAPTER 3

MATERIALS AND EXPERIMENTS

3.1. Synthesis of C_{60} nanorods

C_{60} nanorods were grown on Si (111) substrate by using a molecular recognition or self-assembly based method known as liquid-liquid interfacial polymerization method [1]. In this synthesis, 80 mg of C_{60} (99% purity Sigma Aldrich) powder (shown in figure 3.1) was dissolved in a 1ml volume of toluene ($C_6H_5CH_3$) to obtain a concentration of 0.1 M.

Figure 3. 1: C_{60} (99.9% purity Sigma Aldrich) powder in a bottle.

The dissolution was performed at ~25 ^{o}C under normal light. 1 ml of the initial $C_{60}/C_6H_5CH_3$ solution (as shown in figure 3.2) was poured into five different glass containers, and then 1 ml of $CH_3CHOHCH_3$ (IPA) was added gently in the containers with $C_{60}/C_6H_5CH_3$ solution to create a liquid-liquid interface with $CH_3CHOHCH_3$ forming the upper phase as shown in figure 3.3.

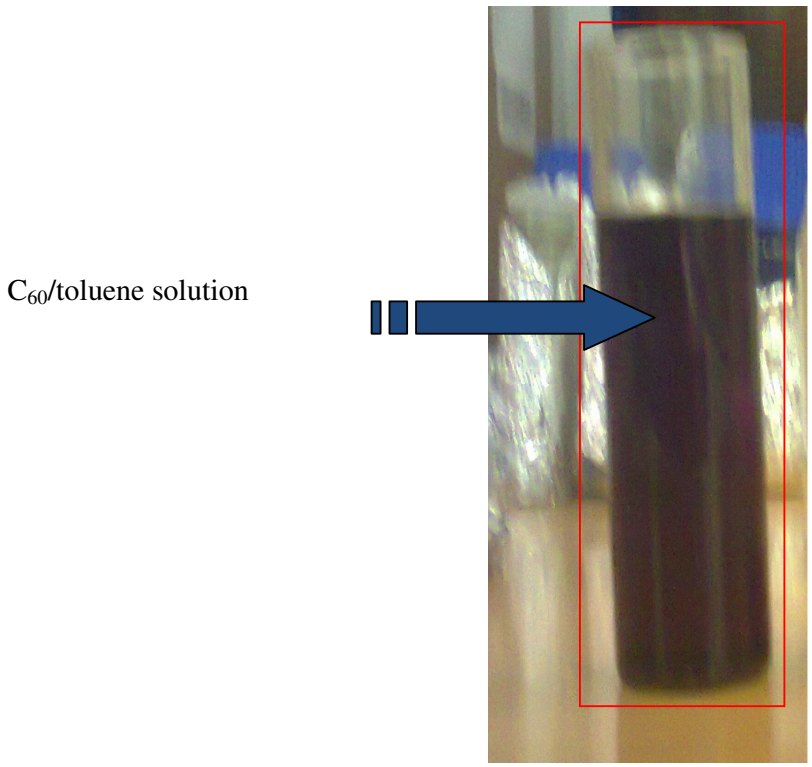

Figure 3. 2: The dissolution of C_{60} (99% purity Sigma Aldrich) powder in toluene performed at ~25^{0}C under normal light.

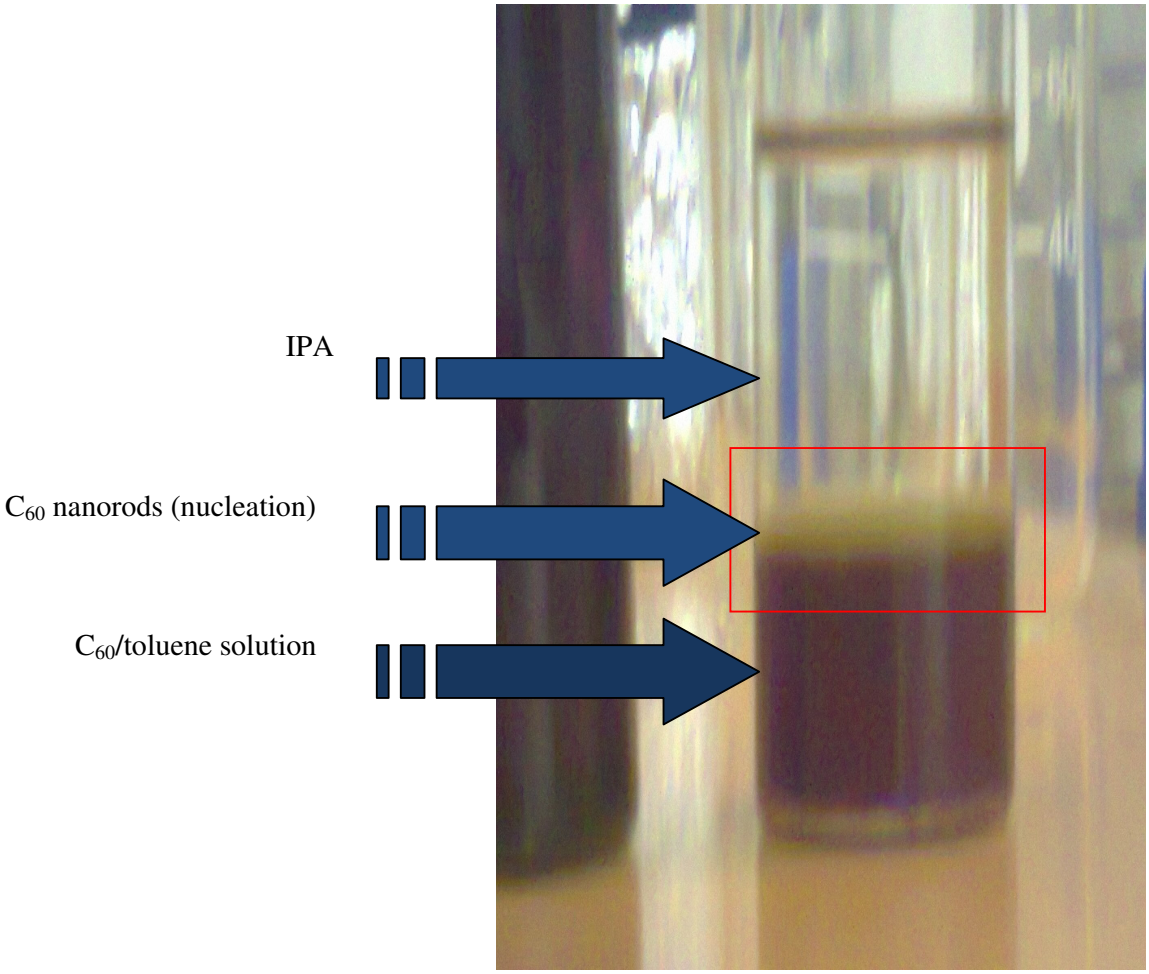

Figure 3.3: A Miyazawa liquid-liquid interfacial precipitation of C_{60} fullerene nanorods immediately after layering isopropanol (IPA) atop freshly prepared C_{60} fullerene-toluene solution [1,2].

A standard cleaned Si (111) substrate of 10 × 10 mm^2 size was immersed in all five containers in order to grow the nanorods of C_{60} on it. All containers were capped fully with aluminium foil to avoid any photo-induced effect and kept at ~25 ^{o}C until the precipitates of rods-like crystals of C_{60} formed. Following the growth phase as shown in figure 3.4, the coated Si (111) substrates with nanorods were taken out for preliminary characterization before the irradiation process.

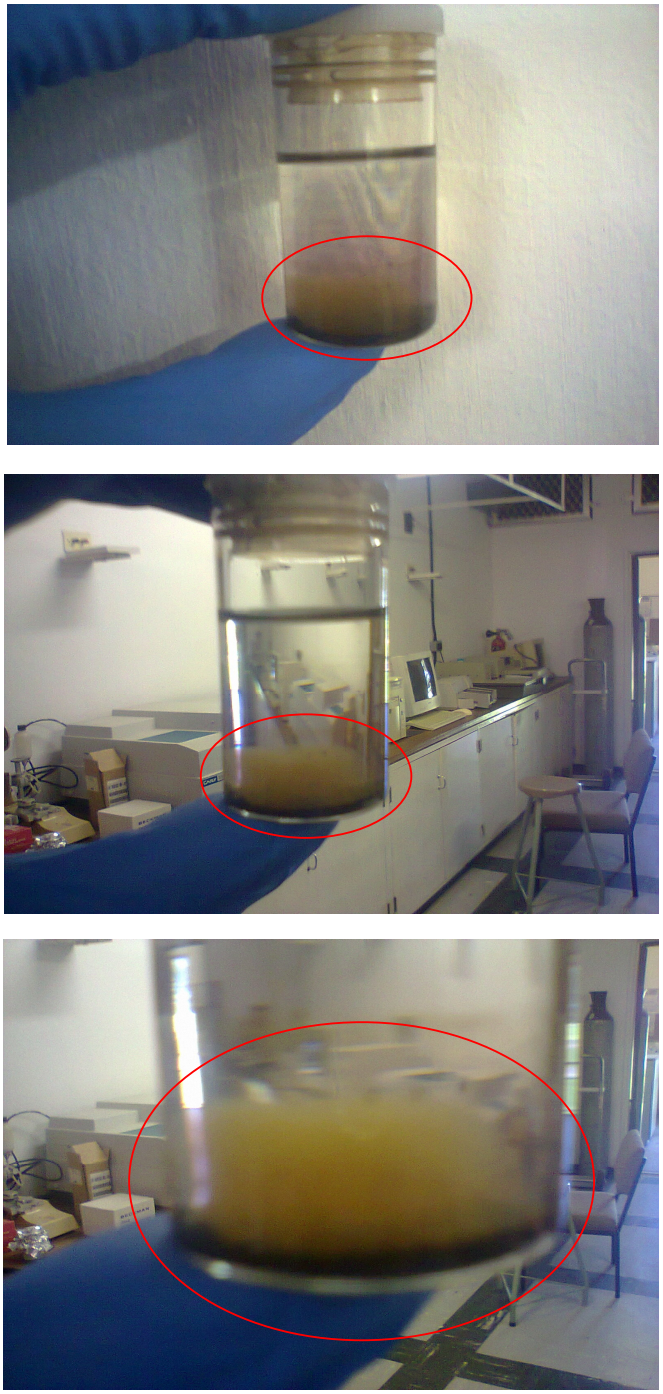

Figure 3. 4: growth phase of C_{60} nanorods at room temperature show (a) on incomplete process, (b) almost complete process, and complete process.

3.2. Irradiation of nanorods on Si (111) substrate

3.1.1. Proton irradiation

Proton irradiation experiment was performed at iThemba LABS facility at the Materials Research Department (MRD). A 2 MeV proton beam produced by the van der Graff accelerator which has five beam lines (ABCDE) as in figure 3.5. The beam line which was used in this project was B-line indicated by red dots.

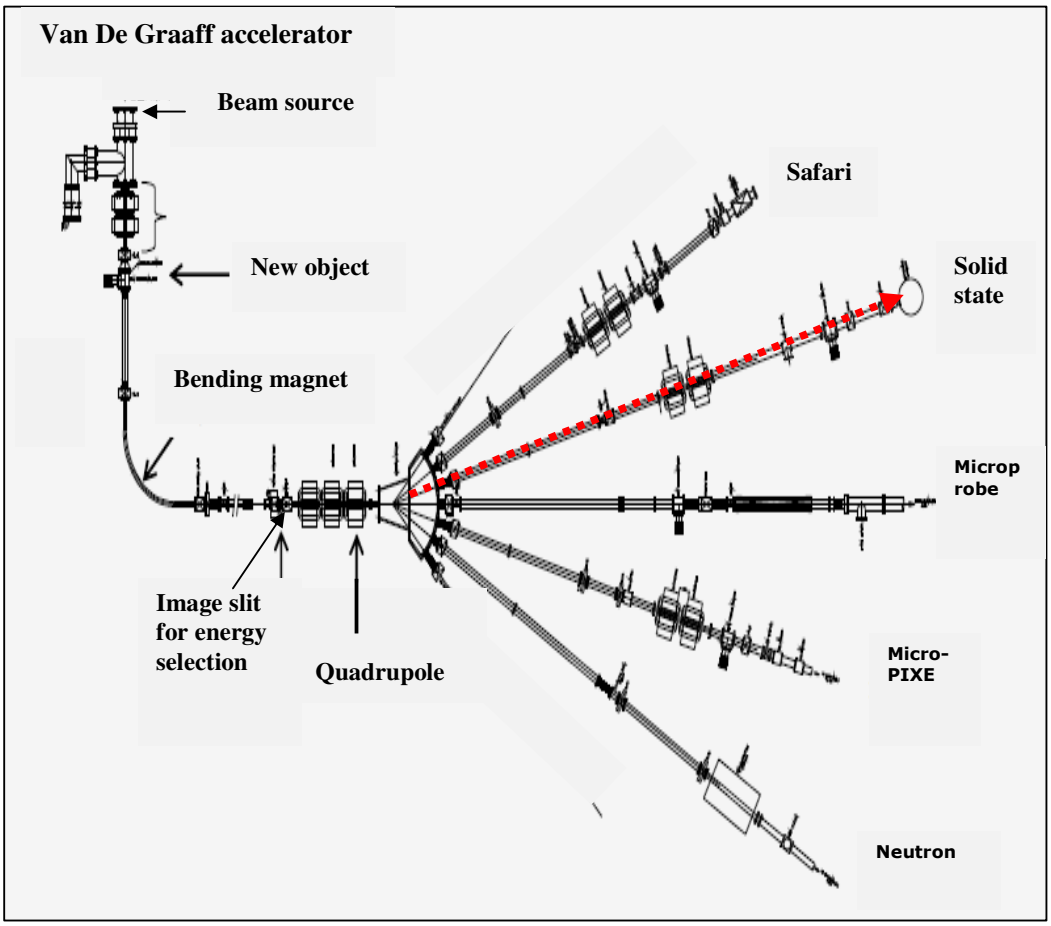

Figure 3.5: Schematic diagram of the van der Graff accelerator LABS with dotted line showing beam line used for proton irradiation.

The beam was then channelled vertically downwards and passed through a 90° bending magnet to be bent it horizontally. After passing the bending magnet the proton beam entered a beam line consisting of a series of components such as steering coils, slits and quadruples to be focused to a diameter of 2 mm. The beam line was kept under high vacuum of about 10^{-5} mbar to prevent collision of protons with gas particles within the beam line.

The beam was allowed to travel the distance of about 7 m before reaching the chamber. This is normally done to allow enough space and time for tuning the beam into a required size which is 2 mm in this case. The chamber as shown in figure 3.6 was kept at vacuum pressure of about 10^{-5}mbar to prevent scattering of beam inside the chamber.

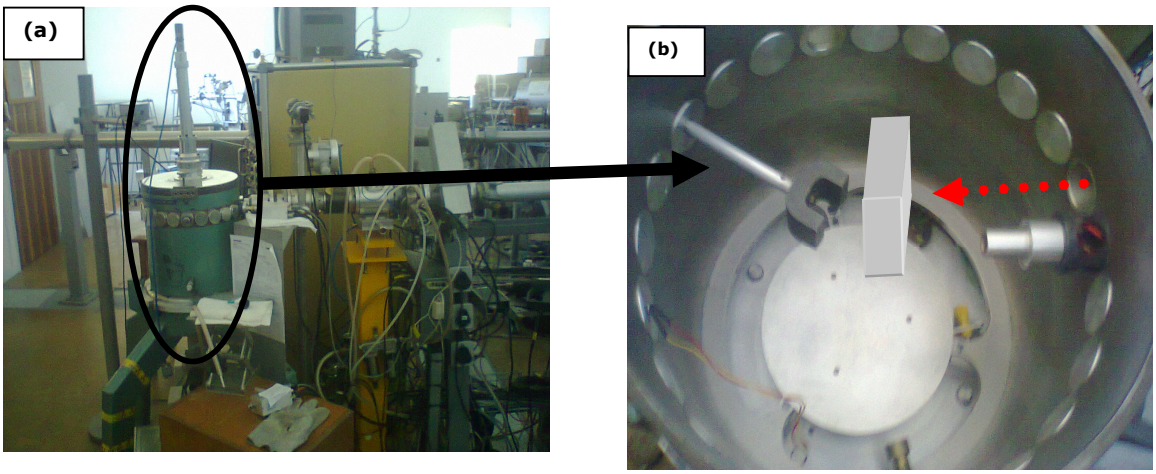

Figure 3.6: Irradiation chamber (a) outside the chamber and (b) inside part of the chamber with dotted line showing the direction of the beam.

No detectors were used in this experiment due to the fact that the aim of the project was to irradiate only. Five samples were mounted on the aluminium ladder shown in figure 3.7 which is used to hold samples.

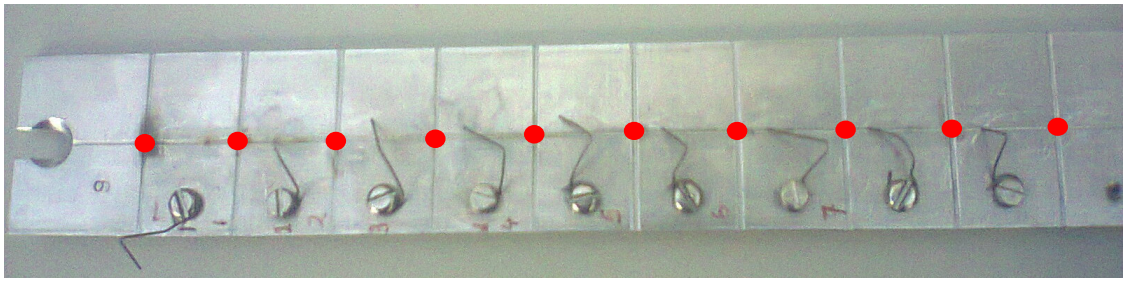

Figure 3.7: The ladder used to mount samples with dots showing the position of the beam in relation to the sample being irradiated.

The orientation of all samples were in such a way that the beam hits directly perpendicular to the sample as shown in figure 3.8.

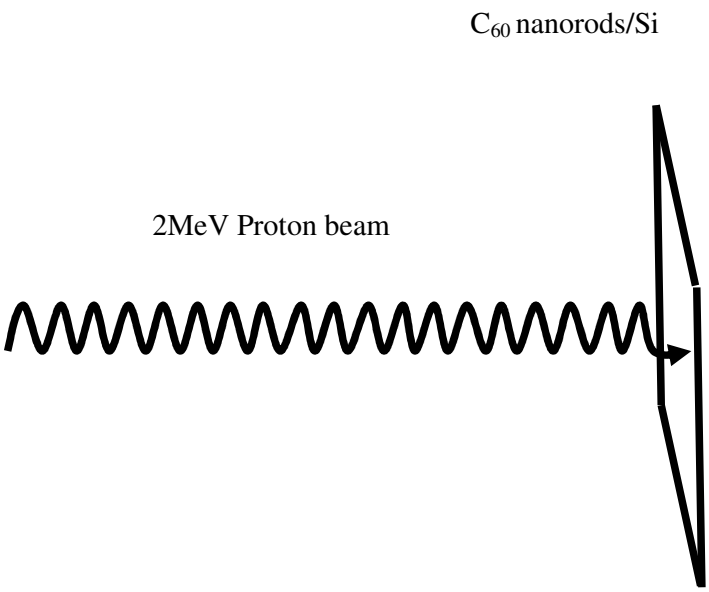

Figure 3.8: Schematic diagram of the sample with the beam hitting the it directly perpendicular.

The movement of the ladder to locate the sample to be irradiated was achieved by means of goniometry automatic system. This system allows the changing of samples without breaking the vacuum. For the whole duration of th experiment, the beam current was maintained at about ~50 nA and beam energy kept at 2 MeV. In order to induce as much damage as possible, the charge was varied in an increasing order by varying time as shown in table 3.1.

Table 3. 1: Various doses used for proton irradiation of individual samples

Sample no.	Fluence ($x10^{16}$ ions/cm^{-1})
1	1.79
2	3.58
3	5.37
4	7.16
5	8.96

3.1.2. Gamma irradiation

Gamma irradiation experiments were carried out at Centre de Recherche Nucléaire de Draria (CRND), BP.43 in Algeria. The source of gamma rays was synthetic radioactive isotope of cobalt (cobalt 60 ($^{60}_{27}Co$)). This source has half-life of 27 years. It is not found in nature due to its half-life. The only way to produce it is through neutron activation process of the isotope $^{59}_{27}Co$. $^{60}_{27}Co$ decays by beta decay to the stable isotope nickel-60 ($^{60}_{28}Ni$).

In order to produce gamma rays, nickel nucleus must be activated. The activated nickel nucleus emits two gamma rays with energies of 1.17 and 1.33 MeV, hence the overall nuclear equation of the reaction is shown in figure 3.9.

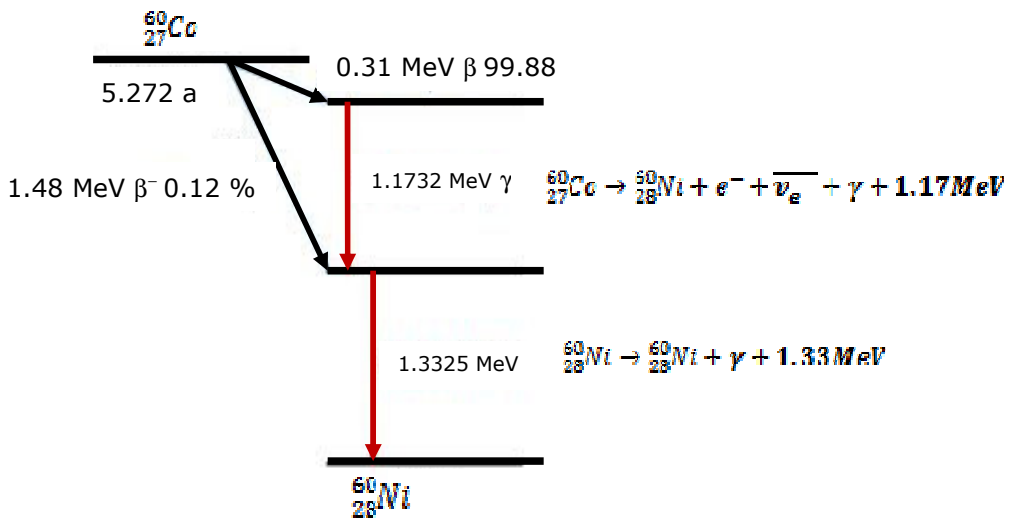

Figure 3.9: Schematic diagram showing the production of gamma rays from decay process of cobalt-60.

During gamma irradiation of C_{60} nanorods, seven samples were exposed to the cobalt 60 source during the activation process as shown in figure 3.10.

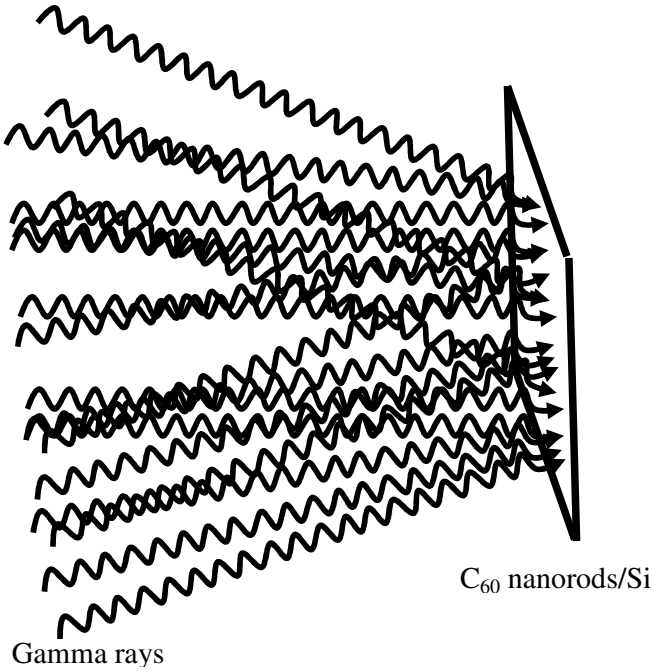

Figure 3. 10: Schematic diagram of gamma rays of energy 1.17 and 1.33 MeV interacting with the sample of C_{60} nanorods on Si substrate.

The sample was positioned in such a way that it received maximum exposure of gamma rays with 1.33 MeV and 1.77 MeV. The Source had an activity of 14 kCurie. In order to achieve maximum damage, the dose was increased by increasing time of exposure as shown in table 3.2. The dose rate was 48.13 Gy/mn or 2888 Gy/h. This dose rate was used to calculate dose (kGy).

Table 3. 2: Various doses used for gamma irradiation of individual samples

Sample no.	Dose (KGy)
1	50
2	100
3	200
4	400
5	600
6	800
7	1000

3.1.3. Fast neutron irradiation

Fast neutron irradiation experiment was carried out at Centre de Recherche Nucléaire de Draria (CRND), BP.43 in Algeria. It was carried out in a reactor with reactor source of 15 MW, IB of 0.01A as shown in Figure 3.11 and doses ranging from 3.2×10^{17} neutrons.cm^{-2} to 1.6×10^{18} neutrons.cm^{-2} as shown in Table 3.4.

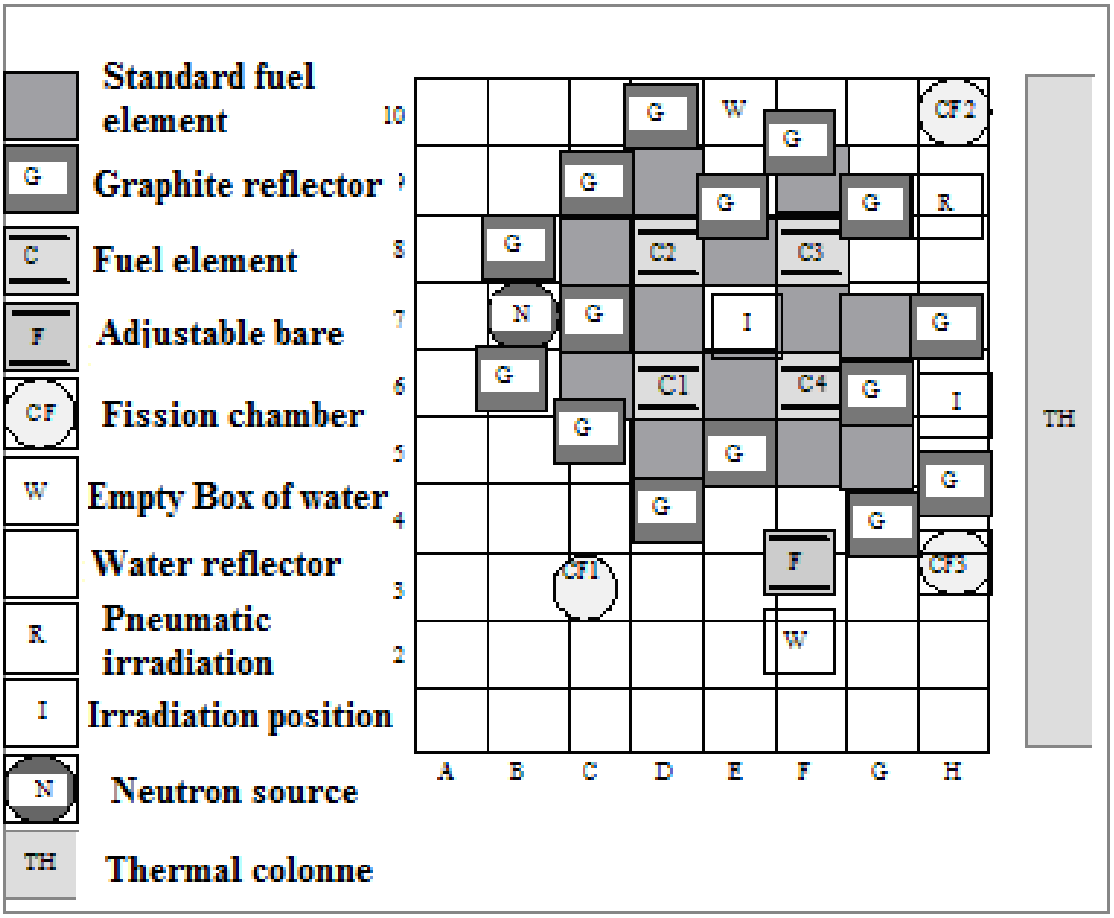

Figure 3. 11: Diagram showing the irradiation position and the source arrangement.

Table 3. 3: Various doses used for fast neutron irradiation of individual samples

Sample	Dose (n/cm^2)
1	3.2×10^{17}
2	6.4×10^{17}
3	9.6×10^{17}
4	1.6×10^{18}

3.3. Annealing effects experiment

Annealing of the fullerene C_{60} nanorods was carried out at University of Zululand physics department using AJA Orion 5 Sputtering System heating stage shown in figure 3.12. The samples were annealed at 400 ^{o}C, 600 ^{o}C, and 800 ^{o}C for two hours at 10^{-5} torr.

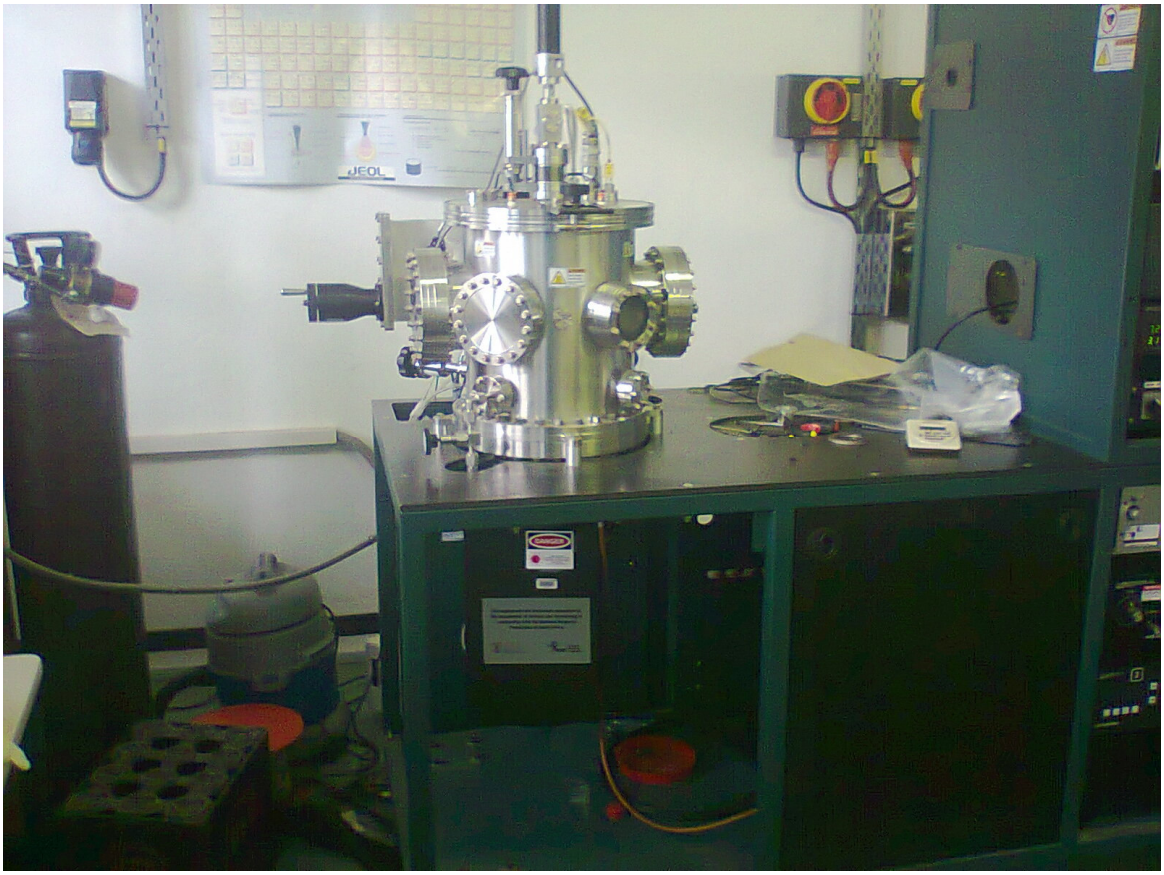

Figure 3. 12: AJA Orion 5 Sputtering System at University of Zululand.

3.4. Reference

[1] **Miyazawa, K., Minato, J., Yoshii, T., Suga, T.,** Characterization of fullerene nanotubes prepared by the liquid–liquid interfacial precipitation method, *Science and Technology of Advanced Materials* 6, 388–393, 2005.

[2] **Mtshali, C., Hamidi, D., Kerdja, T., Buah Bassuah P., Haneda, H., Maaza M. *,** Laser beam defractometry and C_{60} polymerized nanorods dynamics by surface interdiffusion, *optics Communications* (2012), doi:10.1016/j.optcom.2012.03.007.

CHAPTER 4

PROTON IRRADIATION

Abstract

This chapter focuses on the characterization of self-assembled fullerene (C_{60}) nanorods on hydrogen-passivated Si (111) substrates which were irradiated with 2 MeV protons at fluences ranging from 1.79×10^{16} to 8.96×10^{16} ions/cm^2. All the results from stereo microscope, scanning electron microscope (SEM), transmission electron microscope (TEM), and atomic force microscope (AFM), Raman spectroscopy and Fourier Transform Infra-Red (FTIR) spectroscopy, X-ray diffraction (XRD) are presented and discussed.

4.1. Introduction

In addition to the background discussed in chapter 1, the theoretical studies have been done with a purpose of understanding the mechanism of the ion irradiation damage on the C_{60} nanostructure. Furthermore, it was confirmed experimentally that beam irradiation affects both the spatial atomic arrangement as well as the electronic configuration in the bulk material [1-5]. Narayanan et al also proved experimentally that ion implantation affects the structure of C_{60} [6]. However not much work has been done on proton irradiation of C_{60} nanostructure with the aim of quantifying the damage of the structure due to the protons. The main focus of most research on proton irradiation has been only on proton induced magnetism.

The theoretical studies on C_{60} materials have predicted a ferromagnetic phase with a mixture of sp^2 and sp^3 pure carbon phase when bombarded with protons. In addition, Mathew et al [7] reported that polycrystalline fullerene thin films on Si (111) irradiated with 2 MeV protons displays a peculiar ferromagnetic-like behaviour at about 5 K. At 300 K both the pristine and the irradiated films show diamagnetic behaviour. Compared to the pristine films,

magnetization studies of irradiated C_{60} samples at temperature range of 2-300 K under 1T external magnetic field, exhibited stronger temperature dependence. Boukhvalov et al reported on ferromagnetism in fullerenes induced by defects [8]. Kumar et al [9] confirmed the ferromagnetism induced by heavy-ion irradiation in fullerene films while Esquinazi et al [10] reported on the induced magnetic ordering by proton irradiation in graphite.

In a pre-conclusion, one could assert that the bulk of the investigations on the irradiated C_{60} films have exhibited the irradiation induced magnetism. This irradiation induced magnetism has shown a net enhancement of the characteristic Ag and Hg vibrational modes, especially for fluences in the range of 6×10^{15} ions/cm^2 [11, 12].

In this section of the work we conduct a study of 2 MeV proton irradiation on C_{60} nanorods, with the aim of quantifying the damage induced due to irradiation. From literature it has been established that when C_{60} is irradiated with protons there is a magnetic phenomena that is observed due to the irradiation with protons.

4.2. Experiments methods

C_{60} nanorods were grown on Si (111) substrate as discussed in chapter 3. Following the growth phase, the samples were taken out of the solution and dried in air for preliminary characterization before the irradiation process. The proton irradiation was conducted using the conditions discussed in chapter 3.

The as deposited and irradiated samples were characterized using stereo scan optical microscope, scanning electron microscope (SEM) (FET, Quanta 200F), high resolution transmission electron microscope (HRTEM) (JEOLM 2010 with point to point resolution of 0.19 nm and lattice resolution of 0.14 nm, operated at 300 keV, at the University of the Western Cape).

Raman shift spectra were recorded using the laser fundamental NdYAG excitation wavelength of λ = 514 nm (LAB RAM spectrometer with a liquid nitrogen cooled Ge diode detector). Fourier transform infrared spectroscopy (FTIR) (Pekin Elmer spectrum one) was used to compliment the Raman data and x-ray diffraction (XRD) were recorded using a

Bruker D-8 Advanced X-ray diffractometer (at iThemba Laboratory of Accelerator Based Sciences, Cape Town) on the samples using CuK_{α} radiation. XRD data were collected in the 2θ range of 7° to 35° in step 0.010 with a dwell time 10 s at each step.

4.3. Results and discussion

4.3.1. Optical microscope

The optical microscope was used to confirm the deposition of the nanorods on the substrate. Figures 4.1 to 4.6 show optical images of the as-deposited C_{60} nanorods and those irradiated with a 2 MeV proton beam at various fluences.

Irradiated samples in figures 4.2 to 4.6 clearly show the irradiated spot demarcated by a circle and non-irradiated areas around it. The reddish area on the samples is proton irradiated spot while the yellowish is non-irradiated area. It is clear that 2 MeV protons induce electronic property modification, which is observed by the change in colour after irradiation. This colour change is due to loosely bound π-electrons when they are excited by the energies in the visible light [13].

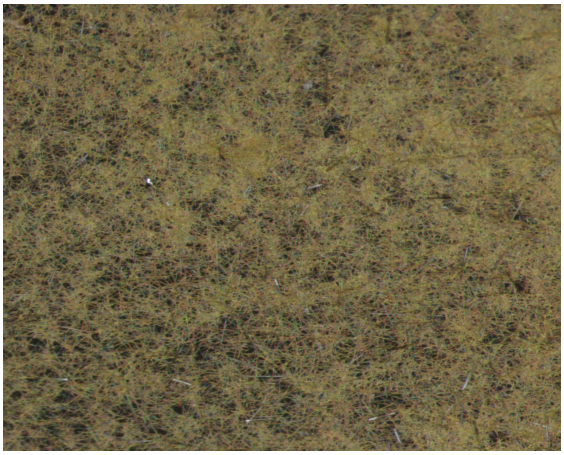

Figure 4. 1: Optical image of C_{60} nanorods on Si substrate before proton beam irradiation.

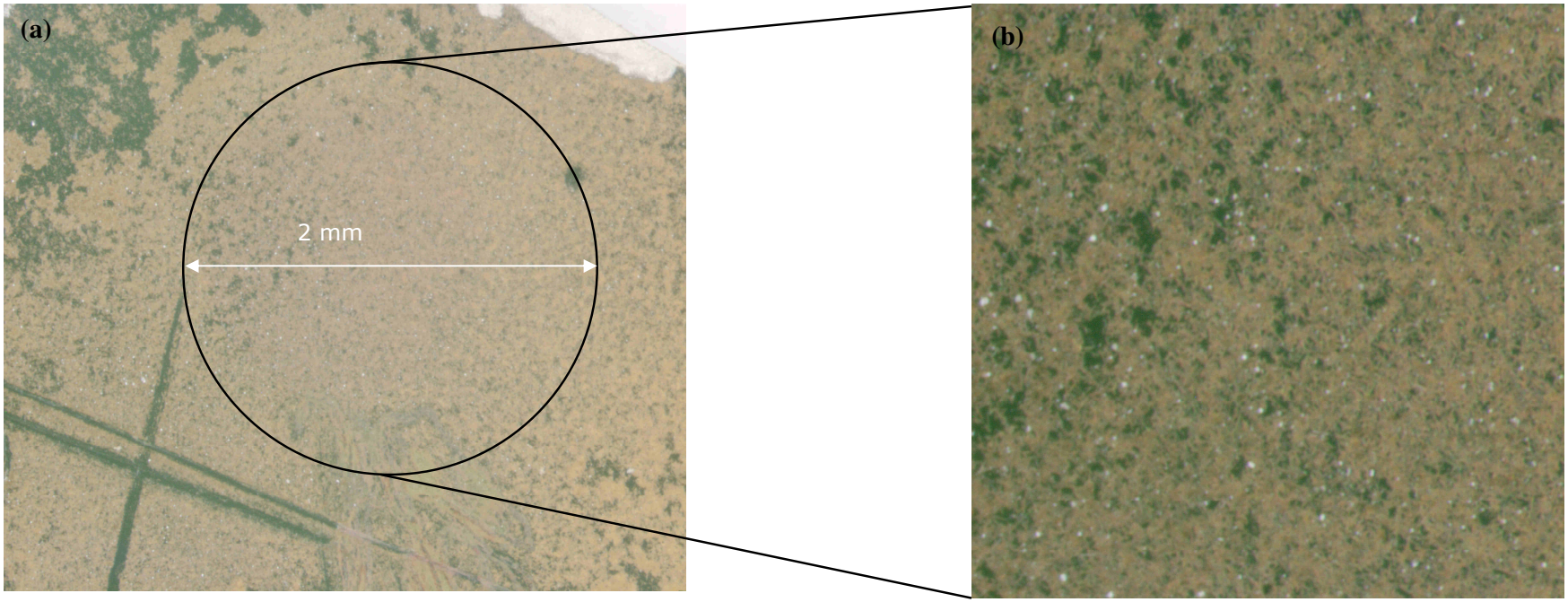

Figure 4.2: **(a)** Optical images of proton irradiated C_{60} nanorods on Si (111) substrate showing proton irradiated area by fluence of 1.79 10^{16} ions/cm^2 indicated by a circle and **(b)** zoomed in irradiated area.

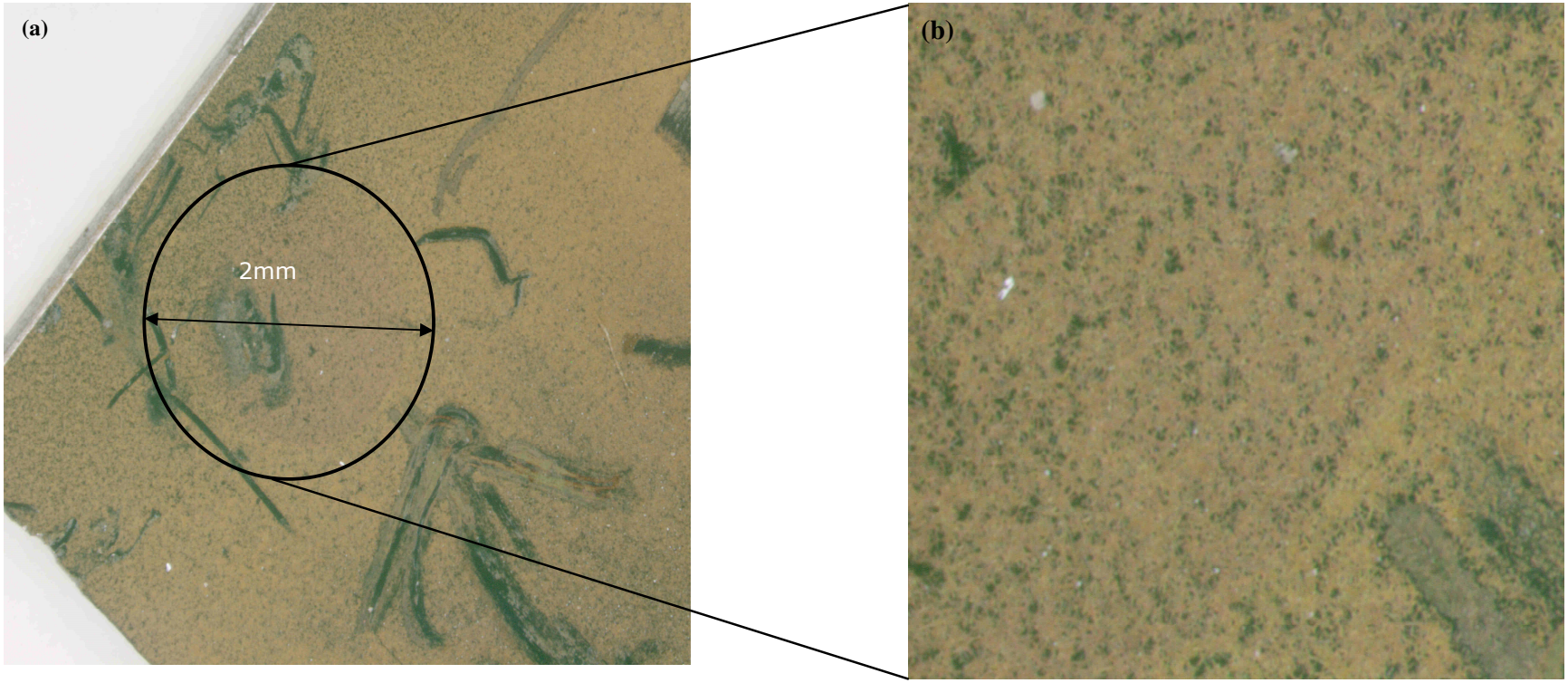

Figure 4.3: **(a)** Optical images of proton irradiated C_{60} nanorods on Si (111) substrate showing proton irradiated area by fluence of 3.58 10^{16} ions/cm^2 indicated by a circle and **(b)** zoomed in irradiated area.

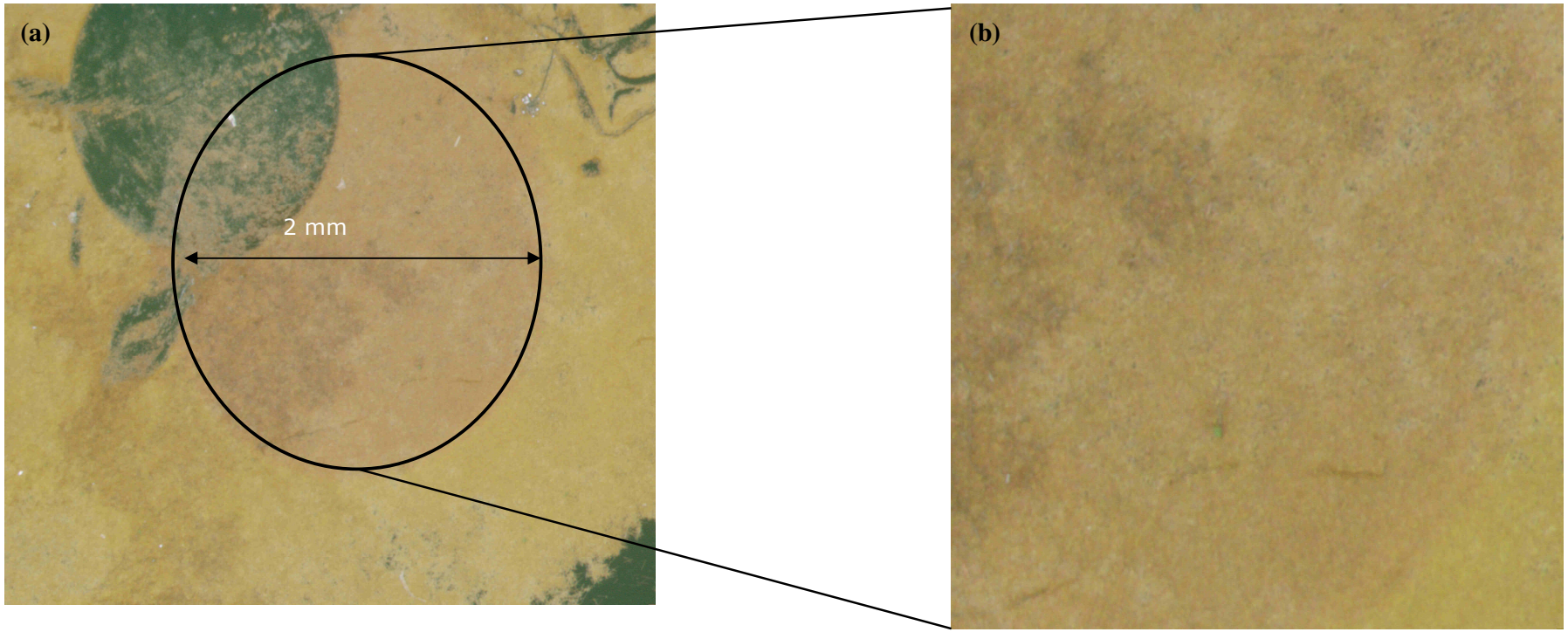

Figure 4.4: **(a)** Optical images of proton irradiated C_{60} nanorods on Si (111) substrate showing proton irradiated area by fluence of 5.37×10^{16} ions/cm^2 indicated by a circle and **(b)** zoomed in irradiated area.

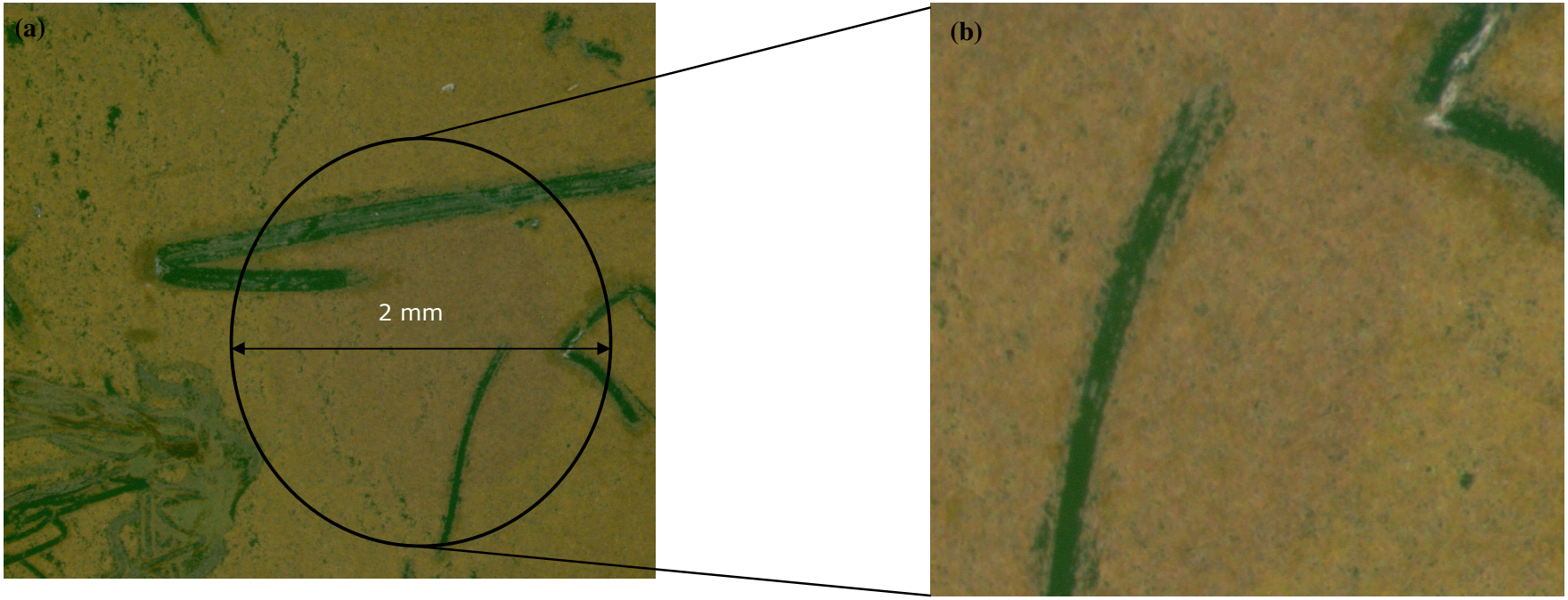

Figure 4.5: (a) Optical images of proton irradiated C_{60} nanorods on Si (111) substrate showing proton irradiated area by fluence of 7.16×10^{16} ions/cm^2 indicated by a circle and (b) zoomed in irradiated area**.**

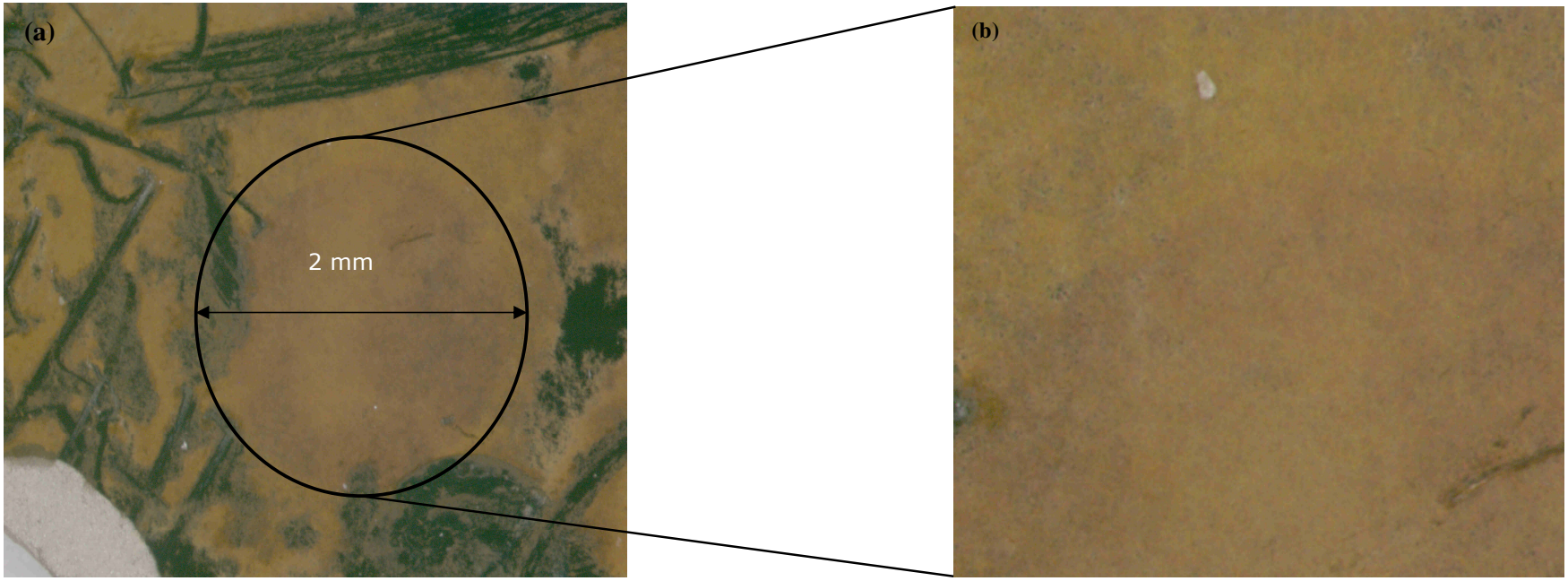

Figure 4.6: (a) Optical images of proton irradiated C_{60} nanorods on Si (111) substrate showing proton irradiated area by fluence of 8.96×10^{16} ions/cm^2 indicated by a circle and (b) zoomed in irradiated area.

4.3.2. Electron Microscope (EM)

After checking the samples in the optical microscope as described above for the confirmation of the presence of C_{60} nanorods, scanning electron microscope (SEM) and transmission electron microscope (TEM) measurements were performed.

The SEM was used to study morphology of the nanorods before irradiation and after 2 MeV irradiation at fluence ranging from 1.79×10^{16} ions/cm^2 to 8.96×10^{16} ions/cm^2. Figures 4.7 and 4.8 show SEM and TEM images of the C_{60} nanorods before irradiation respectively. The average diameter of most nanorods ranges from ~100 to ~900 nm, while the average length of most is several hundreds of micrometers. The majority of the C_{60} nanorods have a diameter below 400 nm, while the finer ones have a diameter of ≤ 200 nm.

Figure 4.9 shows AFM image of nanorods before irradiation. As seen from the figure, the nanorods are randomly oriented in a criss-crossing manner and show no alignment preference.

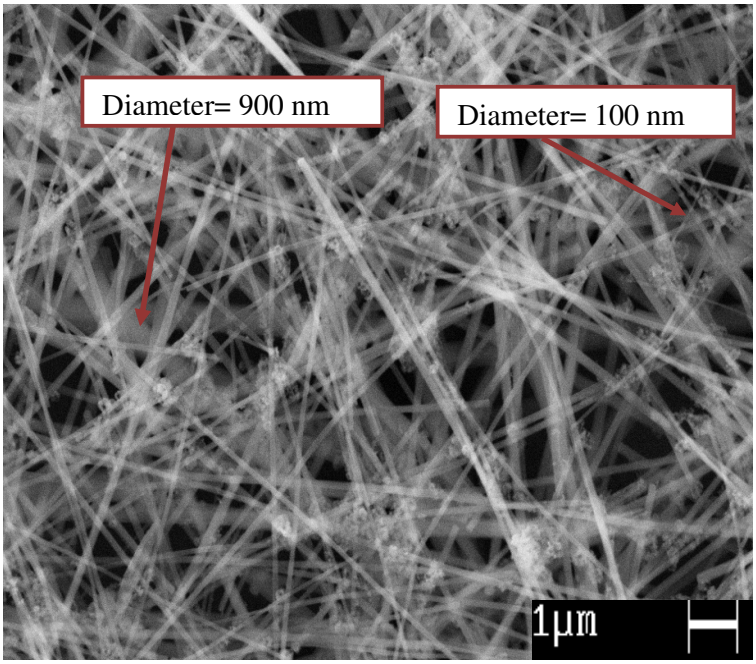

.

Figure 4.7: Scanning electron microscopy image of nanorods of fullerene C_{60} on a Si (111) substrate before proton irradiation.

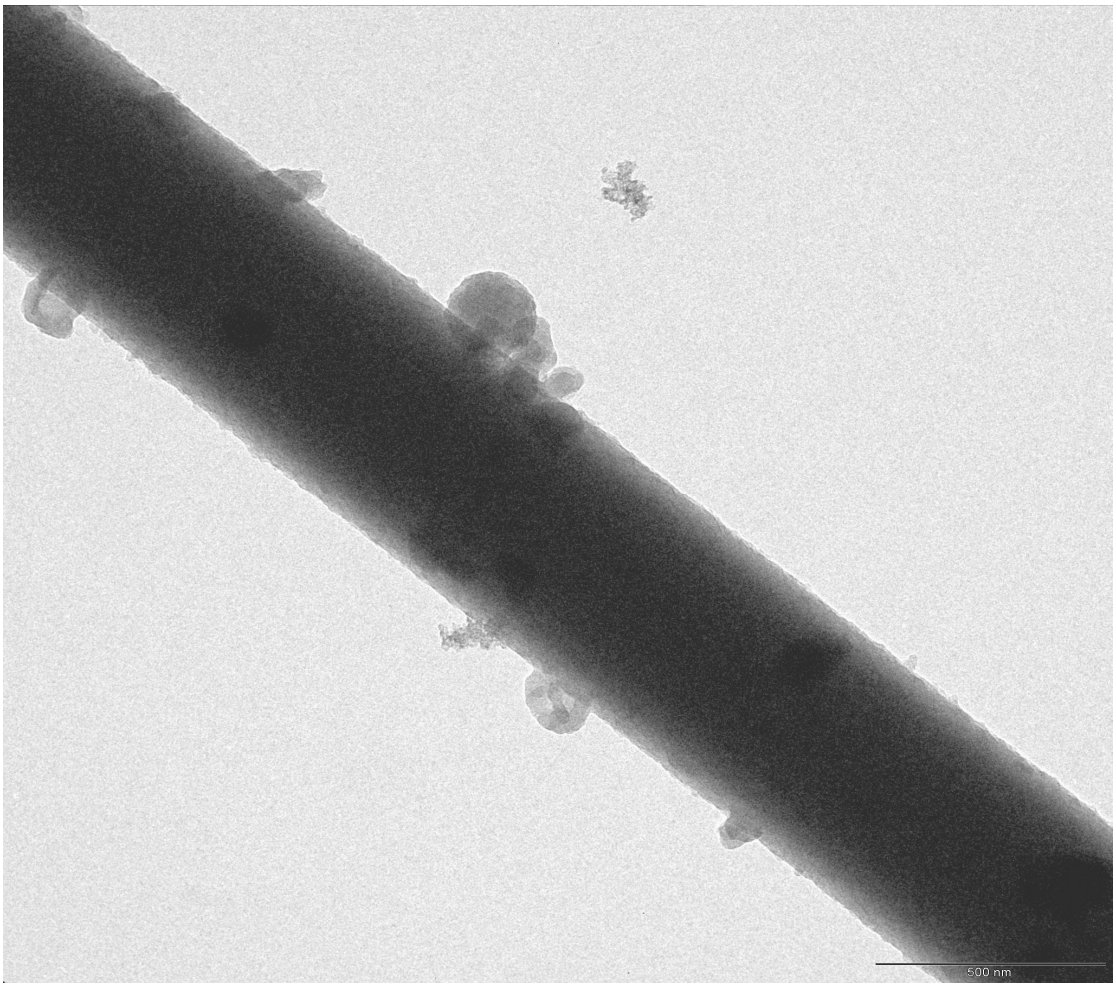

Figure 4.8: Transmission electron microscope (TEM) images of nanorod of fullerene C_{60} on a Si (111) substrate before irradiation.

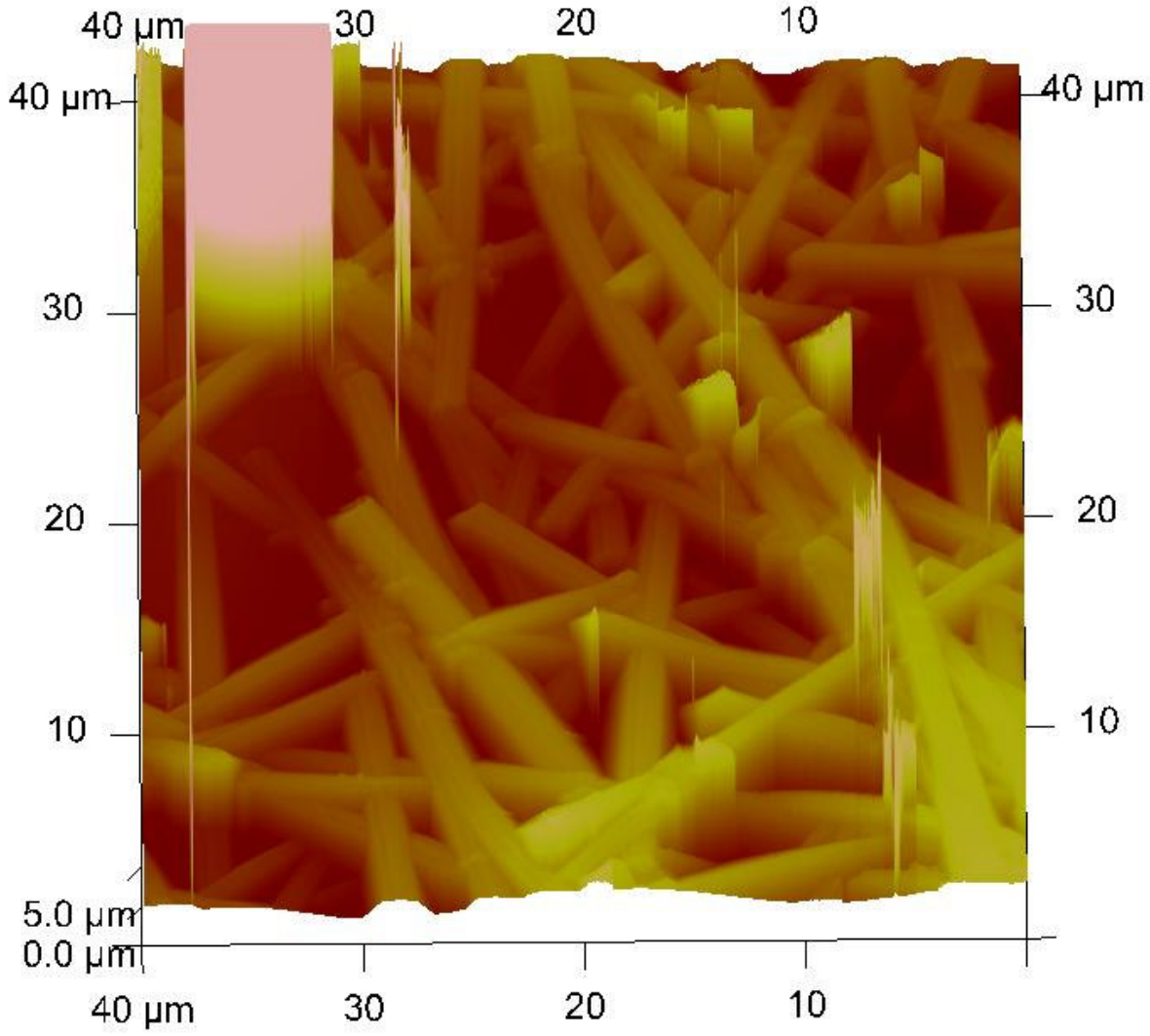

Figure 4. 9: AFM image of nanorods of fullerene C_{60} on a Si (111) substrate before irradiation.

4.3.3. Raman spectroscopy

In order to investigate structural changes of non-irradiated and irradiated C_{60} nanorods, Raman spectroscopy was used. The advantage of using this technique is that C_{60} has a well-known signature which has been confirmed in literature [14]. Also any changes in the C_{60} nanostructure are easily recognized without any ambiguity.

The Raman spectroscopy profiles on pristine C_{60} powder and non-irradiated samples are shown in figure 4.10. Fullerene C_{60} is highly symmetric molecule described by icosahedral point symmetry group (Ih) and has 120 symmetric operations. It also has 180 degree of freedom "3 per atom" (3 translational + 3 rotational + 174 vibrational = 180). Out of these, there are 10 Raman active even parity modes "2Ag +8Hg". In figure 4.9, all the characteristic vibrational modes in the spectral range of 400 - 4000 cm^{-1} are observed i.e. the 2 Ag and 8 Hg modes.

The difference in peaks' intensities observed in the non-irradiated C_{60} nanorods compared to the standard C_{60} powder suggests a minor suppression of the modes due to compact structure of nanorods which limits the breathing Ag(2) mode. This corroborates with the general growth process via molecular recognition/self-assembly.

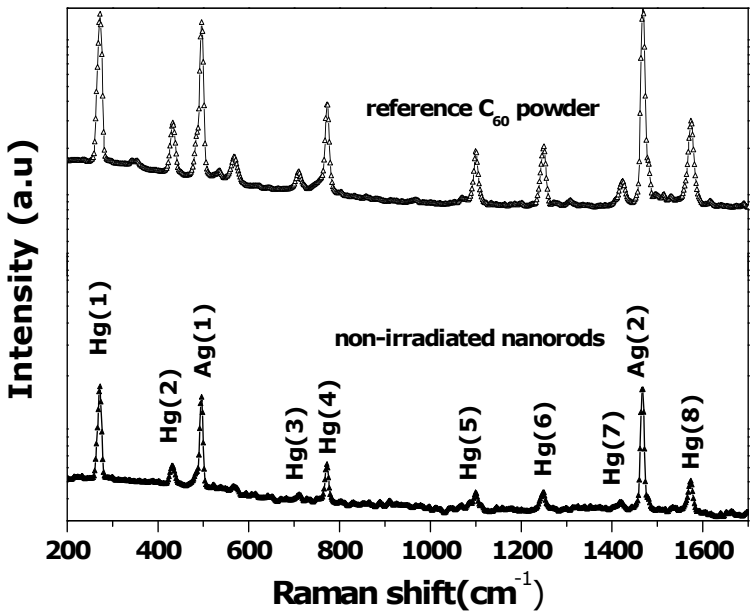

Figure 4.10: Raman spectra of as purchased fullerene C_{60} powder and non-irradiated C_{60} nanorods on Si (111) substrates.

Figure 4.11 reports on the fluence evolution of the Raman shift intensities in relation to the fluence of the 2 MeV beam. All the characteristic vibrational modes of the 2 Ag and 8 Hg in the spectral range of 400 - 4000 cm^{-1} are observed as shown in figure 4.10, but some modes tend to disappear after irradiation as observed in figure 4.11. Of all the Raman active modes, only Ag (2) mode is known to be non-degenerate, therefore can be used as sensor of mixed material phases. In addition, the background observed in the spectral range between 1000 to 1700 cm^{-1} is due to the Raman laser heating.

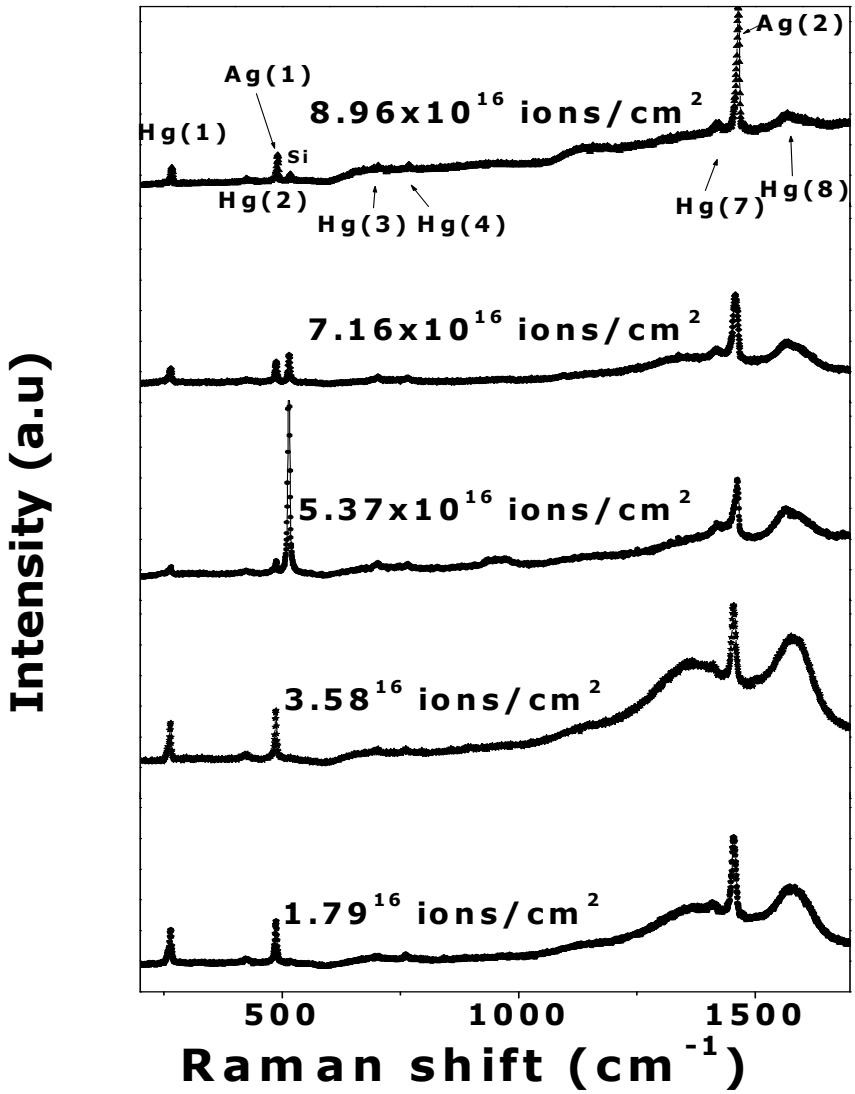

Figure 4.11: Raman spectra of C_{60} nanorods subjected to fluence ranging from $1.79x10^{16}$ to $8.96x10^{16}$ ions/cm^2 of 2 MeV protons.

Based on the fact that Ag (2) mode is regarded as a sensor, its fitted data is plotted in order to show a clear difference of the effect of various fluencies. It is noticeable that there is a variation in Raman shift and intensities due irradiation as shown in table 4.1. This was extracted from the data fitted using Lorenzian and plotted as shown in figures 4.12 (a-c).

Table 4. 1: Position, FWHM and relative intensity of Ag (1) and Ag (2) modes.

	Ag(1)			Ag(2)		
Irradiation fluence (10^{16} ions/cm^2)	ω(cm^{-1})	FWHM (cm^{-1})	Relative intensity	ω(cm^{-1})	FWHM (cm^{-1})	Relative intensity
1.79	487.22	5.1471	74.114	1454.8	11.149	148.66
3.58	486.78	4.6242	85.132	1454.4	11.339	145.1
5.37	487.84	4.5385	18.831	1454.4	23.121	64.856
7.16	487.22	5.346	37.702	1456.5	8.9124	93.904
8.96	490.72	4.0921	47.097	1463.7	7.1997	210.71

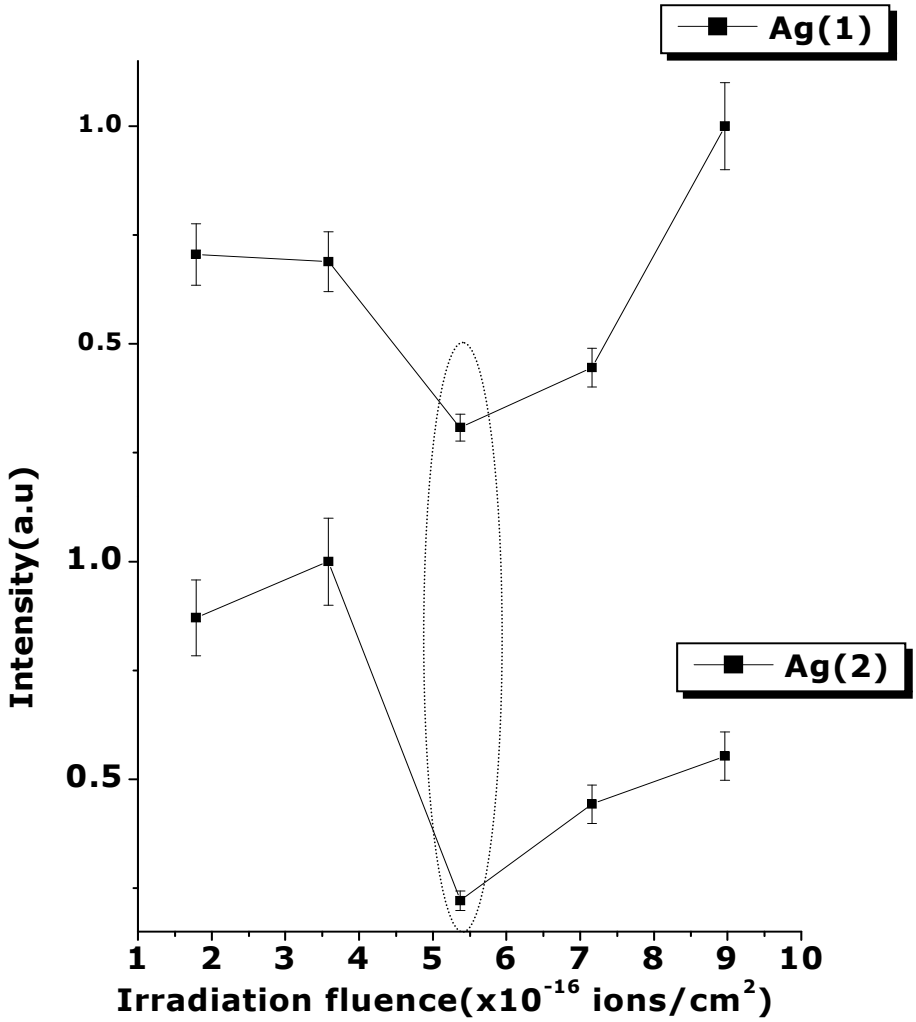

Figure 4.12: (a) Variation of the Raman intensities vs. irradiation fluences for Ag(1) and Ag(2) modes of irradiated C_{60} nanorods on Si (111).

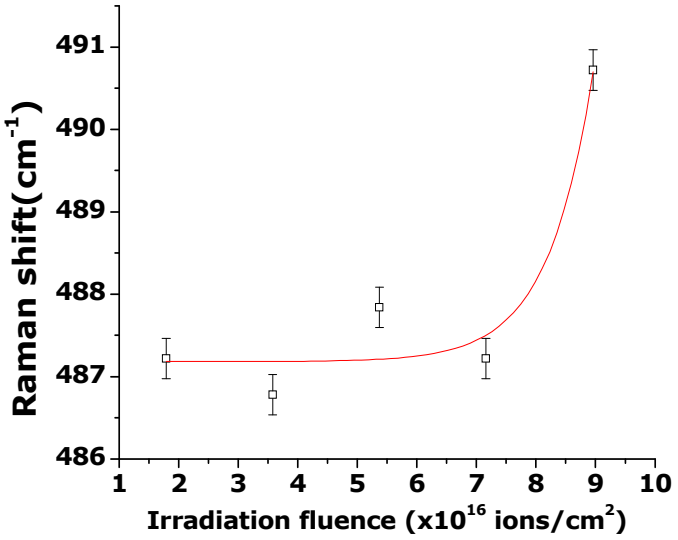

Figure 4.12(b): Variation of the Raman shift vs irradiation fluence for Ag (1) mode of irradiated C_{60} nanorods on Si (111).

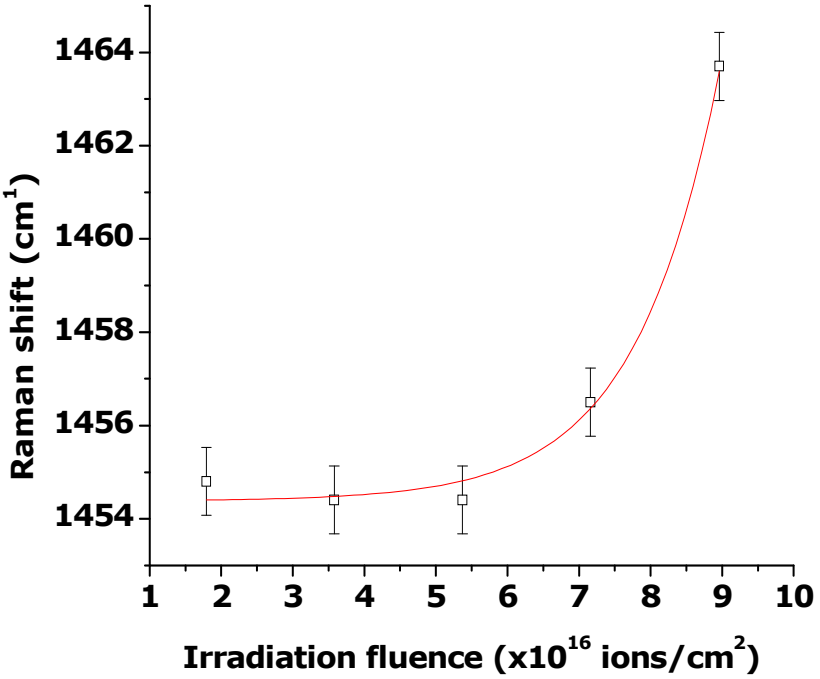

Figure 4.12 (c): Variation of the Raman shift vs irradiation fluence for Ag (2) modes of irradiated C_{60} nanorods on Si (111).

The minimum change in intensity as a function of fluence is only observed at 5.37 x 10^{16} ions/cm^2 for both Ag (1) and Ag (2) modes (figure 4.12(a)) which is then followed by recovery of the structure as observed. An exponential growth of Raman shift as a function of fluence for both Ag (1) and Ag (2) modes is noticed in figure 4.12(b) and (c). These changes indicate the rearrangement of the bonds between individual adjacent C_{60} molecules.

Furthermore it is not possible to split an Ag (2) mode, so whenever there is an additional peak or a shoulder in the Ag (2) mode it means that multiple phases are present due the number of the intermolecular bonds, each resulting in a slightly different Ag (2) mode frequency. The creation of intermolecular bonds stops the molecular rotation and lowers the overall symmetry of the solid. This reorganization affects the frequency of the Ag (2) pentagonal pinch mode which is visible as a downshift of the Ag (2) peak position in the Raman spectrum [15].

Moreover, the magnitude of this shift is roughly proportional to the number of broken double bonds that have re-attached themselves to satisfy the stable closed shell configuration of carbon within C_{60}. The population of broken and re-attached bonds is noticeable above the threshold value of 5.4 10^{16} ions/cm^2.

It is worthwhile to mention that the range of the 2 MeV protons calculated using SRIM programme for amorphous carbon with the density of C_{60} is ~50 μm [16]. Since the diameter of the nanorods ranges from 100 – 900 nm, the protons that were used to irradiate the nanorods passed through the nanorods and got embedded in Si substrate

Although we observed a change in Ag (2) mode (which is due to the structural change), the structure is regained as the fluence is increased further as shown from figure 4.12(a). This suggests that as the proton beam interacts with the nanorods, there is reorganization of bonds between individual C_{60} molecules. This reorganization could results to the formation of C_{60} nanotubes with the same outside appearance but hollow inside.

4.3.4. FTIR spectroscopy

To support the results discussed in the Raman spectroscopy, Fourier transform infrared (FTIR) spectroscopy was used as a complementary technique. The results of FTIR spectroscopy measurements on non-irradiated and irradiated samples are shown in figure 4.13. Characteristic IR active modes at 1428 cm^{-1} (t1u (4)) and 1182cm^{-1} (t1u (3)), 573 cm^{-1} (t1u (2)) and 524 cm^{-1} (t1u (1)) [17] are labelled in figure 4.13.

The first two peaks at 573 cm^{-1} (t1u (2)) and 524 cm^{-1} (t1u (1)) arise mainly from the radial motion of C_{60} molecules, whereas the latter two peaks arise mainly from their tangential motion in cage motion. The peaks at 573 cm^{-1} (t1u (2)) and 1182cm^{-1} (t1u (3)) respectively, include both tangential and radial motions. It can be easily seen that C_{60} nanorods show all FTIR bands similar to the non-irradiated C_{60} nanorods.

The dose dependence FTIR spectra of C_{60} nanorods on Si (111) irradiated with protons is clearly observed figure 4.13. The pentagonal pinch mode appearing at 1428 cm^{-1} is the most sensitive band for the orientation ordering transition. We can see that all IR peaks tend to disappear after irradiation. This means that proton irradiation induces chemical modification with the nanorods which then results in a change in the optical properties connected with structural changes. The band at 524 cm^{-1} (t1u (1)) decreases with radiation due to the fact that the radial motion changes gradually as compared to the non-irradiated nanorods. This change in this band indicates and confirms the reorganization of C_{60} nanorods structure which suppresses this band after proton irradiation.

The band also at 573 cm^{-1} (t1u (2)) decreases until it disappears with increasing dose. This mean that the bond population between neighbouring C_{60} molecules within a nanorods increases due to reorganization or cross linking process, which then suppress the vibration as the dose is increased.

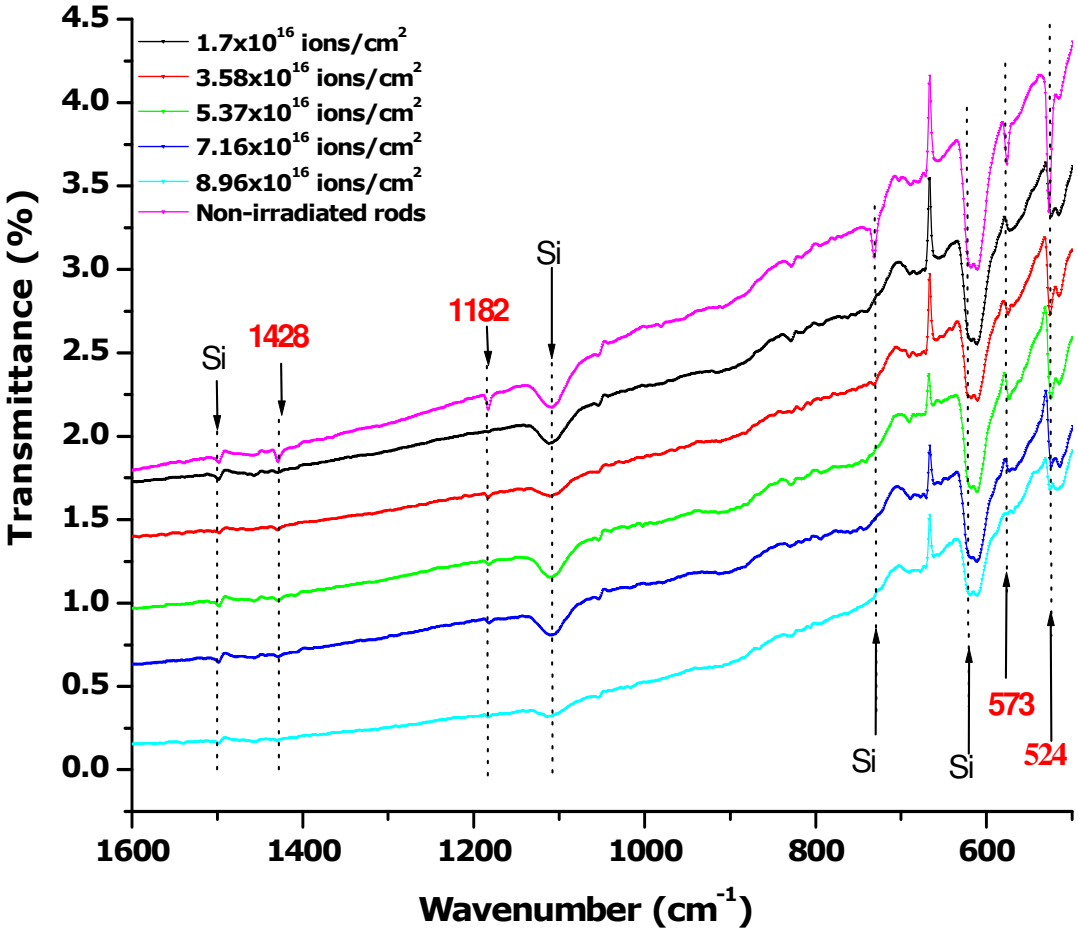

Figure 4.13: FTIR spectra of pristine C_{60}, non-irradiated and irradiated fullerene C_{60} nanorods.

On the other hand, the peak at 1182 cm^{-1} (t1u (3)) disappears after proton irradiation, this may be due to the fact that this mode arises from the C_{60} positive Gaussian-curved structure and tangential motion that disappears after proton irradiation, indicating an increase in the bond population between individual C_{60} molecules in the nanorods. The peak at 1428 cm^{-1} (t1u (4)) for the non-irradiated disappear after proton irradiation, which indicates additional polymerization that could attribute to the formation of various structures as shown in figure 4.14 [18].

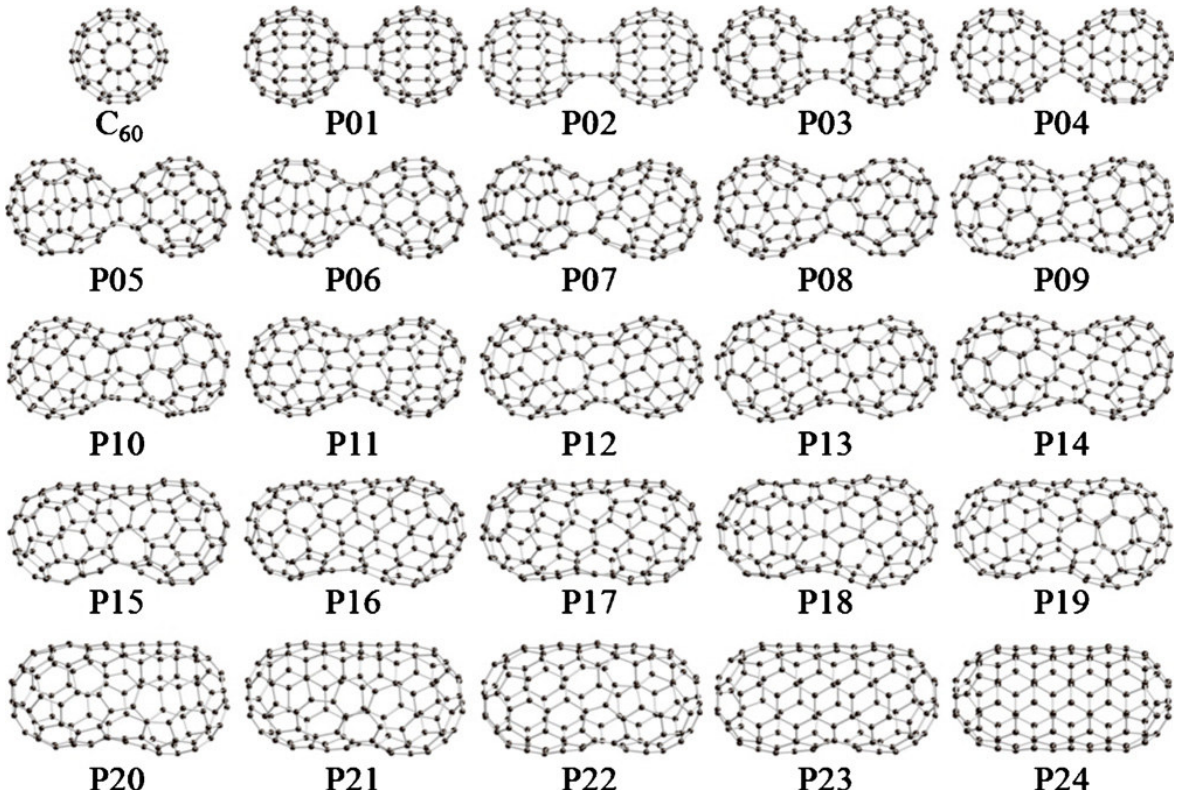

Figure 4.14: Possible various structures formed after irradiation of C_{60} + C_{60} nanostructure [18].

4.3.5. X-ray diffraction (XRD)

Raman spectroscopy and Fourier transform infrared (FTIR) spectroscopy showed minimal changes in the structure of C_{60} nanorods. To further investigate the structure of the nanorods after irradiation XRD patterns of the samples were collected at room temperature for five different samples under the same operational conditions. The advantage of using this technique in studying nanostructures of C_{60} is that C_{60} has a well-known signature which is available in the literature and a model of the crystallographic planes is shown in figure 4.15 [19]. Also any changes in the C_{60} nanostructure are easily recognizable without any ambiguity.

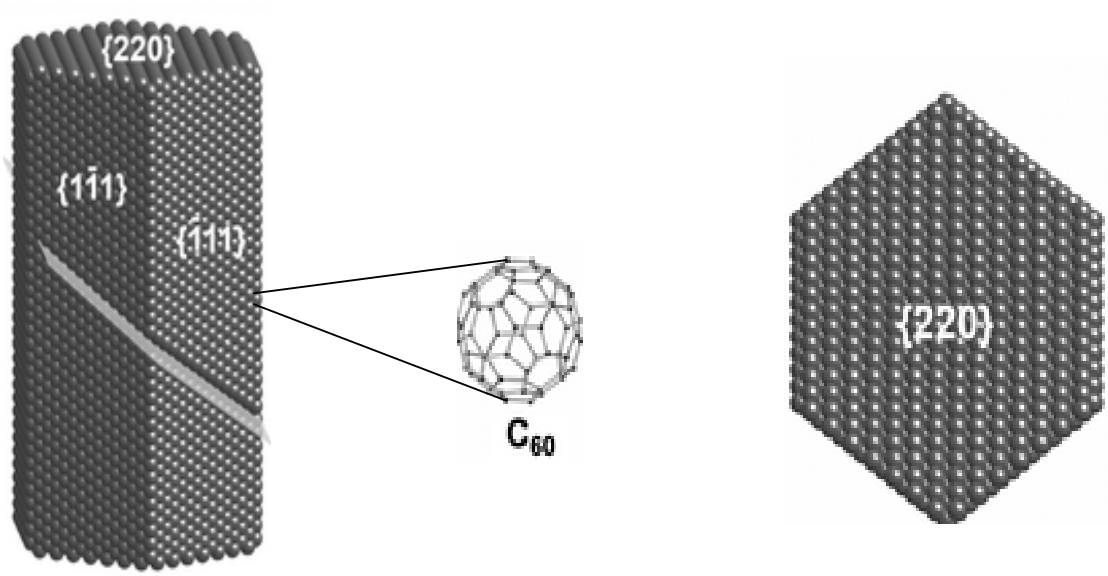

Figure 4.15: Model of the C_{60} molecules in a nanorod with the diffraction plane highlighted [19].

Spectra of pristine C_{60} powder and non-irradiated C_{60} nanorods samples are shown in figure 4.16 while that of irradiated C_{60} nanorods are shown in figure 4.16. Figure 4.16 confirms the fcc crystalline structure of the non-irradiated C_{60} nanorods with the (111), (220), (311) and (222) Bragg peaks as shown in figure 4.15 [19].

The Rietveld treatment showed the C_{60} nanorods to have a lattice parameter of ~1.415 Å, this is very close to the bulk value of 1.417 Å, indicating that the non-irradiated nanorods C_{60} are minimal stress. The most intense characteristic Bragg peak of the pristine C_{60} is observed with a preferential growth orientation along (111), this direction this is in line with what has been reported in literature [19, 20, 21]. Figure 4.16 clearly show a shift in a prominent (111) Bragg peak as shown in figure 4.18.

While there is a significant shift of the Bragg peaks with the increase of the fluence as shown in figure 4.18, figure 4.19 also display a variation of peak position as function fluence.

Hence, one can conclude that protons irradiation induces stress which results in the shifting of the Bragg peaks indicating change in d-spacing.

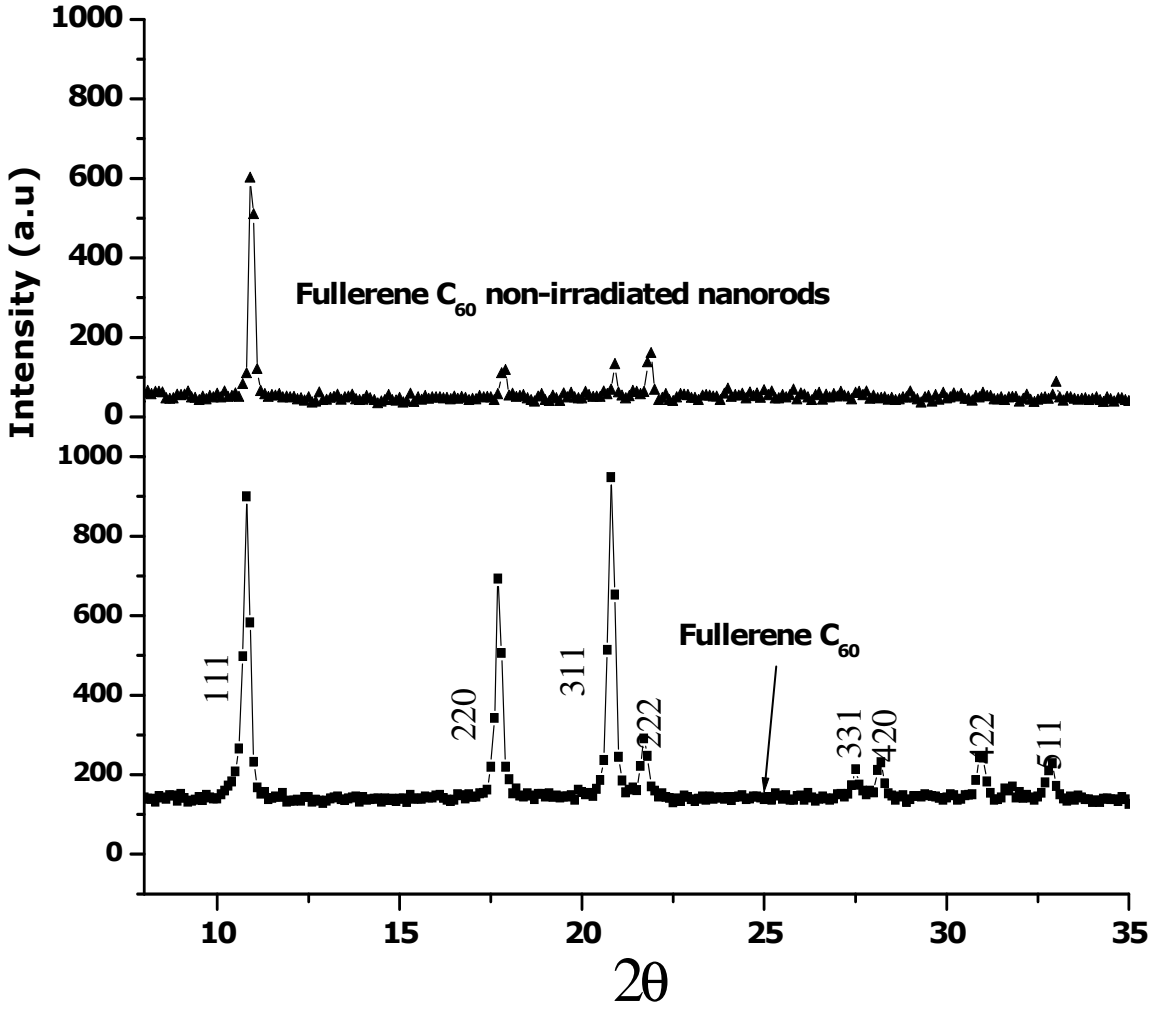

Figure 4.16: X-ray diffraction patterns of as purchased fullerene C_{60} powder and non-irradiated C_{60} nanorods on Si (111) wafer.

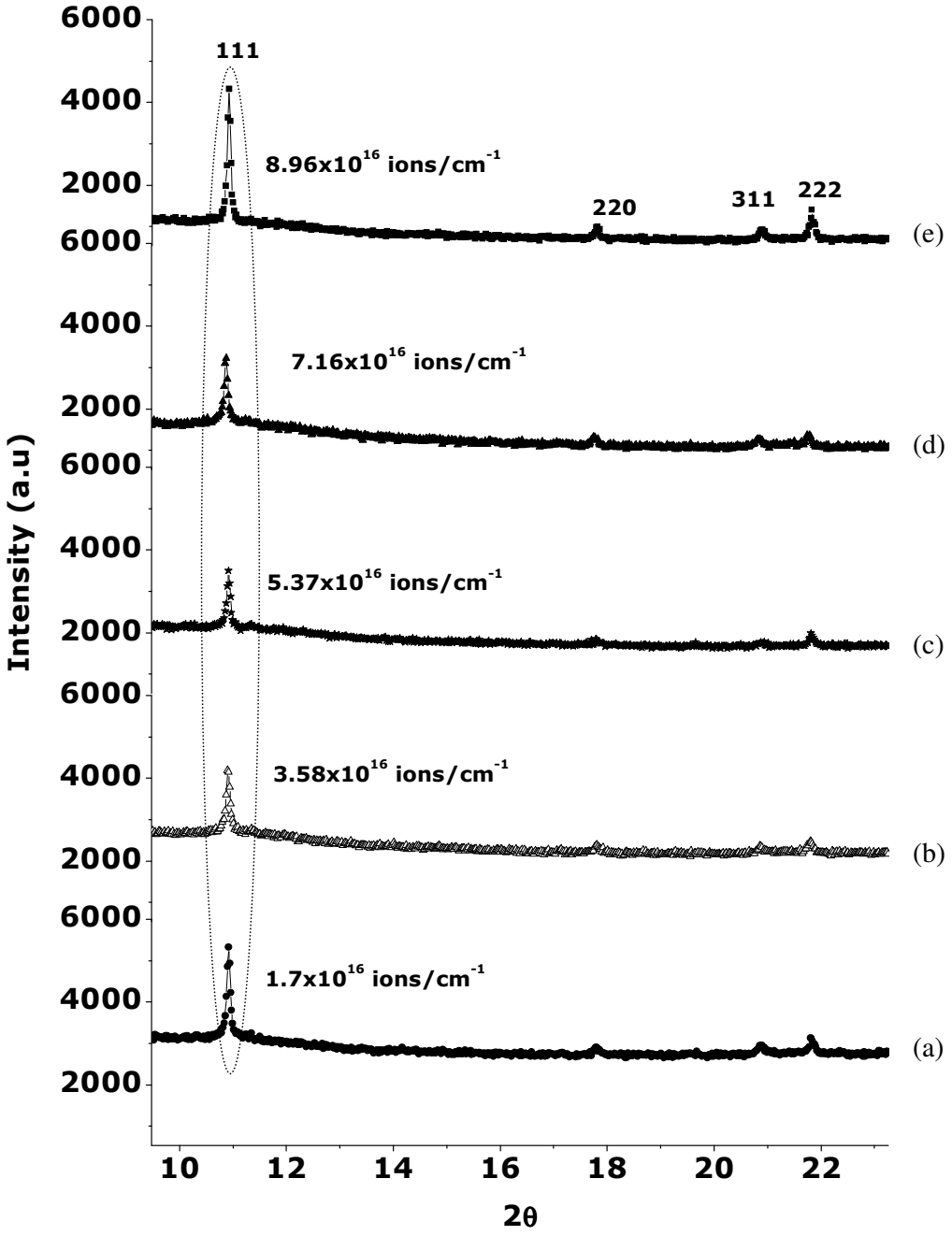

Figure 4.17: X-ray diffraction patterns of the 2 MeV protons irradiated C_{60} nanorods subjected to the following doses: (a) 1.79×10^{16}, (b) 3.58×10^{16}, (c) 5.37×10^{16}, (d) $7.16 \times 10^{16}$and (e) 8.96×10^{16} ions/cm^2.

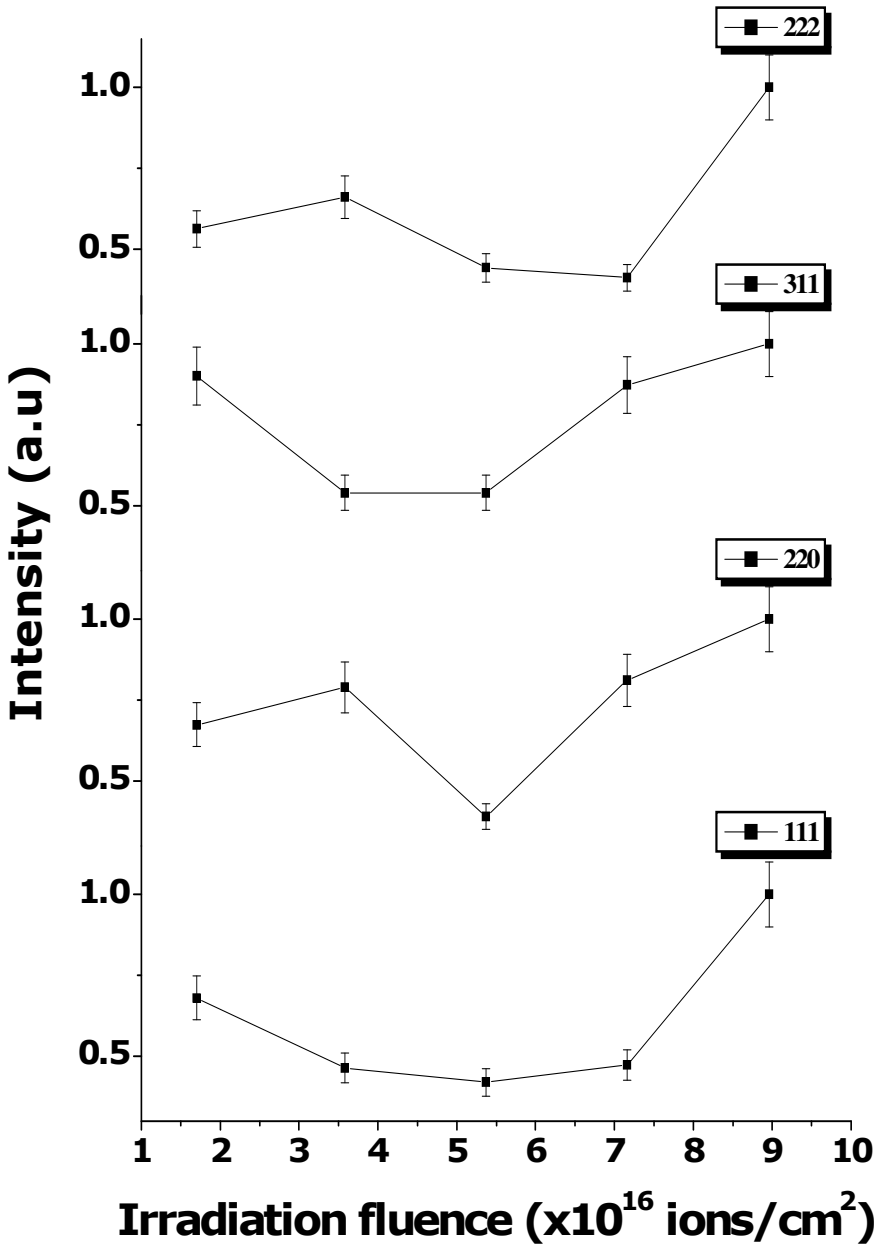

Figure 4.18: Normalised intensity versus fluence of X-ray diffraction peaks fitted with Lorentz fitting for the irradiated nanorods.

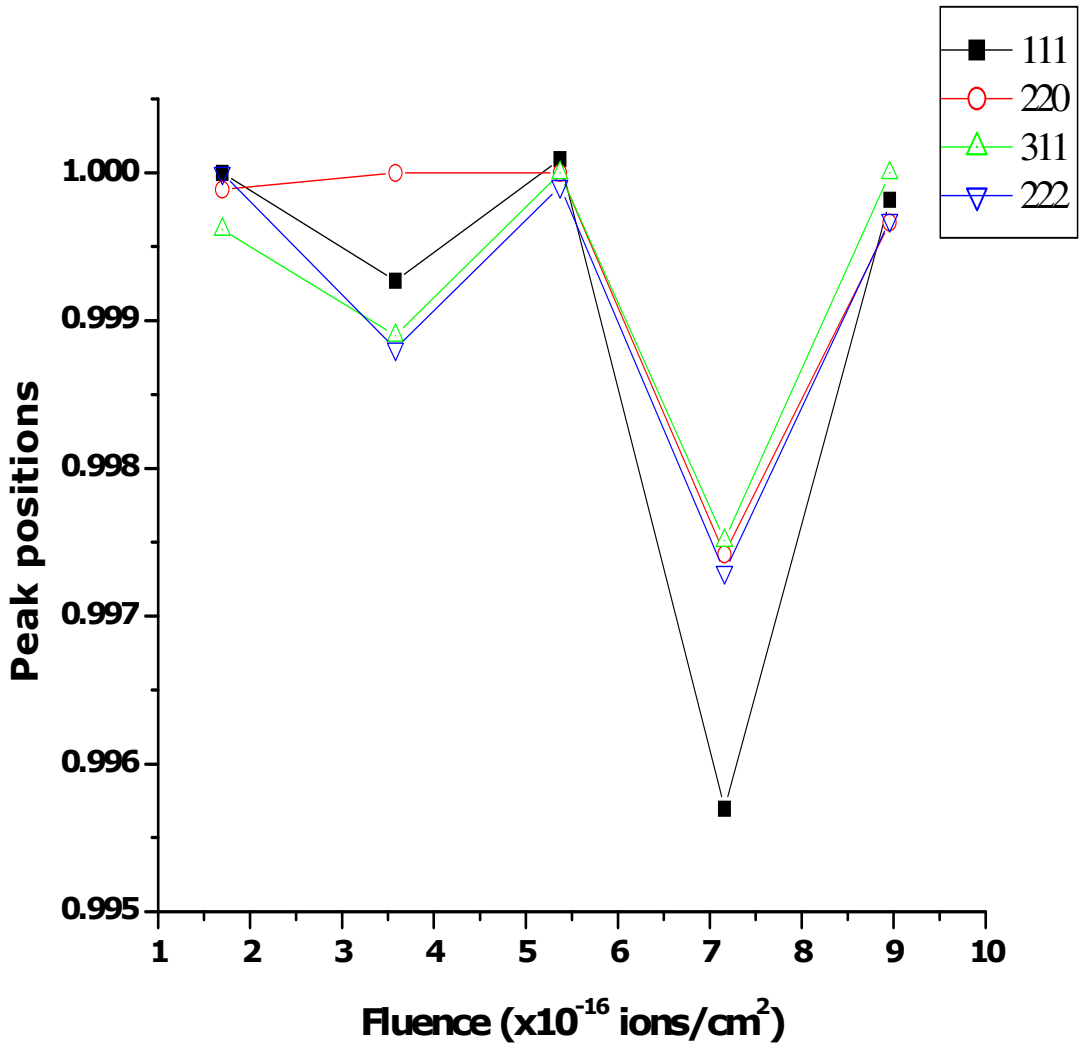

Figure 4.19: Normalised peak position versus fluence of X-ray diffraction peaks fitted with Lorentz fitting for the irradiated nanorods.

4.3.6. Optical images after soaking in toluene

After characterizing proton irradiated samples, the same samples were soaked in toluene solvent for the period of twelve hours, with the aim of investigating the effect of proton irradiation on the solubility of these C_{60} nanorods in toluene. Toluene solvent was chosen simply because it is the same solvent used to dissolve C_{60} powder which was then used to synthesize C_{60} nanorods.

The reason behind this investigation is the fact that it is not very clear as to what extent do proton irradiation alter the structure of C_{60} nanorods. Techniques used to characterize proton irradiated C_{60} nanorods before soaking in toluene showed the difference between irradiated nanorods and non-irradiated nanorods. This section investigates the solubility of C_{60} nanorods before irradiation and after irradiation.

Figures 4.20 to 4.24 shows optical images taken after the samples were soaked in toluene and taken out to be dried in air. It is clear in all images that proton irradiated nanorods do not dissolve in toluene any more, while non-irradiated nanorods dissolved to a certain extend. The dissolution resulted in a change of colour of non-irradiated nanorods as compared to irradiated nanorods with no colour change.

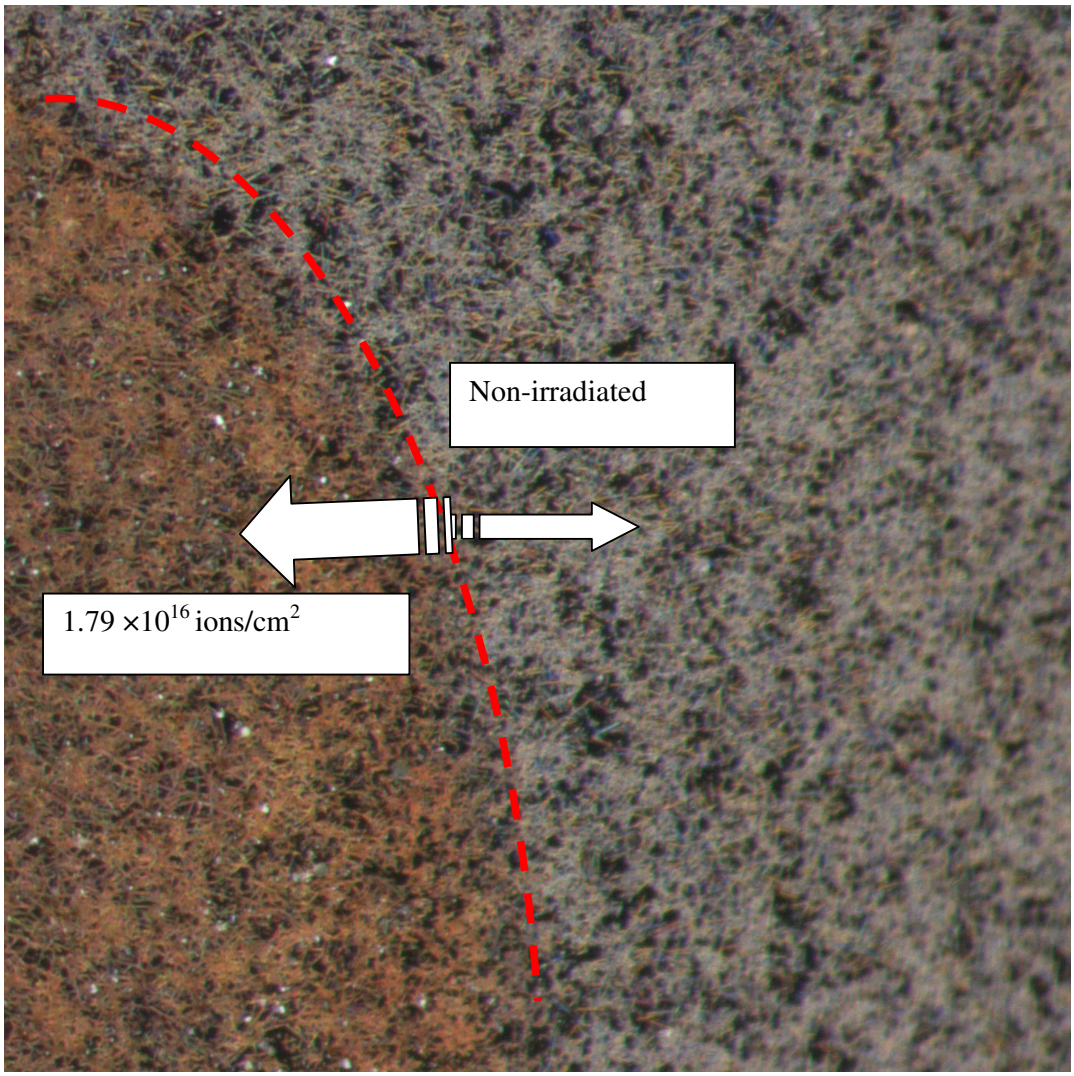

Figure 4.20: Optical image of C_{60} nanorods on Si (111) substrate showing proton irradiated area (big arrow) with fluence of 1.79×10^{16} ions/cm^2 and non-irradiated area (small arrow).

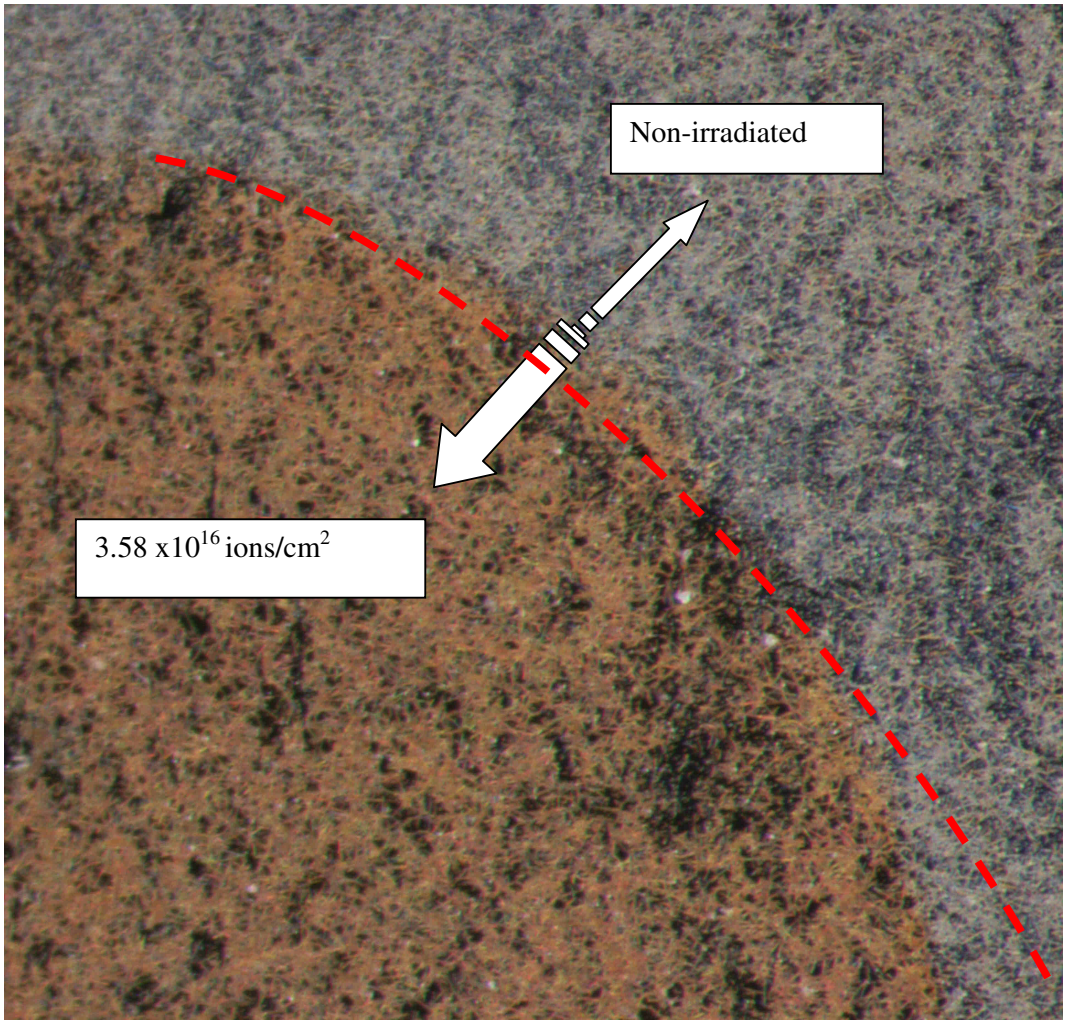

Figure 4.21: Optical image of C_{60} nanorods on Si (111) substrate showing proton irradiated area (big arrow) with fluence of 3.58×10^{16} ions/cm^2 and non-irradiated area (small arrow).

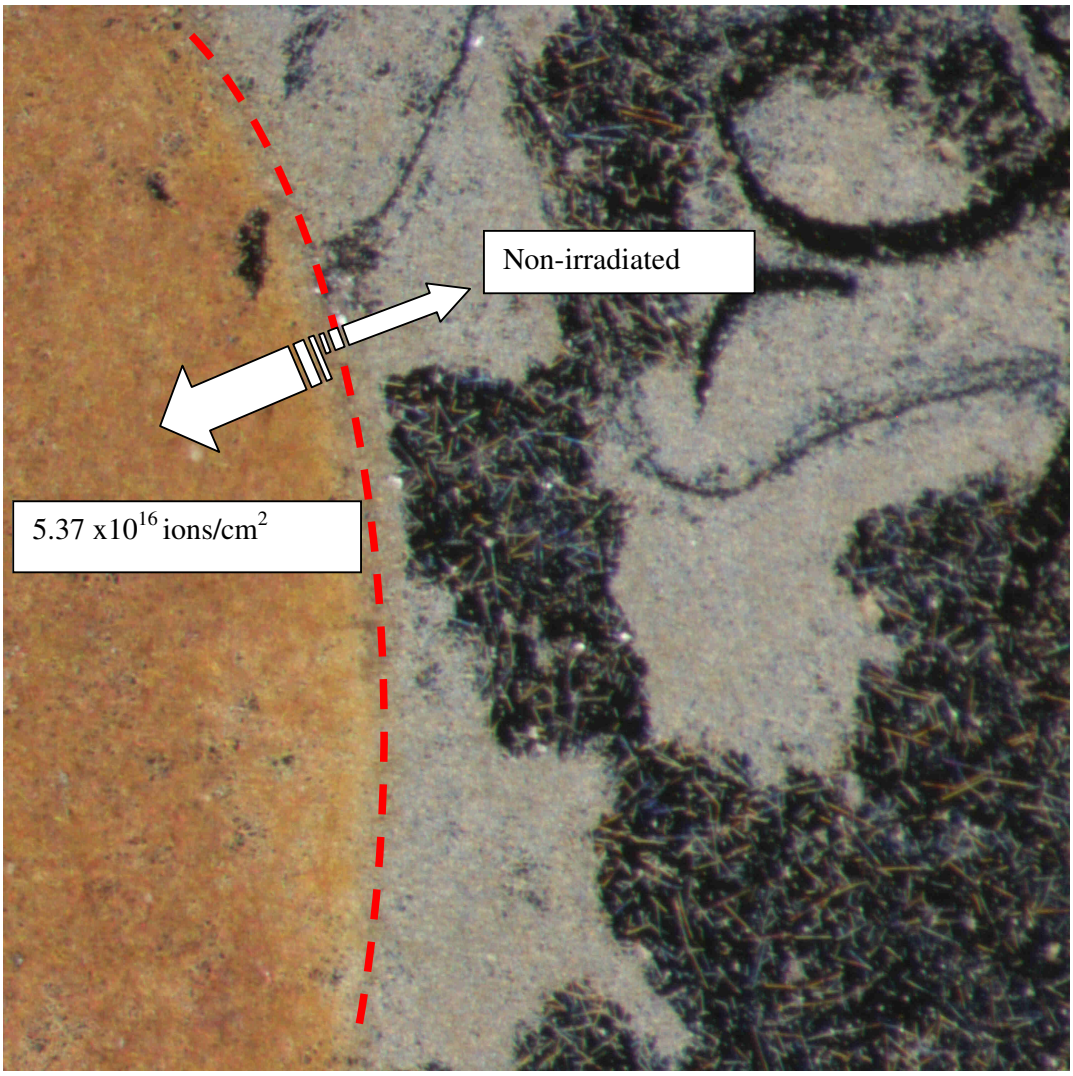

Figure 4.22: Optical image of C_{60} nanorods on Si (111) substrate showing proton irradiated area (big arrow) with fluence of 5.37×10^{16} ions/cm^2 and non-irradiated area (small arrow).

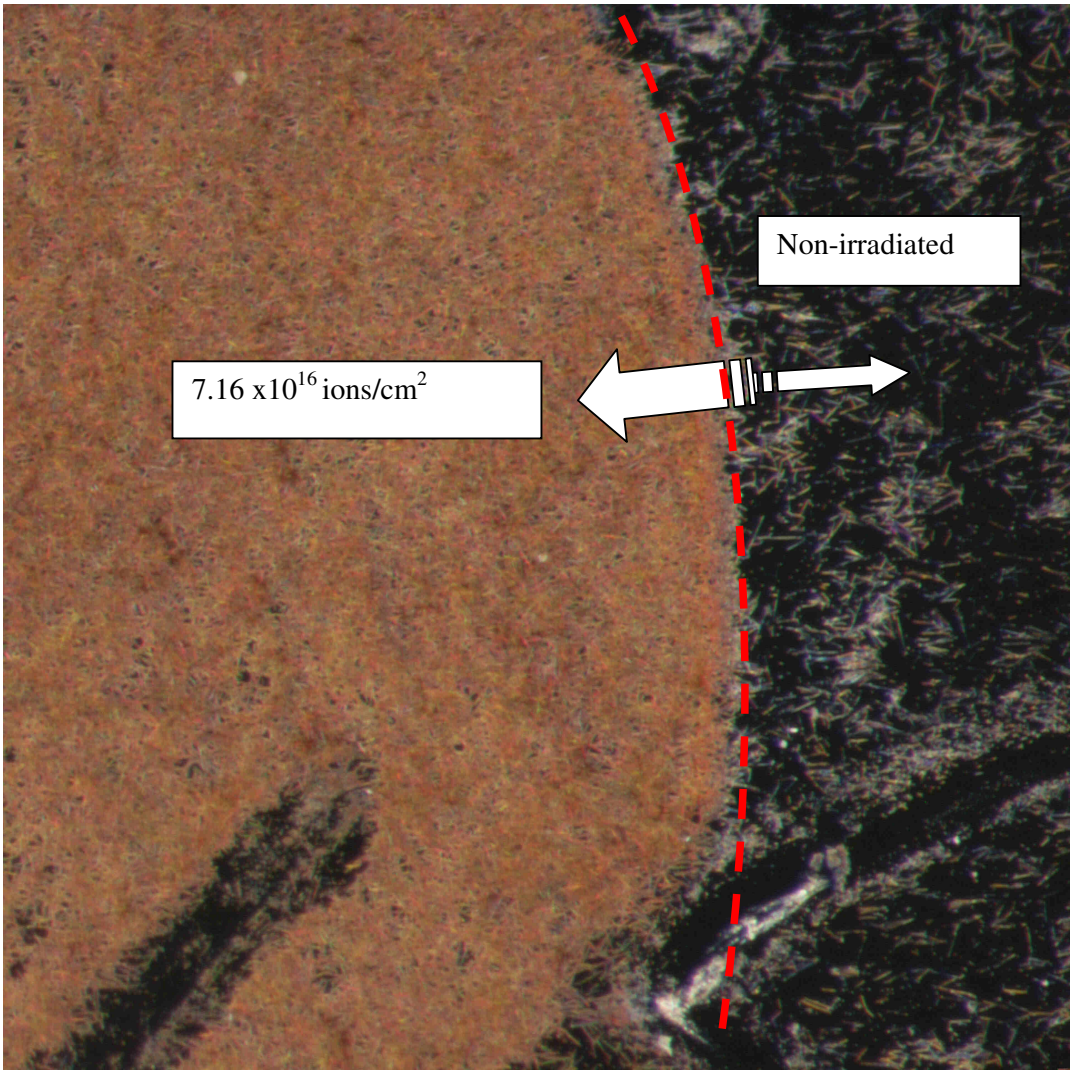

Figure 4.23: Optical image of C_{60} nanorods on Si (111) substrate showing proton irradiated area (big arrow) with fluence of 7.16×10^{16} ions/cm^2 and non-irradiated area (small arrow).

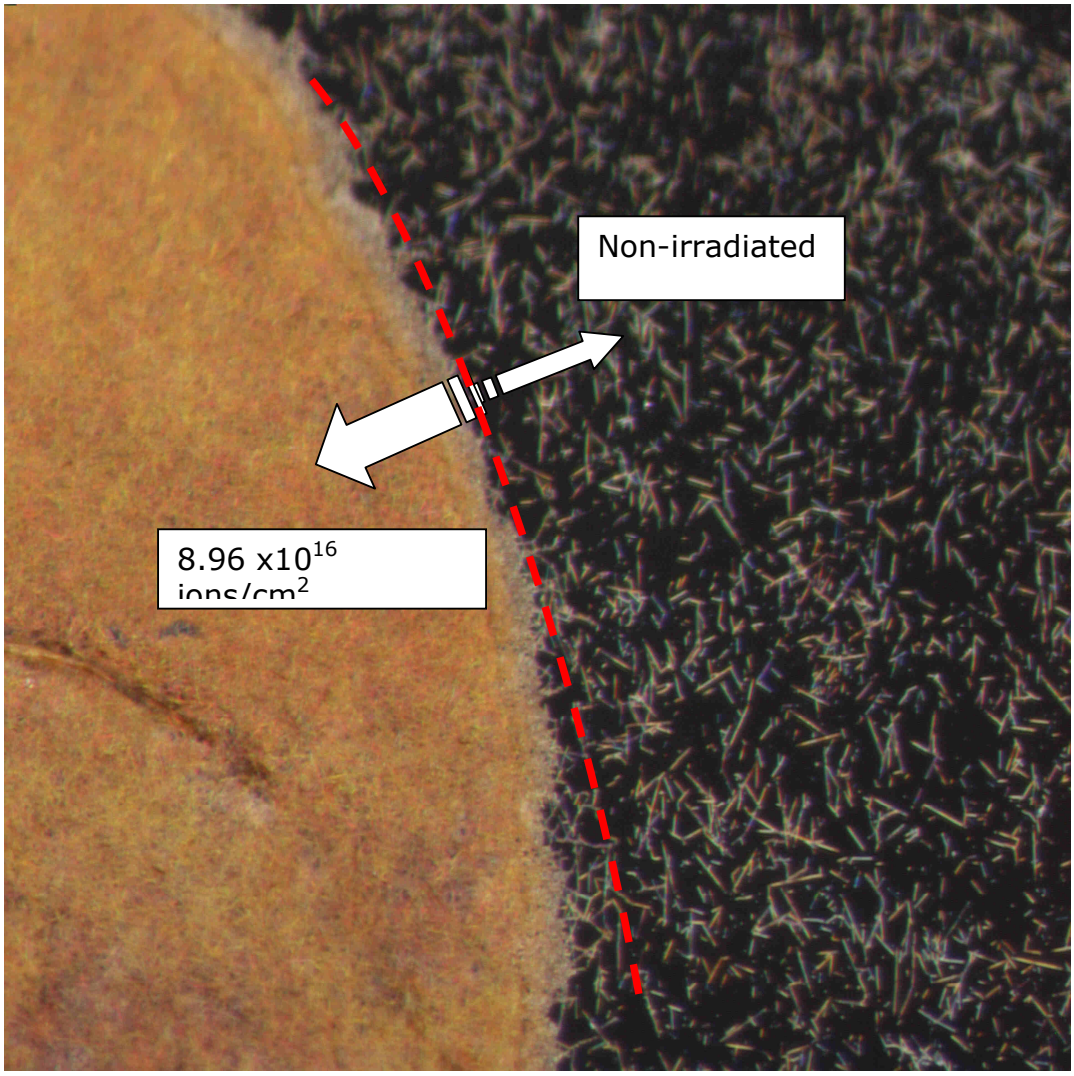

Figure 4.24: Optical image of C_{60} nanorods on Si (111) substrate showing proton irradiated area (big arrow) with fluence of 8.96 10^{16} ions/cm^2 and non-irradiated area (small arrow).

4.3.7. SEM images after soaking in toluene

SEM was used to further study the surface morphology on all samples inside proton irradiated area after being soaked in toluene and viewed under the optical microscope. All images in figures 4.25 – 4.29 show no morphological changes after been soaked in toluene after proton irradiation.

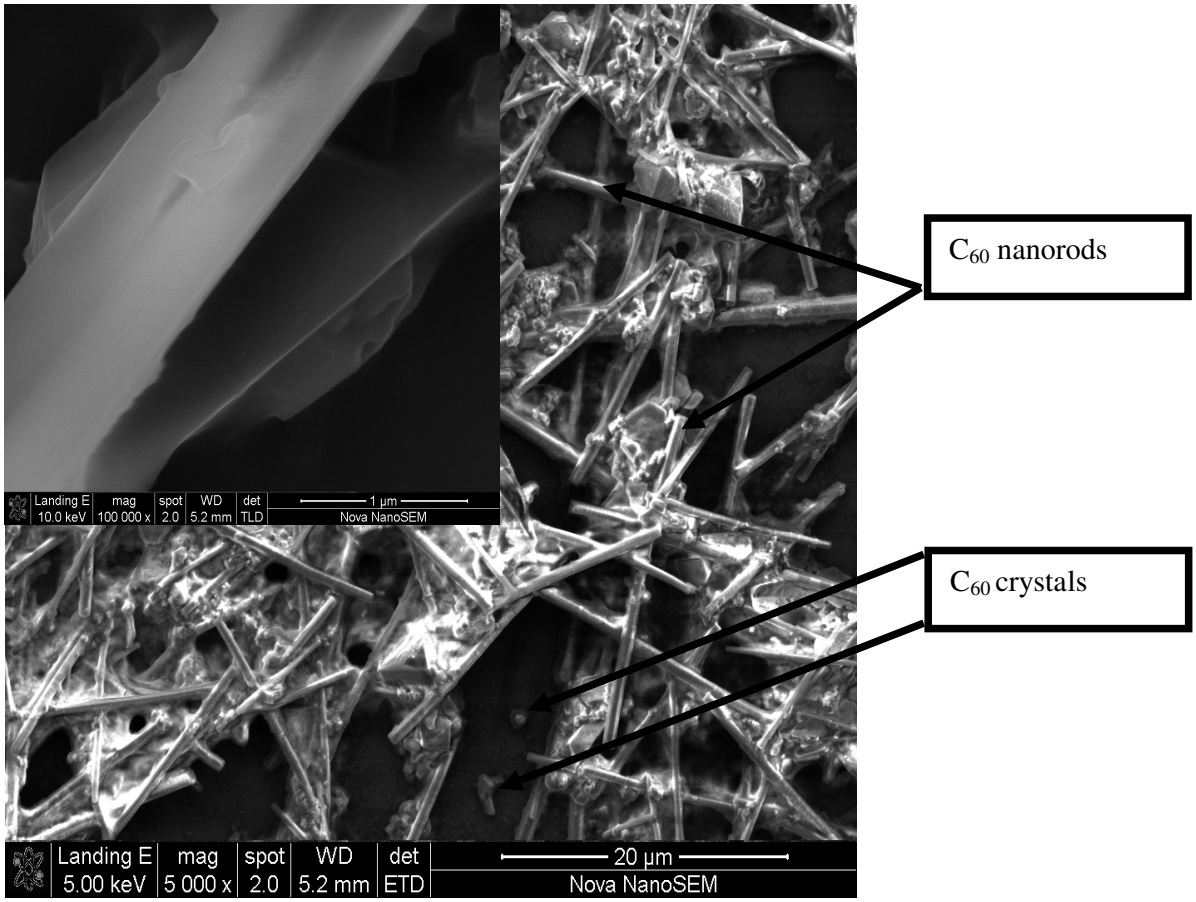

Figure 4.25: SEM image of irradiated C_{60} nanorods with a fluence of 1.79×10^{16} ions/cm^2 on Si (111) substrate after being soaked in toluene.

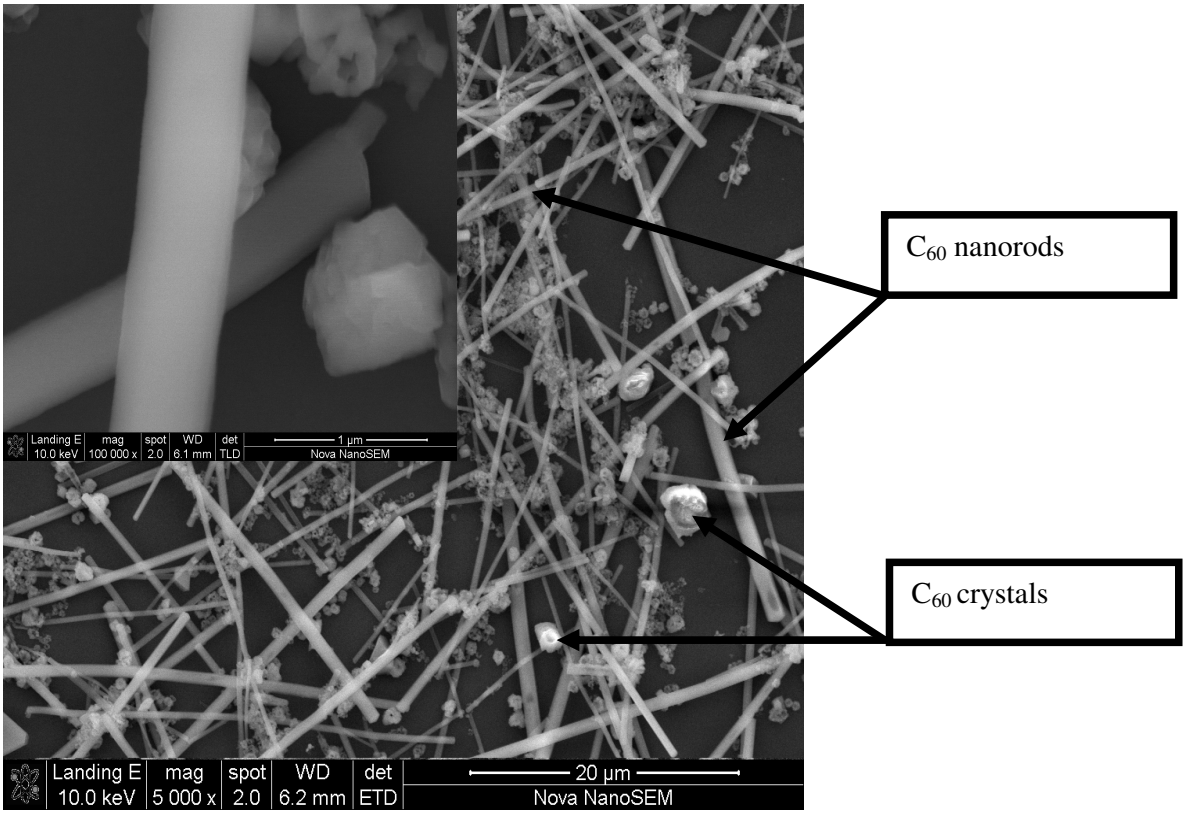

Figure 4.26: SEM image of irradiated C_{60} nanorods with a fluence of 3.58×10^{16} ions/cm^2 on Si (111) substrate after being soaked in toluene.

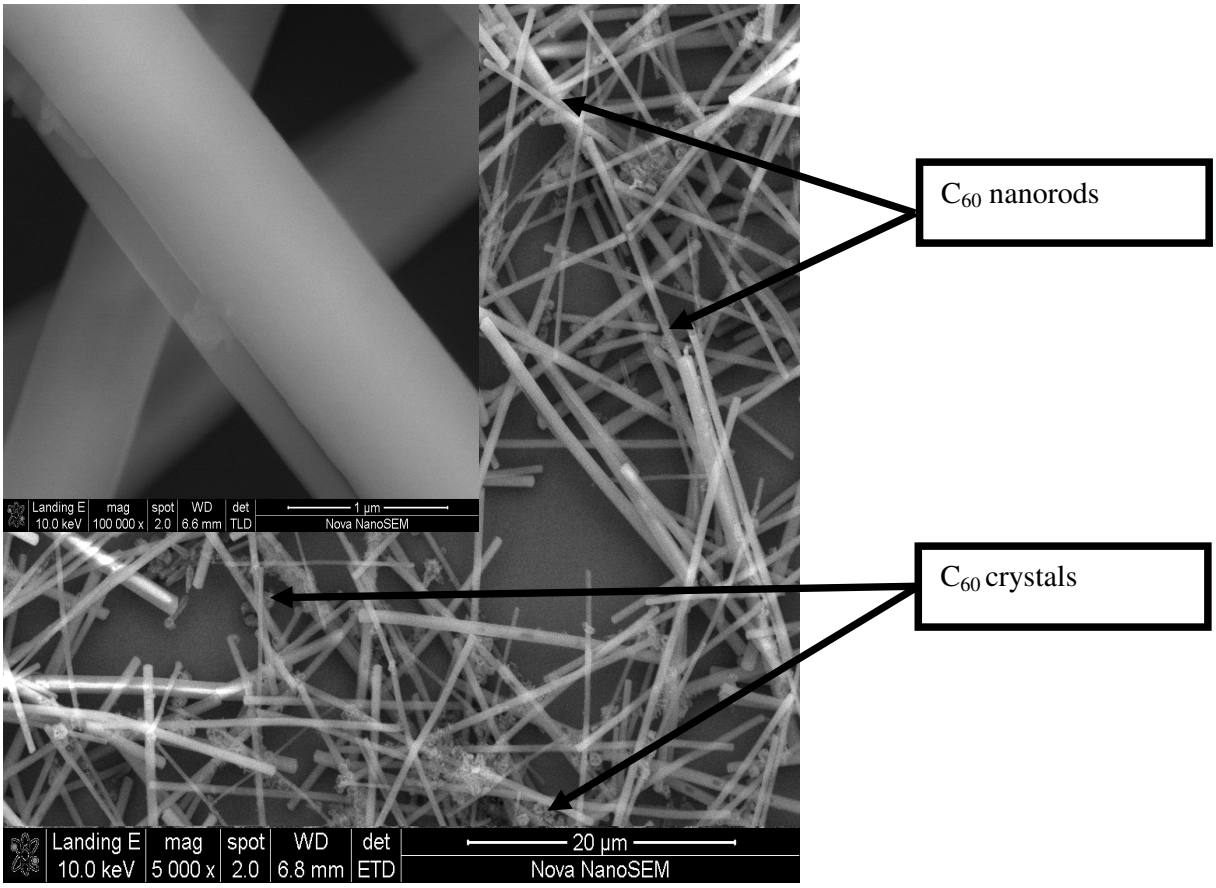

Figure 4.27: SEM image of irradiated C_{60} nanorods with a fluence of 5.37×10^{16} ions/cm^2 on Si (111) substrate after being soaked in toluene.

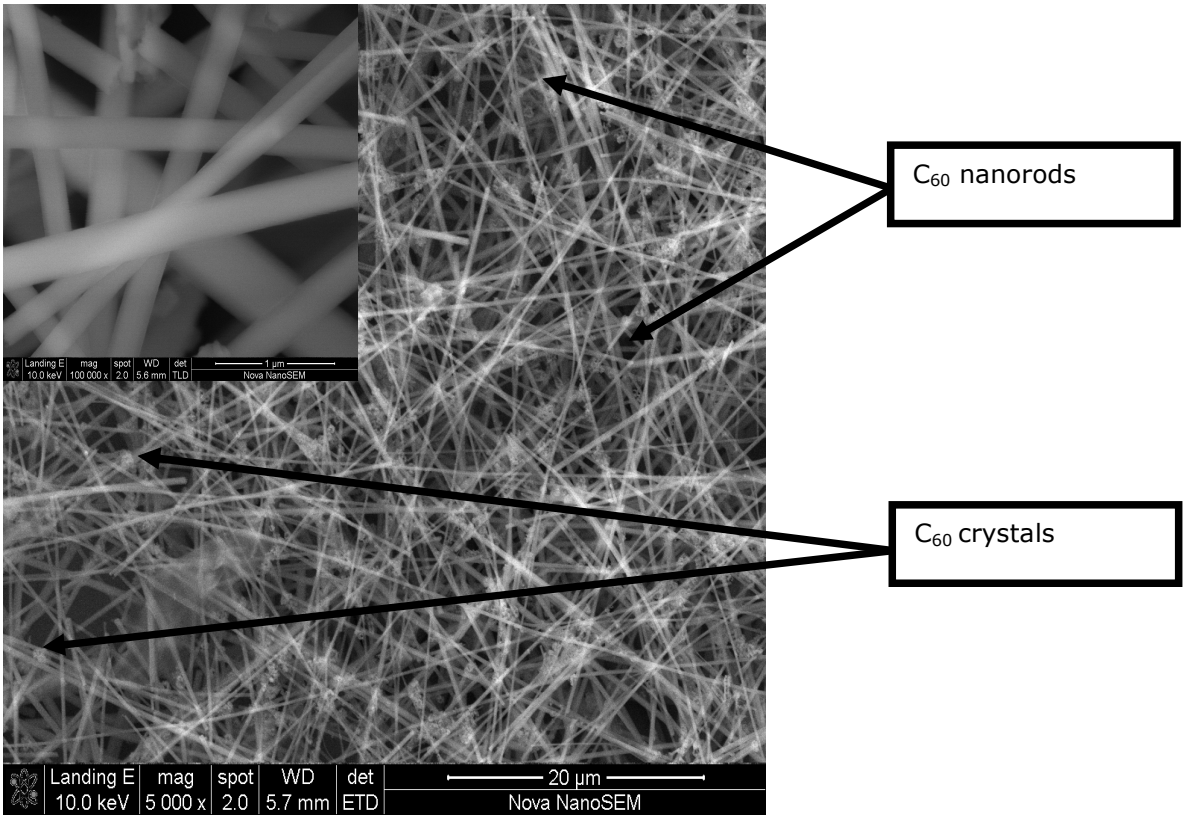

Figure 4.28: SEM image of irradiated C_{60} nanorods with a fluence of 7.16×10^{16} ions/cm^2 on Si (111) substrate after being soaked in toluene.

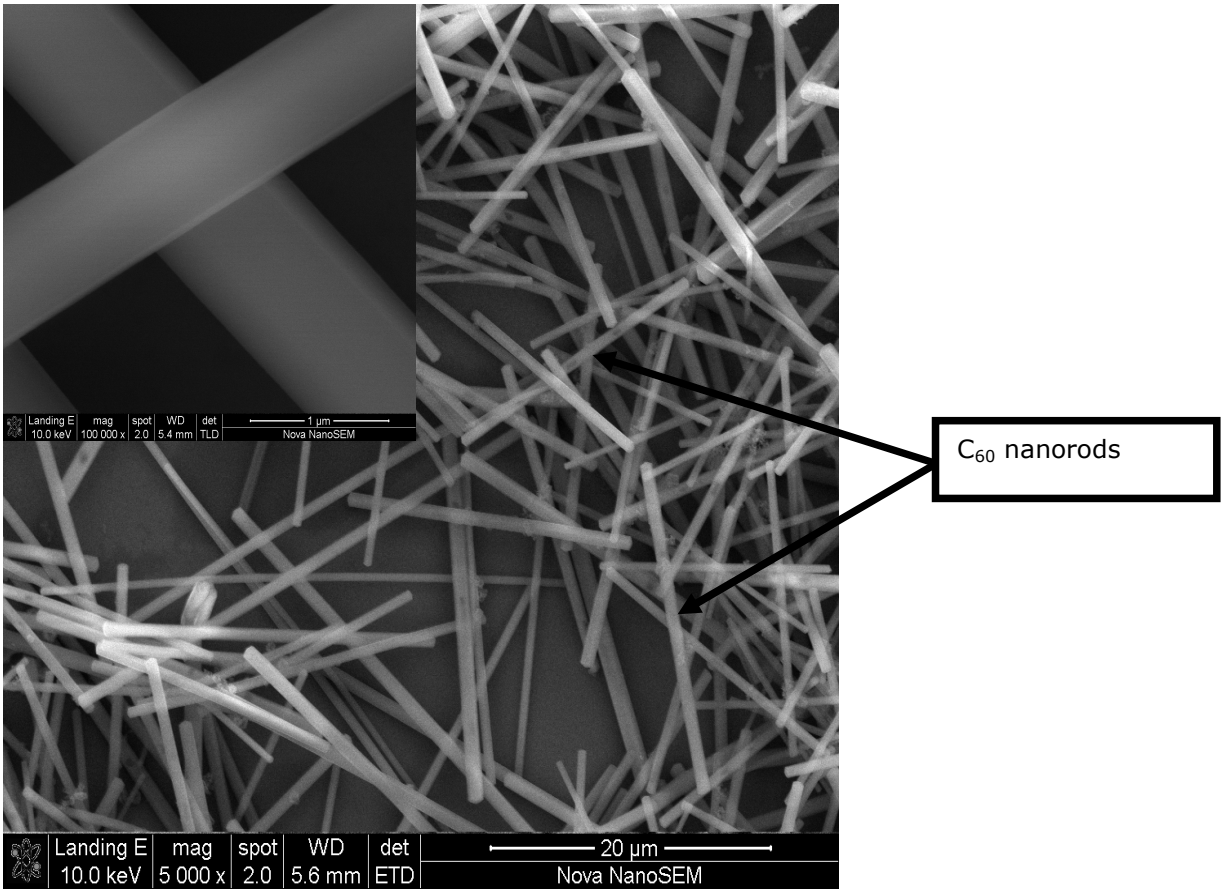

Figure 4.29: SEM image of irradiated C_{60} nanorods with a fluence of 8.96×10^{16} ions/cm^2 on Si (111) substrate after being soaked in toluene.

4.3.8. High Resolution Transmission Electron Microscope (HRTEM)

After studying the irradiated nanorods in the SEM and seeing no signs of any morphological change, it was crucial to do further investigation using HRTEM. This technique was used to investigate detailed crystal structure of the C_{60} nanorods before proton irradiation and after irradiation and after being soaked in toluene. Since the majority of the C_{60} nanorods have a diameter below 400 nm with the finer ones having a diameter $\leq$ 200 nm, it was difficult to obtain high quality HRTEM images with reasonable contrast from the body of the nanorods. The images were taken from the thinner part of the nanorods.

Figures 4.30 and 4.31 show HRTEM images taken on non-irradiated and irradiated with 2 MeV protons at a fluence of 8.96×10^{16} ions/cm^2 respectively. It is clear in figure 4.29 that the nanorods is composed of perfect planes with a preferential (111) direction. This is confirmation of the crystalline nature of C_{60} nanorods as reported in literature [23]. The planar spacing of an fcc C_{60} nanorods is clearly seen in the image.

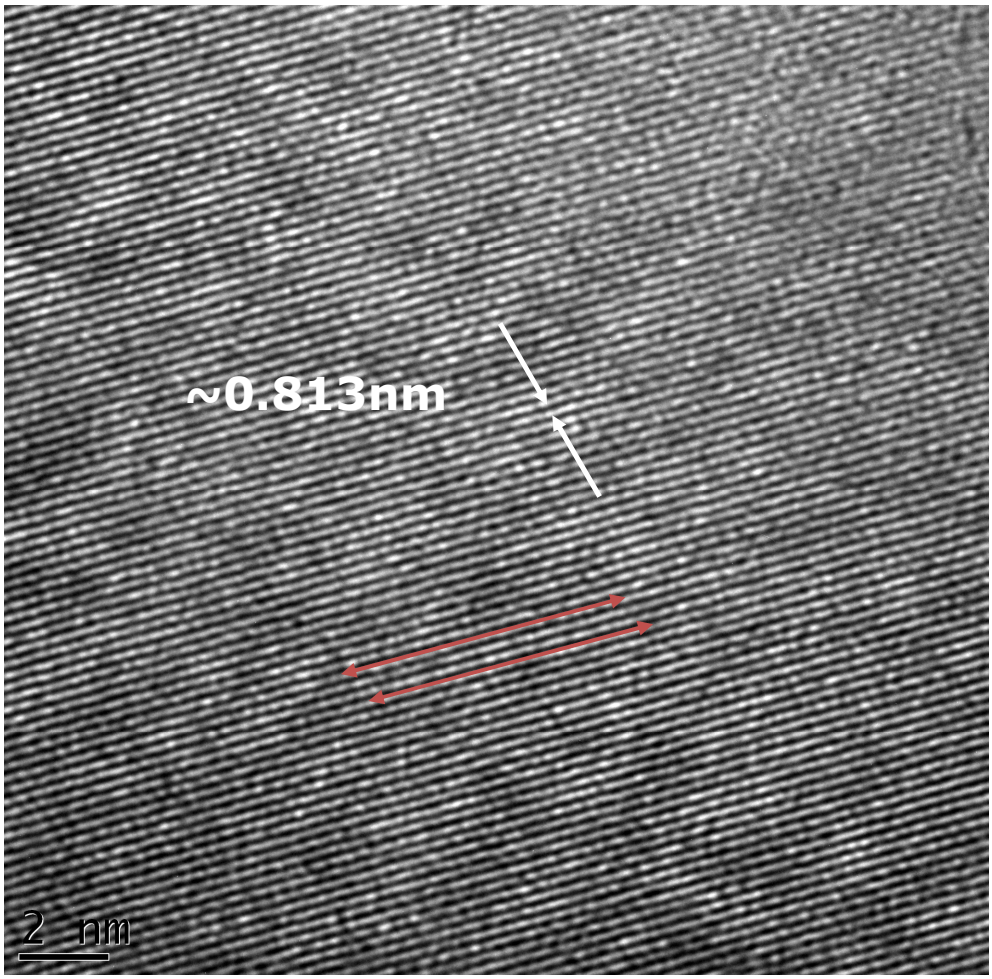

Figure 4.30: HRTEM image of C_{60} nanorod before proton irradiation at 2 MeV on a copper grid.

In Figure 4.31, twinning of crystal planes as compared to the non-irradiation samples is observed as indicated by arrows. This could mean that there is a change in the crystal structure of the C_{60} nanorods as compared to the non-irradiated nanorods, this indicate an extent at which the protons interacted with the nanorods, thus explaining the (111) Bragg peak shift that was observed from the XRD analysis.

Furthermore, there is a continuous penetration of nanorods by protons which limits the regaining of structure after the first proton have passed through the nanorod. This results in the formation of various structures as reported by reference [24].

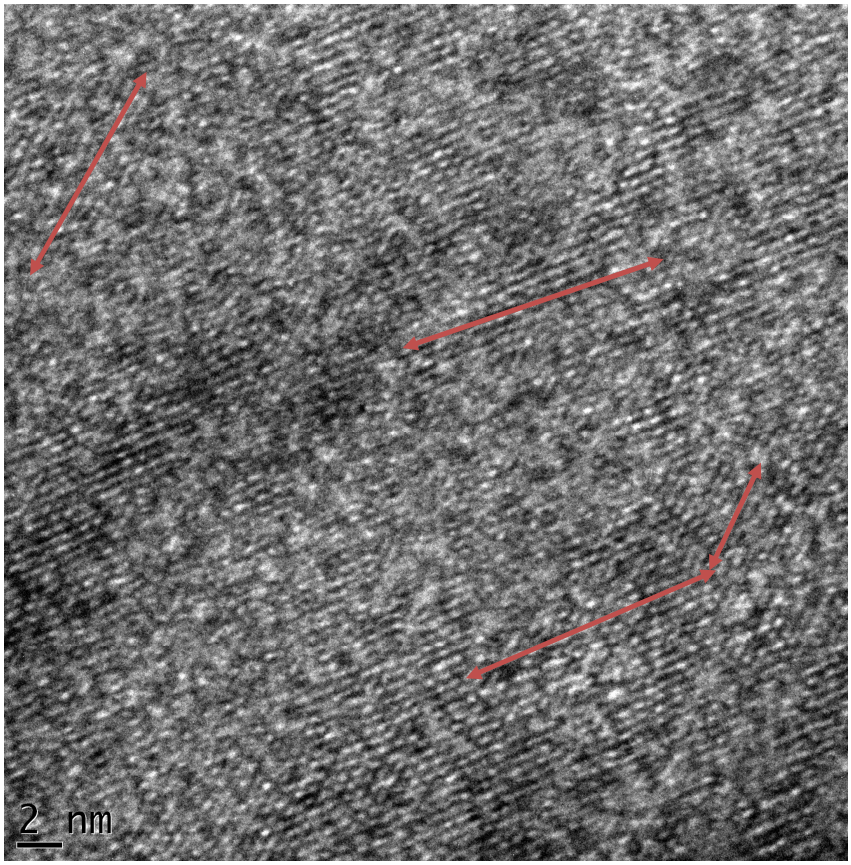

Figure 4.31: HRTEM image of C_{60} nanorod irradiated by 2 MeV protons at 8.96 $\times 10^{16}$ ions/cm^2 fluence on a copper grid showing planes with different orientation.

4.3.9. Magnetism in Fullerene C_{60} nanorods

For many years magnetic materials have been used in many applications such as magnetic storage media, sensors, electromotors, hard-disk drives, loud speakers, windshield wipers, locks, refrigerators, microphones, etc. In each application, a specific structure is required to meet application's specification of these materials. For example, some applications, such as toys, do not usually require high-performance magnets, but hard-disk drives and other high-tech applications require highly sophisticated rare-earth permanent magnets with well-

defined nanostructures. Magnets can be classified into two groups; hard magnets and soft magnets. Hard magnets are highly anisotropic while soft magnets exhibit low magnetic anisotropic. Soft magnets are widely used for flux guidance in permanent-magnet, transformer cores, microwave applications and in recording heads. In advanced soft-magnetic materials, nanostructuring is used to reduce magnetic losses by controlling anisotropy, eddy-current losses, and other properties.

A key application and driving force of magnetic nanotechnology is magnetic recording media. They are also used in audio-visual technology such as audio and video tapes, and also in computer technology such as in hard-disks. Nanostructuring of media read and write heads have helped to increase areal density of data storage devices. Artificial nanostructuring is a breakthrough to new technologies. One area which has dominated research recently is spin electronics. Other developments are in the area of creating magnetic nanostructures such as multilayers and nanojunctions, magnetoresistance of metallic thin films, granular nanostructures and magnetic oxides for sensors. Other recent developments are magnetic nanostructures for quantum computing, multiferroics (where nanoscale effects are exploited to synergize electric and magnetic degrees of freedom), and nanoparticle ferrofluids for cancer treatment, guided by a magnet and delivering high local doses of drugs or radiation.

Recently, there is also been a major discovery of magnetic signal in carbon nanomaterials as highlighted in the introduction of this chapter but this discover has met with speculations and misunderstanding on the issue of the origin of this magnetic signal. Since the discovery of fullerene C_{60} in bulk form in 1991, a lot of interesting properties e.g. magnetic properties and more have been found and that has opened a lot of channels for the researchers to explore more in this field of nanotechnology. The realization of ferromagnetism in materials made purely from carbon has opened another idea of performing experiments to find out whether this magnetic property exists in C_{60} structures.

The prime importance is much based on the magnetic behaviour of carbon-based materials and engineering novel ferromagnetic carbon structures because of the biological compatibility, light weight and low cost, and the possibility of having a room temperature carbon-based metal-ion free magnet. Much research has been conducted in trying to find the origin of magnetism in carbon structures which led to different conclusions.

Yang, et al [25] studied vacancy defects and the ferromagnetism in 70 keV $12C^+$ implanted HOPG samples using PAT and SQUID measurements. Their results indicated a close correlation between vacancy defects due to implantation and the room temperature ferromagnetism. Their theoretical calculations were consistent with the experimental resultsand therefore, concluded that the RT ferromagnetism observed in the HOPG sample is likely due to the itinerant π-electrons in the ‘‘impurity’’ band caused by the vacancies. Furthermore, they concluded that this work also supposes that the magnetization in pure carbon materials, such as graphite, graphene, and carbon nanotubes, may be tuned by controlling the density of vacancies.

Esquinazi et al [26] studied the magnetization on Kish graphite and natural graphite samples with different content of magnetic impurities. Their results ruled out that ferromagnetic impurities can be responsible for the observed magnetic effects in HOPG and Kish graphite. They observed temperature-independent magnetization saturation which remains up to 500 K in contrast to natural graphite samples with at least two orders of magnitude larger than concentration of Fe-impurities which revealed the superparamagnetic behavior of Fe impurities in the carbon matrix. In addition, they reported that long-time annealing at 700 K and 800 K in vacuum of the HOPG samples had weakly affected the hysteresis loops. They acknowledged that the origin of the magnetic behaviour in HOPG is not clear but pointed out some possibilities which are topological defects and the strong Coulomb interaction between electrons in graphite (due to the small electronic density).

Han et al [27] studied the effects of proton irradiation on magnetic properties of oxygen-free and oxygen-rich, graphite-like hard carbon prepared by high pressure-high temperature treatment of C_{60} fullerene using magnetic force microscope. They observed formation of magnetic domains only in the oxygen-free targets.

Wang et al [28] observed room-temperature ferromagnetism in grapheme which is believed to come from the defects on graphene.

Kumar et al [29] studied defect induced intrinsic ferromagnetism in fullerene thin films using superconducting quantum interference device and electron spin resonance and concluded that

the origin of magnetic signal in irradiated films is due to the generation of an amorphous carbon network consisting sp^2/sp^3 bonded carbon atoms.

Talapatra et al [30] showed that ion irradiation of nanodiamond with 15N and 12C shows a signature of ferromagnetism. At low doses, the magnetization was independent of the doped species indicating that it mainly arises from structural deformation of the carbon bonds in nanodiamonds. Implants of 15N exhibit a higher value of the saturation magnetization than 12C implants at higher doses. This difference could be due to extensive defect generation or graphitization and, to some extent, incorporation of nitrogen in the graphitic network and formation of C-N bonds.

Lehtinen et al [31] investigated the magnetic properties of the most prolific defects which appear in graphite under irradiation—vacancies and vacancy-hydrogen complexes. They demonstrated that vacancies are magnetic, but, due to the high mobility of carbon interstitials at room temperature, vacancies will mostly annihilate with interstitials. They also showed that hydrogen will strongly absorb at vacancies in graphite, maintaining the magnetic moment of the defect, and that for small irradiation doses vacancy-hydrogen complexes will give rise to a macroscopic magnetic signal.

Esquinazi et al [32] reported on explicit evidence of ferromagnetism induced by proton irradiation. The report discussed recently obtained results on the ferromagnetism (or ferrimagnetism) induced by proton irradiation on pure pyrolytic graphite, which strengthen the importance of hydrogen in the formation of the magnetic ordering. They concluded that room-temperature ferromagnetism in carbon-based structures containing only p- and s-electrons is a reality.

Kyu Won Lee et al [33] studied magnetic moment in proton-irradiated highly oriented pyrolytic graphite and estimated the magnetic moment per irradiated proton to be 2.4 μB.

Buntar and H W Weber [34] studied magnetic properties of fullerene Superconductors and discovered that measurement of the temperature and magnetic field dependence of the magnetization show that pinning is very strong in fullerenes. However, the nature of flux pinning is unclear at present and we do not know whether strong pinning is an intrinsic or

extrinsic property of the C_{60} molecules and caused by different defects in the alkali metal doped C_{60} lattice.

Han et al [35] investigated proton irradiated spots created on highly oriented pyrolytic graphite surface using magnetic force microscopy and observed that a proton microbeam produces ferromagnetic spots on highly oriented pyrolytic graphite surface. This technique reveals clear irreversible behavior of the magnetic signal at the spots after application of an external DC field. They then concluded that their results leave no doubts on the intrinsic nature of the ferromagnetism in a metal-free carbon structure.

Pablo Esquinazi et al [36] investigated magnetism in carbon structures and concluded that the results after proton irradiation leave no doubt that magnetic ordering exists in a carbon structure without the influence of magnetic ions. Neither the total amount of magnetic impurities is sufficient to account for the measured magnetization nor can the creation of magnetic spots in the micrometer range with the proton micro-beam be understood based on magnetic metalion impurity concentration below 1 ppm as the PIXE results indicated.

Not long time ago, carbon-based structures were basically accepted to be diamagnetic origin special cases, paramagnetic. Any ferromagnetic-like signal was assumed to be due to magnetic impurities [37]. These findings caused a stir amongst the researchers in this area in such a way that Spemann, et al., published a comment on some of their findings saying "No doubt, impurities are a problem when the ''intrinsic'' magnetic signals are relatively small. However, it appears that instead of trying to study systematically the contribution of these impurities to the magnetic signals, the strategy of ''minimum work'' based on prejudices was chosen, indirectly neglecting the existence of interesting magnetic phenomena in carbon structures" [38].

Since these findings are much based on carbon materials and fullerene film, they opened a platform for us to explore much more on our nanorods of C_{60}. Although nanorods of C_{60} are different from the film of C_{60} in terms of the structure but sometimes the film can exhibit some characteristics of C_{60} nanorods, so our main purpose is to use the conditions used on polycrystalline fullerene thin films on hydrogen passivated Si (111) substrates irradiated by 2 MeV protons publication Mathew, et al. as highlighted in the introduction of this chapter to explore the magnetic properties of C_{60} nanorods.

4.3.10. Proton Induced X-ray Emission (PIXE)

An important aspect of the experimental research and of primary importance to study weak magnetic signals in unconventional materials is the characterization of the magnetic impurities in the samples. Therefore, PIXE experiment was conducted on pristine C_{60} powder which was used for the synthesis of nanorods with purpose of PIXE was to check impurities in the C_{60} powder which may contribute to any magnetic signal. Having carbon matrix, this methods reaches a sensitivity of approximately 0.1 ppm Fe and therefore it is convenient for all the elemental analysis prior proton irradiation. Figure 4.32 and 4.33 show PIXE spectra. It is clear that there are no impurities such as Fe, Co, Ni, Cr, which may contribute to magnetic signal.

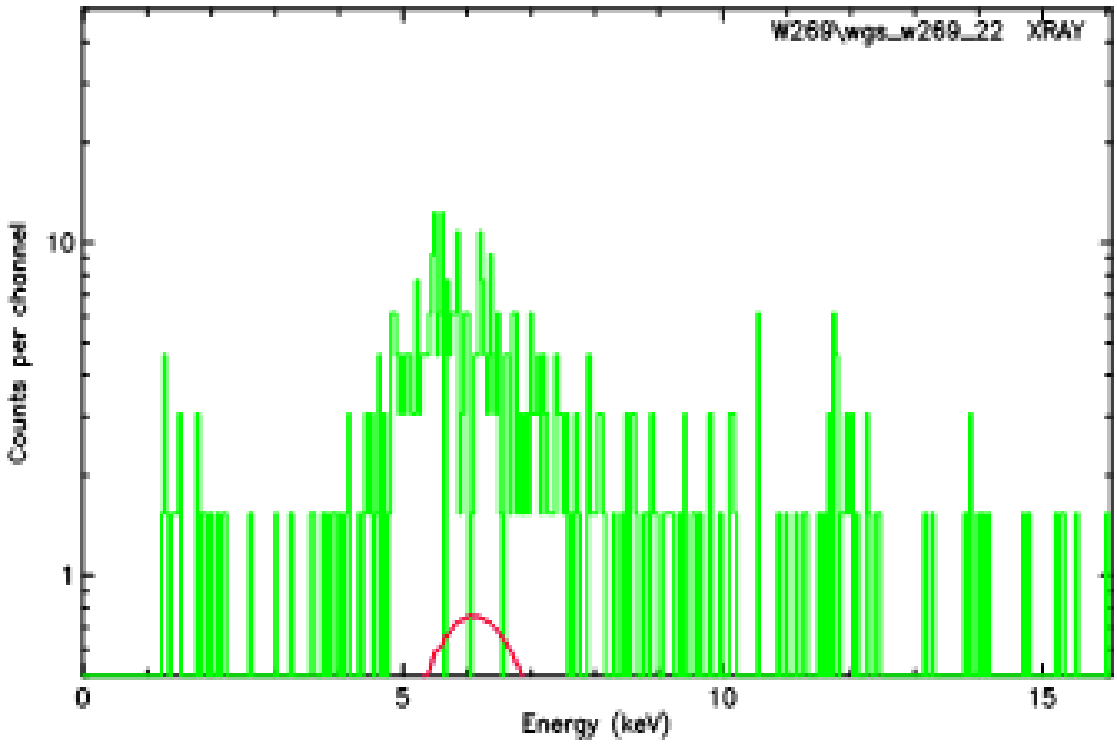

Figure 4. 32: PIXE spectrum of C_{60} powder on araldite Al 102 um filter showing no impurities.

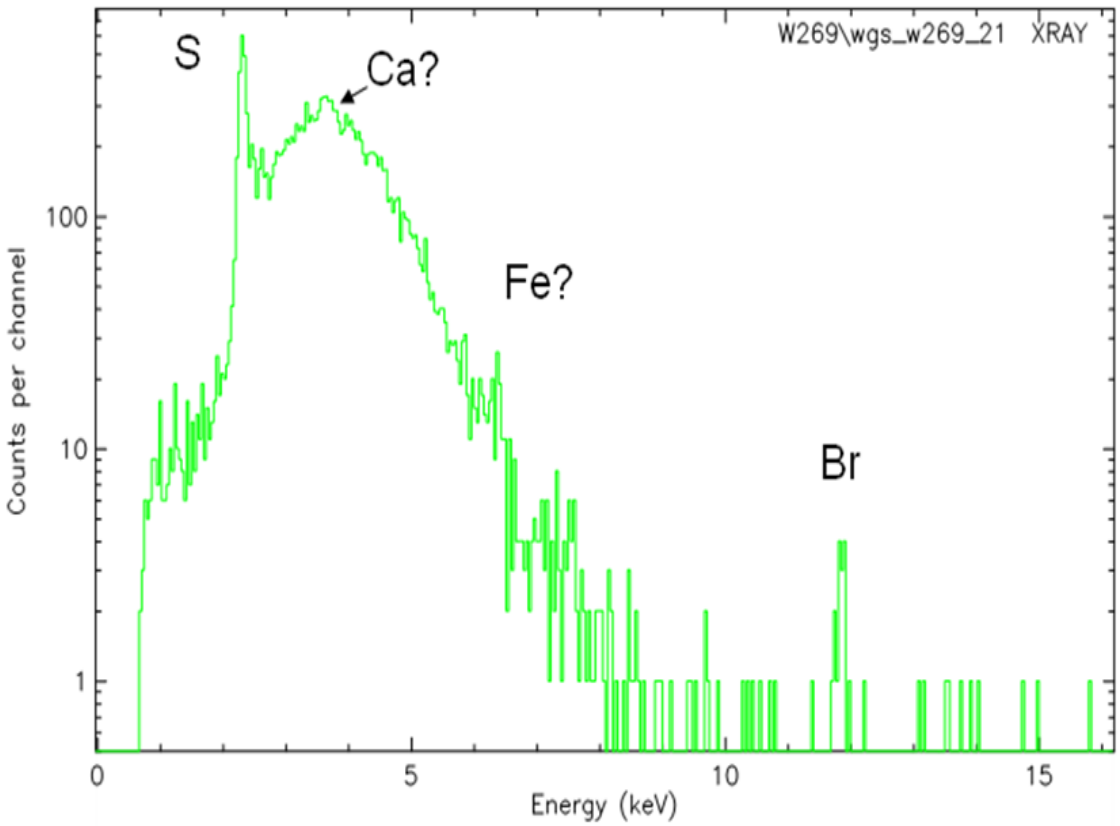

Figure 4. 33: PIXE spectrum of C_{60} powder on araldite kapton 180 um filter showing S and Br with very small Fe peak.

4.3.11. Magnetism measurement experiment

In our effort to follow and contribute to this type of research which is focused in investigating magnetism in carbon nanostructures, we have investigated magnetism in proton irradiated C_{60} nanorods.

Figure 4.34 shows magnetization versus temperature measured using the reciprocating sample option (RSO) in a SQUID magnetometer (MPMS XL, Quantum Design) in the temperature range 2-200K. It can be clearly seen that at 150 K, the irradiated sample show

diamagnetic behaviour but as the temperature is changed as shown in the figure magnetization tends to increase and saturate below 40 K. It can also be observed that the magnetization data in the temperature range of 2 - 200 K, in 1 T applied field, for the irradiated nanorods show is temperature dependence. The possible origin of this magnetism is still a mystery and we do not have explanation for it at the moment.

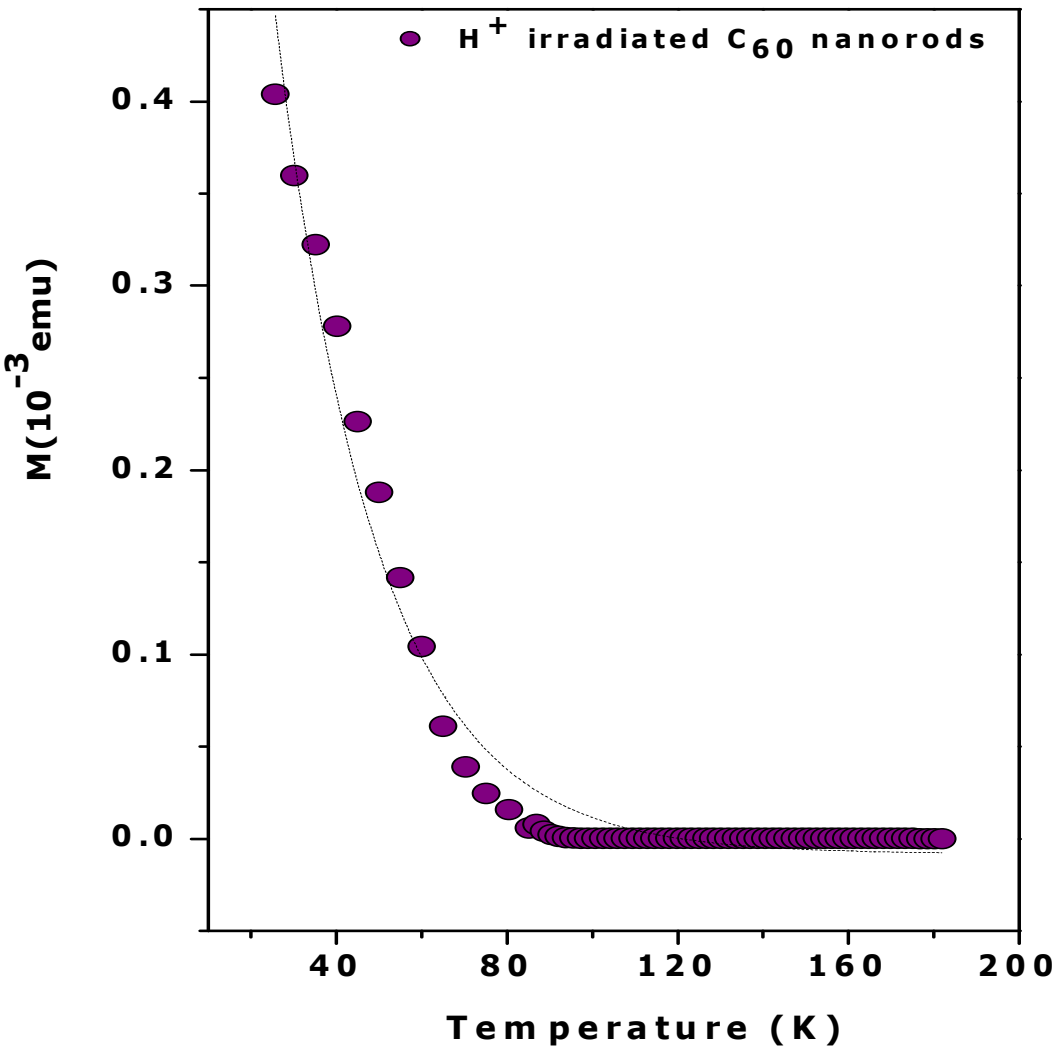

Figure 4. 34: M vs. T for an irradiated C_{60} nanorods at 8.96 10^{16} ions/cm^2 in an applied field of 1 T (substrate [H-Si(111)] contribution subtracted).

4.4. References

[1] **Krasheninnikov, A. V., Banhart, F., Li, J. X., Foster, A. S., and Nieminen, R. M.,** Stability of carbon nanotubes under electron irradiation: Role of tube diameter and chirality, *Physical Review* B 72, 125428, 2005.

[2] **Saito, R., Fujita, M., Dresselhaus, G., Dresselhaus, M.S.,** Electronic structure of chiral graphene tubules, *Applied Physics Letters* 60, 2204, 1992.

[3] **Mintmire, J. W., Dunlap, B. I., and White, C. T.,** Are fullerene tubules metallic?, *Physical Review Letters* 68, 631, 1992.

[4] **Schluter, M., Lannoo, M., Needels, M., and Baraff , G. A.,** Electron-phonon coupling and superconductivity in alkali-intercalated C_{60} solid, *Physical Review Letters* 68, 526, 1992.

[5] **Hamada, N., Sawada, S., and Oshiyama, A.,** New one-dimensional conductors: Graphitic microtubules, *Physical Review Letters* 68, 1579–1581, 1992.

[6]. **Narayanan, K.L., Kojima, N., Yamaguch,i K., Ishikawa, N., Yamaguchi, M.,** Arsenic ion implantation induced structural effects in C_{60} films, *Journal of Materials Science*, 34, 5227-5231, 1999.

[7] **Mathew. S., Satpati, B., Joseph, B., and Dev, B.N.,** Magnetism in C_{60} Films Induced by Proton Irradiation, arXiv:cond-mat/0503315 v 2 (2005)

[8] **Boukhvalov. D.W. and Katsnelson, M.I.,** Defect-induced ferromagnetism in fullerenes, arXiv: arXiv: cond-mat/0712.2928 v1 (2007).

[9] **Kumar, A., Avasthi, D. K., Pivin, J. C., Tripathi, A., and Singh, F.,** Ferromagnetism induced by heavy-ion irradiation in fullerene films, Physical Review B, 74, 153409, 2006.

[10] **Esquinazi, P., Spemann, D., Höhne, R., Setzer, A., Han, K.-H., and Butz, T.,** Induced Magnetic Ordering by Proton Irradiation in Graphite, *Physical Review Letters* 91, 227201, 2003.

[11] **Terrones M., Terrones, H., Banhart, F., Charlier, J.C. and Ajayan, P. M.,** Coalescence of Single-Walled Carbon Nanotubes, *Science* 288, 1226, 2000.

[12] **Mathew, S., Satpati, B., Joseph, B., Dev, B. N., Kesavamoorthy, R.,** Two mega-electron volt proton-irradiation effects on fullerene films, *Radiation Effects & Defects in Solids*, 162, 3–4, 223–228, 2007.

[13] **Ea, X., and Lee, H.,** Ion-beam modification of polymeric materials and fundamental principles and applications, *Nuclear Instruments and Methods in Physics Research* B 151 29-41, 1999.

[14] **Sundar, C. S., Sahu, P. Ch., Sastry, V. S., Rao, G. V. N., Sridharan, V., Premila, M., Bharathi, A., Hariharan, Y., and Radhakrishnan, T. S.,** *Physical Review* B 53, 8180–8183, 1996.

[15] **Núñez-Regueiro, M., Marques, L., Hodeau, J.L., Béthoux, O., and Perroux, M.,** Polymerized: Fullerite Structures, *Physical Review Letters* 74, 278 -1995.

[16] **Mathew, S., Satpati, B., Joseph, B., and Dev, B.N.,** Magnetism in C_{60} Films Induced by Proton Irradiation, arXiv:cond-mat/0503315 v 2 (2005).

[17] **Minato, J., and Miyazawa, K.,** Solvated structure of C_{60} nanowhiskers, *Carbon* 43, 2837–2841, 2005.

[18] **Onoe, J., Nakayama, T., Aono, M., and Hara, T.,** The electron transport properties of photo- and electron-beam-irradiated C_{60} films, *Journal of Physics and Chemistry of Solids* 65, 343–348, 2004.

[19] **Miyazawa, K., Minato, J., Yoshii, T., Suga, T.,** Characterization of fullerene nanotubes prepared by the liquid–liquid interfacial precipitation method, *Science and Technology of Advanced Materials* 6, 388–393, 2005.

[20] **Pusztai, T., Oszla´nyi, G., Faigel, G., Kamara´s, K., Gra´na´sy, L., and Pekker, S.,** *Solid State Communications* 111, 595–599, 1999.

[21] **Katz E.A., Faiman, D., Shtutina, S., and Isakina, A.,** Deposition and structural characterization of high quality textured C_{60} thin films, *Thin Solid Films* 368, 49-54, 2000.

[22] **Lee, E. H.,** *Nuclear Instruments and Methods in Physics Research* B, 151, 29-41, 1999.

[23] **Jin, Y., Curry, R. J., Sloan, J., Hatton, R. A., Chong, L. C., Blanchard, N., Stolojan, V., Kroto, H. W., Ravi, S., and Silva, P.,** Structural and optoelectronic properties of C_{60} rods obtained via a rapid synthesis route, *Journal of Material Chemistry,* , 16, 3715–3720, 2006.

[24] **Onoe, J., Nakayama, T., Aono, M., and Hara, T.,** *Journal of Physics and Chemistry of Solids* 65, 343–348, 2004.

[25] **Yang, X., Xia, H., Qin, X., Li, W., Dai, Y., Liu, X., Zhao, M., Xia, Y., Yan, S., and Wang, B.,** Correlation between the vacancy defects and ferromagnetism in graphite, *Carbon* 4 7, 1 3 9 9 –1 4 0 6, 2 0 0 9.

[26] **Esquinazi, P., Setzer, A., H¨ohne, R., Semmelhack, C., Kopelevich, Y., Spemann, D., Butz, T., Kohlstrunk, B., and L¨osche, M.,** Kish graphite and natural graphite samples with different content of magnetic impurities, arXiv:cond-mat/0203153v1 [cond-mat.str-el] 2002.

[27] **Han, K. H., Makarova, T. L., Zakharova, I. B., Serenkov, I. T. and Sakharov, V. I.,** Proton Bombardment of Hard Carbon, Fullerenes, Nanotubes, and Carbon Nanostructures, 14: 381–384, 2006

[28] **Wang, Y., Huang, Y., Song, Y., Zhang, X., Ma, Y., Liang, J., and Chen Y.,** Room-Temperature Ferromagnetism of Graphene, *Nano letters*, 9, 1, 220-224, 2009.

[29] **Kumar, A., Avasthi, D. K., and Claude, J.,** Defect Induced Intrinsic Ferromagnetism in Fullerene Thin Films, *Applied Physics Express* 1, 125002, 2008.

[30] **Talapatra, S., Ganesan, P. G., Kim, T., Vajtai, R., Huang, M., Shima, M., Ramanath, G., Srivastava, D., Deevi, S. C., and Ajayan, P. M.,** Irradiation-Induced Magnetism in Carbon Nanostructures, *Physical Review Letters PRL* 95, 097201, 2005.

[31] **Lehtinen, P.O., Foster, A. S., Ma, Y., Krasheninnikov, A.V., and Nieminen, R.M.,** Irradiation-Induced Magnetism in Graphite: A Density Functional Study, Ph*ysical Review Letters,* 93, 18.

[32] **Esquinazi, P., Hohne, R., Han, K.-H., Setzer, A., Spemann, D., and Butz, T.,** Magnetic carbon: Explicit evidence of ferromagnetism induced by proton irradiation, *Carbon* 42, 1213–1218, 2004.

[33] **Lee, K. W., Lee, Y., Kim, I. and Lee, C. E.,** Magnetic Moment in Proton-Irradiated Graphite, *Journal of the Korean Physical Society*, 47, 2, 337-338, 2005.

[34] **Buntar, V., and Weber, H. W.,** Magnetic properties of fullerene Superconductors, Topical Review, *Superconductor Science and Technology* 9, 599–615, 1996.

[35] **Han, K.-H., Spemann, D., Esquinazi, P., Hohne, R., Riede, V., and Butz, T.,** Magnetic signals of proton irradiated spots created on highly oriented pyrolytic graphite surface, *Journal of Magnetism and Magnetic Materials* 272–276, 1190–1191, 2004.

[36] **Esquinazi, P., and Ho¨ hne, R.,** Magnetism in carbon structures, *Journal of Magnetism and Magnetic Materials* 290–291, 20–27, 2005

[37] **Sepioni, M., Nair, R.R., Tsai, I.-L, Geim, A.K. and Grigorieva, I.V**., *EPL* 97, 47001, 2012.

[38] **Spemann, D., Rothermel, M., Esquinazi, P., Ramos, M., Kopelevich, Y., and Ohldag, H.,** ArXiv.org/cond-mat, April 16, 2012

CHAPTER 5

GAMMA IRRADIATION

Abstract

This chapter focuses on fullerene C_{60} nanorods deposited on a hydrogen-passivated Si (111) substrate then irradiated with 1.33 MeV and 1.77 MeV gamma rays from a ^{60}Co source. The activity of the source was of 14 kCurie and fluences ranging from 50 kGy-1000 kGy. All the experimental results from stereo microscope, scanning electron microscope (SEM), transmission electron microscope (TEM), and atomic force microscope (AFM) are presented and the Raman and Fourier Transform Infra-Red (FTIR) spectroscopy is discussed.

5.1. Introduction

Increasing interest in nanomaterials for electronics applications, biomedical devices and nanostructured carbon phases are increasingly attracting the attention of the scientific community. The changes in the spatial arrangement of carbon atoms modify the electronic properties of carbon phases, which may be semiconductors, metals, or insulators and this change in electronic properties can be achieved by beam irradiation. [1-5].

So far little attention has been paid towards irradiation of fullerene C_{60} by gamma rays. Dubey et al. [6] studied radiation processed ethylene vinyl acetate- multi-walled carbon nanotubes and nano-composites and discovered that gamma radiation induced crosslinking in multi-walled carbon nanotubes (MWCNTs).

This crosslinking was found to increase with radiation dose. Transport properties of single-walled carbon nanotube transistors after gamma radiation treatment were investigated by Vitusevich et al. [7]. They found that radiation treatment with doses of 1×10^6 and $2\text{x}10^6$ rad

allows a considerable decrease in parasitic conductivity parallel to the nanotube. Furthermore, they observed a shift with maximal conductivity to the voltage range of nearly zero gate voltage that improves the working point of the FETs.

Hulman et al. [8] studied graphite and single-wall carbon nanotubes irradiated by gamma rays of energy of 1.3 MeV using Raman spectroscopy. They found out that gamma irradiation generates defects in the lattice as confirmed by the increase of the intensity of the defect-induced D line in both materials. On the other hand, the intensity of the radial breathing mode of nanotubes is lowered. The intensity of the G line does not change for graphite but increases for carbon nanotubes. Gupta et al. [9] reported that irradiation generates microscopic defects in a hierarchical manner much below amorphization threshold 1×10^3 kGy and that nanocomposites tend to be radiation resilient. They concluded that gamma irradiation generates microscopic defects that are marginal as compared with E-beam considering the energy scale difference as well as the mechanism. This result is due to the fact that for gamma irradiation, a larger fraction of the deposited energy goes into bond breaking rather than atomic displacement.

Xu et al. [10] studied the modification of surface functionality and interlayer spacing of MWCNTs using gamma rays. They found out that gamma ray irradiation could not only functionalize MWCNTs, but also change the inter-wall distance and graphitization of MWCNTs in different conditions. Gupta and Farmer. [11] reported on the structure and physical properties of novel hybrids of multiwalled carbon nanotubes MWCNTs and ultradispersed diamond (UDD) forming nanocomposite ensemble that were subjected to 50, 100, and 103 kGy gamma ray doses. They showed that with increasing irradiation MWCNTs display marginal structural instabilities arising due to microscopic defects in the lattice, as compared to SWCNTs. Thus bond breaking and massive reorganization is more probable than atomic displacement.

Gupta et. al. [12] studied microcrystalline diamond and nanocrystalline carbon thin films prepared by microwave plasma, assisted chemical vapor deposition were subjected to gamma radiation in order to study the radiation-induced structural transformation and the corresponding changes in the electron field emission properties. The effects of gamma radiation over the electron field emission properties and microstructure of microcrystalline diamond and nanocrystalline carbon thin films were investigated. Microcrystalline diamond

showed a dramatic improvement in the emission properties after a cumulative dose of 26 Mrad, while nanocrystalline carbon showed a relatively small but systematic decrease in the turn-on field from 9 to 4 V/mm with increasing gamma radiation dose.

The enhancement in emission characteristics upon radiation shows the critical role of structural defects with their associated electronic defect states of sp^2-bonded carbon channels in the electron field emission mechanism of nanocrystalline carbon. Savopulo and Burakov [13] reported that gamma-irradiation of initial fullerene C_{60} in nitrogen atmosphere causes partial conversion of C_{60} into amorphous carbon and essential increase of graphite content. It should be pointed out that there has been no report on gamma irradiated C_{60} nanorods studies available in the literature.

5.2. Experiment details

C_{60} nanorods were grown on Si (111) substrate by using a low cost method called liquid-liquid interfacial polymerization method as previously discussed in chapter three [14]. Gamma irradiation was then carried out at room temperature by exposing the samples in front of a source of Cobalt source with the activity of 14 kCurie and dose rate of 48.13 Gy/mn or 2888 Gy/h. (^{60}Co, gamma = 1.33 MeV and gamma = 1.77 MeV) for different time series study.

The sample were then characterized using Scanning electron microscope (FET, Quanta 200F) for morphological study, Raman shift spectra were then recorded using the laser fundamental NdYAG excitation wavelength of λ = 1064 nm "LAB RAM spectrometer with a liquid nitrogen cooled Ge diode detector", Fourier Transform Infrared spectroscopy (Pekin Elmer spectrum one) for phonon study.

5.3. Results and Discussion

5.3.1. SEM Gamma irradiation study

This sub-section is focused on the gamma irradiated C_{60} nanorods that are shown in figures 5.1 to 5.5. The gamma rays did not induce any meaningful change on the structure of the nanorods except for 800 kGy. In all images the structure is still preserved after Gamma

irradiation, but it is crucial to support the observation with other techniques such as Raman spectroscopy and FTIR. All the figures display smooth surfaces of the nanorods with the inclusion of C_{60} crystals. The crystals are the result of C_{60} molecules which did not form nanorods.

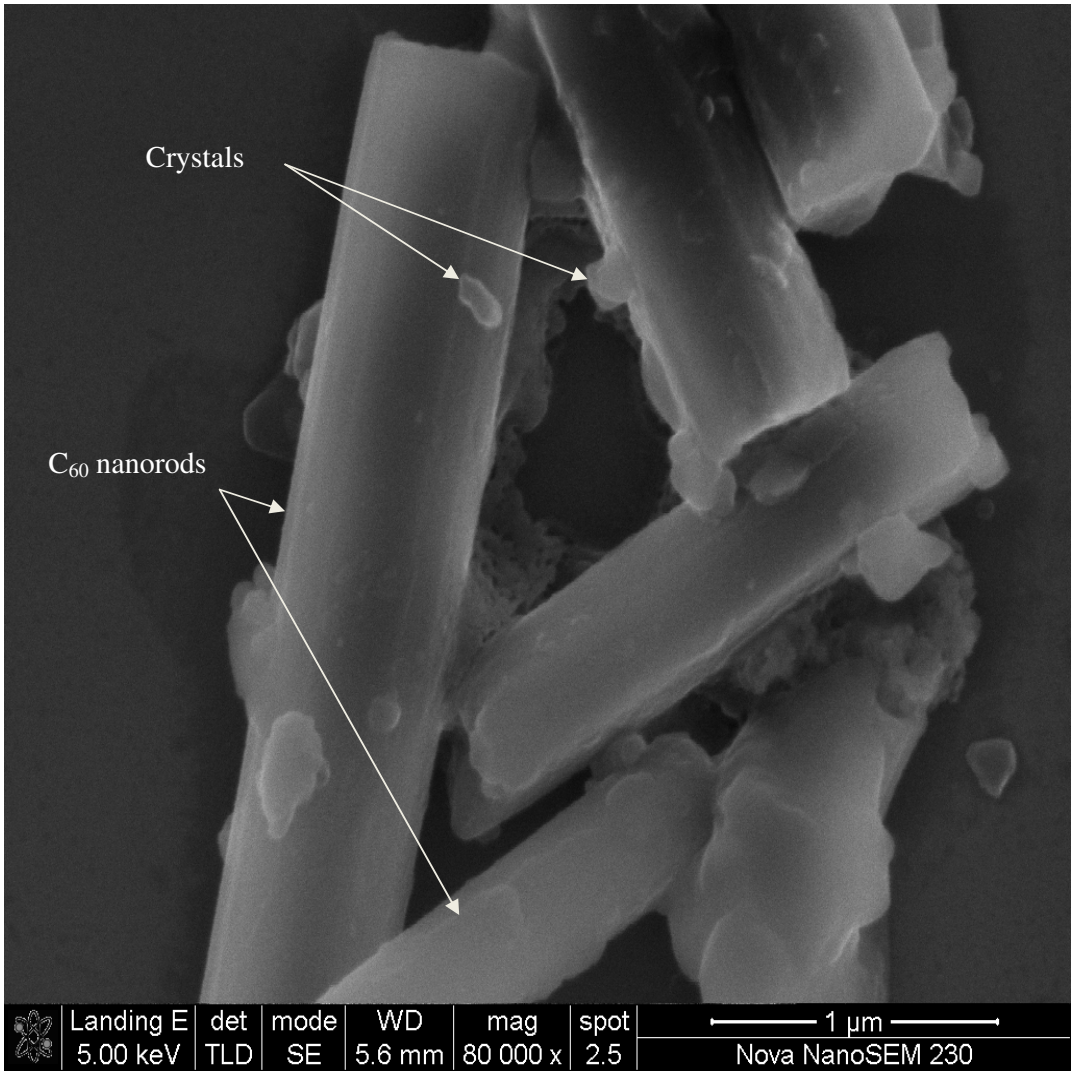

Figure 5. 1: SEM image of C_{60} nanorods on Si (111) substrate irradiated gamma rays at 50 kGy dose.

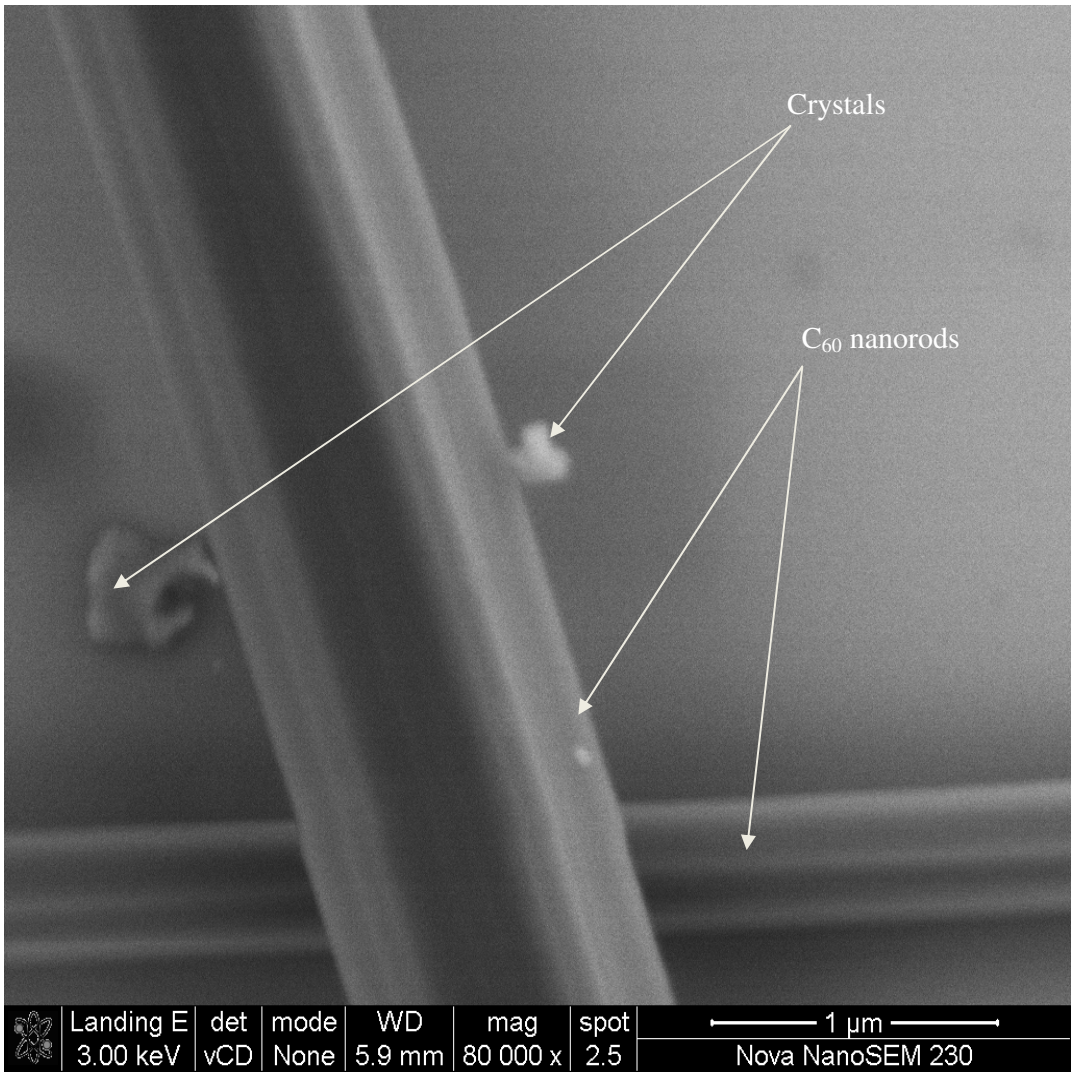

Figure 5. 2: SEM image of C_{60} nanorods on Si (111) substrate irradiated gamma rays at 100 kGy dose.

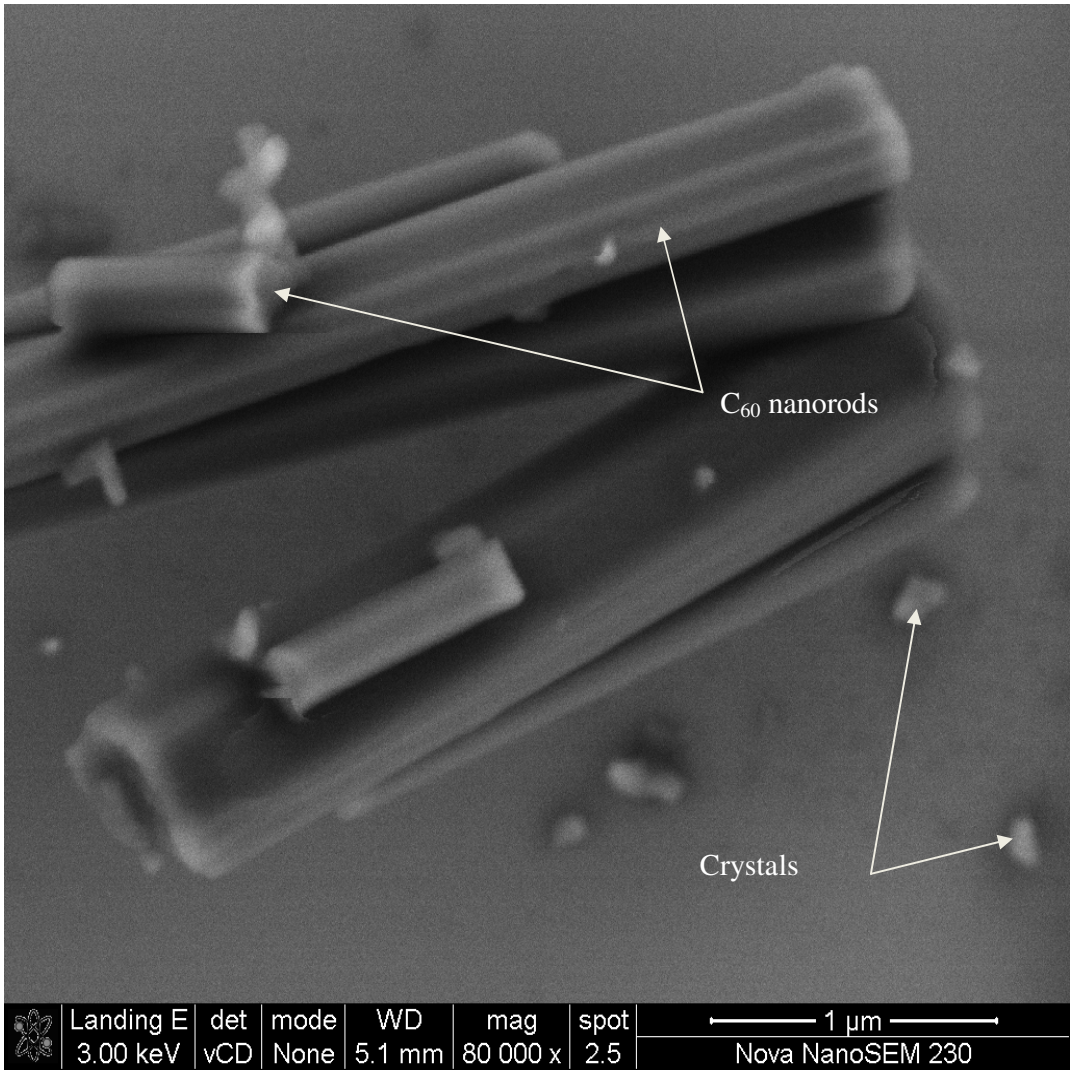

Figure 5. 3: SEM image of C_{60} nanorods on Si (111) substrate irradiated gamma rays at 200 kGy dose.

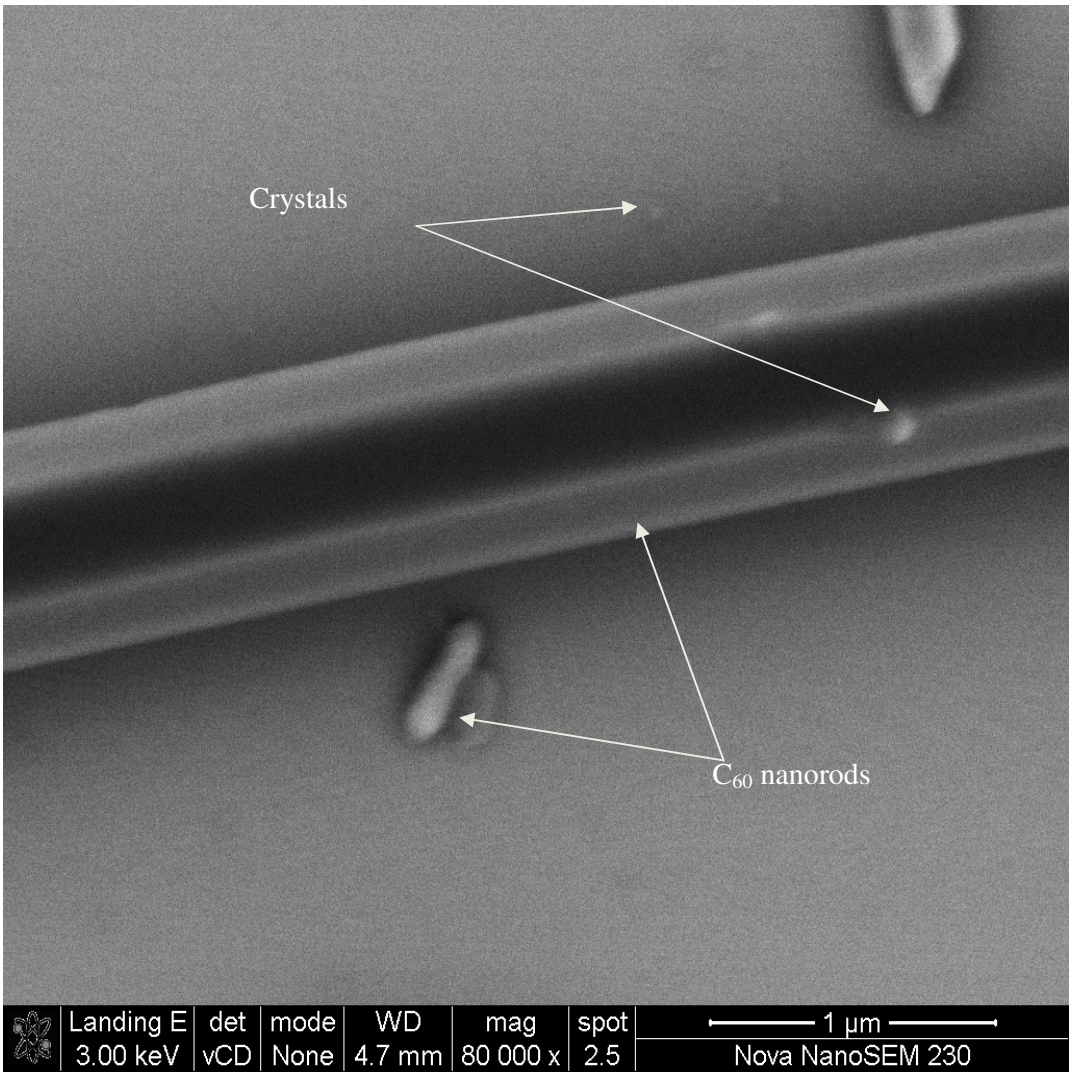

Figure 5. 4: SEM image of C_{60} nanorods on Si (111) substrate irradiated gamma rays at 600 kGy dose

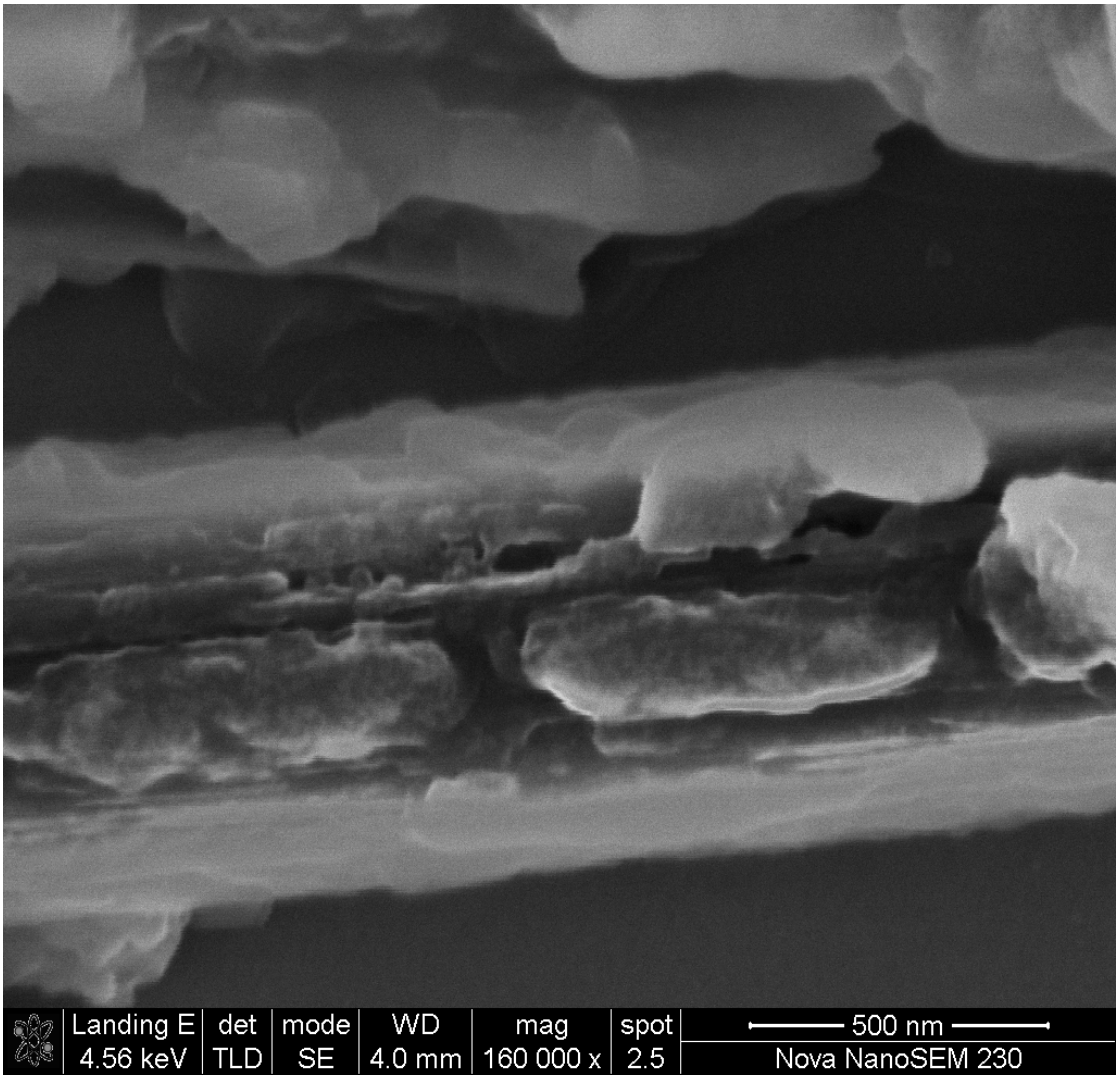

Figure 5. 5: SEM image of C_{60} nanorods on Si (111) substrate irradiated gamma rays at 800 kGy dose.

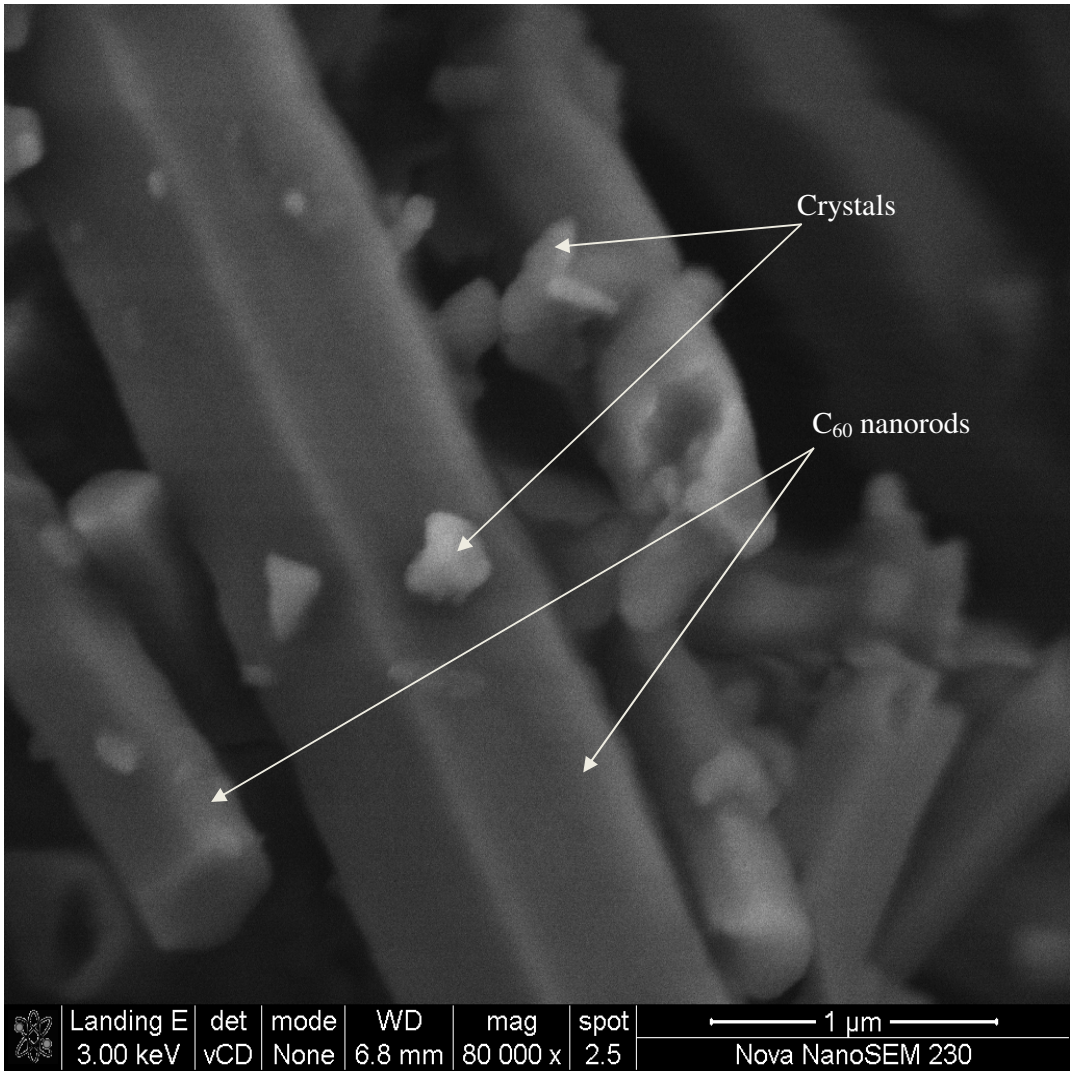

Figure 5. 6: SEM image of C_{60} nanorods on Si (111) substrate irradiated gamma rays at 1 MGy (1000 kGy) dose.

5.3.2. Raman spectroscopy

From the SEM results discussed above, it became clear that structural investigation must be studied at a chemical bond level. Since Raman spectroscopy is a very powerful tool for studying bond vibrations especially for C_{60} nanostructures, therefore it was used to investigate the vibrational mode of the gamma irradiated nanorods.

As mentioned in the previous chapter, C_{60} nanostructure possesses a clear Raman signature which is available in the literature and any change in bonding will be easily recognized. Room temperature measurement was performed on all five different samples under the same operational conditions. Figure 5.7 shows the spectra of non-irradiated and irradiated C_{60} nanorods. All the characteristic modes discussed in chapter 4 (two Ag and eight Hg) are labeled in the figures and are observed in figure 5.11 in the spectral range of 400 - 4000 cm^{-1}.

It is not easy to see any change if the spectra are plotted as in figure 5.7. Furthermore, based on the fact that Ag (2) mode is regarded as a sensor, it is therefore plotted in order to show a clear difference between various fluencies. It is noticeable in figure 5.8 (a) and (b) that there is a variation in Raman shift and intensity. As discussed in chapter 4, Raman spectra indicate the presence of multiple phases resulting in a slightly different Ag (2) mode frequency.

The creation of intermolecular bonds stops the molecular rotation and lowers the overall symmetry of the solid. Any re-organization affects the frequency of the Ag (2) pentagonal pinch mode, which is visible as a downshift of the Ag (2) peak position in the Raman spectrum which is not observed here. It is clear that gamma rays induced reorganization of bonds between individual C_{60} molecules.

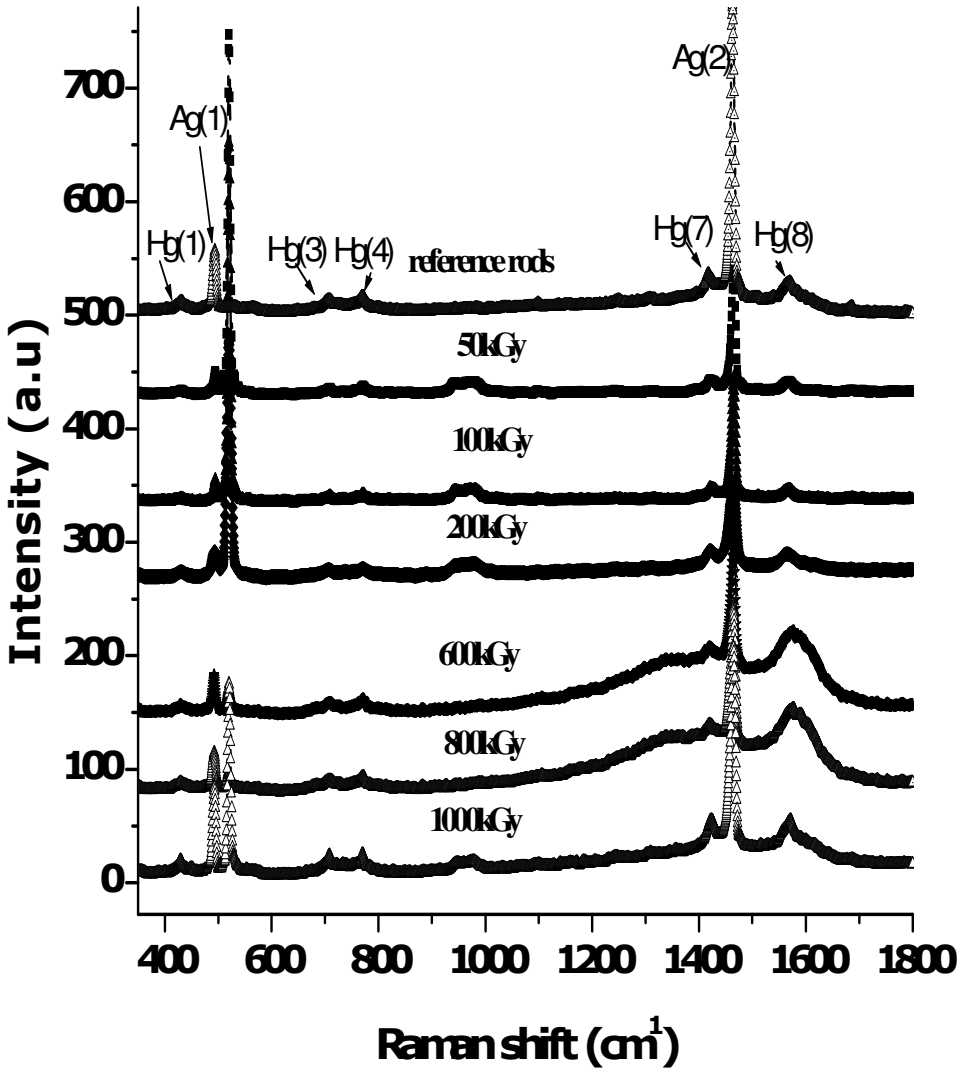

Figure 5. 7: Raman spectra of C_{60} nanorods on Si (111) substrate before and after gamma irradiation at doses ranging from 50 kGy to 1 MGy (1000 kGy).

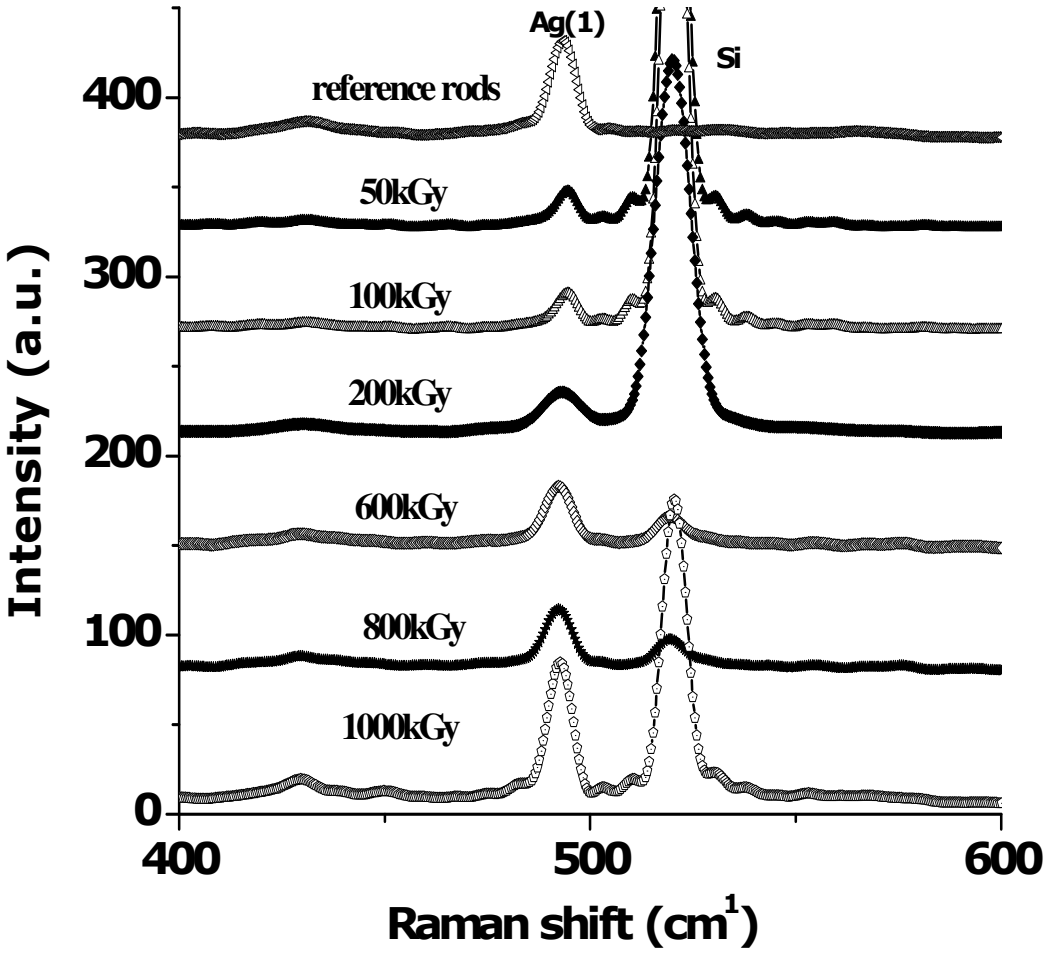

Figure 5. 8 (a): Raman spectra of Ag (1) Raman modes of C_{60} nanorods on Si (111) substrate before and after gamma irradiation at doses ranging from 50 kGy to 1 MGy (1000 kGy).

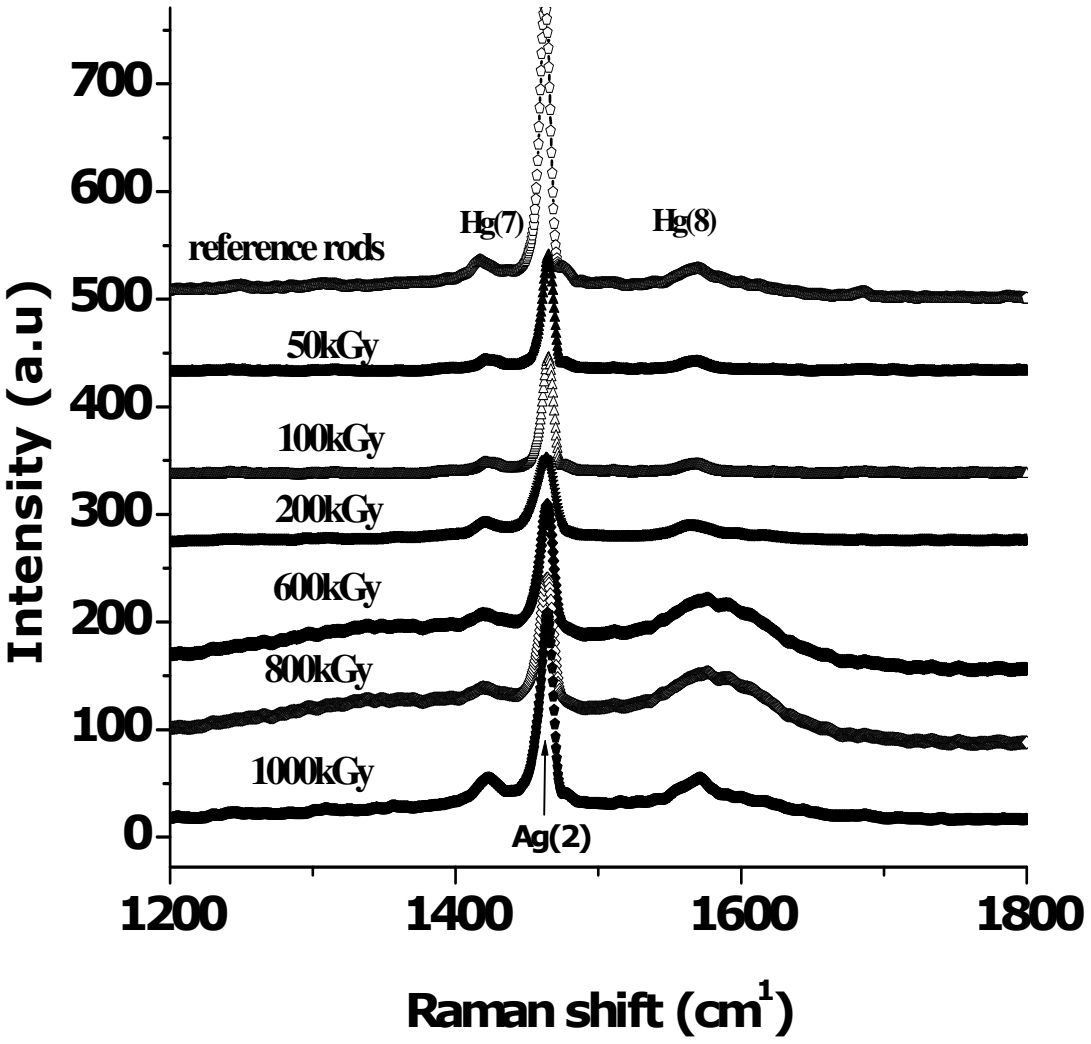

Figure 5. 8 (a-b): Raman spectra of Ag (2) Raman modes of C_{60} nanorods on Si (111) substrate before and after gamma irradiation at doses ranging from 50 kGy to 1 MGy (1000 kGy).

To further analyze these Raman results, only sensitive Raman modes of C_{60} (Ag (1) and Ag (2)) modes were extracted and fitted using Lorenzian model and the data is shown in table 5.1 and plotted in figures 5.9 to 5.10.

Table 5. 1: Position, FWHM and relative intensity of Ag (1) and Ag (2) modes.

	Ag(1)			Ag(2)		
Irradiation fluence (kGy)	ω(cm^{-1})	FWHM (cm^{-1})	Rel. int.	ω (cm^{-1})	FWHM (cm^{-1})	Rel. int.
0	493.39	9.0927	65.918	1462.5	9.9453	304.28
50	494.28	7.3592	21.424	1464.6	9.6847	116.03
100	494.28	7.5239	21.792	1464.5	9.8117	117.59
200	493.4	12.226	23.036	1462.8	15.983	78.949
400	491.61	10.201	40.748	1459.1	23.417	69.681
600	492.22	9.1237	38.53	1463.5	10.88	123.89
800	492.22	9.0972	38.444	1463.6	10.8	122.76
1000	492.62	9.1473	102.31	1463.7	10.802	186.71

In figure 5.9, it can be seen for the initial two doses (50 kGy and 100 kGy) that there is no change of peak position. This observation can be attributed to the fact that at low dose there is minimum energy deposited on the nanorods which cannot alter the bonding configuration. As the dose increases, there is a shift clearly observed to lower values. Further increment leads to a threshold which occurs at 400 kGy. Above the threshold the structure is regained and this is observed by the minimum difference between the last three high doses (600 kGy, 800 kGy and 1000 kGy).

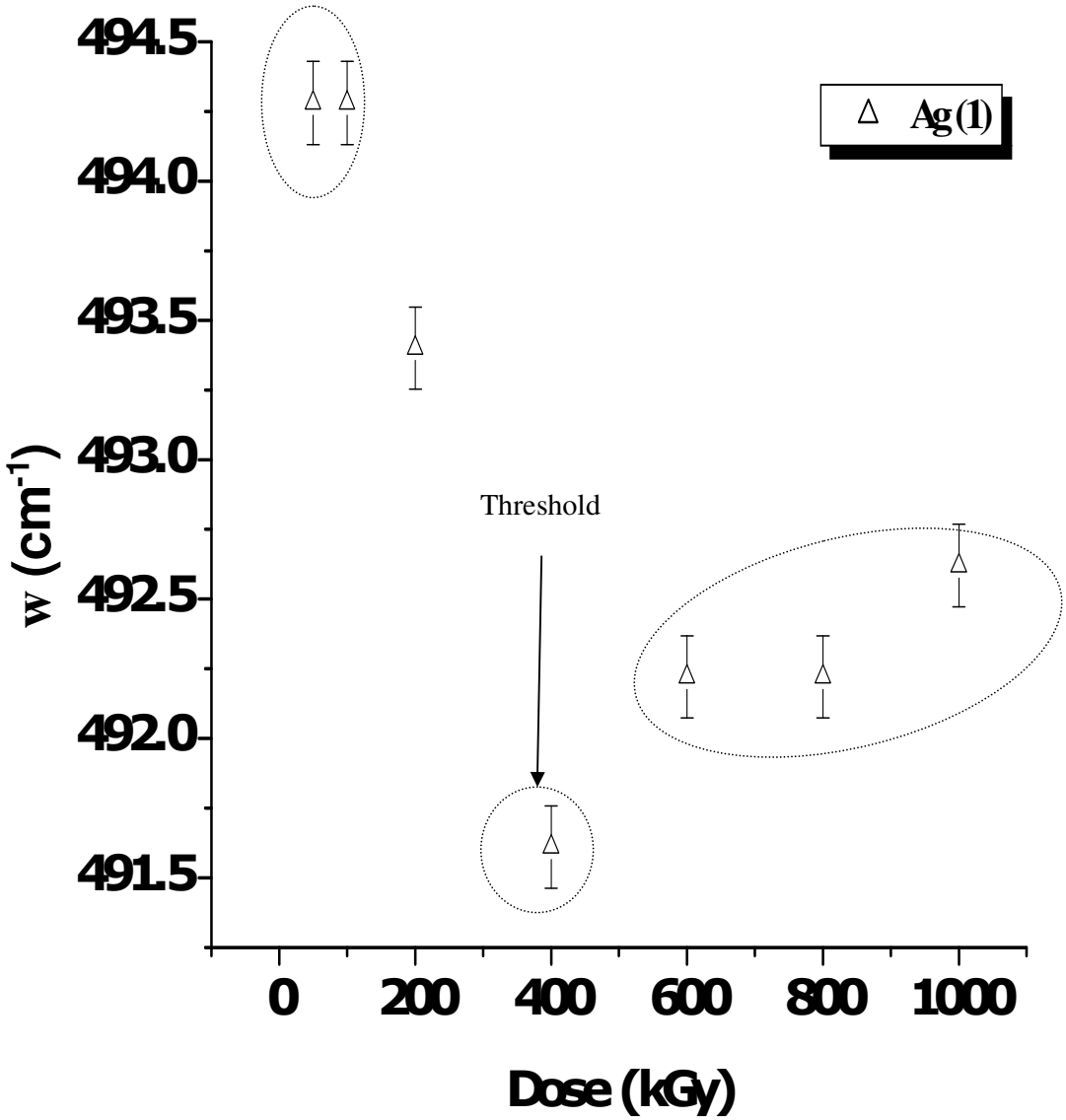

Figure 5.9: (a) Variation of the Raman shift vs. irradiation dose for Ag (1) mode of irradiated C_{60} nanorods on Si (111).

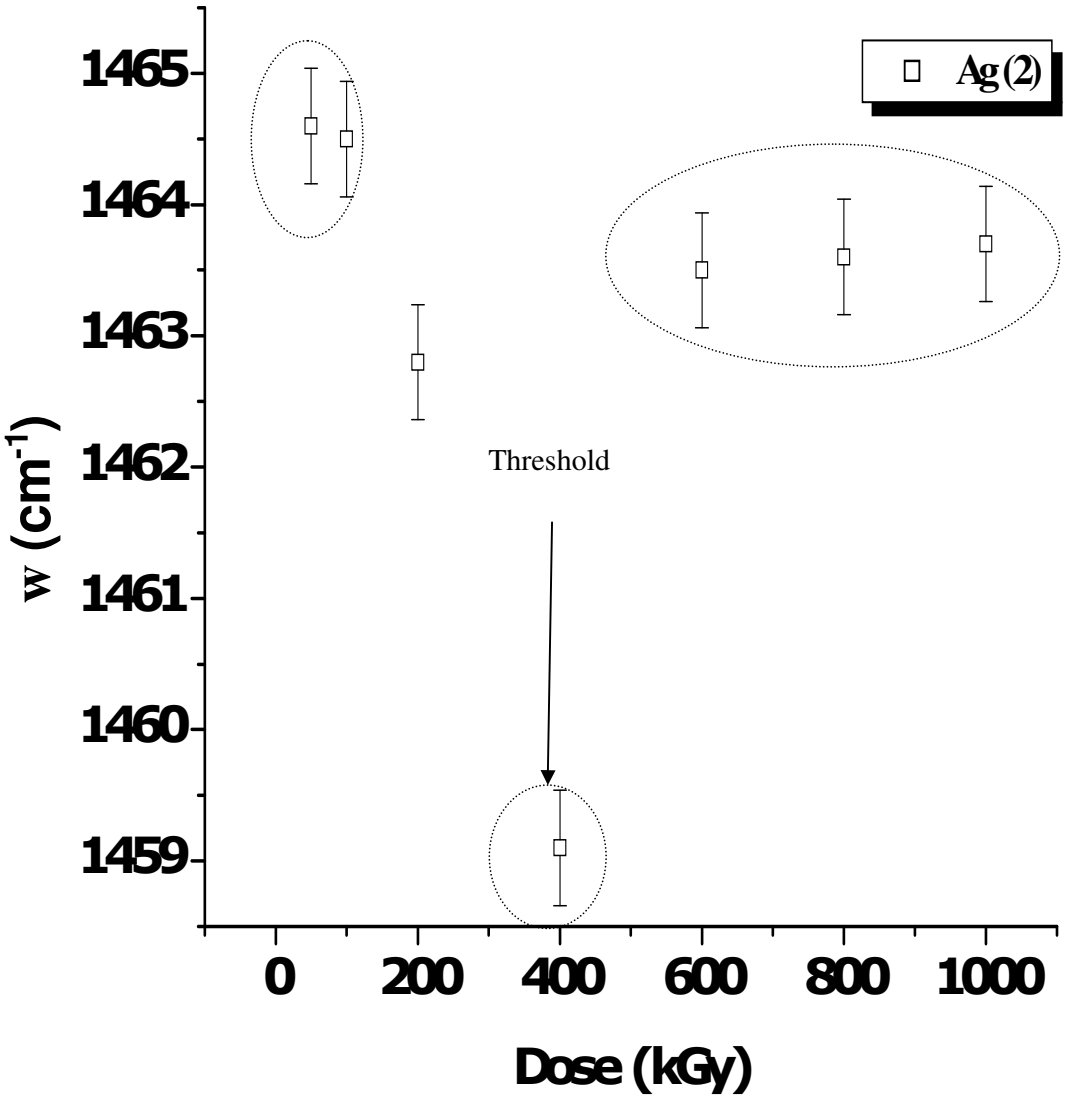

Figure 5. 9 (a-b): Variation of the Raman shift vs. irradiation dose for Ag (2) mode of irradiated C_{60} nanorods on Si (111).

In figure 5.10, one can observe the variation of intensity with increasing dose. At low doses (50 kGy, and 100 kGy), the intensity is stable but as the dose increases it starts to change until it becomes stable again at the high doses (600 kGy and 800 kGy). This observation can

be attributed to the stable phase of the nanorods formed after irradiation. As the dose increases further, the intensity increases again which means there is a change in the structure. So, one can expect this variation as the dose increases especially in Ag (1) sensor mode as indicated in figure 5.10 (a).

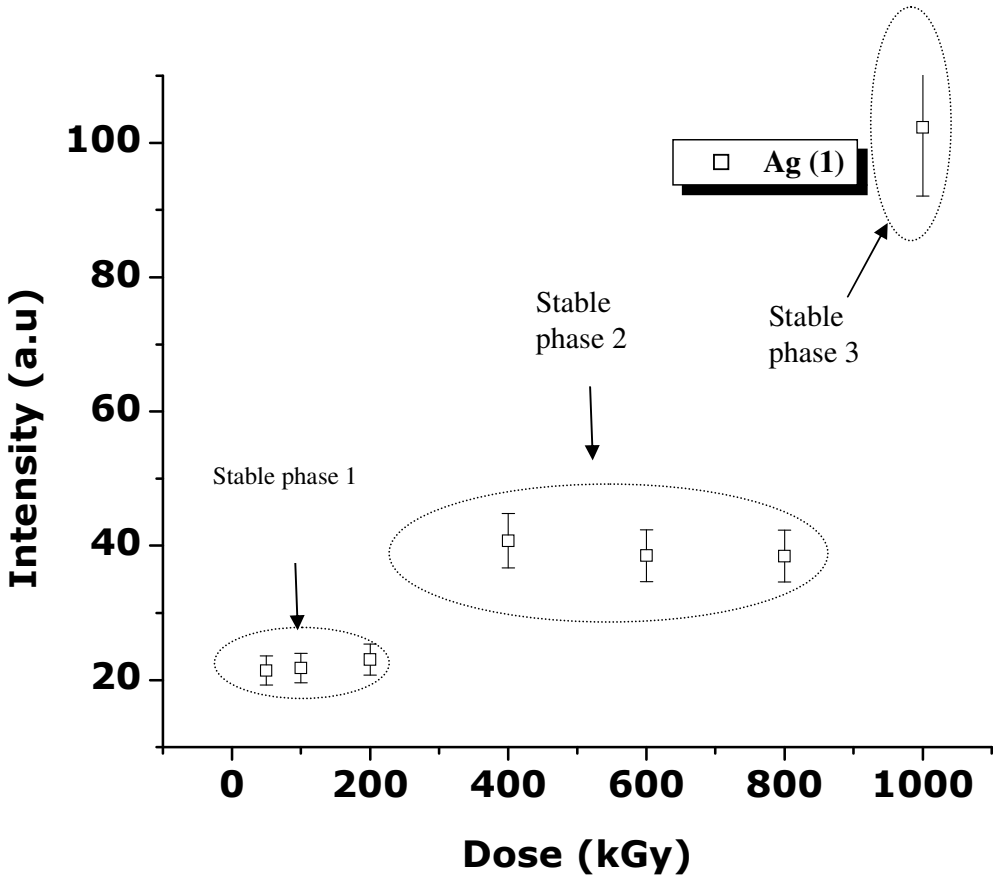

Figure 5. 10: (a) Variation of the intensity versus irradiation dose for Ag (1) mode of irradiated C_{60} nanorods on Si (111).

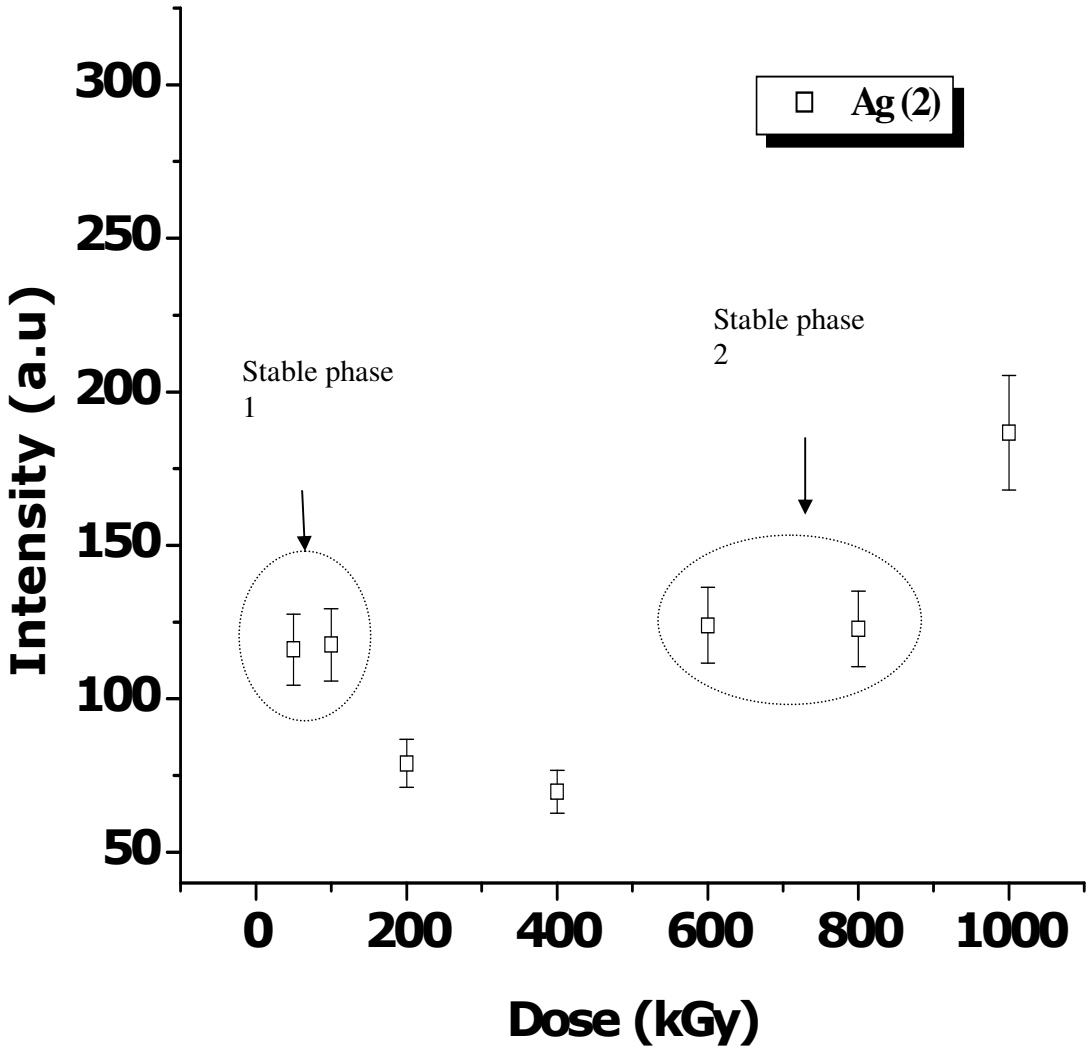

Figure 5. 10 (a-b): Variation of the intensity versus irradiation dose for Ag (1) mode of irradiated C_{60} nanorods on Si (111).

In figure 5.11(a) and 5.11(b), two regions are observed, low dose region and high dose region. At low dose (50 kG y and 100 kGy), there is a very small shift of FWHM. This is the region whereby the reorganization is minimal, hence a small shift. As the dose increases, the threshold is achieved at 200 kGy followed by a smooth exponential decay and saturates at high dose (1000 kGy). This phenomenon explains the concept of reorganization whereby at low dose there is minimal reorganization but more bonds breaking which is followed by saturation at a threshold. After the threshold, the reorganization process begins up to saturation.

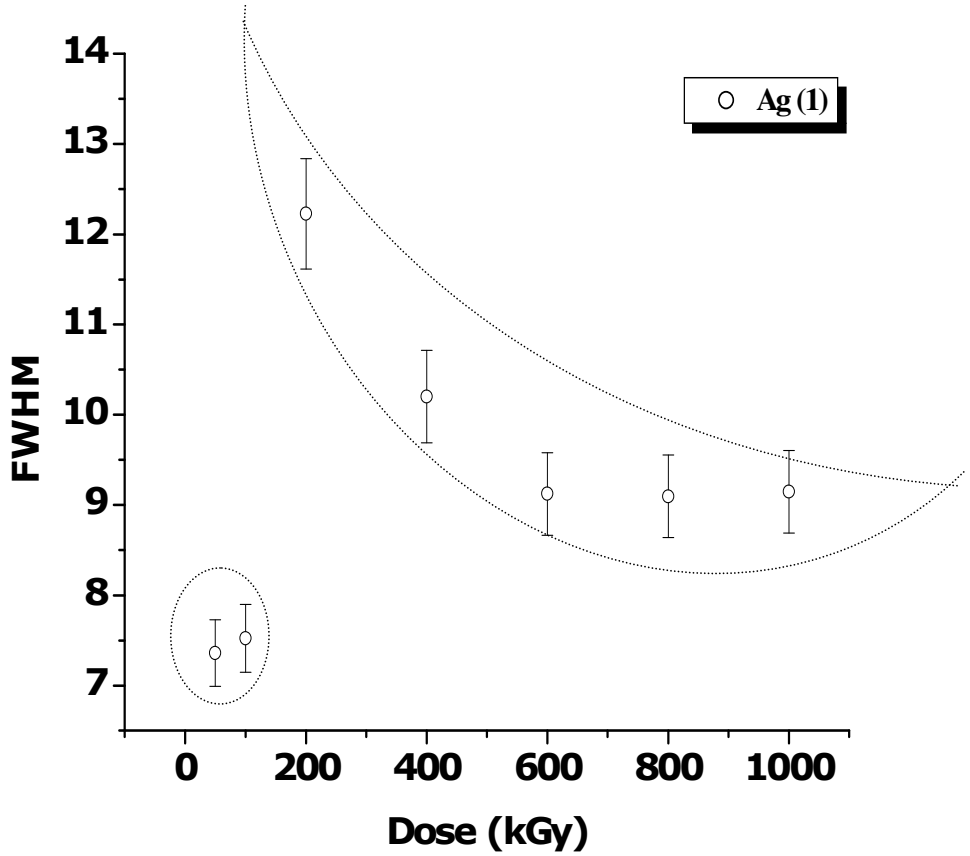

Figure 5.11 (a-b): Variation of the FWHM vs. irradiation dose for Ag (1) mode of irradiated C_{60} nanorods on Si (111).

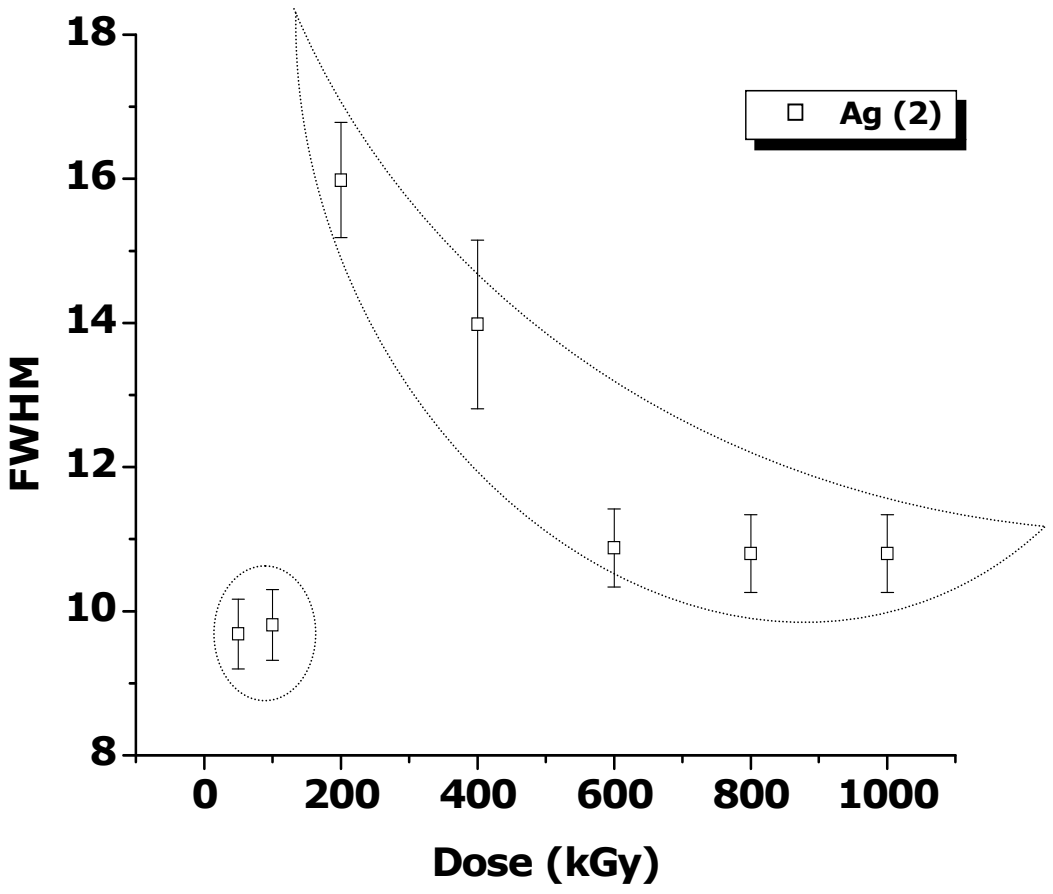

Figure 5.12 (b): Variation of the FWHM vs. irradiation dose for Ag (2) mode of irradiated C_{60} nanorods on Si (111).

Furthermore, this variation suggests the reorganization of bonds inside the structure of individual nanorods. It cannot be confirmed using these results only but further investigation is needed. These results only form the basis of what could be expected in the investigation of this nature. Any re-organization affects the frequency of the Ag (2) pentagonal pinch mode, which is visible as a downshift of the Ag (2) peak position in the Raman spectrum. Although we observed a change in Ag (2) mode, the structure is regained as the dose is increased further. This suggests that as the gamma rays interacts with the nanorods; there is

reorganization of bonds between individual C_{60} molecules. The background observed in the spectra is due to the Raman influence.

5.3.3. FT-IR spectroscopy

Although Raman is a very good analytical technique to study C_{60} nanorods as emphasized in the above discussion, it cannot be conclusive on its own without other complementary technique. Therefore, Fourier transform infra-red (FTIR) spectroscopy was used to complement Raman spectroscopy. The results of Fourier transform infra-red (FTIR) spectroscopy measurements on non-irradiated and irradiated samples are shown in figure 5.16.

As discussed in chapter 4, characteristic IR active modes of C_{60} are expected to appear at 524 cm^{-1} (t1u (1)), 573 cm^{-1} (t1u (2)), 1428 cm^{-1} (t1u (4)), and 1182 cm^{-1} (t1u (3)). The two of them do appear 1428 cm^{-1} (t1u (4)), 1182 cm^{-1} (t1u (3)) but the other two do not appear as shown in figure 5.17 indicating the absence of radial motion. Furthermore, the disappearance of these two peaks indicates the suppression of the radial vibration. The dose dependence of FTIR spectra of C_{60} nanorods irradiated with gamma rays is observed especially at 50 kGy and 200 kGy. The pentagonal pinch mode appearing at 1426 cm^{-1} is the most sensitive band for the orientation ordering transition. One can see that there is a change induced by gamma rays but at minimal. So, the reorganization of bonds is not clear in this case unlike in the proton experiment. Furthermore, no new absorption bands and frequency shifts were found in the IR spectrum except a small deviation from the pristine C_{60} powder which is due to the formation of nanorods. This indicates that the C_{60} nanorods consisted of polymerized pristine C_{60} and the solvents used were totally evaporated.

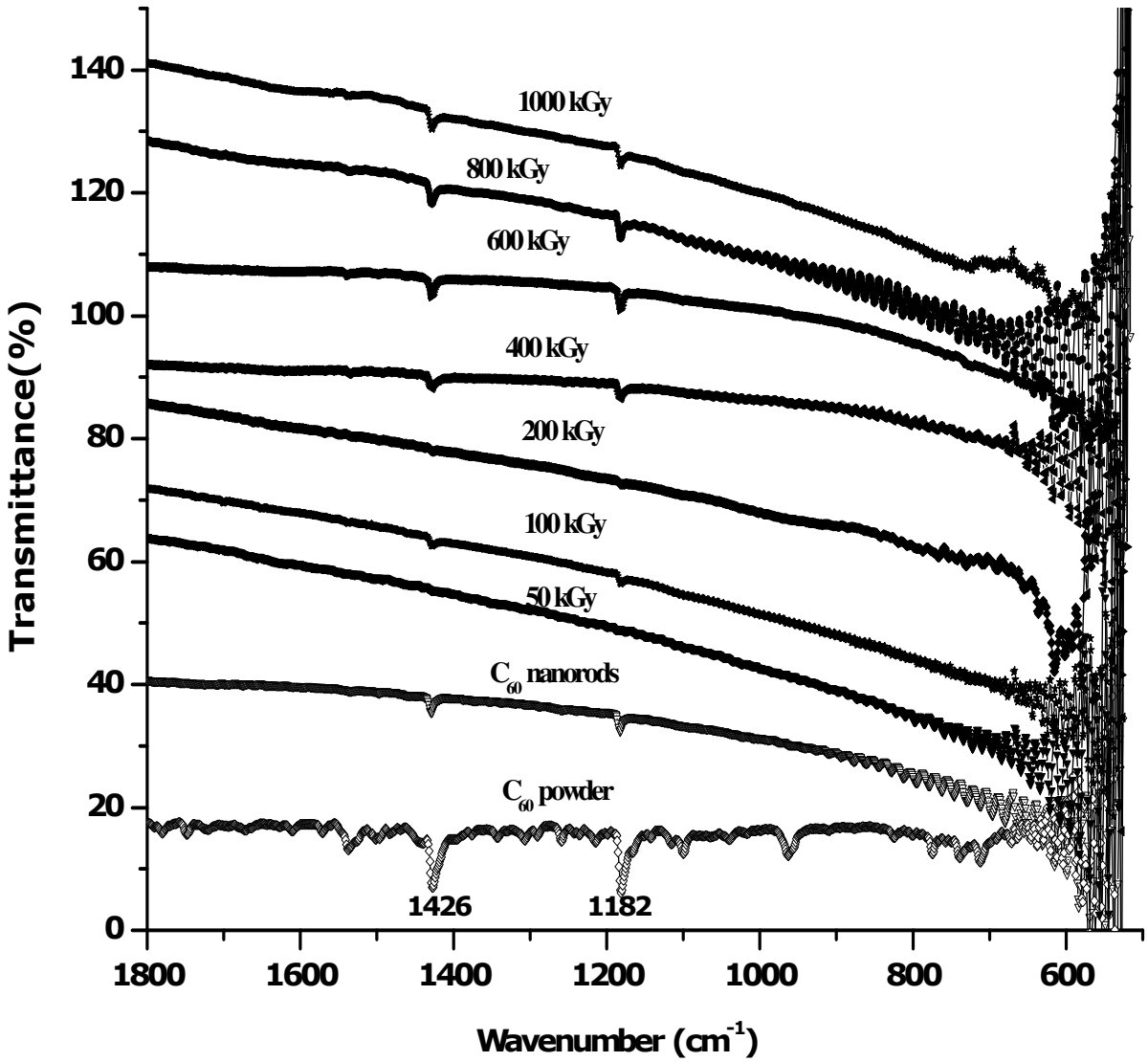

Figure 5. 12: FTIR spectra of pristine C_{60}, non-irradiated and irradiated fullerene C_{60} nanorods,

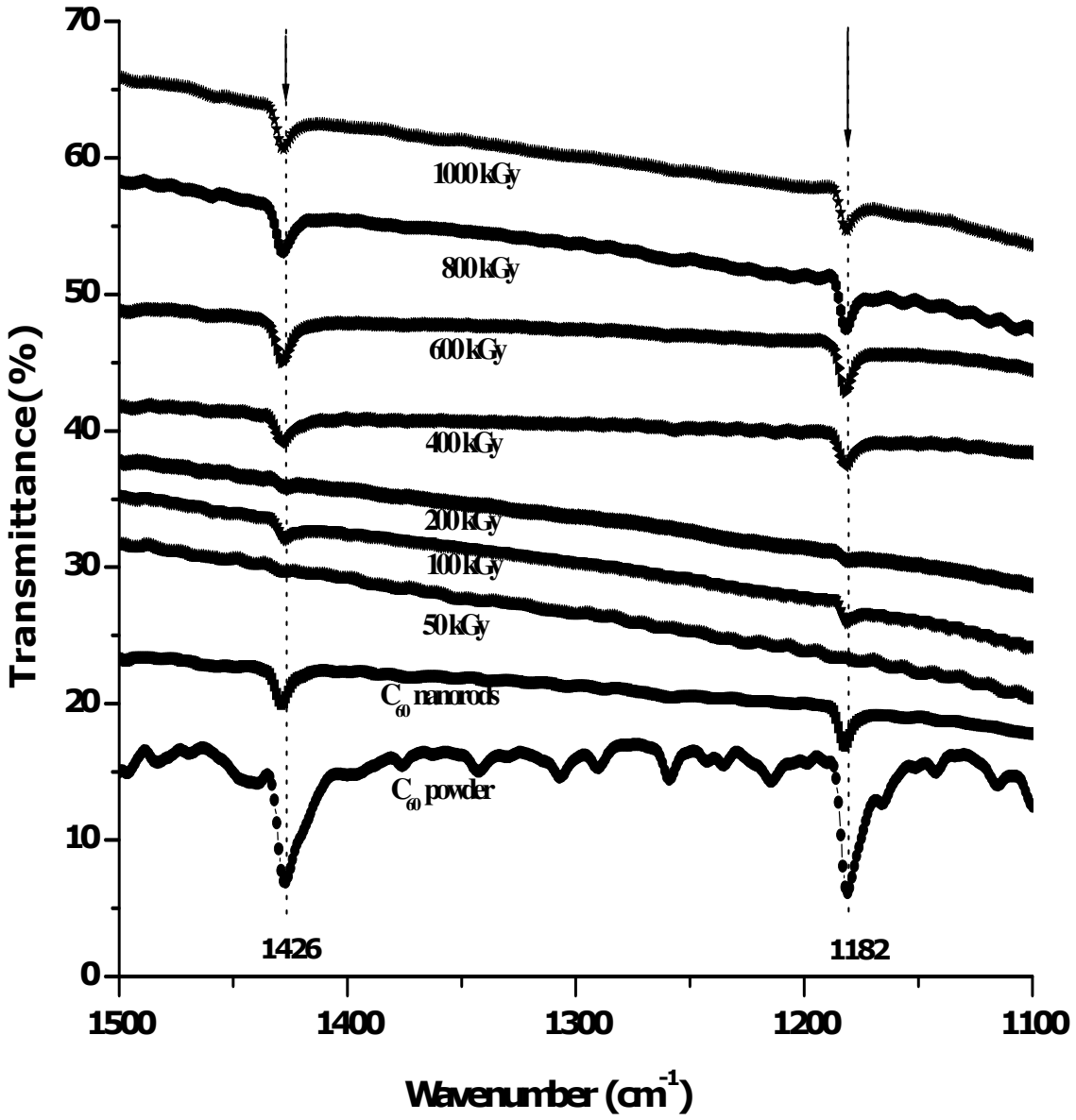

Figure 5. 13: FTIR spectra of pristine C_{60}, non-irradiated and irradiated fullerene C_{60} nanorods showing shift due to the formation of nanorods

5.4. References

[1] **Krasheninnikov, A.V., and Banhart, F.,** *Nature materials* 6, 2007

[2] **Saito, R., et al.,** *Applied Physics Letters* 60, 2204, 1992.

[3] **Mintmire, J. W., et al.,** *Physical Review Letters* 68, 631, 1992.

[4] **Schluter, M., et al.,** *Physical Review Letters* 68, 526, 1992.

[5] **Hamada, N., et al.,** *Physical Review Letters* 68, 1579, 1992.

[6] **Dubey, K. A., Bhardwaj, Y. K., Chaudhari, C. V., Kumar, V., Goel, N. K., Sabharwal, S.,** Radiation processed ethylene vinyl acetate-multiple walled carbon nanotube nano-composites: Effect of MWNT addition on the gel content and crosslinking density, *eXPRESS Polymer Letters* 3, 8, 492–500, 2009.

[7] **Vitusevich, S. A., Sydoruk, V. A., Petrychuk, M. V., Danilchenko, B. A., Klein, N., Offenhäusser, A., Ural, A., and Bosman, G.,** Transport properties of single-walled carbon nanotube transistors after gamma radiation treatment, *Journal of Applied Physics* 107, 063701, 2010.

[8] **Hulman, M., Skákalová, V., Roth, S., Kuzmany, H.,** Raman spectroscopy of single-wall carbon nanotubes and graphite irradiated by rays, *Journal of Applied Physics* 98, 024311, 2005.

[9] **Gupta, S., Scuttler, A. M., and Farmer, J.,** Novel nanocarbon hybrids of single-walled carbon nanotubes and dispersed nanodiamond: Structure and hierarchical defects evolution irradiated with gamma rays, *Journal of Applied Physics* 107, 104308, 2010.

[10] **Xu, Z., Min, C., Chen, L., Liu, L., Chen G., and Wu, N.,** Modification of surface functionality and interlayer spacing of multi-walled carbon nanotubes using c-rays, Journal of *Applied Physics* 109, 054303, 2011.

[11] **Gupta, S., and Farmer, J.,** Multiwalled carbon nanotubes and dispersed nanodiamond novel hybrids:Microscopic structure evolution, physical properties, and radiation Resilience, *Journal of Applied Physics* 109, 014314, 2011.

[12] **Gupta, S., Weiss, B. L., Weiner, B. R., Pilione, L., Badzian, A., Morell, G.,** Electron field emission properties of gamma irradiated microcrystalline diamond and nanocrystalline carbon thin films, *Journal of Applied Physics* 92, 6, 2002.

[13] **Savopulo, M., and Burakov, B. E.,** Development, Fabrication and Study of Fullerene-Containing Carbon Material (FCC) for Immobilization of Iodine, Progress Reports #1-1 and #1-2, UNLV – KRI-KIRSI Agreement 280203-1, Research-Industrial Enterprise "KIRSI", branch of the V.G. Khlopin Radium Institute (KRI).

[14] **Miyazawa, K., Minato, J., Yoshii, T., and Suga, T.,** Characterization of fullerene nanotubes prepared by the liquid–liquid interfacial precipitation method, *Science and Technology of Advanced Materials* 6, 388–393, 2005.

CHAPTER 6

NEUTRON RADIATION

Abstract

Carbon-based materials are being widely used in nuclear reactors, because of their favourable properties, especially with respect to their thermal shock resistance. However, the significant effects resulting from neutron irradiation on the thermal-physical, mechanical properties and on the tritium trapping capacity could preclude the utilization of carbon as a plasma facing material in forthcoming devices. Therefore, the effects of neutron irradiation are of primary concern in the use of carbon materials in the next step devices. Due to the fact that other carbon based materials have been studied extensively and fullerene molecule has not been studied under harsh conditions of nuclear reactor. The neutron irradiation effects on fullerene nanorods were studied. This chapter is focused on investigation of physical effects of fast neutrons on C_{60} nanorods.

6.1. Introduction

Carbon-based materials are used extensively in experimental fusion energy reactors for plasma facing components. They are an attractive choice because of their superior thermal shock resistance, and low neutron activation. Consequently, the effect of neutron flux on the components has been a cause of concern in nuclear reactors. Properties of carbon-carbon composite materials can be evaluated as alternative components in the nuclear reactors. A great deal of research has been conducted on the effect of neutron irradiation on some other carbon-based materials but not much has been done on the fullerenes.

It was reported that neutron irradiation in carbon-based material produces radiation-induced defects and changes in the microstructure. In some cases this lead to a change in the chemical composition of the materials due to transmutation and as a result, changes in physical and mechanical properties [1-3]. Koizlik et al did experiment on neutron irradiation test matrix for carbon-based materials for the first wall of fusion reactors and reported that neutron irradiation induced reductions in the thermal conductivity of two, three-directional carbon–carbon composites and there is a recovery of thermal conductivity due to thermal annealing. The main reason is the formation of the radiation defects, which act as obstacles for the phonon propagation. The size and concentration of the radiation defects depends on irradiation temperature and fluence and, as a result, the thermal conductivity also depends on these parameters. An increase of the neutron fluence leads to a decrease in the thermal conductivity [4-6]. Maruyama and Harayama, reported on neutron irradiation effect on the thermal conductivity and dimensional change of graphite materials such as fine-grained isotropic graphites, a carbon/carbon composite material, glassy carbon and bulk-boronized graphites. They found that the neutron irradiation reduces the thermal conductivity of the graphite materials, and that the materials irradiated under the same irradiation condition had the same magnitude of thermal conductivity [7,8].

Similar observation was reported by Wu et al in their study on the investigations of the effects of neutron irradiation on the thermal-physical, mechanical properties and tritium retention behaviour of various graphites and carbon/carbon fiber composites for the doses of 10^{-3} and irradiation temperatures of 200–1500°C [9,10]. Wu et al also did an experiment on the effect of high-dose neutron irradiation on the properties of graphite and silicon carbide and found that neutron irradiation induced swelling, changes in thermal and mechanical properties of two different ultrafine grain isotropic polygranular graphites and two grades of silicon carbides [11-13].

Bonal et al reported on neutron induced dimensional change in carbon materials at high temperatures and high damage doses. These changes are due to the fact that neutron irradiation leads to formation of the displaced carbon atoms, which form the dislocation loops and additional graphite planes at specific irradiation conditions. These cause the extension of the graphite crystal in the z-direction [14-17]. Atsumi, et al reported on hydrogen behaviour in carbon-based materials and its neutron irradiation effect and found that after neutron irradiation at 1.9×10^{24} n/m^2 (~ 0.2 dpa), the hydrogen retained becomes 20–50 times a

larger than that of non-irradiated samples. Hydrogen atoms will be trapped at dangling carbon bonds at edge surfaces of crystallite which are thermally stable even at high temperatures above 1000°C [18].

When it comes to C_{60} irradiated with neutrons there is not enough body of knowledge available in the literature, only T. Kubo et al studied the effect of fast neutron irradiation of fullerene superconductor Rb_3C_{60} at neutron fluences 1.0×10^{16} n/cm^2, 1.8×10^{16} n/cm^2 and 3.3×10^{16} n/cm^2, and the post-annealing was made at a temperature of 473 K for 3 h. They observed the loss in superconductivity in Rb_3C_{60} powder when the neutron irradiation fluence exceeds 1.0×10^{16} n/cm^2, and the lost superconductivity was completely recovered by the post-annealing at 473 K for 3 h [19].

6.2. Experiment details

C_{60} nanorods were grown on Si (111) substrate by using a low cost method called liquid-liquid interfacial polymerization method as previously discussed in chapter three [14]. Neutron irradiated was carried out in a reactor with reactor source of 15 MW, IB of 0.01A by exposing the samples to neutrons at a dose ranging from 3.2×10^{17} neutrons.cm^{-2} to 1.6×10^{18} neutrons.cm^{-2}. The GAXRD patterns were recorded using Philips X'PERT PRO MPD model at grazing incidence angle ($\theta = 0.3°$).

6.3. Results and discussion

6.3.1. Optical microscope

Figure 6.1 shows optical images taken after the samples were prepared as described in chapter 3 and taken out to be dried in air before irradiated by neutrons with fluences ranging from 6.4×10^{17} n/cm^2 to 1.6×10^{19} n/cm^2. Figure 6.2 - 6.4 show optical images after irradiated with neutrons at various fluencies as mentioned above. According to these results, it seems that at a moderate fluence the nanorods are still preserved but as the fluence is increased they tend to disintegrate into small pieces. This is due to the fact that at higher fluence, a maximum kinetic energy of about 570 keV can be transferred from fast neutrons of 2 MeV to carbon nucleus via elastic collision. These ions displace in the sample and produce

a large cascade of multiple displacements. So, C_{60} nanorods cannot stand for higher neutron fluencies.

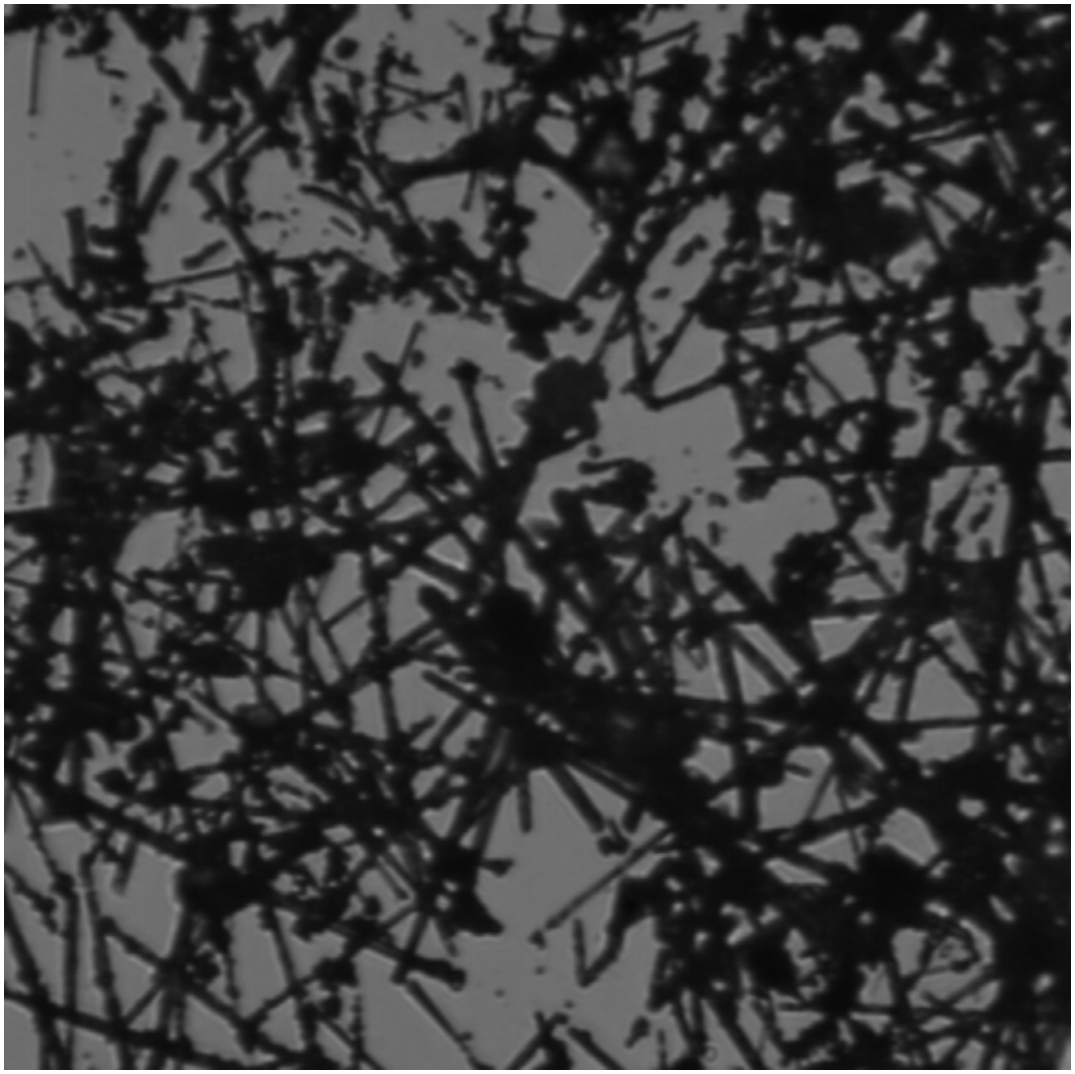

Figure 6.1: Optical microscopy image of nanorods of fullerene C_{60} on a Si (111) substrate before neutron irradiation.

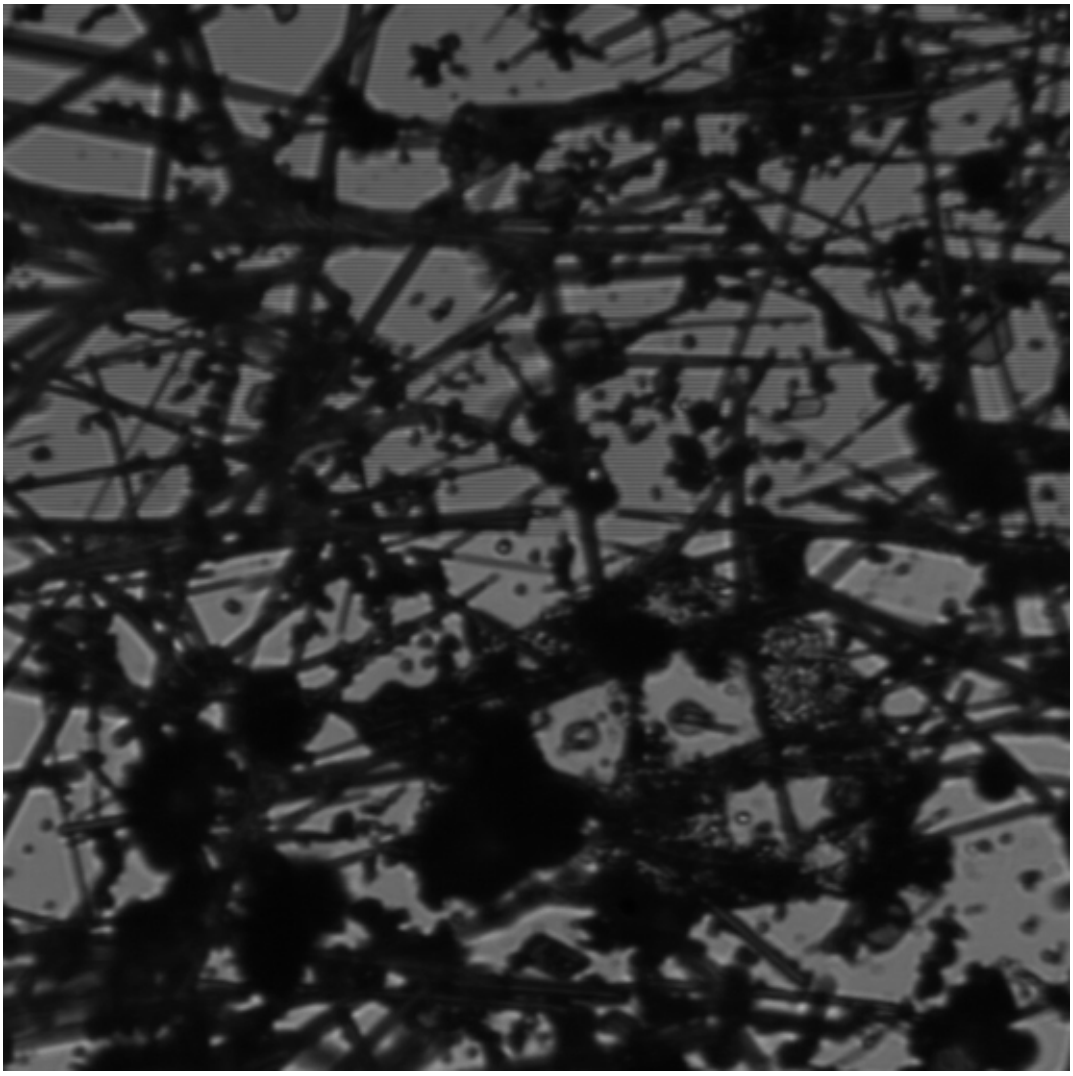

Figure 6.2: Optical microscopy image of nanorods of fullerene C_{60} on a Si (111) substrate after neutron irradiation at 3.6×10^{17}n/cm^2.

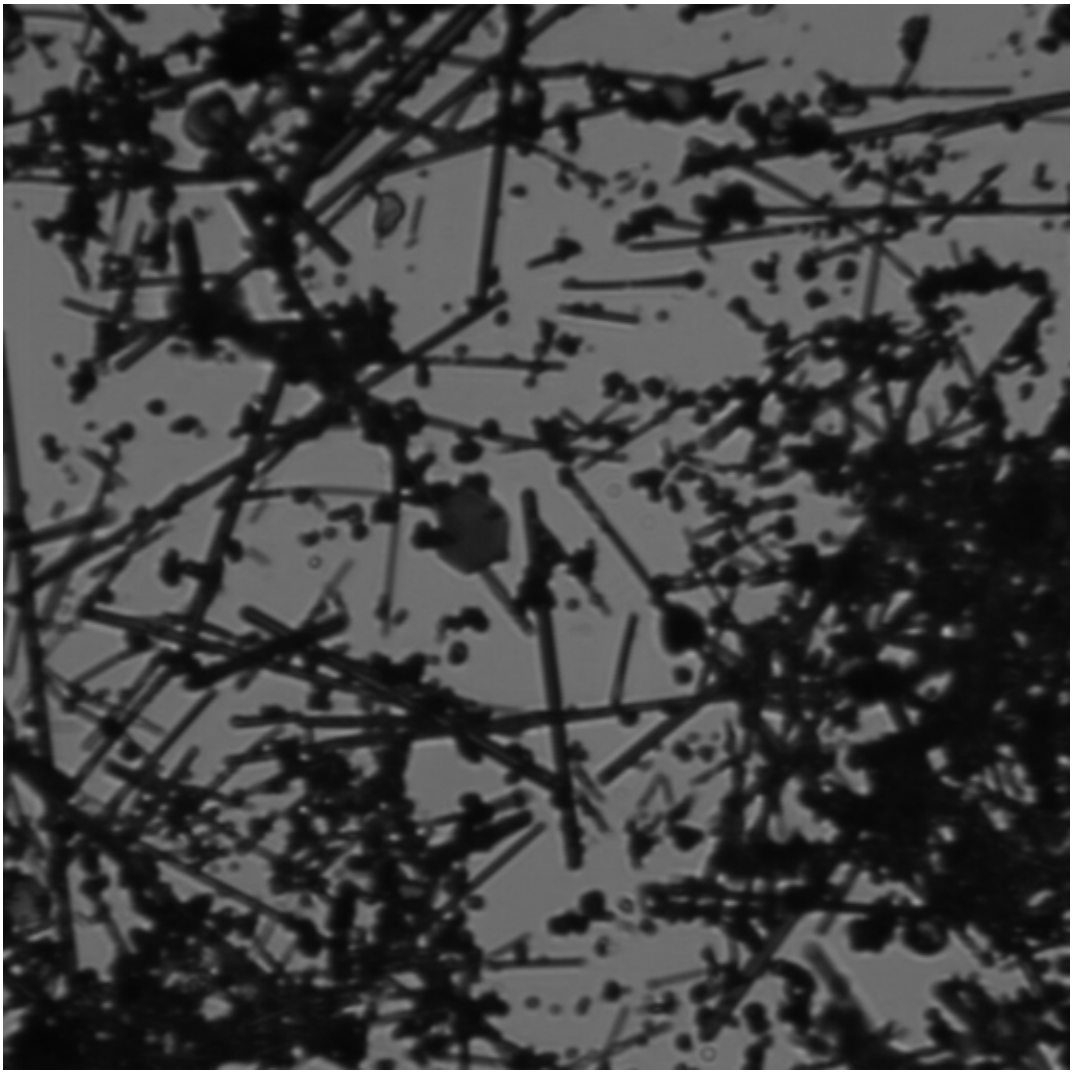

Figure 6.3: Optical microscopy image of nanorods of fullerene C_{60} on a Si (111) substrate after neutron irradiation at 9.6×10^{17}n/cm^2.

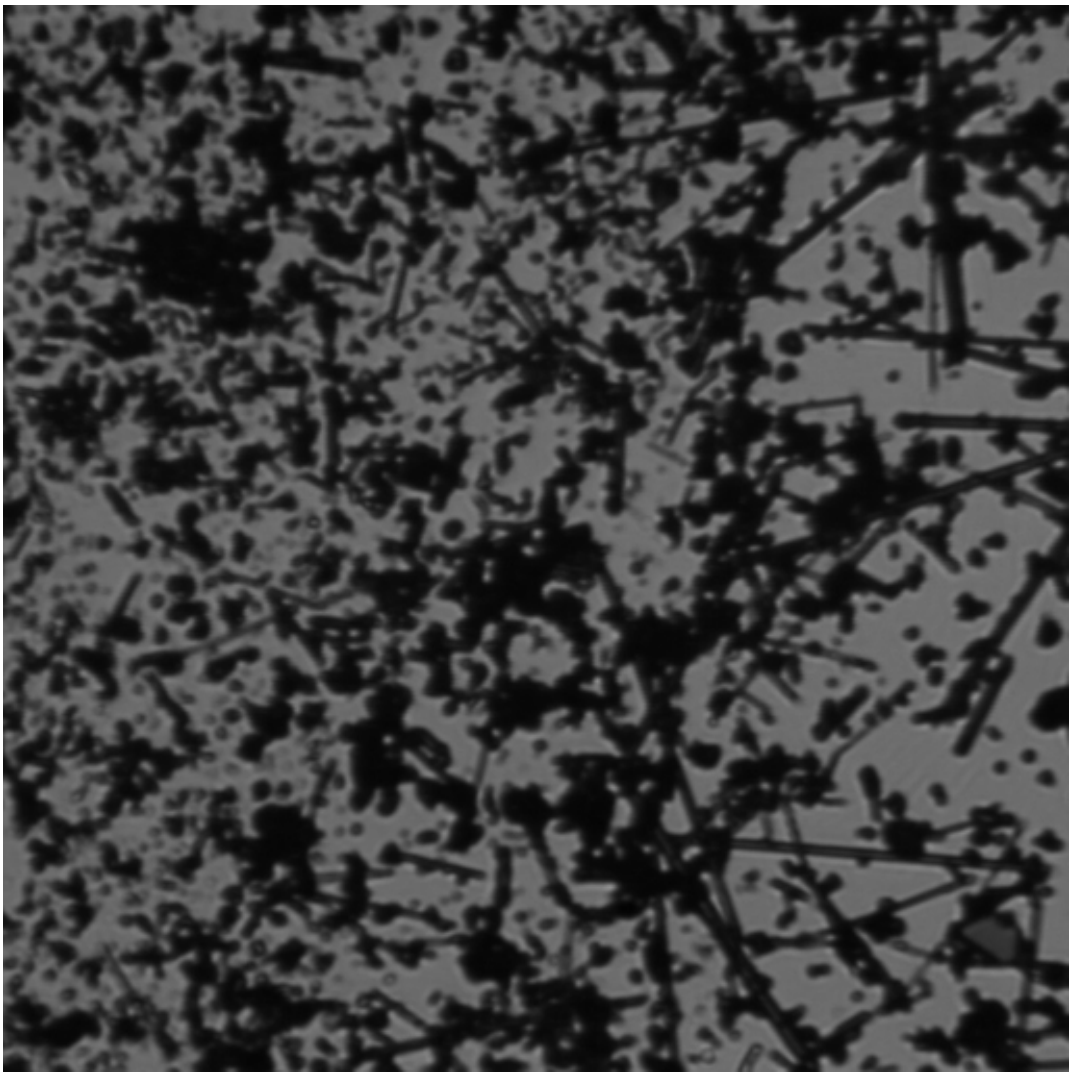

Figure 6.4: Optical microscopy image of nanorods of fullerene C_{60} on a Si (111) substrate after neutron irradiation at 1.6×10^{18}n/cm^2.

6.3.2. Grazing X-ray diffraction analysis (GAXRD)

The GAXRD analysis of the samples before and after irradiation is presented in figures 6.5-6.7. The GAXRD patterns are recorded at grazing incidence angle (θ = 0.3°). All characteristic XRD peaks of fullerene C_{60} are clearly observed from 8° to 35°. With increasing fast neutrons fluences (indicated in the figures) one can see the following: At lower fluences (< 6.4 $x10^{17}$ n/cm^2), the intensity of all the peaks decreases little bit and the peak at 2 θ = 51.14° disappears. After being irradiated at 9.6 $x10^{17}$ n/cm^2, the peak (111) intensity increase and the peak at 2 θ = 51.14° reappear again as shown in figure 6.8. Whereas the other peaks intensity decreases, at higher fluence (> 1.6 $x10^{18}$ n/cm^2), the peak (111) intensity decreases and the peak at 2 θ = 51.14 ° become dominant. According to these results, it seems that at a moderate fluence, (between 6.4 $x10^{17}$ and 9.6 $x10^{17}$ n/cm^2), the crystallite with (111) direction increases as shown in figure 6.8 - 6.10. The same results are also observed in other thin films where the crystallinity increases with irradiation. But at higher fluence, a maximum kinetic energy of about 570 keV can be transferred from fast neutrons of 2 MeV to carbon nucleus via elastic collision. These ions displace in the sample and produce a large cascade of multiple displacements. These defects destroy the crystallinity and probably induce the breaking of the carbon rods.

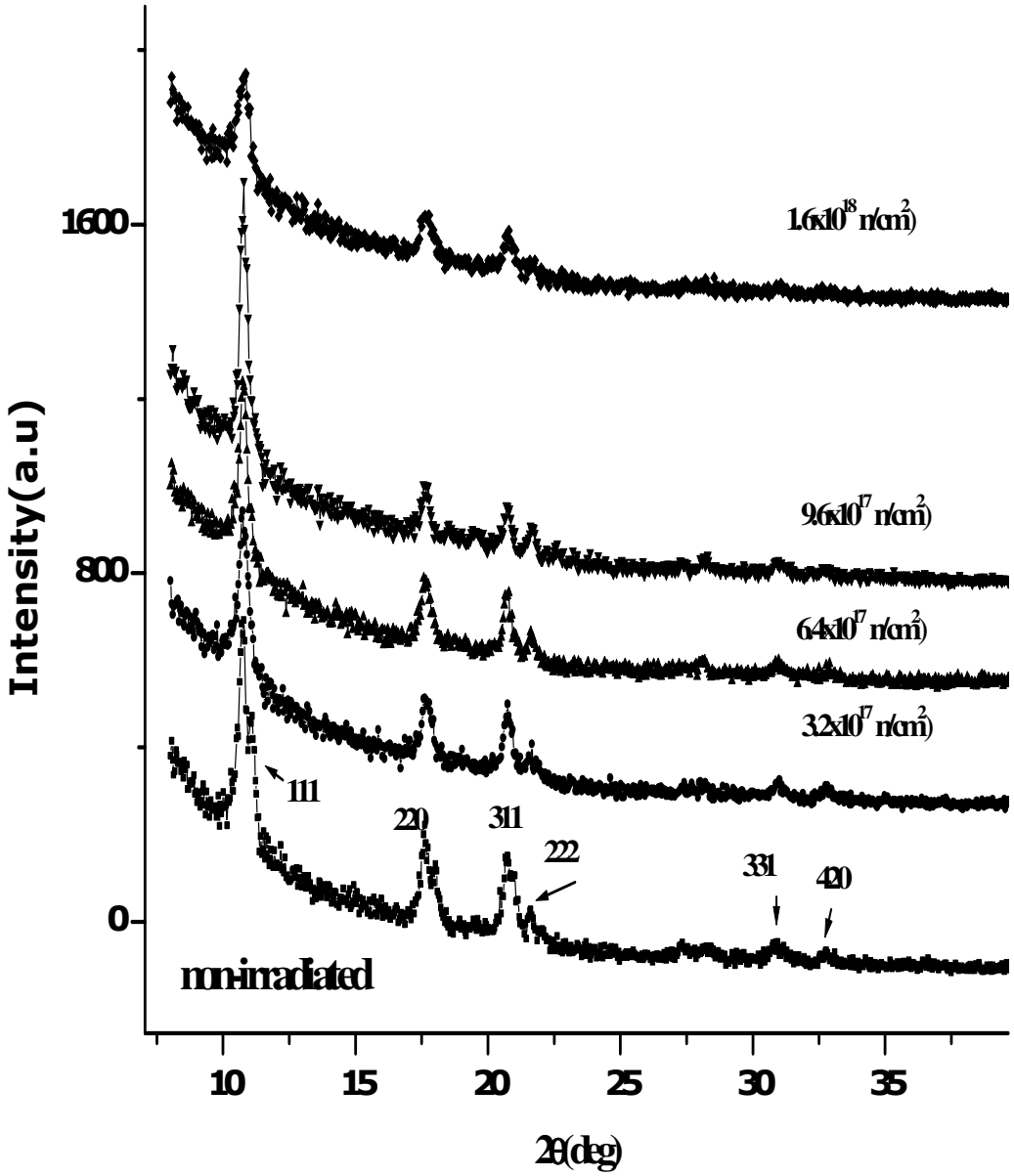

Figure 6.5: GAXRD patterns of C_{60} nano-rods irradiated at different fast neutron fluences.

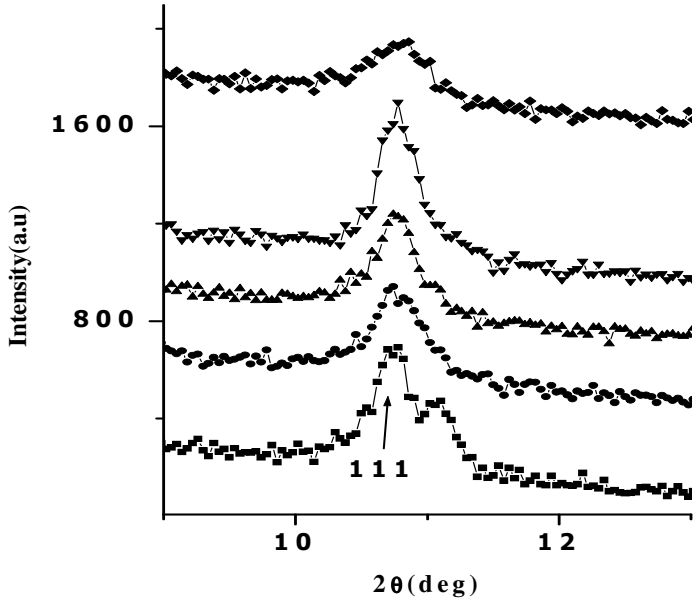

Figure 6.6: GAXRD patterns of C_{60} nanorods irradiated at different fast neutron fluencies for the 111 peak.

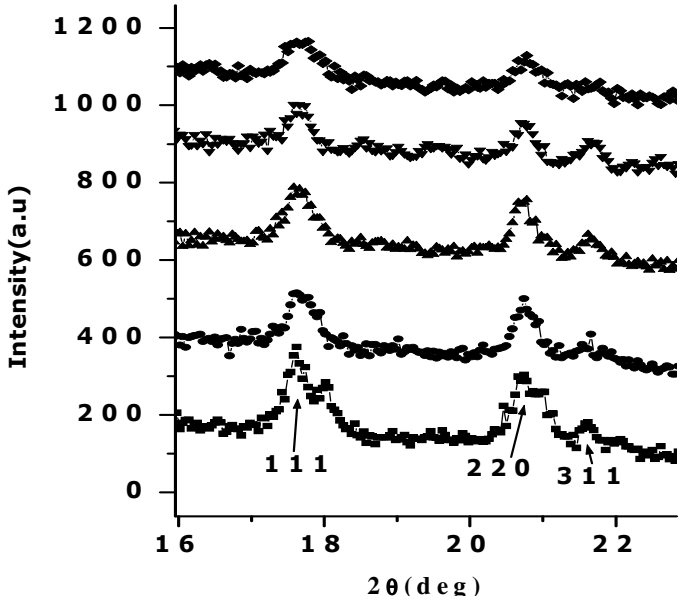

Figure 6.7: GAXRD patterns of C_{60} nanorods irradiated at different fast neutron fluencies for labeled peaks.

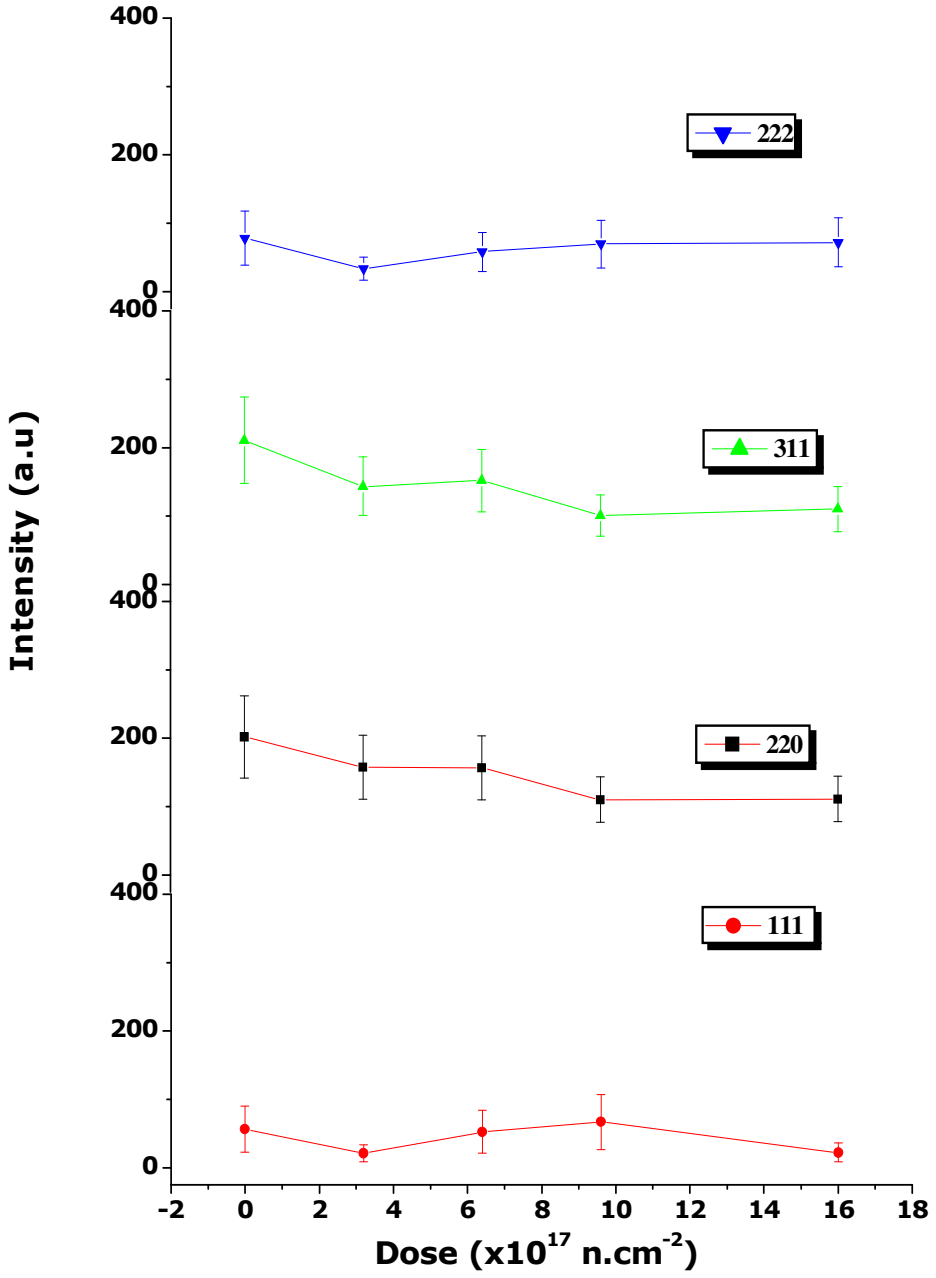

Figure 6.8: Grazing X-ray diffraction peaks intensities fitted with Lorentz fitting for the irradiated nanorods.

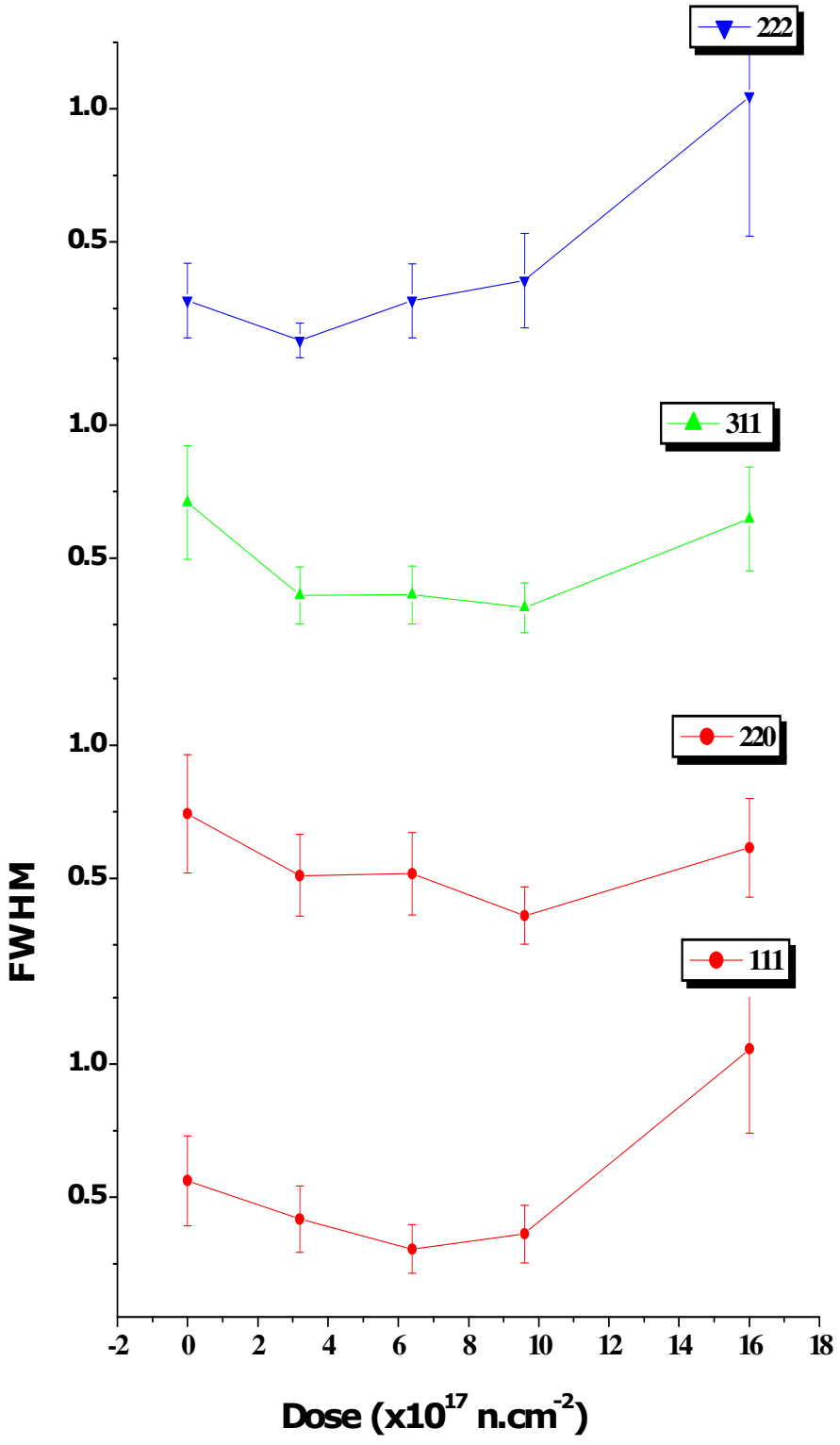

Figure 6.9: Grazing X-ray diffraction peaks FWHM fitted with Lorentz fitting for the irradiated nanorods.

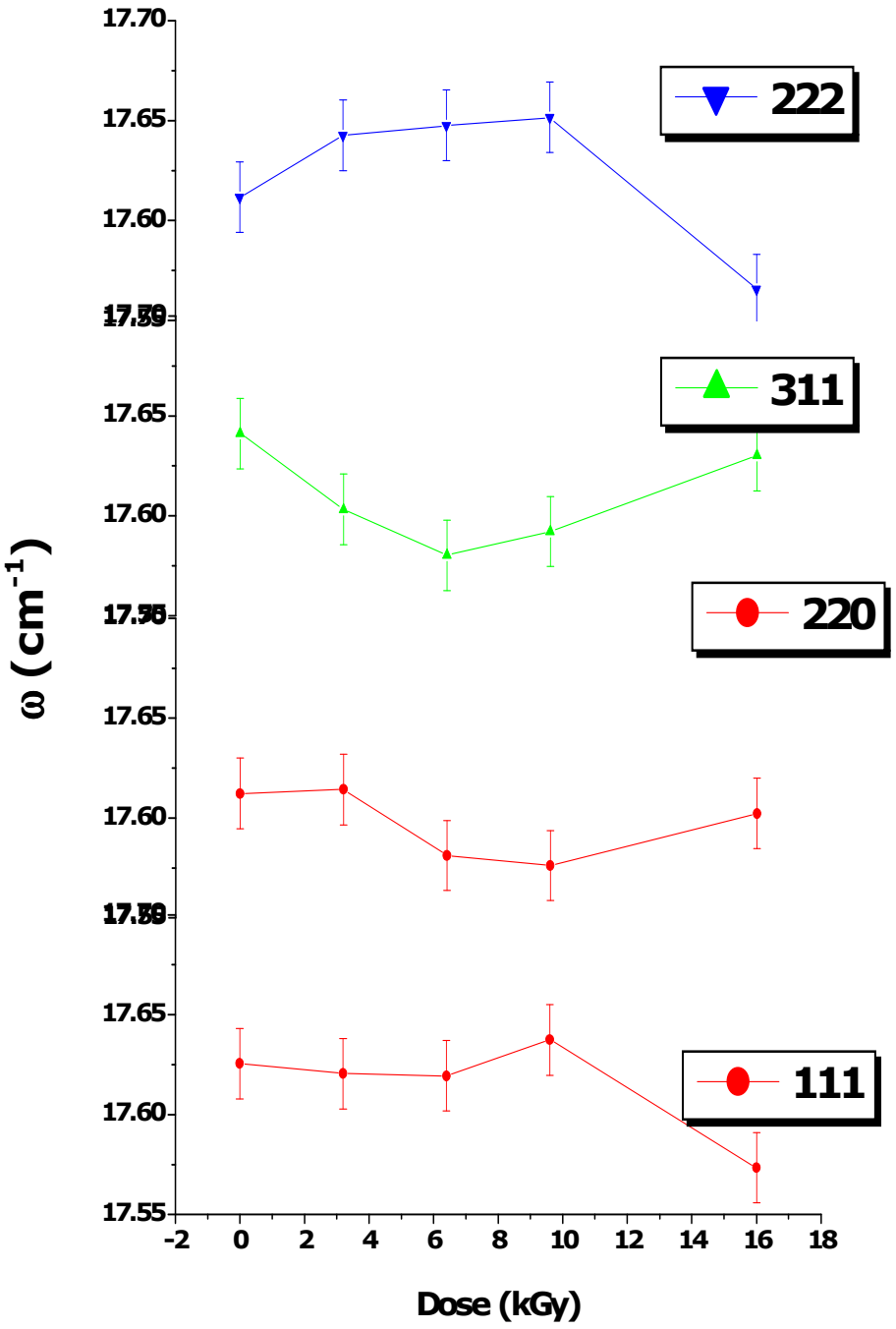

Figure 6.10: Grazing X-ray diffraction peaks FWHM fitted with Lorentz fitting for the irradiated nanorods.

6.4. References

[1] **Khripunov, B.I., Chugunov, O.K., Gureev, V.M., Koidan, V.S., Kornienko, S .N., Kuteev, B.V., Latushkin, S.T., Muksunov, A.M., Petrov, V.B., Ryazanov, A.I., Smirnov, V.P., and Unezhev, V.N.,** Effect of gamma adiation damage on material erosion in plasma, *34th EPS Conference on Plasma Physics Warsaw*, 2 - 6 July 2007 ECA Vol.31F, O-2.003, 2007.

[2] **Rödig, M., Kühnlein, W., Pitzer, D., Merola, M., and Schedler, B.,** Effect of Neutrons on Carbon Based Materials, *10th International Workshop on Carbon Materials for Fusion Applications, Jülich*, Sept. 17 – 19, 2003

[3] **Barabash, V., Federici, G., Linke, J., and Wu, C.H.,** Material/plasma surface interaction issues following neutron damage, *Journal of Nuclear Materials* 313–316, 42–51, 2003.

[4] **Koizlik, K., Linke, J., and Nickel, H.,** Neutron irradiation test matrix for carbon-based materials for the first wall of fusion reactors, *Journal of Nuclear Materials* 179-181, 2, 1100-1103, 1991.

[5] **Burchell, D.,** Radiation damage in carbon–carbon composites: structure and property effects, *Physics Scr* 17, 1996.

[6] **Yu. S. Virgil'ev and Lebedev, I. G.,** Effect of Neutron Irradiation on Properties of Glassy Carbon, *Inorganic Materials* 38, 7, 668-673, DOI: 10.1023/A:1016232223288.

[7] **Maruyama, T., and Harayama, M.,** Neutron irradiation effect on the thermal conductivity and dimensional change of graphite materials, *Journal of Nuclear Materials* 195, 1-2, 44-50, 1992.

[8] **Bonala, J.P, and Wu, C.H.,** Neutron irradiation effects on carbon based materials at 350°C and 800°C, *Journal of Nuclear Materials* 277, 2-3, 351-359, 2000.

[9] **Wu, C.H., Bonal, J.P., Thiele, B., Tsotridis, G., Kwaste, H., Werlef, H., Coad, G., Federicia, G. Vieidera,** Neutron irradiation effects on the properties of carbon materials, *Journal of Nuclear Materials* 212-215, 1, 416-420, 1994.

[10] **Bonal, J.P., and Wu, C.H.,** Neutron irradiation effects on the thermal conductivity and dimensional stability of carbon fiber composites at divertor conditions, *Journal of Nuclear Materials* 228, 2

[11] **Wu, C.H., Bonal, J.P., and Kryger, B.,** The effect of high-dose neutron irradiation on the properties of graphite and silicon carbide, *Journal of Nuclear Materials* 208, 1-2, 1-7, 1994.

[12] **Snead, L.L., Katoh, Y., and Ozawa, K.,** Stability of 3-D carbon fiber composite to high neutron fluence, *Journal of Nuclear Materials* 417, 1-3, 629-632, 2011.

[13] **Barabash, V., Federicim G., Rödig, M., Snead, L.L, and Wu, C.H**, Neutron irradiation effects on plasma facing materials, *Journal of Nuclear Materials* 283-287, 1, 138-146, 2000.

[14] **Bonal, J.P., Thiele, B., Tsotridis, G., and Wu, C.H.,** Neutron induced dimensional changes in carbon materials at high temperatures and high damage doses, *Journal of Nuclear Materials* 212-215, B, 1218-1222, 1994.

[15] **Burchella, T.D., Eatherlya, W.P., Robbinsa, J.M., and Strizaka, J.P.,** The effect of neutron irradiation on the structure and properties of carbon-carbon composite materials, *Journal of Nuclear Materials* 191-194, A, 295-299, 1992.

[16] **Snead, L.L., Burchell, T.D., and Katoh, Y.,** Swelling of nuclear graphite and high quality carbon fiber composite under very high irradiation temperature, *Journal of Nuclear Materials* 381, 1-2, 55-61, 2008.

[17] **Platonova, P. A., Novobratskaya, I. F., Yu. P. Tumanova, Karpukhina, V. I., and Alekseyev, S. I.,** Effect of neutron irradiation on the dimensional stability of graphite pre-treated at different temperatures, *Radiation Effects* 54, 1-2, 1981.

[18] **Atsumi. H., Iseki. M., and Shikama. T.,** Hydrogen behavior in carbon-based materials and its neutron irradiation effect, *Journal of Nuclear Materials* 233-237, 2, 1128-1132, 1996.

[19] **Kubo, T., Terai, T., Suzuki, A., and Chikumoto, N.,** Effect of fast neutron irradiation on magnetic properties of fullerene superconductor Rb_3C_{60}, *Physica C*, 469, 15-20, 1143-1145.

CHAPTER 7

ANNEALLING EFFECTS

Abstract

This chapter focuses on studying the physical effect of temperature on C_{60} nanorods. These nanorods on hydrogen-passivated Si (100) substrates were synthesized via self-assembly LLIP method as discussed in chapter 3 and annealed at different temperatures ranging from 400^0C to 800^0C under 10^{-5} mbar vacuum. All the results from stereo microscope, scanning electron microscope (SEM), Raman are presented and discussed here.

7.1. Introduction

Thermal properties of fullerene C_{60} have drawn much interest to researchers because of their dynamics of interactions between fullerene molecules and its structural phase transition at lower temperatures and at higher temperatures [1,2]. High-pressure-high-temperature (HPHT) treatment of C_{60} crystals on the other hand also allows us to create a new carbon structures such as super hard fullerite materials [3-5]. Fullerene C_{60} crystal can be transformed into different structures when subjected to HPHT i.e. super hard fullerites, amorphous carbon, amorphous diamond.

The super hard fullerites have features similar to the amorphous diamond in its structure and physical properties. HPHT treatment of fullerene C_{60} crystal may create 3D polymers with crystalline and amorphous structures or a cellular nanostructure of mixed sp^2- and sp^3-hybridized carbon atoms under HPHT treatment and shear deformation conditions [6]. Also by application of non-hydrostatic pressure above 20 GPa at room temperature, solid C_{60} is converted into polycrystalline cubic or amorphous diamond. 5 GPa treatment of C_{60} in the 30 ^{o}C and 800 ^{o}C temperature range under quasi-hydrostatic conditions results in the formation of two high-pressure phases with face centered cubic and rhombohedral structure [7-11].

7.2. Experiment details

Fullerene C_{60} nanorods were grown on Si (111) substrate by using a low cost method called liquid-liquid interfacial polymerization method (LLIP) as discussed in chapter 3. Annealing of the fullerene C_{60} nanorods was carried out at 400 ^{o}C, 600 ^{o}C, and 800 ^{o}C in the heating stage of AJA Orion 5 Sputtering System for 2 h under at 10^{-5} mbar vacuum and the samples were allowed to cool down to room temperature

7.3. Results and Discussion

7.3.1. Optical microscope

Figure 7.1 shows optical image taken after the samples were prepared and taken out to be dried in air before annealed at 400 ^{o}C to 800 ^{o}C. Figures 7.2 - 7.4 show images of 400 ^{o}C, 600 ^{o}C and 800 ^{o}C annealed samples respectively taken using optical microscope.

After annealing the diameter of the nanorods decreased and the colour changed from brownish into whitish a colour. At 400 ^{o}C not all nanorods had changed from brownish colour to white, meaning that the transformation of the nanorods is not complete. As the temperature is further increased they are completely changed indicating a complete conversion of the nanorods from brownish to white colour.

Figure 7.1: Optical image of nanorods of fullerene C_{60} on a Si (111) substrate before annealing.

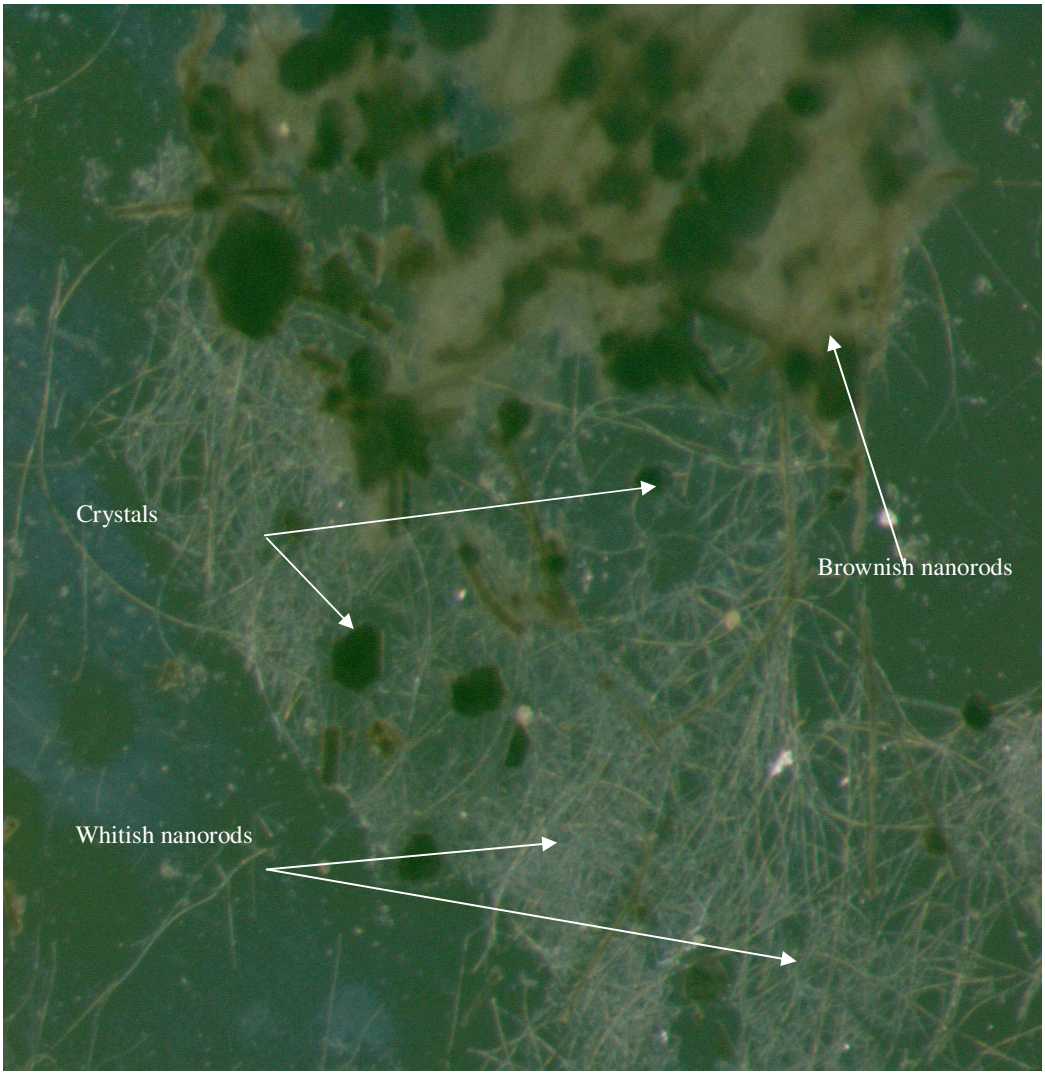

Figure 7.2: Optical image of nanorods of fullerene C_{60} on a Si (111) after annealing at 400 ^{o}C.

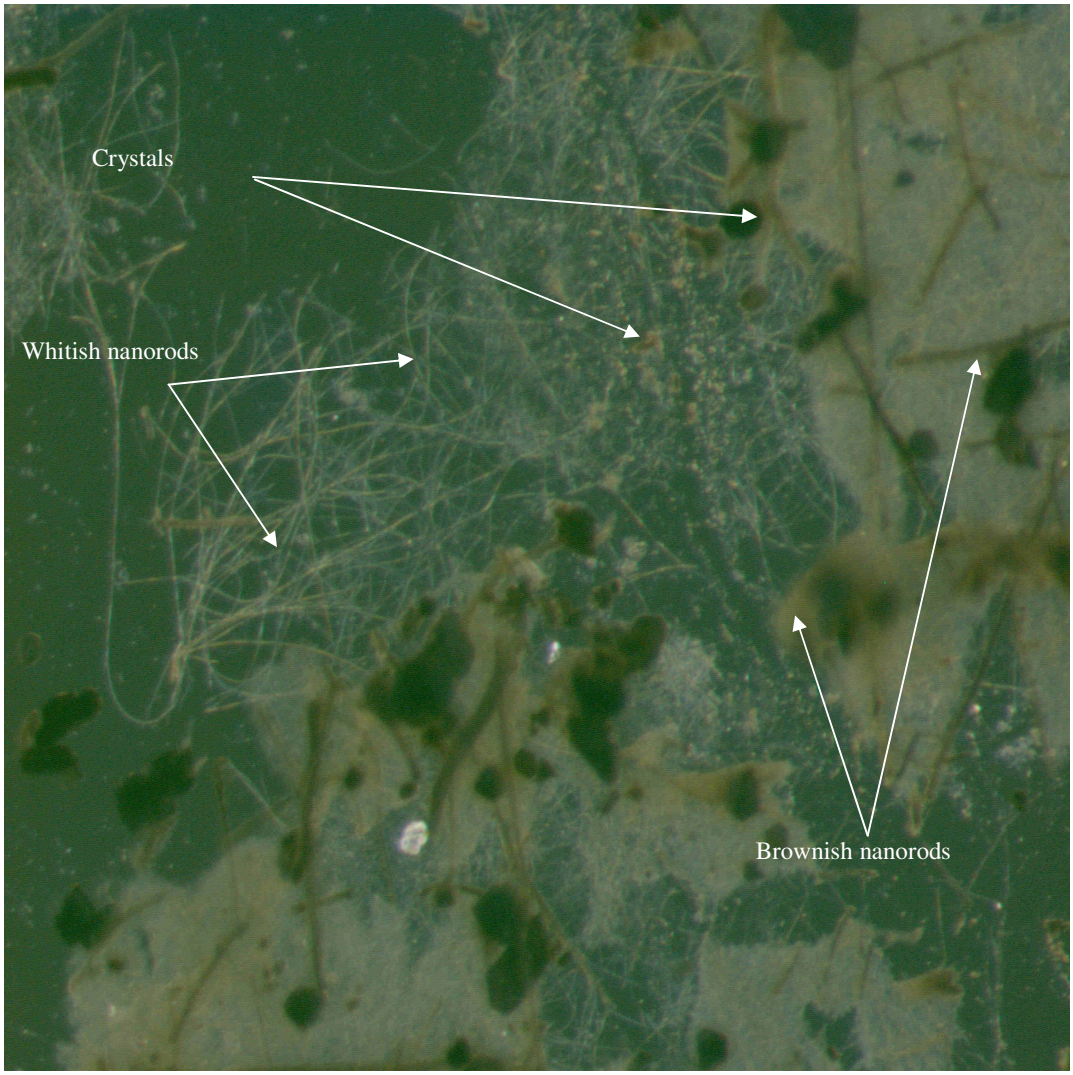

Figure 7. 3: SEM image of nanorods of fullerene C_{60} on a Si (111) after annealing at 600 ^{o}C.

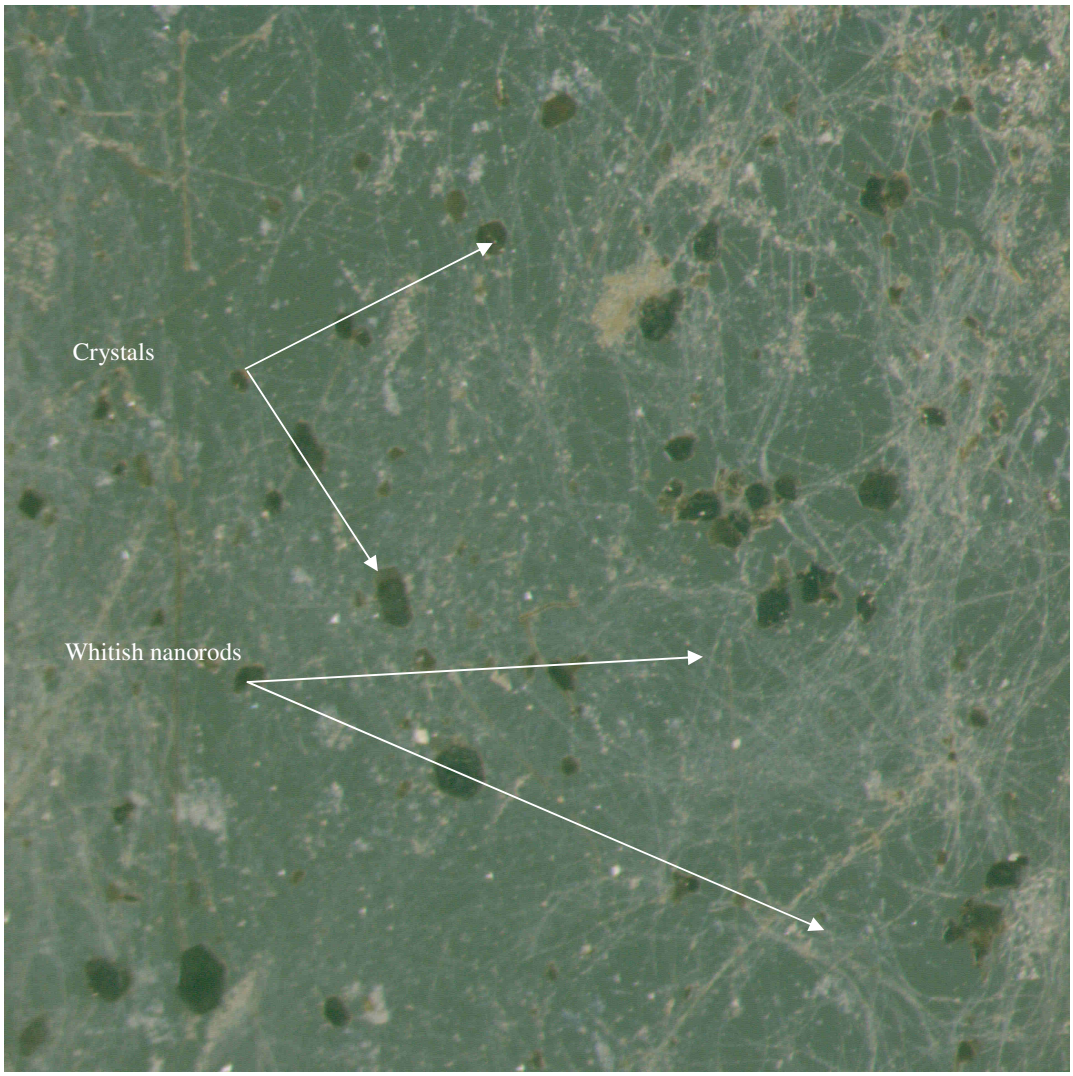

Figure 7. 4: Optical image of nanorods of fullerene C_{60} on a Si (111) after annealing at 800 ^{o}C.

7.3.2. Scanning Electron Microscope (SEM)

As observed from the optical microscopy it is not easy to fully quantify the morphology and the size of the nanorods. Scanning electron microscope (SEM) was therefore used to study the morphology and to determine the sizes of the nanorods. Figure 7.6 shows scanning electron microscope (SEM) image of the C_{60} nanorods before annealing on Si (111) substrate.

Figures 7.7 - 7.9 show the scanning electron microscope (SEM) images of the C_{60} nanorods before annealing and after annealing at 400 ^{o}C, 600 ^{o}C, and 800 ^{o}C for 2 h under vacuum 1.33×10^{-5} mbar. The images clearly show that the annealed C_{60} nanorods are changing in their morphology as evident by their change in diameter as the temperature increases. Comparing the nanorods annealed at 400 ^{o}C with those annealed at 600 ^{o}C is shown in figure 7.7 and figure 7.8, we can see that the C_{60} nanorods are starting to be affected by the heat treatment but are still preserved to some extent.

After annealing treatment at 600 ^{o}C for 2 h as shown in Figure 7.8, the C_{60} nanorods have transformed into amorphous carbon. Furthermore, after annealing treatment at 800 ^{o}C for 2 h the C_{60} nanorods have transformed into some strips of amorphous [26].

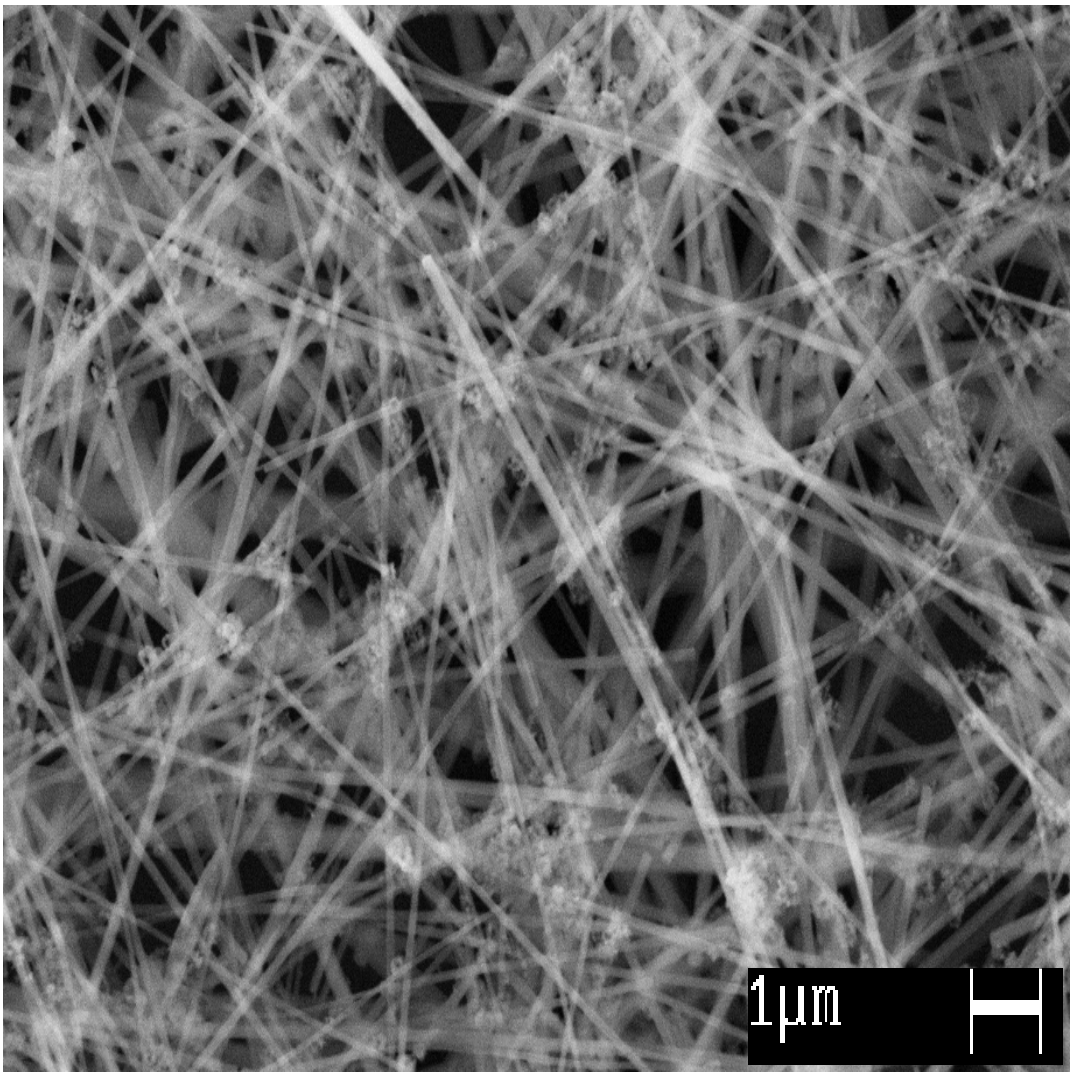

Figure 7.5: SEM image of nanorods of fullerene C_{60} on a Si (111) substrate before annealing.

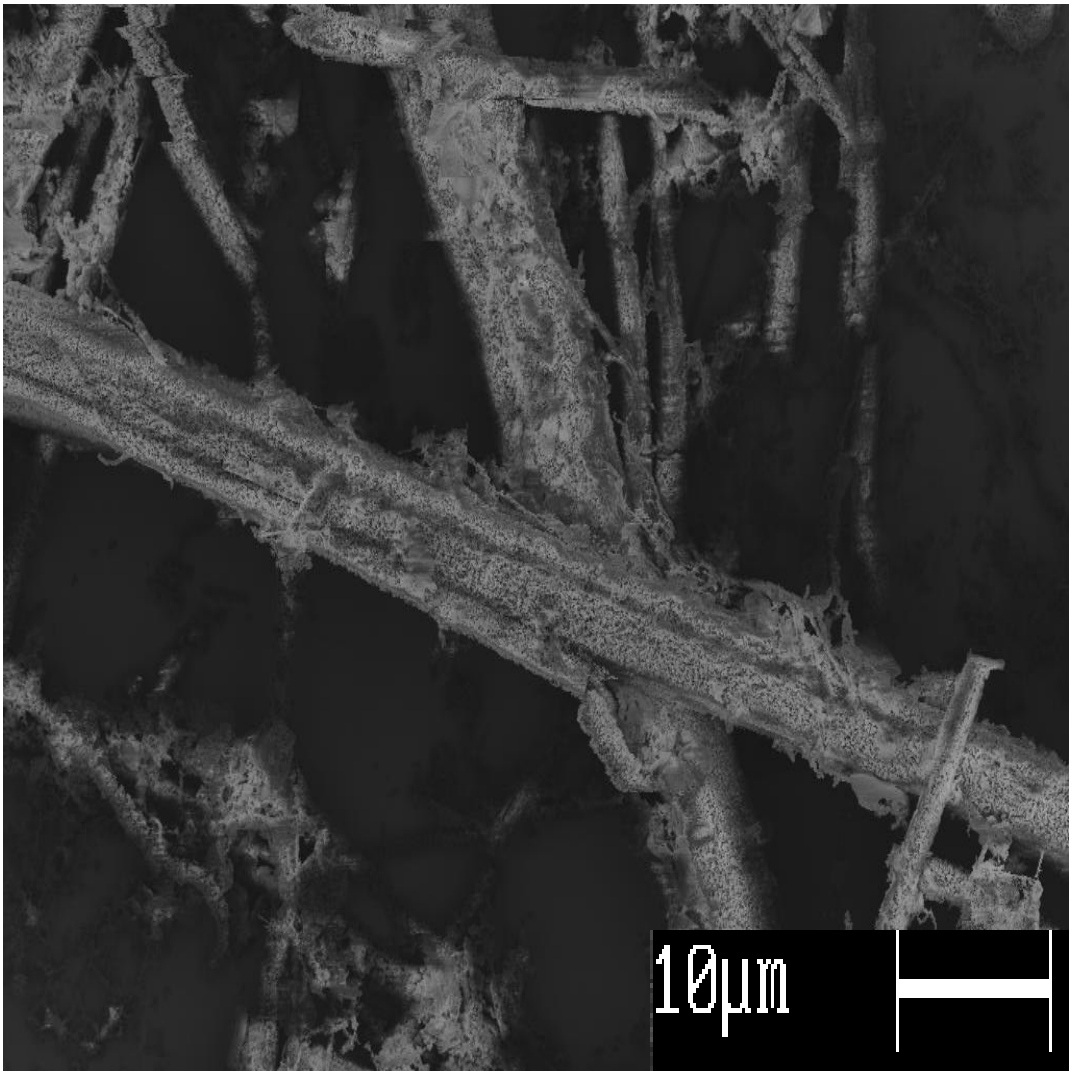

Figure 7.6: SEM image of nanorods of fullerene C_{60} on a Si (111) substrate after annealing at 400 ^{o}C.

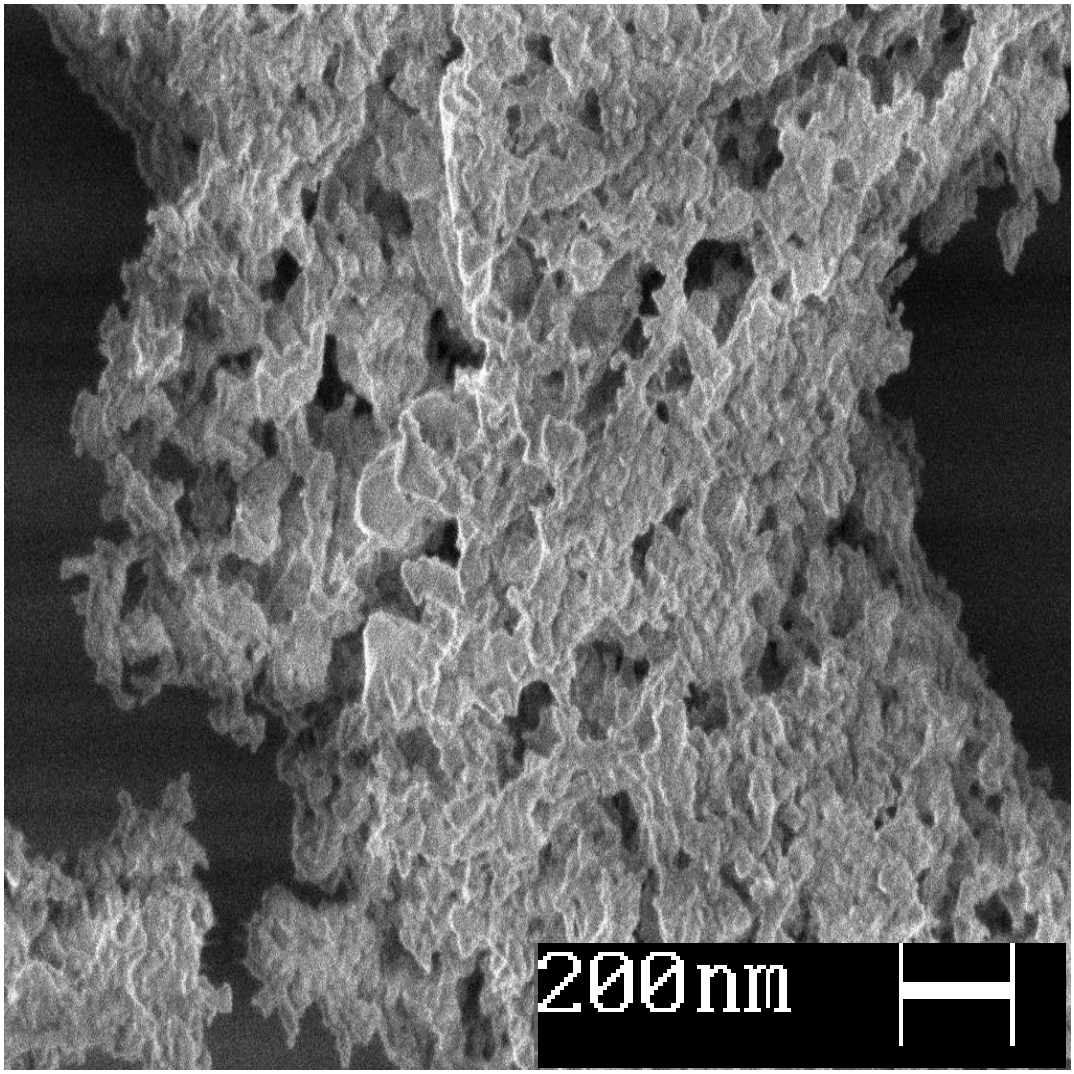

Figure 7.7: SEM image of nanorods of fullerene C_{60} on a Si (111) substrate after annealing at 600 ^{o}C.

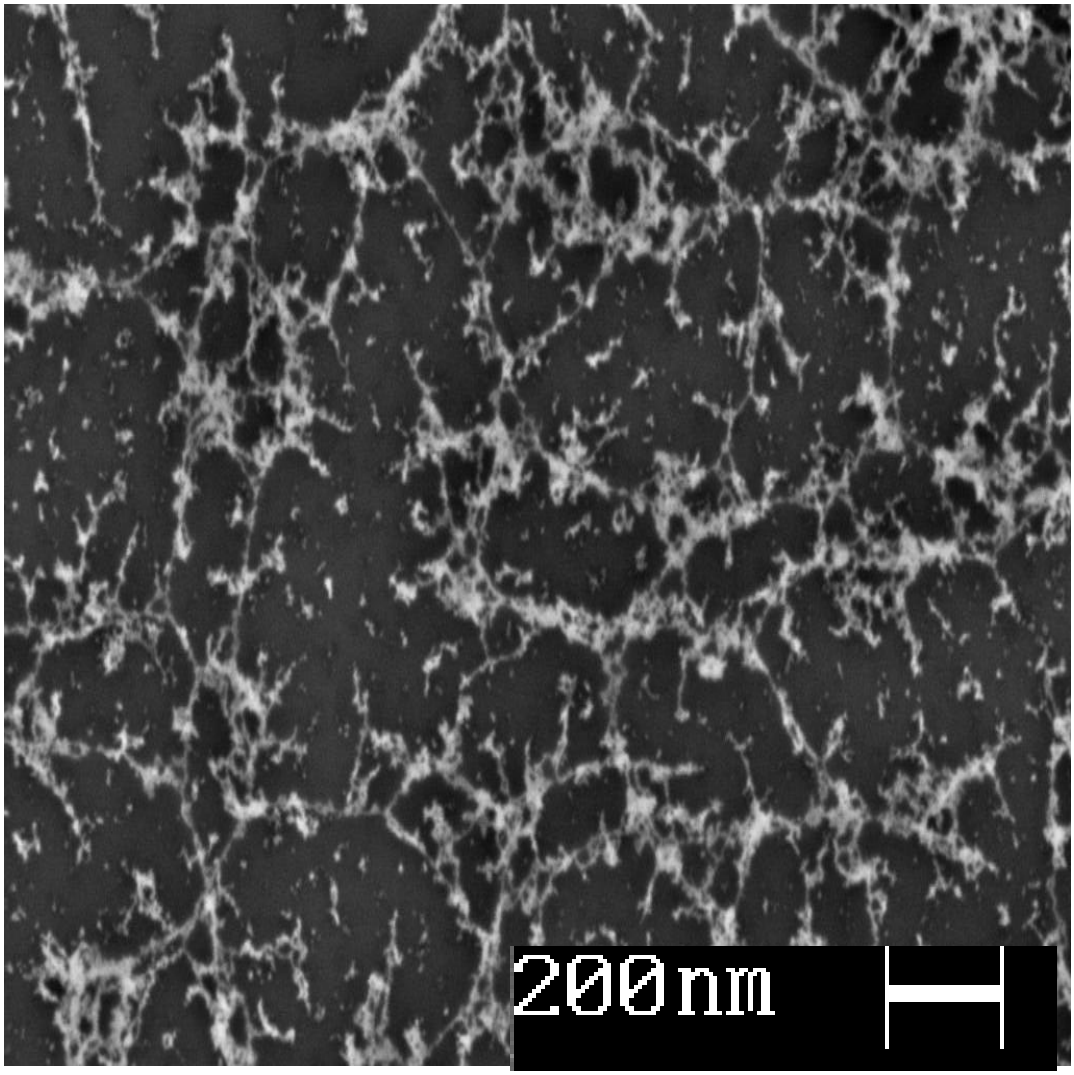

Figure 7.8: SEM image of nanorods of fullerene C_{60} on a Si (111) after annealing at 800 ^{o}C.

7.3.3. Raman spectroscopy

Room temperature experiment was performed in all samples under the same operational conditions. The results of Raman spectroscopy measurements on pristine and irradiated samples are shown in Figure 7.10. All the characteristic modes (two Ag and eight Hg) are labeled in the figures. It can be seen clearly that C_{60} nanorods show all Raman active modes that are present in the C_{60} powder as reported in chapter 4. Apart from the Ag and Hg modes of C_{60}, vibrational mode of the substrate Si is also visible. It can be easily seen that the C_{60} molecule lines around 487 cm^{-1} and 1464 cm^{-1} Ag (1) and Ag (2) respectively, known as 'pentagon pinch' modes and Hg (1) modes are prominent in pristine C_{60} but diminishing as the temperature increases and this indicate the destruction of C_{60} molecule.

To further analyze the results, the characteristic vibrational Ag (1) and Ag (2) mode spectra were extracted and fitted using Lorenzians for 600 ^{o}C and 800 ^{o}C annealed nanorods as shown in Figure 7.11 and figure 7.12. These Raman results confirm the transformation of fullerene nanorods into amorphous carbon [26].

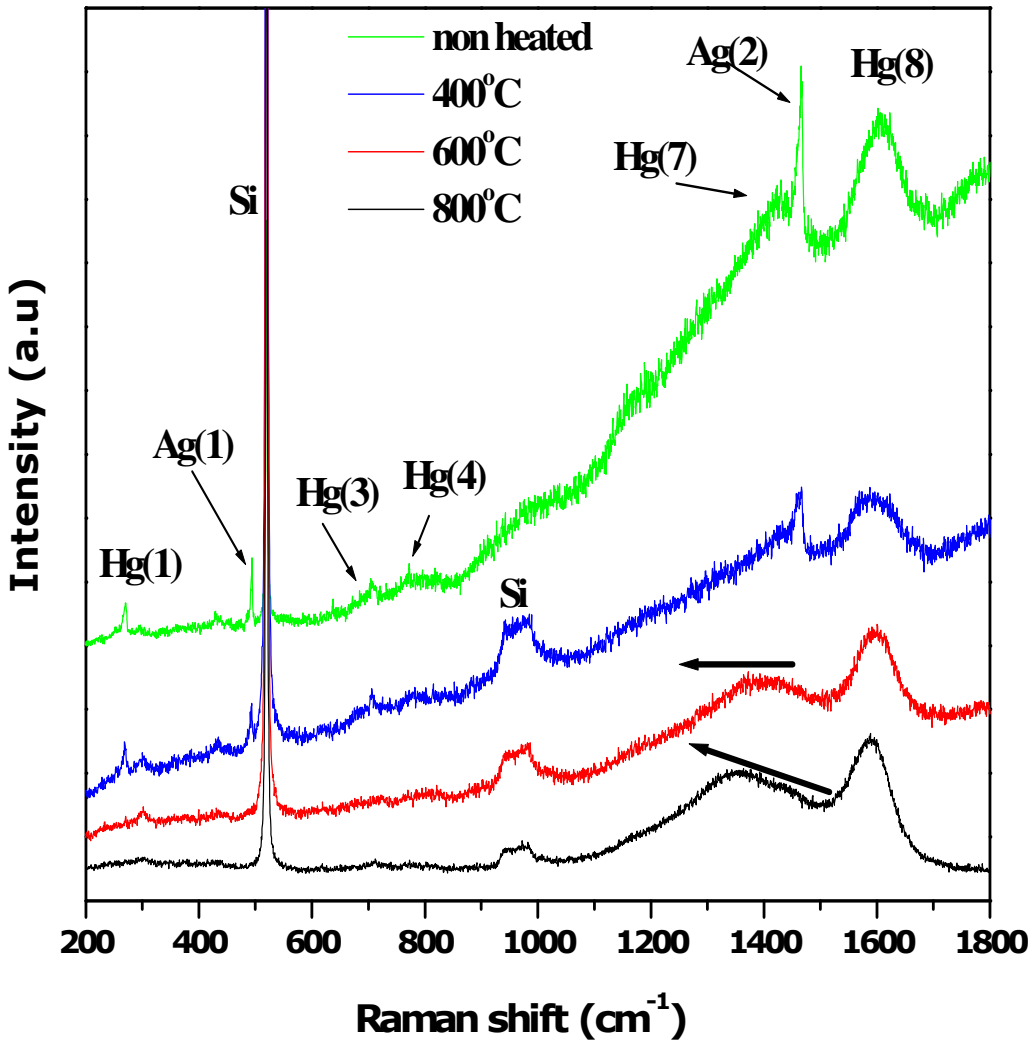

Figure 7.9: Raman spectra of nanorods of fullerene C_{60} on a Si (111) substrate before annealing, at 400 °C, at 600 °C and at 800 °C.

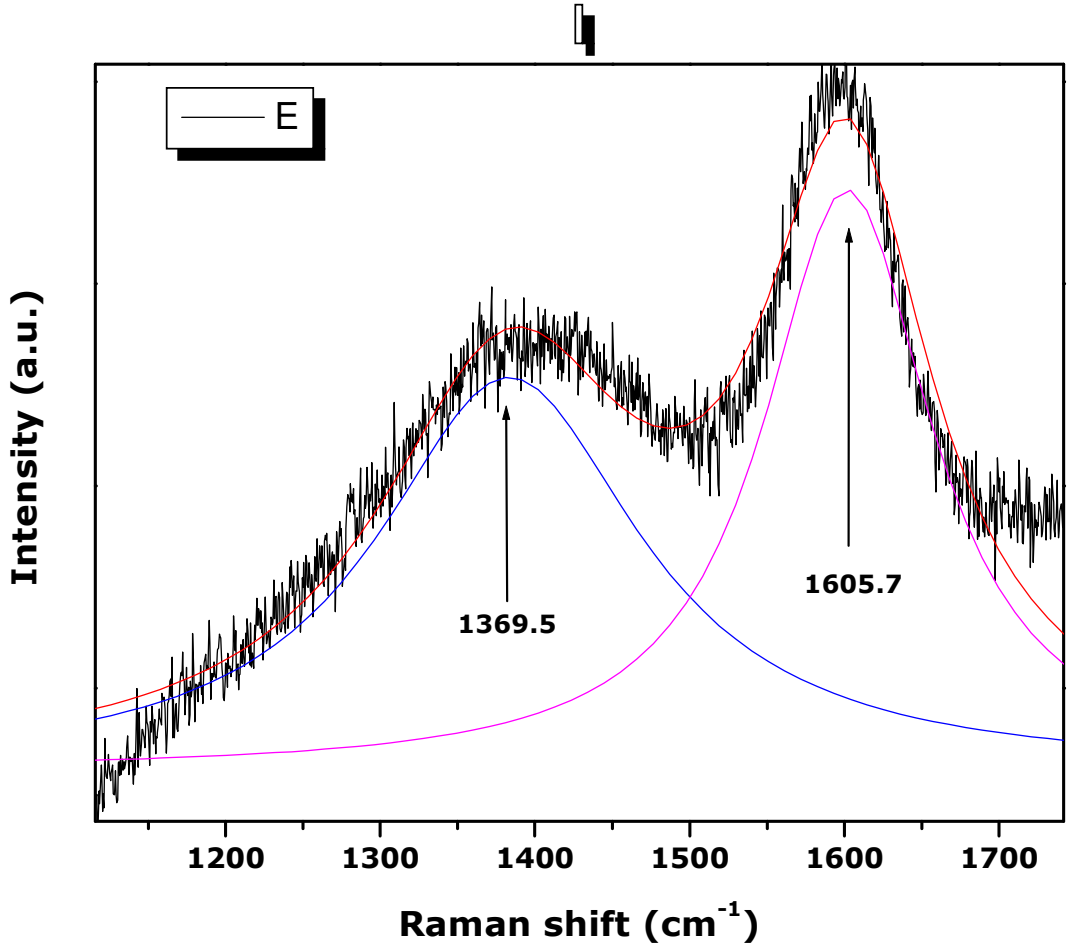

Figure 7.10: Lorentz fitted Raman spectra of nanorods of fullerene C_{60} on a Si (111) substrate annealed at 600 ^{o}C.

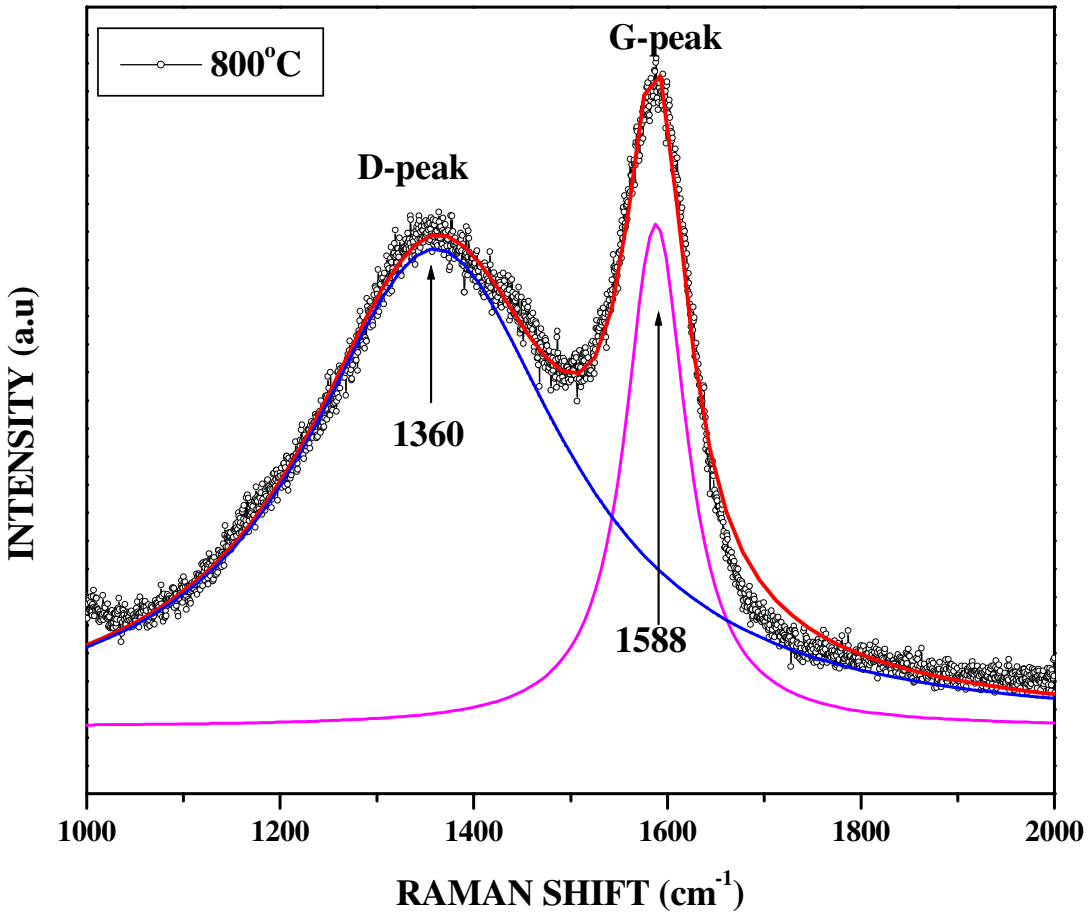

Figure 7.11: Lorentz fitted Raman spectra of nanorods of fullerene C_{60} on a Si (111) substrate annealed at 800 °C.

In this study we have seen the diminishing of the pentagonal pinch mode Ag (2) to such a way that it disappears and the appearance of the D-peak and G-peak at 1360 and 1588 cm^{-1} respectively as shown in table 7.1. According to the literature [26], these peaks are assigned to the formation of the CNT or amorphous carbon.

Table 7. 1: Lorentz fitted values of D- and G-peaks at 600 ^{0}C and 800 ^{0}C.

	Peak	Area	Center	Width	Height	I_D/I_G
600 ^{0}C	G-peak	12823	1605.7	179.53	45.471	
	D-peak	12666	1369.5	244.45	32.985	0.725407
800 ^{0}C	D-peak	22484	1360.1	332.66	43.028	
	G-peak	5370.8	1588.3	76.221	44.859	0.959183

7.4. Conclusion

The results have indicated the formation of new structure with the characteristics of CNT. Raman results showed all characteristic peaks of fullerene C_{60} nanorods in non-heated nanorods but the peaks disappeared when the annealing temperature was increased to 800 ^{0}C. Further vibrational and electronic spectroscopy measurements are necessary to explore the mechanisms involved in the formation of the new structure.

7.5. References

[1] **Kroto, H. W., Heath, J. R., O'Brien, S. C., Curl, R. F. and Smalley, R. E.,** C_{60}: Buckminsterfullerene, *Nature* 318, 162 – 163, 1985; doi:10.1038/318162a0.

[2] **Valsakumar, M. C., et al,** *Physical Review* B 48, 9080–9085, 1993 and Sundar, C.S., Bharathi, A., Hariharan, Y., et al., *Solid State Commununications* 84, 823, 1992.

[3] **Pusztai, T., Oszla´nyi, G., Faigel, G., Kamara´s, K., Gra´na´sy, L., Pekker,** S., *Solid State Communications* 111, 595–599, 1999.

[4] **Guan, L., Suenaga, K., Shi, Z., Gu, Z., Iijima, S.,** Direct imaging of the alkali metal site in K-doped fullerene peapods, *Physical Review Letters* 94, 4, 045502, 2005.

[5] **Lee, J., et al.,** *Nature* 415, 1005, 2002.

[6] **Zeng, C. G., Wang, H. Q., Wang, B., Yang, J. L., and Hou, J. G.,** *Applied Physics Letters* 77, 3595, 2000

[7] **Kopelevich, Y., and Esquinazi, P.,** Ferromagnetism and Superconductivity in Carbon-Based Systems, arXiv: cond-mat/0609497 v1 (2006).

[8] **Krasheninnikov, A.V., and Banhart, F.,** *Nature materials* 6, 2007

[9] **Saito, R., Fujita, M., Dresselhaus, G., Dresselhaus, M.S.,** Electronic structure of chiral graphene tubules, *Applied Physics Letters* 60, 2204, 1992.

[10] **Mintmire, J. W., Dunlap, B. I., and White, C. T.,** Are fullerene tubules metallic? *Physical Review Letters* 68, 631, 1992.

[11] **Schluter, M., Lannoo, M., Needels, M., and Baraff, G. A.,** Electron-phonon coupling and superconductivity in alkali-intercalated C_{60} solid, *Physical Review Letters* 68, 526, 1992.

[12] **Hamada, N., Sawada, S., and Oshiyama, A.,** New one-dimensional conductors: Graphitic microtubules, *Physical Review Letters* 68, 1579–1581, 1992.

[13] **Changa, C.W., et al.** *Solid State Communications* 128, 359–363, 2003.

[14] **David, W. I. F., Ibberson, R . M., et al.** *Europhysics Letters* 18, 3, 219-225, 1992.

[15] **Blank, V. D., et al.,** *Physics Letters* A, 220, 149, 1996.

[16] **Brazhkin, V. V., et al.,** *Physical Review* B, 56, 11465, 1997.

[17] **Blank, V. D., et al.,** *Physica* B, 339, 39, 2003.

[18] **Horikawa, T., Suito, K., Kobayashi, M., and Oshima, R.,** *J.J.A.P.,* 44, 3141, 2005.

[19] **Blank, V. D., et al.,** *Physics Letters* A, 220, 149, 1996.

[20] **Regueim, M.N., Monceau, P., and Hodeau, J.L.,** *Nature* 355, 237, 1992.

[21] **Hirai, H., and Konda, K.,** *Applied Physics Letters* 64, 1797, 1994.

[22] **lwasa, Y., et al.,** *Science* 264, 1570, 1994.

[23] **Bashkin, S.I.,** *Journal of Physics: Condense Matter* 6, 7491, 161, 1994.

[24] **Kozlov, M. E., and Yakushi, K.,** *Journal of Physics: Condense Matter* 7, 1999, (L209-LZ16)

[25] **Miyazawa K., Minato J., Yoshii T., Suga T.,** Characterization of fullerene nanotubes prepared by the liquid–liquid interfacial precipitation method, *Science and Technology of Advanced Materials* 6, 388–393, 2005.

[26] **Wang, Y.Y., et al.,** *Diamond and Related Materials* 13, 1287–1291, 2004.

CHAPTER 8

CONCLUSION AND OUTLOOK

8.1. Synthesis of nanorods

The nanorods of C_{60} were successfully synthesized as described in chapter 3, and characterized using the techniques described in chapter 2. The average diameters of most nanorods were ranging from ~100 to ~900 nm, while the average length of most is several hundreds of micrometers. The majority of the C_{60} nanorods have a diameter below 400 nm and the finer ones were found to have a diameter ≤ 200 nm.

Structural investigation was done on the pristine C_{60} powder used in the synthesis and also on the non-irradiated C_{60} nanorods. As expected, the structure of the synthesized nanorods cannot be exactly the same as that of pristine C_{60} due to compact structure of nanorods which induces minimal stress. Thus, the result of this induced minimal stress caused the difference in peaks' intensities and minor shift in Raman and XRD spectra. The Rietveld treatment showed the C_{60} nanorods to have a lattice parameter of ~1.415 Å, this is very close to the bulk value of 1.417 Å, indicating that the non-irradiated nanorods C_{60} are under a minimal stress.

8.2. Protons irradiation

Proton irradiation investigation has revealed some interesting properties in relation to the structure and optical point of view, which could be utilized in the near future applications. Firstly, this study has revealed that after proton irradiation, the colour of the nanorods had changed from brownish into reddish colour. This change is attributed to optical band gap alteration which results in more loosely bound π-electrons being excited by the energies in the visible light.

Secondly, protons induced a change in the structure of nanorods which is attested by the Raman and FTIR spectra recorded in chapter 4. In all the figures from Raman spectroscopy, we noticed a variation of different characteristics of the spectra such as intensity, shift, and FWHM as a function of increased fluence. These are vital characteristics when it comes to

structural investigations in solids. The behaviour of a sensory Ag (2) mode has indicated an increase in the bond population between C_{60} molecules. It should be noted that this increase does not come without breaking of certain bonds; there should be breaking and reattachment of bonds which then results in the reorganization of the whole structure. Hence, sensory Ag (2) mode has the ability to pick that up as we have observed and discussed in this investigation (chapter 4). The population of broken and re-attached bonds is noticeable above the threshold value of 5.4 10^{16} ions/cm^2. This reorganization could result to the formation of C_{60} nanotubes with the same outside appearance but hollow inside as reported by reference [18].

Furthermore, FTIR has confirmed the transformation and rearrangement of the structure which is seen by the suppression of sensitive FTIR mode of C_{60} at 1428 cm^{-1} (t1u (4)). This means that proton irradiation induces chemical modification with the nanorods which then results in a change in the optical properties connected with structural changes. The peak at 1428 cm^{-1} (t1u (4)) for the non-irradiated disappear after proton irradiation, which indicates additional polymerization that could attribute to the formation of various structures as reported by reference [18].

In addition, XRD confirmed the presence of induces stress which resulted in the shifting of the Bragg peaks indicating change in d-spacing. We can conclude that, 2MeV protons rearranged the structure and induce twinning of crystal planes as observed in HRTEM images.

Thirdly, it was discovered that proton irradiation at 2 MeV enhanced surface adhesion between the nanorods and the substrate (Si) as reported in chapter 4.

Fourthly, it was discovered that proton irradiation at 2 MeV enhanced insolubility of C_{60} nanorods in toluene solvent as reported in chapter 4. SEM showed no changes due to toluene.

Lastly but not the least, magnetic signal was observed. The drive behind this investigation is because of the necessity of having biological compatibility, light weight and low cost, with room temperature carbon-based metal-ion free magnet. We have observed that at 150 K, the irradiated sample show diamagnetic behaviour but as the temperature is changed magnetization tends to increase and saturate below 40 K. It can also be observed that the magnetization data in the temperature range of 2 - 200 K, in 1 T applied field, for the

irradiated nanorods show is temperature dependence. This results form the background of our long term project.

8.3. Gamma irradiation

Gamma irradiation revealed interesting behavior of nanorods when investigated using Raman spectroscopy. The structural transformation or structural reorganization occurs in stages as observed and discussed in chapter 5. At low doses the breaking and reattachment of bonds was minimal which can be called phase or stage 1 as shown in the figures but as the dose is increased there was a sudden reorganization that led to the second stage. We can say that in stage 1 the energy of gamma rays was being absorbed by the bond between individual molecules up until the bonds could no longer resist but then broke (between stage 1 and 2) and start reorganizing to reach saturation at stage 2 where the structure is stable. The process repeats itself to stage 3. We can say that under gamma irradiation the nanorods did not reach a stage where they can be destroyed completely at least in the range up to 1000kGy. FTIR as a complementary technique to Raman has shown almost the same behavior with SEM showing no sign of damage.

8.4. Neutron irradiation

Neutron irradiation induced maximum damage on the nanorods. At a moderate fluence the nanorods still survived but as the fluence is increased they disintegrated into small pieces. This is due to the fact that at higher fluence, a maximum kinetic energy of about 570 keV can be transferred from fast neutrons of 2 MeV to carbon nucleus via elastic collision resulting in ion displacements which produced large cascade of multiple displacements. Hence, C_{60} nanorods cannot stand for higher neutron fluencies. These defects destroy the crystallinity and probably induce the breaking of the carbon rods.

8.5. Annealing effects

Annealing nanorods at high temperature has revealed that they cannot be used in high temperature environment. After annealing, the diameter of the nanorods decreased and the

colour changed from brownish to whitish. At 400 ^{o}C not all nanorods had changed from brownish colour to white, meaning the transformation of the nanorods is not complete. As the temperature is further increased they are completely changed, then there is a complete conversion of the nanorods from brownish to white colour. After annealing treatment at 600 ^{o}C for 2 hours, the C_{60} nanorods have transformed into amorphous carbon. Furthermore, after annealing treatment at 800 ^{o}C for 2 hours the C_{60} nanorods have transformed into some strips of amorphous with the Raman signature as reported by reference [26].

8.6. Appendix

Table 1. 1: Summary of major physical characteristics of C_{60} molecules

Quantity	Value
Average C-C distance	0.144nm (1.44Å)
C-C bond length on a pentagon	0.146nm (1.46 Å)
C-C bond length on a hexagon	0.14nm (1.40 Å)
C_{60} mean ball diameter	0.7nm (7.0 Å)
C_{60} out diameter	1.034nm (10.34 Å)
Binding energy per atom	7.4 eV
Electron affinity	2.65±0.05 eV
First ionization potential	7.58 eV
Second ionization potential	11.5 eV
Optical absorption edge	1.65 eV
Refractive index at 600nm)	2.2
Absorption coefficient at 220nm)	6.07×10^{-5} cm^{-1}

Table 1. 2: Physical constants for the crystalline C_{60} in the solid state.

Parameter	Value
fcc lattice constant	1.417nm(14.17 Å)
C_{60}-C_{60} distance	1.002nm(10.02 Å)
C_{60}-C_{60} cohesive energy	1.6 eV
Tetrahedral interstitial site radius	0.112nm(1.12 Å)
octahedral interstitial site radius	0.207nm(2.07 Å)
Mass density	1.72g/cm^3
Compressibility (-dlnV/dP)	6.9 x10^{-12}cm^2/dyn
Young's modulus	15.9 GPa
Transition temperature	261 K
Optical absorption edge	1.7 eV
Thermal conductivity(300K)	0.4 W/mK
Electrical conductivity(300K)	1.7 x10^{-7} S/cm
Sublimation temperature	800K

Table 1. 3: Summary of possible application of fullerene C_{60} **[69].**

Applications	Description
Organic photovoltaics(OPV)	Fullerene can be used as organic photovoltaics where it acts as the n-type semiconductor (electron acceptor)
Antioxidants and biopharmaceuticals	Fullerenes are powerful antioxidants, there are used in skin care products to prevent free radical from damaging cell and other medical applications i.e. drug delivery.
Skin care products	Anti-oxidation & anti-aging, Myth of keeping YOUTH. Instant moisturized. Long lasting moisturizing and deep nourishment. Completely block out melanin to regain whitening. Improve the skin of fine lines and the elasticity.
Polymer additives	Fullerenes and fullerenic black are chemically reactive and can be added to polymer structures to create new copolymers with specific physical and mechanical properties. They can also be added to make composites. Much work has been done on the use of fullerenes as polymer additives to modify physical properties and performance characteristics.
Catalysts	Marked ability to accept and to transfer hydrogen atoms; hydrogenation and hydrodealkylations. Highly effective in promoting the conversion of methane into higher hydrocarbons. Inhibits coking reactions.
Vehicles	Enhanced durability, lower heat build-up, and better fuel economy with use of fullerene black/rubber.